AN APPROACH TO DETERMINING REASSESSMENT INTERVALS THROUGH CORROSION

Final Report
SwRI® Project 18.11027
Contract Number: DTRS 56-04-T-0002

Prepared for

U.S. Department of Transportation
Pipeline Hazardous Materials Safety Administration
400 Seventh Street, SW, Room 2103
Washington, DC 20590

Prepared by

Frank Song and Narasi Sridhar
Southwest Research Institute®
6220 Culebra Road
San Antonio, TX 78238

October 2006

SOUTHWEST RESEARCH INSTITUTE®
SAN ANTONIO HOUSTON WASHINGTON, DC

AN APPROACH TO DETERMINING REASSESSMENT INTERVALS THROUGH CORROSION

Final Report
SwRI® Project 18.11027
Contract Number: DTRS 56-04-T-0002

Prepared for

U.S. Department of Transportation
Pipeline Hazardous Materials Safety Administration
400 Seventh Street, SW, Room 2103
Washington, DC 20590

Prepared by

Frank Song and Narasi Sridhar
Southwest Research Institute®
6220 Culebra Road
San Antonio, TX 78238

October 2006

APPROVED:

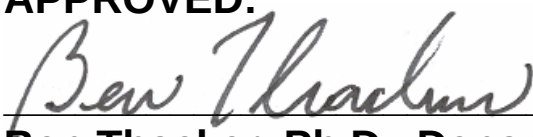

Ben Thacker, Ph.D., Department Director
Materials Engineering Department

EXECUTIVE SUMMARY

Problems Statement

For natural gas pipelines, the Code of Federal Regulations, Title 49, Part 192, Sub-part 939 defines the maximum integrity reassessment interval to be seven years. Depending on the pipeline operating conditions, the reassessment interval can be extended to 10 years for pipelines operating at greater than 50% of Specified Minimum Yield Strength (SMYS), 15 years for pipelines operating at 30 to 50% of SMYS, and 20 years for pipelines operating below 30% of SMYS. Although the growth of a defect is governed by a number of factors such as, cyclic loading and stress corrosion cracking, the most important factor leading to defect growth is corrosion. It is important that the corrosion rate be determined for a confident estimation of the pipeline reassessment interval.

Corrosion of pipelines can be either from the soil side (external corrosion) or from the product side (internal corrosion). For external corrosion, the corrosion rate can depend on seasonal weather conditions (e.g., temperature, precipitation, water table level and movement, freeze-thaw cycles), geography (e.g., dry land, river bottom, transition zones, casings), soil chemistry (e.g., pH, chloride concentration, resistivity, presence of bacteria), the adequacy and distribution of cathodic protection (CP), degradation and performance of the coatings and the interactions between CP and coatings. For internal corrosion of gas pipeline, the corrosion rate can depend on gas quality (CO_2, H_2S, O_2, water contents, presence of solids, bacteria), inhibitor, temperature, gas flow parameters, and the elevation profile of the pipeline. The internal corrosion of liquids pipeline can depend on the water cut, segregation of aqueous layer, hydrocarbon content, inhibitors, and other impurities (e.g., salt). Because these conditions vary along a pipeline and change with time, the corrosion rates can also vary from location to location and can be time-dependent. Despite the complexity of the environmental and pipeline conditions, the corrosion rate must be estimated to determine the reassessment interval.

In the field, successive inline inspection (ILI) runs are performed to determine the defect size and the corrosion rate for piggable pipelines. The alignment of successive pig runs and the identification of ILI anomalies with corrosion induced defect can be challenging. For non-piggable pipelines, the corrosion rate and hence, the reassessment interval rely on a combination of corrosion monitoring and rate prediction. However, the corrosion monitoring has limitations in that it is difficult to know *a priori* the best location for placing the monitoring probe, particularly for wet gas internal corrosion and external corrosion. Lacking pipeline-specific corrosion rate data, the NACE Recommended Practice for External Corrosion Direct Assessment (ECDA, RP0502) suggests a corrosion rate of 0.4 mm/y (16 mils per year) based on long-term studies of unprotected, buried, steel objects. For internal corrosion, there is at present no recommended corrosion rate. A general approach is proposed in this project to estimate external and internal corrosion rates.

Approach

The overall approach to developing methods for corrosion rate estimation is illustrated in Figure E-1. In this approach, the detailed physical models (also called physics-based or

mechanistic models) form the foundation for estimation of the corrosion rates. The main advantage of such models is they are developed based on natural laws or fundamental principles and can be applied to a broader range of conditions where no experimental data is yet available and development of such data is prohibitively expensive or impossible. Because the physical models depend on fundamental parameters that are independent of a specific field application, they often have access to a wider range of data. For example, electrochemical parameters such as, Tafel slope for iron oxidation, used to estimate corrosion rate, are not predicated on the use of steel in a pipeline application. These models and parameters are valid whether they are used for a pipeline or rebar in metal-reinforced concrete as long as the corrosion mechanisms do not change. On the other hand, purely empirical data cannot be extended beyond the specific application for which they were developed since the parameters in the model have no physical meaning and it is unclear whether they will depend on the corrosion mechanisms, the environmental parameters and material properties. The detailed physical models also have the disadvantage of being mathematically complex and difficult to use by field personnel whose expertise is not in theoretical corrosion modeling. Furthermore, these models cannot incorporate all the complexities of field conditions unless the mechanism effects by the corrosion factors are all clear.

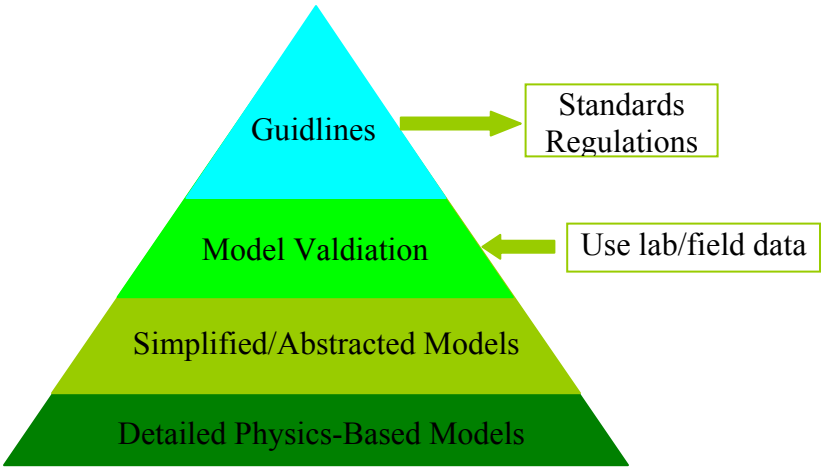

Figure E-1. Illustration of the tiered approach to corrosion rate estimation.

Simplified or abstracted models are the next level of user friendliness in application. These models, to be fundamentally sound, must be developed following fundamental principles and their predictions of corrosion rate must be consistent with those of the detailed models. One effective and reliable way to develop such simple models is to simplify the detailed physics-based models based on rate controlling mechanisms and for each mechanism, only the critical variables that control the rate are used in the model. The number of model parameters thus reduced reduces the complexity of the model. This is an approach that has been successfully used in other industries. This is different from the approach to developing empirical models which rely purely on correlation of experimental data without fundamental support and therefore, have distinct disadvantages in being not confident in use for rate prediction beyond the experimental data range. The exact relationship between the simplified model and the detailed model may

vary for different applications. For pipeline corrosion rate estimation purposes, we developed simple models that have sound fundamental bases whose prediction of corrosion rates can be confident. These simplified models should be validated further with laboratory or field data to ensure that the models can indeed be useful for the specific practical prediction of the corrosion rate. From the simplified models, guidelines are developed for what critical parameters in the field need to be measured before the local corrosion rate can be estimated. These guidelines can be directly incorporated in standards or regulatory documents.

In this study, the development of the guideline for corrosion rate estimation involved five tasks: (1) external corrosion model and rate prediction for pipeline corrosion under a disbonded coating with a holiday, (2) internal corrosion model and analysis for internal pipeline corrosion in the presence of CO_2, H_2S and O_2, (3) validation of the model with independent laboratory data, (4) validation of the model with independent laboratory data and with field data, (5) report and publication of the work to public domain.

A modeling framework that can consider both external and internal corrosion is presented in Section 2. Because of the plethora of environmental operating conditions impacting a pipeline, comprehensive modeling of all the scenarios is not possible within a finite project resource. Reasonably conservative but application oriented pipeline corrosion scenarios are used for developing corrosion rate estimates. For external corrosion, a model is developed in Section 3 and validated with extensive laboratory data in Section 5 for active pipeline steel corrosion under a disbonded coating with a holiday, with and without flow. For internal corrosion, the model was developed in Section 4 and validated with independent laboratory and field data in Section 6 for active pipeline steel corrosion under a solution layer in gas containing CO_2, H_2S, and O_2. A summary of the results and recommendations for the use of the results in operations and for future work are provided in Section 7.

Results

External Corrosion

By investigation of the effects of critical variables on the corrosion rate under disbonded coating with a holiday for neutral or alkaline pH soil chemistry, the following results are found:

- Without convective flow in the disbondment, if CP is effective near the holiday region, the corrosion rate at the holiday is negligibly low. Inside the disbondment where CP is ineffective, the corrosion rate is negligibly low only if the pH is neutral and alkaline.

- Without convective flow in the disbondment, either without CP or with inadequate CP, the corrosion rate is high near the holiday and decreases into the disbondment, provided the O_2 concentration in soil solution near the holiday is high.

- Without convective flow, corrosion under a disbonded coating in aerated soil solution can be measured by simulation test in lab by using deaerated solution.

- Without convective flow, a simple algorithm has been developed following sound fundamental principles and can reproduce the comprehensive disbondment corrosion model. This simplified model has been validated quantitatively with extensive independent laboratory data.

- Without convective flow, a procedure is developed for pipeline operators who can measure only the critical variables to be able to estimate the corrosion rate in the entire disbondment. The critical variables include holiday potential, open circuit potential (OCP) of steel in the environment, and the polarization resistance of the steel.

- Regardless of CP, with convective flow (e.g. at a rate of 1 cm/min) the corrosion rate inside the disbondment can be high. The flow carries dissolved O_2 into the disbonded region to cause significant corrosion while there CP is ineffective.

Internal Corrosion

In Section 4, the steady state behavior of internal steel pipeline corrosion was investigated for the case without inhibitor. Based on the model results and extensive theoretical investigation of the fundamental equations, the corrosion model is simplified to simple algebraic equations. The simplified corrosion models are validated in Section 6 with extensive independent laboratory data and with field data. The effect of CO_2, H_2S and O_2 are investigated.

Conclusions and Recommendations

◊ Without flow in the disbondment, given no knowledge of O_2 content, the rate of field pipeline corrosion under a disbonded coating can be computed from the simple external corrosion algorithm, given an estimate of the crevice gap and the measured or estimated.holiday potential Only these parameters and the OCP and the linear polarization resistance (R_p) of a pipe steel in simulated deaerated soil solution are needed as input variables to the simple algorithm. The OCP and R_P can easily measured in lab in deaerated solution.

◊ Without flow in the disbondment, as the worse case scenario that CP is not present the pipeline crevice corrosion rate due to dissolved O_2 in the disbonded region is smaller than the uniform corrosion rate, 0.4 mm/y. It seems that the current estimate for reassessment interval based on corrosion rate of 0.4 mm/y is reasonably conservative.

◊ With flow, if there is full aeration in soil, the corrosion rate in the disbonded region can exceed 0.4 mm/y. In such a case, the current estimate for reassessment interval based on the uniform corrosion rate of 0.4 mm/y is non-conservative.

◊ For a normal operating condition for pipeline, at a total pressure of 1000 psi and CO_2 content of 3%, by neglecting the effect of inhibitor, the internal pipeline corrosion rate can exceed 0.4 mm/y. Hence, depending on the effectiveness of the inhibitor used and the

gas quality in terms of CO_2 content, the current reassessment interval may or may not be conservative.

◊ Both external and internal corrosion rate prediction for evaluation of the current reassessment interval needs to be conducted further for more extensive corrosion scenarios.

ACKNOWLEDGMENTS

The project was conducted under DOT Contract DTRS56-04-T-0002. James Merritt (PHMSA/DOT) provided management oversight for the project. The authors thank the U.S. Department of Transportation (DOT), Pipeline Research Council International (PRCI), Gaz de France, Southern California Gas, Valero Energy, for their support. The project benefited from the input of a number of industry representatives. The authors wish to acknowledge the work of Fabrice Bernard, Gaz de France in the laboratory validation of external corrosion model for disbonded coating. The input and guidance of Michel Meyer, and Xavier Campaignole, both from Gaz de France, during the project is greatly appreciated. The authors also thank Laurie Perry and Daniel Shapiro of Southern California Gas Company for providing field data on internal corrosion. Finally, the authors thank Alan Carlile from Valero energy for enabling the placement of Multielectrode Array Sensor in their plant to monitor internal corrosion of their liquids line. The authors thank Brian Derby for his assistance in disbondment corrosion tests and Lori Salas for her assistance in preparing the report.

TABLE OF CONTENTS

TABLE OF CONTENTS (Continued)

TABLE OF CONTENTS (Continued)

LIST OF FIGURES

LIST OF FIGURES (Continued)

LIST OF FIGURES (Continued)

LIST OF FIGURES (Continued)

LIST OF FIGURES (Continued)

LIST OF FIGURES (Continued)

LIST OF FIGURES (Continued)

LIST OF FIGURES (Continued)

LIST OF FIGURES (Continued)

LIST OF TABLES

1.0 INTRODUCTION

1.1 Background

Continuous integrity management of pipelines involves the location and characterization of external and internal defects and periodic monitoring (reassessment) of these defects to ensure that timely mitigation can be performed. For natural gas pipelines, the Code of Federal Regulations, Title 49, Part 192, Sub-part 939 defines the maximum integrity reassessment interval to be 7 years. But, depending on the estimation of defect growth rates, the pipeline companies can extend the reassessment interval to 10 years for pipelines operating at greater than 50% of Specified Minimum Yield Strength (SMYS), 15 years for pipelines operating at 30 to 50% of SMYS, and 20 years for pipelines operating below 30% of SMYS. For liquid pipelines, 49CFR 195.452 defines the maximum reassessment interval to be 5 years, but pipeline companies can extend the reassessment interval depending on the demonstrated growth rate of defects. The defects can grow under a variety of circumstances, but a major contributor to the growth of defects is the long-term corrosion of the pipe. Therefore, defining the corrosion rate is an important aspect of estimating reassessment interval.

External corrosion (Figure 1-1) can occur at holidays in the coating if the CP is inadequate and regardless CP, the corrosion may occur underneath disbonded coatings where CP can be shielded from penetration[1-8]. In both cases, corrosion can reduce the pipe wall thickness, thereby elevating the stress. In CP shielded areas, corrosion can also occur in the crevice form in the presence of oxygen (O_2) while CP is not sufficient.

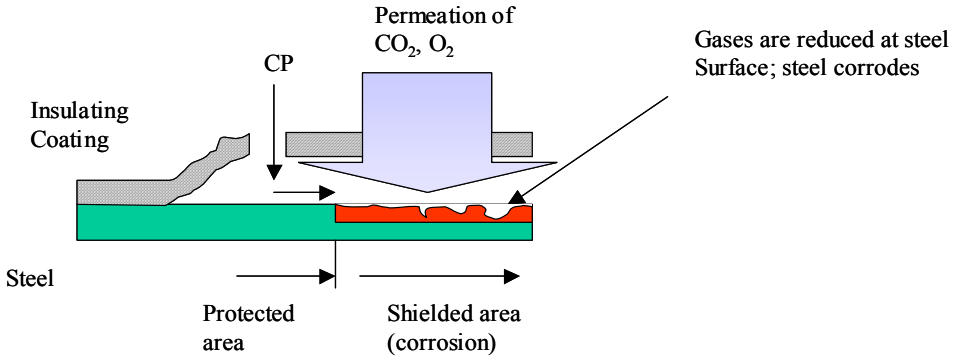

Figure 1-1. Illustration of CP shielding under a disbonded insulating coating and local corrosion.

Internal corrosion occurs due to presence of water along with acid impurities in natural gas, carbon dioxide and hydrogen sulfide[9-10]. Although gas quality specifications attempt to control the levels of these acid gases and water content, these specifications are not uniform between gas companies. If there is condensation of water, with the acid gases dissolved in it and/or if O_2 ingress inside the pipeline occurs (e.g., when the lines are under slight vacuum), severe general or localized corrosion can result.

Many approaches have been explored to estimate the growth rate of defects. In Table 1-1, it is apparent that no single approach will provide all the necessary information for decision-making. For example, successive ILI runs can be used to estimate the growth rate of internal and external corrosion[11], but it is not applicable for non-piggable pipelines. For non-piggable pipelines, reassessment interval has to be estimated through a combination of monitoring and corrosion rate calculation. Monitoring of corrosion has limitations in that it is difficult to know *a priori* the best location for placing the monitoring probe. Although for internal corrosion of nominally dry gas lines, known locations of critical pipeline elevations can be used for monitoring, this approach is not fully applicable for wet gas where corrosion can occur anywhere in the pipe[12]. Such locations are generally not obvious for external corrosion. Even if monitoring probes can be appropriately located, it is difficult to monitor disbonded/CP shielded areas due to difficulties in correlating coupon geometry to the actual pipeline geometry.

Table 1-1. Methods to Estimate Reassessment Interval from Corrosion Growth Rate

Rate Prediction Method	Advantage	Limitation
Bare pipe corrosion rate (external corrosion only)	Simple to incorporate	Does not apply to shielded coatings. Does not apply to internal corrosion.
Average rate from baseline examination/ILI	Relies on measured value, simple to incorporate	Can be non-conservative (does not account for initiation time or new flaws).
Multiple ILI readings and computerized superposition	Provides more accurate estimation of external and internal defect growth	Cannot be used in non-piggable lines.
Coupons and probes	Can provide detailed information on corrosion modes and distribution	Coupon corrosion rates cannot be related to actual pipe wall loss. Probes provide information at only selected locations.
Internal corrosion rate model	Can be used in non-piggable lines and for making judgment on gas quality issues	Many rate models do not consider important factors such as O_2. Some factors are too complex to consider in detail.

The NACE Recommended Practice for External Corrosion Direct Assessment (ECDA, RP0502) suggests that the corrosion rates can be obtained either by calculating it from measured defect size over the exposure time period or estimating it based on a buried, unprotected carbon steel corrosion rate of 0.4 mm/y. A safety factor is introduced by assuming the reassessment interval to be twice the calculated time for through-wall propagation. However, these techniques may be too conservative in some cases and non-conservative in others. To calculate the

corrosion rate in CP shielded areas, one needs an understanding of how far the CP penetrates into these areas and the effect of chemistry change in the shielded area (Figure 1-1). The corrosion rate in this area is a function of the actual potential (i.e., how much the potential deviates from the protection criterion) as well as the environmental chemistry.

For estimation of internal corrosion rates in gas pipelines, the semi-empirical CO_2 corrosion model originally developed by de Waard and Milliams[13]:

$$\mathrm{Log(C.R., mm/y)} = 5.8 - \frac{1780}{\mathrm{T(°C)}} + 0.67\,\mathrm{Log(pCO_2)} \qquad (1\text{-}1)$$

has been used in the industry. Equation (1-1) was later modified by de Waard and associates to include liquid flow, inhibition and other factors[14-16]. Since Equation (1-1) and its modified formats were developed for no-H_2S downhole systems whose temperature is relatively high and which do not contain O_2, these models are not directly applicable for use to estimating internal corrosion of transmission pipelines where the operating temperature is low and the gas could contain H_2S and O_2. Some other related CO_2 corrosion models[17-40] suffer limitations in that they were not developed for pipeline-relevant conditions at lower temperature and also, most of these models are embedded in proprietary software, which is not readily accessible and not cost-effective for operators to use occasionally. The very model[41-44] that was developed for gas pipelines at low temperatures can be used as the basis and after simplification be used for predicting internal pipeline corrosion rate.

1.2 Objectives and Approaches

The objectives of this program are to develop methods based on sound fundamental principles to estimate: (1) external corrosion rates, especially in CP shielded areas and (2) internal corrosion rates by considering pipeline-relevant factors for gas and liquid lines. Mathematical models will be developed to achieve the above goal. The models will be compared with field and laboratory data for validity and the models will be simplified to a format that is applicable to pipeline operators to estimate pipeline external or/and internal corrosion rate. It is recognized that the development of fundamental, physics-based model to predict corrosion rates for each of these areas is a daunting task. Therefore, this project aims to develop models that can be used to predict the pipeline corrosion rate in some scenarios that are relatively conservative and are expected to occur more commonly in the field. The goals were accomplished through five tasks as described as below.

1.2.1 External Corrosion Rate Calculation (Task 1)

A mathematical model is developed that combines external soil conditions (e.g., soil water chemistry), applied CP levels (e.g., variable CP levels), coating characteristics (e.g., permeability to O_2 and carbon dioxide), shielding characteristics (e.g., length and gap of the shielded areas) to predict the corrosion potential and rate inside the shielded area. The model is made to simulate disbondment corrosion found in the field.

The model is augmented to include convective flow in the disbonded region. In some practical cases, the disbonded region has two holiday areas that permit constant replenishment of

electrolyte inside the disbondment. This scenario is being simulated in the Gaz de France (GDF) experiments.

The corrosion rate affected by a number of factors will be computed including steady-state and unsteady state conditions, various CP conditions, soil chemistries.

Simplification of the model is taken for the model to be applicable for practical application. The operator does not have to know any detail of the model but is able to calculate the interested variable, corrosion rate. Dimensional analysis of mathematical equations that govern a physical process will be used to determine the groups of variables that control/limit the ongoing process.

1.2.2 Internal Corrosion Rate Calculation (Task 2)

A physics-based approach similar to that used for external corrosion modeling, but incorporating different boundary conditions and reactions, was implemented. The effect of CO_2, and O_2 on the electrochemical kinetics was incorporated. It must be noted that the effect of H_2S is complex, involving formation of semi-protective films as well as increasing the cathodic reaction kinetics. The adsorption theory used by others[18] was employed to calculate corrosion rate as a function of H_2S in this program.

1.2.3 Validation of the External Corrosion Rate Calculation (Task 3)

The external corrosion rate model developed in Task 1 is validated using a combination of field and controlled laboratory data. For the validation purpose, laboratory studies were conducted by a GDF staff member using SwRI facilities as part of a 6-month staff exchange program. Previous literature data were also used for validation.

1.2.4 Field Validation of the Internal Corrosion Rate Calculation (Task 4)

Validation of the internal corrosion rate model was performed using a combination of laboratory data and field data. The internal corrosion rate data from the field were obtained using Field signature Method (FSM). Corrosion monitoring was conducted using Multielectrode Array Sensor (MAS) to measure corrosion rate of pipelines containing gas mixtures containing various contaminants and pipelines containing liquid. Although the test results are reported in this work, since the gas or liquid chemistry and water content are not fully known, validation of the model using such data will not be conducted. The data were used to compare to model predictions.

1.2.5 Reporting and Recommendations for Corrosion Rate Determination (Task 5)

The methodologies for estimating external and internal corrosion rates arising from this project are presented in this draft report.

Extensive modeling work has been done. Since the fundamentals used to describe the corrosion process are the same regardless external and internal pipeline corrosion, the general equations used for the modeling is described in the following section.

1.3 References

1. N. Sridhar, "Modeling the Conditions under Disbonded coating Crevices – A Review", in Proceedings of the Corrosion/2004 Research topical Symposium: Corrosion Modeling for Assessing the Condition of Oil and Gas Pipelines, F. King and J. Beavers (eds.), Houston, TX: NACE/2004, 53-92.
2. Xavier Campaignolle, Stéphane Gastaud, Sébastien Karcher, Michel Meyer, "Corrosion of Pipelines under CP in the Presence of Coating Disbonding", EUROCORR/2004, Paper 074.
3. Philippe Carpentiers, René Gregoor, Antoine Pourbaix, "Corrosion under Disbonded Coatings of Cathodically Protected Pipelines", EUROCORR/2004, Paper 543.
4. F.M. Song, D.W. Kirk, J.W. Graydon and D.E. Cormack, "Steel Corrosion under a Disbonded Coating with a Holiday, Part 1: The Model and Validation", Corrosion 58(12) (2002) 1015-1024.
5. F.M. Song, D.W. Kirk, J.W. Graydon and D.E. Cormack, "Steel Corrosion under a Disbonded Coating with a Holiday, Part 2: Corrosion Behavior", Corrosion 59(1) (2003) 42-49.
6. F.M. Song, D.A. Jones and D.W. Kirk, "Corrosion and Current Flow within a Pipeline Disc Crevice", Corrosion, 60(2) (2005) 145-154.
7. F.M. Song and N. Sridhar, "Predicting Pipeline SCC Conditions through Simulation of Under-Disbondment Chemistry and Potential", International Pipeline Conference, Calgary, Alberta, Canada, Oct. 4-8, 2004.
8. Orazem, M.E., D.P. Reimer, C. Qiu and K. Allahar, "Computer Simulations for Cathodic Protection of Pipelines", in Proceedings of the Corrosion/2004 Research topical Symposium: Corrosion Modeling for Assessing the Condition of Oil and Gas Pipelines, F. King and J. Beavers (eds.), Houston, TX: NACE/2004, 25-52.
9. Narasi Sridhar, Frank Song, and Marybeth Nored, "Guidelines/Quality Standards for Transportation of Gas Containing Mixed Corrosive Constituents", Contract GTI PF00021435, PRCI ID Number PR-015-03131, SwRI® Project 18-06974, Feb. 2004.
10. Narasi Sridhar, Darin George, Eric Kelner, Frank Song, and Chris Waldhart, "Decision Making Procedure for Acceptance of Out-of-Specification Gas", 2005, Final Report to CenterPoint Energy Pipeline Services, SwRI® Project 18.11700, Nov. 2005.
11. G. Desjardins, Determining corrosion rates and assessing future pipeline reliability from ILI data, in Proceedings of the Corrosion/2004 Research Topical Symposium: Corrosion Modeling for Assessing the Condition of Oil and Gas Pipelines, F. King and J. Beavers (eds.), Houston, TX: NACE International, (2004).
12. O.C. Moghissi, L. Perry, B. Cookingham, and N. Sridhar, 2003, 'Internal Corrosion Direct Assessment of Gas Transmission Pipelines – Application,' CORROSION/2003 Paper #03204, NACE International, Houston, TX.

13. C. de Waard, D.E. Milliams, Corrosion 31 (5) (1975) 177-181.

14. C. de Waard, U. Lotz, D.E. Milliams, Corrosion 47 (12) (1991) 976-985.

15. C. de Waard, U. Lotz, "Prediction of CO2 Corrosion of Carbon Steel", Corrosion/93, Paper 69. Houston, TX: NACE International.

16. C. de Waard, U. Lotz, A. Dugstad, "Influence of Liquid Flow Velocity on CO2 Corrosion: A Semi-Empirical Model", Corrosion/95, Paper 128. Houston, TX: NACE International.

17. A. Anderko and Young, R.D., "Simulation of CO2/H2S Corrosion Using Thermodynamic and Electrochemical Models, Corrosion/99, Paper 31, Houston, TX: NACE International.

18. A. Anderko, "Simulation of FeCO3/FeS Scale Formation Using Thermodynamic and Electrochemical Models", Corrosion/00, Paper 00102, Houston, TX: NACE International.

19. R. Baldwin, 1999. Survey of tariff quality gas for GMRC. Personal communication.

20. M.R. Bonis and J.L. Crolet, "Basics of the Prediction of the Risks of CO2 Corrosion in Oil and Gas Wells", Corrosion/89, Paper 466.

21. E. Dayalan, de Moraes, F.D., Shadley, J.R., Shirazi, S.A. and Ribicki, S.A., "CO2 Corrosion Prediction in Pipe Flow under FeCO3 Scale-Forming Conditions", Corrosion/98, Paper 51, Houston, TX: NACE International.

22. C.L. Durr and J.A. Beavers. 1996. Effect of oxygen on the internal corrosion of natural gas pipelines, Corrosion/96, Paper 612, Houston, TX: NACE International.

23. Y.M. Gunaltun, "Combining Research and Field Data for Corrosion Rate Prediction", Corrosion/96, Paper 27.

24. Y.M. Gunaltun and Larrey, D., "Correlation of Cases of Top of Line Corrosion with Calculated Water Condensation Rates", Corrosion/2000, Paper 71.

25. A.M.K. Halvorsen and Sontvedt, T., "CO2 Corrosion Model for Carbon Steel Including a Wall Shear Stress Model for Multiphase Flow and Limits for Production Rate to Avoid Mesa Attack", Corrosion/99, Paper 42.

26. M.S. High, Wagner, J., Natarajan, S. 2000,, "Mechanistic Modeling of Mass Transfer in the Laminar Sublayer in Downhole Systems, Corrosion/2000, Paper 62, Houston, TX: NACE International.

27. W.P. Jepson, Kang, C., Gopal, M. and Stitzel, S., "Model for Sweet Corrosion in Horizontal Multiphase Slug Flow", Corrosion/97, Paper 11.

28. F.F. Lyle, 1996. "Carbon Dioxide/Hydrogen Sulfide corrosion Under Wet Stagnant Gas Pipeline Conditions in the Presence of Bicarbonate, Chloride, and Oxygen". PRCI Report PR-15-9313. Pipeline Research Council International.

29. S. Nesic, Postlethwaite, J., Olsen, S., Corrosion 52 (1996) 280.

30. M. Nordsveen, Nesic, S., Nyborg, R. and Stangeland A., Corrosion 59(5) (2003) 443-456.

31. C.A., Palacios, T. and Corpoven, S.A., "Application of Simulation Techniques for Internal Corrosion Prediction", Corrosion/97, Paper 2.

32. B.F.M. Pots, 1995, “Mechanistic Models for the Prediction of CO2 Corrosion Rates under Multi-phase Flow Conditions”, Corrosion/95, Paper 137; NACE International, Houston, TX.

33. B.F.M. Pots and Hendriksen, E.L.J.A., 2000, “CO2 Corrosion under Scaling Conditions – The Special Case of Top-of-Line Corrosion in Wet Gas Pipelines”, Corrosion/2000, Paper 31. NACE International, Houston, TX.

34. K. A. Sangita, and Srinivasan, S., “An Analytical Model to Experimentally Emulate Flow Effects in Multiphase CO2/H2S Systems”, Corrosion/2000, Paper 58.

35. D.W. Shannon, D.D. Pierce, R.J. Robertus, and R. Wang. 1984. “Effect of Water Chemistry on Internal Corrosion Rates in Offshore Natural Gas Pipelines”. PRCI Report PR-3-152. Pipeline Research Council International.

36. N. Sridhar, D.S. Dunn, A. Anderko, and M. Lencka. 1998. “The Effects of Water Chemistry on Internal Corrosion of Steel Pipelines”. PRCI Report PR-15-9712. Pipeline Research Council International.

37. N. Sridhar, Dunn, D.S., Anderko, A.M., Lencka, M.M. and Schutt, H.U., 2001, Corrosion 57 (3) 221-235.

38. M. Sundaram, Raman, V., High, M.S., Tree, D.A., Wagner, J., 1996, “Deterministic Modeling of Corrosion in Downhole Environments”, Corrosion/96, Paper 30, NACE International, Houston, TX.

39. K. Videm and Kvarekval, J., 1995, Corrosion 51(4), 260-269.

40. Zhang, Gopal, M., Jepson, W.P., “Development of a Mechanistic Model for Predicting Corrosion Rate in Multiphase Oil/Water/Gas Flows”, Corroison/97, Paper 601, NACE International, Houston, TX.

41. F.M. Song, D.W. Kirk and D.E. Cormack, “Modeling CO_2 Corrosion in Oil and Gas Transmission Systems”. Held April 3-7, 2005 (Houston, TX: NACE, 2005) Paper: 05180.

42. F.M. Song, D.W. Kirk, J.W. Graydon and D.E. Cormack, “CO_2 Corrosion of Bare Steel under an Aqueous Boundary Layer”, Corrosion 60(8) (2004) 736-748.

43. F. M. Song, Kirk, D.W., Graydon, J.W. and Cormack, D.E., 2002, J. of Electrochem. Soc., 149(11) (2002) B479-B486.

44. F.M. Song, D.W. Kirk and D.E. Cormack, “Determination of Precipitates for CO_2 Corrosion of Steel under an Aqueous Boundary Layer”, Journal of Corrosion Science and Engineering, Volume 3, Paper 24 (2004).

2.0 THE GENERAL MATHEMATICAL EQUATIONS FOR BOTH EXTERNAL AND INTERNAL CORROSION

2.1 General Transport Equations

Regardless of internal or external corrosion, the general transport equations in the solution are the same and can be written as[1-3]:

$$\frac{\partial}{\partial t}(\phi S\psi_j) + \nabla \cdot \Omega_j = -\phi(\sum_k \nu_{jk} I_k + \sum_m \nu_{jm} I_m) - s(\sum_k \nu^e_{jk} I^e_k + \sum_m \nu^e_{jm} I^e_m) \quad (2\text{-}1)$$

where j's are the original independent species in the crevice solution and k's the products of the irreversible reactions (new independent species). m's are minerals in the system whose concentrations are unity. ϕ is porosity, S volumetric liquid saturation and s specific surface area of solid reactive surface over solution volume. ν_{jk} and ν_{jm} are stoichiometric constants of the j species in respectively the homogeneous and heterogeneous irreversible reactions, I^e's the electrochemical reaction rates and I's the non-electrochemical reaction rates. ψ_j is generalized concentration defined as:

$$\Psi_j = c_j + \sum_i \nu_{ji} c_i \quad (2\text{-}2)$$

c_j is concentration of the independent species j and c_i the concentration of any complex species formed in a reversible reaction among j and k species. ν_{ji} is the stoichiometric constant of the species j in the above reversible reaction containing species j. In Equation (2-1), Ω_j is generalized flux

$$\Omega_j = N_j + \sum_i \nu_{ji} N_i \quad (2\text{-}3)$$

where $N_j = -\tau\phi[\nabla \cdot (D_j c_j) + z_j u_j c_j \nabla\Phi]$, flux of j species. The same format applies to N_i. τ is tortuosity, u mobility and Φ electrostatic potential in the crevice solution.

Equation (2-1) also applies to species k. If j's and k's are replaced by the common subscript l, the transport equation for all independent species can be written commonly as:

$$\frac{\partial}{\partial t}(\phi S\psi_l) + \nabla \cdot \Omega_l = -\phi(\sum_{i'} \nu_{li'} I_{i'} + \sum_m \nu_{lm} I_m) - s(\sum_{i'} \nu^e_{li'} I^e_{i'} + \sum_m \nu^e_{lm} I^e_m) \quad (2\text{-}4)$$

where l is either j or k. $\nu_{li'}=1$ and $\nu_{li'}{}^e=1$ when $l=i'$.

Electroneutrality in the solution determines

$$\sum_l z_l \Psi_l = 0 \quad (2\text{-}5)$$

With the following relations,

$$\sum_{i'} z_l \nu_{li'} = 0 \tag{2-6}$$

$$\sum_{m} z_l \nu_{lm} = 0 \tag{2-7}$$

$$\sum_{i'} z_l \nu^e_{li'} = n_{i'} \tag{2-8}$$

$$\sum_{m} z_l \nu^e_{lm} = n_m \tag{2-9}$$

multiplying $z_l F$ on both sides of Equation (2-4) and summation yield:

$$\nabla \cdot i = -Fs\left(\sum_{i'} n_{i'} I^e_{i'} + \sum_{m} n_m I^e_m\right) \tag{2-10}$$

where $n_{i'}$ and n_m are the number of electrons transferred in an elemental electrochemical reaction with respect to a dissolved species and a mineral species respectively.

For simplification of the system, the tortuosity, porosity and saturation of the pores are ignored. The diffusivity is assumed constant in the dilute solution. Equation (2-4) becomes:

$$\frac{\partial}{\partial t}\psi_l + \nabla \cdot \Omega_l = -\left(\sum_{i'} \nu_{li'} I_{i'} + \sum_{m} \nu_{lm} I_m\right) - s\left(\sum_{i'} \nu^e_{li'} I^e_{i'} + \sum_{m} \nu^e_{lm} I^e_m\right) \tag{2-11}$$

where in the generalized flux expression (Ω_l), $N_l = -D_l(\nabla \cdot c_l + \frac{z_l F}{RT} c_l \nabla \Phi)$. The mobility is replaced by diffusivity based on: $u_l = \frac{z_l F}{RT} D_l$.

For a system containing n independent species, it has n+1 independent variables. They must be balanced by n+1 independent equations to have a unique solution. The independent equations are n equations of Equation (2-11) for independent concentrations plus Equation (2-10) for potential. Equation (2-10) is obtained from electroneutrality.

In solving the crevice corrosion with CO_2 and O_2, application of the above generalized transport equations is demonstrated in the model derivation.

2.2 Chemical Equilibrium and Transport Equations for Steel Corrosion Systems with Both O_2 and CO_2

For a crevice solution containing dissolved CO_2 and supporting ions due to dissolution of NaCl, the independent solution species may be selected as:

Na^+ --(1), Cl^- --(2), Fe^{2+} --(3), H^+ --(4), $O_2(aq)$ --(5), $CO_2(aq)$ --(6), $H_2(aq)$ --(7), $FeCO_3$ --(8), Fe --(9), and H_2O --(10)

Then, the secondary complex species are:

OH^- --(11), CO_3^{2-} --(12), HCO_3^+ --(13), H_2CO_3 ---(14), $FeOH^+$ --(15), $FeHCO_3^+$ -- (16).

The reversible reactions in the crevice solution with the complex species expressed by the independent species are[4-6]:

$$H_2O - H^+ \leftrightarrow OH^- \qquad R_1 \qquad c_4c_{11} = K_w \qquad (2\text{-}12)$$
$$(H_2O \leftrightarrow H^+ + OH^-)$$

$$FeCO_3 - Fe^{2+} \leftrightarrow CO_3^{2-} \qquad R_2 \qquad c_3c_{12} = K_{spFeCO_3} \qquad (2\text{-}13)$$
$$(FeCO_3 \leftrightarrow Fe^{2+} + CO_3^{2-})$$

$$FeCO_3 - Fe^{2+} + H^+ \leftrightarrow HCO_3^- \qquad R_3 \qquad \frac{c_4c_{12}}{c_{13}} = K_{2H_2CO_3} \qquad (2\text{-}14)$$
$$(HCO_3^- \leftrightarrow H^+ + CO_3^{2-})$$

$$FeCO_3 - Fe^{2+} + 2H^+ \leftrightarrow H_2CO_3 \qquad R_4 \qquad (\frac{c_4c_{13}}{c_{14}} = K_{11H_2CO_3}) \qquad (2\text{-}15)$$
$$(H_2CO_3 \leftrightarrow H^+ + HCO_3^-, K_{11H2CO3}) \qquad (K_{11H_2CO_3} = K_{1H_2CO_3} / K_h)$$
$$(CO_2(aq) + H_2O \leftrightarrow H^+ + HCO_3^-, K_{1H2CO3})$$

$$Fe^{2+} + H_2O - H^+ \leftrightarrow FeOH^+ \qquad R_5 \qquad \frac{c_4c_{15}}{c_3} = K_1 \qquad (2\text{-}16)$$
$$(Fe^{2+} + H_2O \leftrightarrow FeOH^+ + H^+)$$

$$FeCO_3 + H^+ \leftrightarrow FeHCO_3^+ \qquad R_6 \qquad \frac{c_3c_{13}}{c_{16}} = K_{cx1} \qquad (2\text{-}17)$$
$$(FeHCO_3^+ \leftrightarrow Fe^{2+} + HCO_3^-)$$

The irreversible reaction is CO_2 hydration:

$$CO_2 + H_2O + Fe^{2+} \leftrightarrow FeCO_3 + 2H^+ \qquad r_{CO2} \qquad (2\text{-}18)$$
$$(CO_2 + H_2O \leftrightarrow H_2CO_3)$$

The electrochemical reactions are:

$$Fe \rightarrow Fe^{2+} + 2e^- \qquad r_{Fe} \qquad (2\text{-}19)$$
$$H^+ + e^- \rightarrow 0.5H_2 \qquad r_H \qquad (2\text{-}20)$$
$$H^+ + e^- \rightarrow 0.5H_2 \qquad (H_2O + e^- \rightarrow 0.5H_2 + OH^-) \qquad r_{H2O} \qquad (2\text{-}21)$$
$$4H^+ + O_2 + 4e^- \rightarrow 2H_2O \qquad r_{O2} \qquad (2\text{-}22)$$
$$H^+ + e^- \rightarrow 0.5H_2 \qquad (H_2CO_3 + e^- \leftrightarrow HCO_3^- + 0.5H_2) \qquad r_{H2CO3} \qquad (2\text{-}23)$$

Written in the form of Equation (2-11), the following equations are obtained:

$$\frac{\partial c_1}{\partial t} + \nabla N_1 = 0 \qquad (2\text{-}24)$$
$$\frac{\partial c_2}{\partial t} + \nabla N_2 = 0 \qquad (2\text{-}25)$$
$$\frac{\partial (c_3 - c_{12} - c_{13} - c_{14} + c_{15})}{\partial t} + \nabla (N_3 - N_{12} - N_{13} - N_{14} + N_{15}) = r_{Fe} / a - r_{CO_2} \qquad (2\text{-}26)$$

$$\frac{\partial(c_4-c_{11}+c_{13}+2c_{14}-c_{15}+c_{16})}{\partial t}+\nabla(N_4-N_{11}+N_{13}+2N_{14}-N_{15}+N_{16}) = -\frac{r_H+r_{H2O}+4r_{O_2}+r_{H_2CO_3}}{a}+2r_{CO_2} \quad (2\text{-}27)$$

$$\frac{\partial c_6}{\partial t}+\nabla N_6 = -r_{CO_2} \quad (2\text{-}28)$$

$$\frac{\partial c_7}{\partial t}+\nabla N_7 = \frac{r_H+r_{H_2O}+r_{H_2CO_3}}{2a} \quad (2\text{-}29)$$

where the N_j is flux of the j^{th} species.

The transport equation for O_2 without including its permeation through the coating, equivalent to that in a previous work for steady state[7-11], can be written as unsteady state as:

$$\frac{\partial \bar{c}_5}{\partial t}+\nabla N_5 = \frac{3D_{O_2}\bar{c}_5}{3\lambda 10^{\frac{-\varphi}{b_{O_2}}}-a^2} \quad (2\text{-}30)$$

where $\lambda=\frac{an_{O2}FD_{O2}c_{5ref}}{i_{O_2ref0}}$, $i_{O_2ref0}=-i^0_{O_2ref}10^{\frac{-(E_0-E^{Eqref}_{O_2})}{b_{O_2}}}$ and $N_5=-D_{O_2}\frac{\partial \bar{c}_5}{\partial z}$. $\bar{c}_5$ is average O_2 concentration across the gap.

Multiplying z_j to individual species concentration over all the transport equations of the independent species and summation yield an equivalent equation to Equation (2-10) expressed as:

$$\nabla(z_1N_1+z_2N_2+z_3N_3+z_4N_4+z_{11}N_{11}+z_{12}N_{12}+z_{13}N_{13}+z_{15}N_{15}+z_{16}N_{16}) = \frac{2r_{Fe}-(r_H+r_{H2O}+4r_{O_2}+r_{H_2CO_3})}{a} \quad (2\text{-}31)$$

Equations (2-24 – 2-31) can be solved simultaneously to obtain all concentrations of the independent species, the corrosion rate and potential. By substitution of the solution into the equilibrium equations (2-12 – 2-17), the concentrations of the complex species can be computed.

As shown in Equations (2-12 – 2-17), all concentrations of the secondary species can be expressed by the concentrations of c_3 and c_4. Thus, the model system has eight primary solution species: φ, c_1-c_7. The concentrations of minerals are unity. If the spatial variation of hydrogen partial pressure inside the crevice is in equilibrium with soil pressure constant at 1 atm, there are only seven independent variables φ, c_1-c_6 which require only seven equations, (2-24 – 2-28) and (2-30 – 2-31), for a complete numerical solution.

For boundary conditions at the crevice mouth, φ can be a random value and is assumed zero (φ_0=0), the concentrations of c_{01} and c_{02} are known and c_{03} can be expressed by c_{04} based on electroneutrality by φ and c_4 as:

$$c_{03}=\frac{-p+\sqrt{p^2-4rq}}{2r} \quad (2\text{-}32)$$

where $p = z_1 c_{01} + z_2 c_{02} + z_4 c_{04} + z_{11} c_{011} + z_{16} c_{016}$, $q = z_{12} K_{spFeCO_3} + z_{13} \frac{c_4 K_{spFeCO_3}}{K_{2H_2CO_3}}$, and $r = z_3 + z_{15} \frac{K_1}{c_4}$. Besides, $c_{011} = \frac{K_w}{c_{04}}$, $c_{012} = \frac{K_{spFeCO_3}}{c_{03}}$, $c_{013} = \frac{c_{04} K_{spFeCO_3}}{c_{03} K_{2H_2CO_3}}$, $c_{015} = \frac{c_{03} K_1}{c_{04}}$ and $c_{016} = \frac{c_{04} K_{spFeCO_3}}{K_{cx1} K_{2H_2CO_3}}$. Not used in the derivation, $c_{014} = \frac{c_{04}^2 K_{spFeCO_3}}{c_{03} K_{11H_2CO_3} K_{2H_2CO_3}}$.

If equilibrium is assumed between CO_2 and H_2CO_3 at the mouth due to convection for example, the partial pressure of CO_2 can be calculated (from the pH) based on Henry's law.

2.3 Electrokinetic Equations

By assuming $\varphi_0 = 0$ at the crevice mouth, the measured potential there versus a reference electrode such as saturated $Cu/CuSO_4$ is known (E_0), the Tafel equations at the holiday mouth for iron oxidation and ferrous ion reduction are respectively:

$$i_{Fe0a} = i^0_{Feref} 10^{\frac{E_0 - E^{Eqref}_{Fe}}{b_{Fea}}} \quad \text{(iron oxidation)} \tag{2-33}$$

$$i_{Fe0c} = -i^0{}_{Feref} \frac{c_{03}}{c_{3ref}} 10^{\frac{-(E_0 - E^{Eqref}_{Fe})}{b_{Fec}}} \quad \text{(ferrous ion reduction)} \tag{2-34}$$

For hydrogen ion oxidation, water reduction, O_2 reduction and carbonic acid reduction, their Tafel equations at the holiday mouth are respectively:

$$i_{H0} = -i^0{}_{Href} \frac{c_{04}}{c_{4ref}} 10^{\frac{-(E_0 - E^{Eqref}_{H})}{b_H}} \tag{2-35}$$

$$i_{H_2O0} = -i^0{}_{H_2Oref} 10^{\frac{-(E_0 - E^{Eqref}_{H_2O})}{b_{H_2O}}} \tag{2-36}$$

$$i_{H_2CO_30} = -i^0{}_{H_2CO_3ref} \frac{c_{014}}{c_{14ref}} 10^{\frac{-(E_0 - E^{Eqref}_{H})}{b_{H_2CO_3}}} \tag{2-37}$$

For O_2 reduction, the Tafel equation in terms of O_2 surface concentration is:

$$i_{O_2s0} = -i^0_{O_2ref} \frac{c_{05s}}{c_{5ref}} 10^{\frac{-(E_0 - E^{Eqref}_{O_2})}{b_{O_2}}} \tag{2-38}$$

Expressed by the kinetic equations at the mouth, the kinetic equations anywhere inside the crevice can be written as below. For iron, the Butler-Volmer equation including the anodic and cathodic portions is:

$$i_{corr} = i_{Fe0a} 10^{\frac{-\varphi}{b_{Fea}}} + i_{Fe0c} \frac{c_3}{c_{03}} 10^{\frac{\varphi}{b_{Fec}}} \quad (2\text{-}39)$$

For the cathodic reactions, the Tafel equations are:

$$i_H = i_{H0} \frac{c_4}{c_{04}} 10^{\frac{\varphi}{b_H}} \quad (2\text{-}40)$$

$$i_{H_2O} = i_{H_2O0} 10^{\frac{\varphi}{b_{H_2O}}} \quad (2\text{-}41)$$

$$i_{H_2CO_3} = i_{H_2CO_3 0} \frac{c_{14}}{c_{014}} 10^{\frac{\varphi}{b_{H_2CO_3}}} \quad (2\text{-}42)$$

$$i_{O_{2s}} = i_{O_{2s}0} \frac{c_{5s}}{c_{05s}} 10^{\frac{\varphi}{b_{O_2}}} \quad (2\text{-}43)$$

Equation (2.43) has been used in the derivation of Equation (2-30).

The above current density expressions can be converted to the reaction rates by: $r_l = \frac{i_l}{n_l F}$ where l represents Fe, H, H_2O, H_2CO_3 and O_2 and r_l is the reaction rate of the l^{th} electrochemical reaction.

The above equations will be used in modeling both the external and internal corrosion. Wherever appropriate, the equations may be modified to fit the specific system. Corresponding to the geometry of a specific system (external and internal corrosion), the related boundary conditions will be described in order for the above equations to be solved and the corrosion rate to be computed. These will be described in sections that follow.

2.4 References

1. F.M. Song and N. Sridhar, "Predicting Pipeline SCC Conditions through Simulation of Under-Disbondment Chemistry and Potential", International Pipeline Conference, Calgary, Alberta, Canada, Oct. 4-8, 2004.
2. N. Sridhar, D.S. Dunn, and M. Seth, 2001, Application of a general reactive transport model to predict environment under disbonded coatings, Corrosion, 57 (7), 598-613.
3. P.C. Lichtner, "Modeling Reactive Flow and Transport in Natural Systems", in "Proceedings of the Rome Seminar on Environmental Geochemistry", Luigi Marini and Giulio Ottonello (Eds), held in Castelnuovo di Porto on May 22-26 (1996) and published by Dipartimento di Scienze della Terra – Universita di Genova (1998).
4. F.M. Song, D.W. Kirk and D.E. Cormack, "Modeling CO_2 Corrosion in Oil and Gas Transmission Systems". Held April 3-7, 2005 (Houston, TX: NACE, 2005) Paper: 05180.
5. F.M. Song, D.W. Kirk, J.W. Graydon and D.E. Cormack, "CO_2 Corrosion of Bare Steel under an Aqueous Boundary Layer", Corrosion 60(8) (2004) 736-748.

6. F.M. Song, D.W. Kirk, J.W. Graydon and D.E. Cormack, "CO_2 Corrosion of Bare Steel under an Aqueous Boundary Layer with Oxygen", Journal of The Electrochemical Society, 149(11) (2002) B479-B486.

7. F.M. Song and N. Sridhar, "A 2D Crevice Corrosion Model for Steel Corrosion under a Disbonded Coating due to O_2 with or without Cathodic Protection—Part 1: Full Numerical Solution", Corrosion, submitted.

8. F.M. Song and N. Sridhar, "A 2D Crevice Corrosion Model for Steel Corrosion under a Disbonded Coating due to O_2 with or without Cathodic Protection—Part 2: Model Simplification for Practical Application", Corrosion, submitted.

9. F.M. Song, D.W. Kirk, J.W. Graydon and D.E. Cormack, "Steel Corrosion under a Disbonded Coating with a Holiday, Part 1: The Model and Validation", Corrosion 58(12) (2002) 1015-1024.

10. F.M. Song, D.W. Kirk, J.W. Graydon and D.E. Cormack, "Steel Corrosion under a Disbonded Coating with a Holiday, Part 2: Corrosion Behavior", Corrosion 59(1) (2003) 42-49.

11. F.M. Song, D.A. Jones and D.W. Kirk, "Corrosion and Current Flow within a Pipeline Disc Crevice", Corrosion, 60(2) (2005) 145-154.

3.0 EXTERNAL CORROSION RATE CALCULATION (TASK 1)

3.1 Background Information

Significant work has been performed in the past on external corrosion of coated pipelines where the coating acts as a diffusion barrier to the corrosive molecular (e.g., water vapor, O_2 and CO_2) and ionic (e.g., Cl^-, HCO_3^-) species.[1-23] If the corrosion rate of steel is controlled by diffusion of O_2 through an intact coating, a simple calculation of this corrosion rate showed an extremely small corrosion rate, in the level of within a few micrometers per year[4-6]. This indicates that corrosion under disbonded coatings, if the coatings are still intact without holidays, should not be worried. Similarly, the CO_2 penetration through the coating is low and the hydrophobic nature of the coating determines that the coating is not permeable to ions. The CP penetration of fusion bonded epoxy (FBE) which is somewhat hydrophilic is not certain. It is noted that steel corrosion under thick coatings, which are generally used for protection of pipelines, are different from a thin paint which does not have good adhesion strength and is more readily permeable to corrosive species.[4]

When the coating on the pipe is disbonded, if there is a holiday in the disbonded coating which can form due to reasons such as, to name a few, manufacturing defect, damages during storage, transportation and installation, in-service damage and chemical deterioration,[5,7] the corrosion around the holiday becomes localized. This localized crevice corrosion has been extensively studied experimentally and computationally.[5-23] In terms of modeling, by neglecting the spatial variation of chemistry, the effects on crevice corrosion rate and potential of the crevice length, CP potential, resistivity of the crevice solution, permeation of O_2 through the coating, the geometrical parameters of the crevice (gap, holiday size and coating thickness) and the environmental temperature have been performed previously.[7-10] In this program, the work that has been done in previous work will try not to be repeated. The focus is to broaden the previous study and to establish a methodology that can translate the complex model effort into practical recommendations so that pipeline operators can use modeling results conveniently.

3.2 External Corrosion with O_2, with and without CP

Crevice corrosion in deaerated solution has been modeled broadly in 1D while with O_2 the difficulty arises because O_2 concentration cannot be simply assumed uniform across the gap due to its slow diffusion (Figure 3-1). Also, linear O_2 diffusion in that dimension is also not reasonable because of the dissolved O_2 concentration gradient near the steel surface and the coating can be significantly different. This problem has been overcome in recent work[7-9] where a parabolic relation of O_2 concentration across the gap is used. In the following modeling effort, the crevice corrosion, which is significantly influenced by O_2, is the focus of this work.

3.2.1 Transient Computational Results for Solution Chemistry Containing NaCl

The transient behavior is investigated of the crevice corrosion of steel under a disbonddisbonded coating. The solution is assumed to be saturated throughout the crevice by $Fe(OH)_2$ and it contains following species: Na^+ --(1), Cl^- --(2), Fe^{2+} --(3), H^+ --(4), O_2 --(5),

OH^- --(11), $FeOH^+$ --(15). $Fe(OH)_2$ easily saturates the solution because of its low solubility. The transport equations to be solved are Equations (2-24, 2-25, 2-30) and:

$$\delta_t \frac{\partial c_4}{\partial t} + \nabla(z_3 N_3 + z_4 N_4 + z_{11} N_{11} + z_{15} N_{15}) = \frac{2r_{Fe} - (r_H + r_{H2O} + 4r_{O_2})}{a} \quad (3\text{-}1)$$

and

$$\nabla(z_1 N_1 + z_2 N_2 + z_3 N_3 + z_4 N_4 + z_{11} N_{11} + z_{15} N_{15}) = \frac{2r_{Fe} - (r_H + r_{H2O} + 4r_{O_2})}{a} \quad (3\text{-}2)$$

where $\delta_t = z_4 + z_3 c_{3p} + z_{11} c_{11p} + z_{15} c_{15p}$ and $c_{jp} = \frac{dc_j}{dc_4}$ where j=3, 11, 15. These equations are solved simultaneously to compute corrosion rate at any instant time. The Tafel equation was used to express the iron dissolution current density.

The computation was done under conditions that the bulk O_2 pressure dissolved in solution is 0.21 atm, the gap between the disbonded coating and the steel surface is 0.5 mm, the solution is saturated by $Fe(OH)_2$, and the initial and bulk NaCl concentration is 0.003 mol/L which corresponds to a solution resistivity of 25 Ω·m. Assume dissolved O_2 establishes steady-state quickly after initiation of the crevice corrosion, which is valid because O_2 can penetrate only a small distance into the crevice and this requires little time compared to other species which can go deep into the crevice. It is assumed that a gradient of potential within the crevice is instantly established before any ion diffuses and migrates. The initial O_2 concentration and initial potential distributions used in this work are respectively $\frac{\bar{c}_5}{\bar{c}_{05}} = e^{-x\sqrt{3}/a}$ and $\frac{E - E_{ocp}}{E_0 - E_{ocp}} = 2 - e^{-\alpha x/a}$ or $\frac{\varphi}{\varphi_{ocp}} = e^{-\alpha x/a} - 1$ where α=0.05, E is the crevice potential and relates to the electrostatic potential by: $\varphi = E - E_0$. The transient behavior of the concentrations of the solution species and that of the corrosion potential and rate are discussed below.

3.2.1.1 No CP

Transient Behavior of the Solution Species: The O_2 concentration profile in the crevice is shown in Figure 3-2, which is independent of the presence of CP. This profile does not change with time because it is diffusion-limiting. Once this O_2 diffusion reaches steady-state, the O_2 concentration profile is set in the crevice, independent of variations of crevice potential and transport of ionic species in the solution.

In the case of no CP, the potential at the holiday is computed to be -0.8071 V. The spatial and temporal variation of pH in the crevice is shown in Figure 3-3 for the six times of 0, 10^2, 10^4, 10^6, 10^7 and 10^9 s. All the curves start from the same left point due to constant concentrations as a boundary condition. Similarly, since no mass passes through the coating, the concentrations are flat near right end (Figure 3-3b). The pH varies in the range of 7.5 - 10. Due to slow ionic migration, the pH and the concentrations of solution species (to be shown soon) inside the crevice start to change only after some time. The pH decreases with time there because of hydrolysis (saturation of $Fe(OH)_2$) and of the fact that the steel there is anodically polarized. This anodic polarization is to be described later. Due to this anodic polarization there, the total positive charge carried by ferrous ions increases exceeding the increase of the negative

charge carried by hydroxide ions due to hydrogen ion and water reductions. It is the excessive ferrous ions that form ferrous hydroxide to decrease the pH. To be described later, without CP there exists an internal current in the crevice which is induced by a differential O_2 concentration cell. The O_2 concentration is highernear the holiday than inside the crevice and the positive ionic current flows from inside to the holiday region. The pH near the holiday first increases with time (Figure 3-3a) because of high rate of O_2 reduction there which generates hydroxides. With time, as Cl^- and OH^- migrates into the crevice and Na^+ and Fe^{2+} to the holiday, which is carried by the internal current, the pH near the holiday region gradually decreases.

Figure 3-4 shows the variation of Na^+ concentration, and Figures 3-5 – 3-6 respectively of Fe^{2+} and Cl^- concentrations. At the beginning of the corrosion process (time less than 10^2 s), Na^+ concentration has an increase near the holiday region (Figure 3-4a) because of formation of OH^- by O_2 reduction whose charge is balanced by migration of Na^+. Fe^{2+} concentration is low then (Figure 3-5) and unable to balance the negative charge increased by OH^-. The Na^+ concentration in the crevice decreases with time (Figure 3-4b) because of formation of Fe^{2+} from corrosion which repels Na^+. Fe^{2+} formation rate inside the crevice is enhanced because of internal anodic polarization there. The minimum concentration of Na^+ in the crevice near the holiday indicates balance between migration to the holiday of Na^+ and the restrictions of its transport due to a fixed concentration imposed at the holiday. The concentration of Cl^- in the crevice increases with time (Figure 3-6) because it migrates into the crevice, driven by the internal current, and there it balances the increasing positive charge generated from the increasing concentration of Fe^{2+}. The Cl^- and Fe^{2+} concentrations are much larger than others and hence, the dominant species in the crevice solution when steady state is being approached.

Transient Behavior of the Crevice Corrosion Potential and Rate: The transient behavior of the internal current created by the O_2 concentration cell is shown in Figure 3-7. The current is calculated based on a 1 mm width of the crevice in the direction perpendicular to the model geometry. The total current is zero at the left boundary because of no CP (Figure 3-7a). This current levels off near the right boundary (Figure 3-7b) because of zero current flow through the coating. That the positive ionic current flows from inside the crevice to the holiday area is because the steel potential is lower in the crevice than near the holiday (Figure 3-8). The potential does not show a significant change from time zero to 10^9 s (corrosion at steady state already). Due to the unique exponential relation between potential and corrosion rate, this feature of potential profile determines a similar feature of the corrosion current density (or rate) (Figure 3-9). The above results indicate that the transient change of the concentrations and internal currents poses an insignificant effect on the crevice corrosion rate and potential. This signifies that the crevice potential and rate evaluated at time zero can be used to approximate these quantities at any time during evolution of the corrosion process.

The corrosion rate and potential decrease from the holiday area into the crevice because without external CP, the O_2 concentration near the holiday is higher than inside the crevice. Even though there is internal cathodic polarization near the holiday (the anodic and cathodic regions are separated by the minimum current near the holiday in Figure 3-7), the corrosion rate there is still greater than inside the crevice because this internal current is not strong enough to decrease the corrosion rate near the holiday sufficiently. There, O_2 reduction is still dominant and the function of the cathodic polarization is its decrease of the corrosion current density to be

smaller than O_2 reduction current density (Figure 3-10). If the disbonded coating otherwise does not exist, the corrosion current density would be approximately the same as O_2 reduction current density because water reduction current is very small. Since O_2 diffusion is a limiting step and is present only very near the holiday, this crevice corrosion induced by the O_2 concentration cell would be very localized near the holiday region if there does exist the internal current. This internal current carries the anodic current further into the disbondment so that this otherwise localized corrosion becomes less. The corrosion penetration depth due to this O_2 concentration cell can depend on the solution conductivity. The higher the conductivity the more likely less corrosion near the holiday area. Very deep inside the crevice, since the internal current is zero, this O_2 effect diminishes.

The internal current inside the crevice is closely related to the net current density, the sum of all anodic (Fe) and cathodic (O_2, H_2O, H^+) current densities, which flows from the steel surface out into the crevice solution. This net current density is shown in Figure 3-10 together with O_2 reduction current density. That this net current is negative near the holiday indicates cathodic polarization. Conversely, this current is positive inside the crevice indicates that the steel there is anodically polarized. Since there is no external CP, the integration of the net current density over the total steel surface area is zero. This net current density is related to the internal current by that the latter is the integration of the former over the steel surface area starting from the holiday. The crosspoint between the i_{net} curve and the horizontal dashed line is where the net current density is zero and this location of x/gap is consistent with the minimum internal current, indicating that at that local point, the net polarization is zero, or no polarization, or the anodic and cathodic current densities are just locally balanced by each other. That this net current density is large near the holiday indicates high cathodic polarization there. This cathodic polarization locates near the holiday region because of the presence of O_2 and because the O_2 reduction current density (i_{O2}) dominates over iron oxidation and water reduction current densities. Moving into the crevice, there is no O_2 and the polarization to the steel decreases.

3.2.1.2 With CP (Holiday Steel Potential Polarized to –0.9 V)

With an O_2 pressure of 0.21 atm at the holiday, the highest potential of the crevice steel is located at the holiday, being -0.8071 V. Any potential at the holiday that is below this potential is indication of presence of CP. The level of CP depends on the potential at the holiday. The lower the potential the greater is the CP. Here, a potential of -0.9 V is used at the holiday. By fixing this potential, the transient behaviors of the concentrations of solution species and the corrosion potential and rate are computed under this CP condition.

Transient Behavior of the Solution Species: With a potential of -0.9 V at the holiday, the crevice solution pH varies between 9 and 12 and increases with time (Figure 3-11b). Since there is time required for the ions to migrate between the holiday and inside the crevice, the pH deep inside the crevice starts to vary only after some time, here more than 10^4 s. Eventually, the pH inside the crevice is greater than near the holiday. The reason for this pH variation is that OH^- formed from O_2 reduction and CP tends to diffuse and migrate into the crevice due to fixed pH at the holiday and the negative charge carried by the OH^- in the crevice can be neutralized more readily by diffusion of Na^+ from the holiday than local formation of Fe^{2+} due to high pH inside the crevice indicating low corrosion rate. Unlike the case of no CP where the dominant species are Cl^- and Fe^{2+}, here the dominant species are OH^- and Na^+. The concentration of Na^+ in the

crevice (Figure 3-12) becomes much greater than Cl^- concentration (Figure 3-13) as the system approaches steady state. Due to formation of OH^- in the crevice, Cl^- is pushed out and its concentration in the crevice decreases with time. The continuous transport into the crevice of Na^+, which is driven mainly by external CP, increases Na^+ concentration in the crevice.

Transient Behavior of the Crevice Corrosion Potential and Rate: Since at this CP level the external current flowing into the crevice is sufficient to consume all O_2 diffusing into the crevice, the O_2 concentration cell is thus eliminated and without internal current, the current in the crevice is all cathodic indicated by positive values (Figure 3-14). The current has a sharp change near the holiday because it is there that O_2 is present and reduced by CP. Into the crevice, without O_2 the CP current increases reduction of water. The H^+ reduction is weak due to high pH. The current on the left boundary of the crevice represents the significance of CP, which in the case of no CP is zero. The CP current increases with time because of transport of ions in the crevice which increases the solution resistivity to be shown later in Steady .

With increasing time, as more CP current penetrates into the crevice, the crevice potential (Figure 3-15) and corrosion current density (Figure 3-16) decrease, although the magnitudes of the decreases are small. The decrease of corrosion current density between the times of 0 s and 10^9 (steady state) is less than 1/3. This result indicates that estimation of the crevice potential and rate by using their values at time zero would be conservative by 1/3 of the steady state corrosion rate. The potential and corrosion rate increase within increasing distance into the crevice due to the less significance of CP further down into the crevice.

The transient net corrosion current density is shown in Figure 3-17. It is negative throughout the crevice, indicating cathodic polarization. With the CP to consume all O_2 in the crevice, the local polarization at the steel surface, reflected by the net current density, is not affected by the ionic transport in the crevice.

3.2.2 Steady-State Computational Results for Solution Chemistry Containing NaCl

From the transient computation in 3.2.1 it is clear that steady state is reach at time 10^7 s from which time forward the computational results are constant. The above solution was obtained by using the Tafel equation for iron oxidation, a method that has been used traditionally to calculate steel corrosion rate.

Use of Tafel equation is limited to the condition that the corrosion rate is large or the corrosion potential is sufficiently higher than the equilibrium potential. Then, the cathodic portion of the rate of the Fe vs. Fe^{2+} redox reaction is insignificant compared to its anodic portion. When there is a significant increase of Fe^{2+} concentration inside the crevice, the equilibrium potential of the redox reaction increase significantly and the computational error can be ignored if this cathodic portion were neglected. In the steady state computations to follow, the crevice corrosion behavior is investigated for both conditions: with and without the neglect of this cathodic portion. The results are compared to see the significance of this cathodic portion. In the steady state calculation, the same solution composition used for unsteady state computations is also used here. The transport equations to be solved are Equation (2-30) and:

$$\nabla(z_1N_1 + z_2N_2 + z_3N_3 + z_4N_4 + z_{11}N_{11} + z_{15}N_{15}) = \frac{2r_{Fe} - (r_H + r_{H2O} + 4r_{O_2})}{a} \quad (3\text{-}3)$$

They are solved for steady state solution.

3.2.2.1 Effects of Different Expressions for Steel Corrosion Rate

The solution resistivity and chemistry composition with and without CP at steady state calculated from using Tafel equation is shown in Figure 3-18, which is shown to coincide with the result from transient state calculation at time of 10^9 s.

For the holiday potential of -0.807 V, without CP and with O_2 reduction at the holiday which is similar to anodic polarization to the steel surface, negatively charged Cl^- is electrically driven to migrate into the crevice. To neutralize the charge, Fe^{2+} generated from corrosion stays inside the crevice. Very near the holiday the charge is neutralized by Na^+ in the bulk solution.

With CP at the holiday potential of -0.900 V, Na^+ is electrically driven to flow inside the crevice and its concentration here is higher. The positive charge carried by Na^+ is neutralized mainly by OH^- which is generated mainly by O_2 reduction near the holiday and water reduction in the entire crevice. Cl^- is repelled out from the crevice by OH^-.

The crevice solution resistivity under the holiday potential of -0.807 V is lower than with CP at the holiday potential of -0.900 V due to the greater ionic concentrations in the former than in the latter.

Figure 3-19 is a comparison of the corrosion potential and rate computed from the two expressions used to calculated the rate of Fe vs. Fe^{2+} redox reaction: Tafel equation and the more accurate Butler-Volmer (BVE) equation. Although the corrosion potential and current density are nearly the same when the potential applied at the holiday is -0.900 V, those at the holiday potential of -0.807 V are clearly greater inside the crevice if computed from the Butler-Volmer equation.

Figure 3-20 shows that for each holiday potential the solution resistivity computed from the BVE and Tafel equations appears identical due to the nearly identical values of ionic concentrations. For holiday potential of -0.807 V, the solution resistivity inside the crevice computed is larger near the holiday and then levels off inside the crevice, consistent with the potential distribution. This potential is greater than that computed from using Tafel equation because of the corresponding variation of ionic concentrations inside the crevice.

For two holiday potentials, the corrosion potentials or current densities computed from BVE do not converge inside the crevice because of the term of c_3/c_{03} in the cathodic portion of the Butler-Volmer equation, which becomes huge inside the crevice (>1000). This term is significant with BVE while not present in the Tafel equation.

3.2.2.2 No CP, Effect of O_2 Pressure on the Crevice Corrosion

Since the effect of CP on the crevice corrosion rate at a particular CP level has been discussed in previous work, here the focus is centered on crevice corrosion without external CP at different O_2 pressures. The computation conditions are exactly the same with only O_2 pressure to vary. The Nernst-Plank equations and the BVE for the Fe vs. Fe^{2+} redox reaction are used for the computation.

Without external CP the potential at the holiday increases as O_2 pressure increases due to higher anodic polarization that O_2 imposes to the steel surface near the holiday (Figure 3-21). This increase in holiday potential with O_2 pressure appears to be in an exponential manner because of the corrosion rate is approximately proportional to O_2 pressure due to O_2 diffusion limiting.

The crevice potential profiles for four O_2 pressures are shown in Figure 3-22 and corrosion current densities in Figure 3-23. Both the potential and current density decrease from the holiday into the crevice and deep inside, they are shown approximately flat indicating very low polarization at the steel surface. Because the solution chemistry deep inside varies with O_2 pressure, the OCP there varies with O_2 pressure. The higher the O_2 pressure, the greater is OCP. Since the internal positive current flows from inside to the holiday region and pumps Cl^- into the crevice, the pH inside the crevice is lower and the higher the O_2 pressure the lower is the pH . It is noted that even without O_2 (or deaerated solution) the crevice potential should vary inside the crevice. But, because the solution chemistry is alkaline and the corrosion rate is small, the corrosion potential is nearly uniform in the crevice. Although the potential deep inside the crevice varies with O_2 holiday pressures, the corrosion current density inside appears overlapped. This results from the cathodic term in the BVE, which contains a high concentration ratio of ferrous ion, is relatively significant.

The positive internal ionic current flow in the crevice is shown in Figure 3-24. No CP indicates zero current at the holiday. The current is zero deep into the crevice because of no current flowing across the coating. The current increases from the holiday to a maximum and then decreases for each O_2 pressure. The broken curve passing through the maximum currents separates the cathodic (near the holiday) and anodic (inside the crevice) regions due to internal polarization. At the maximum, where the net current flow from or to the steel surface is zero, the local polarization by the external current is zero. O_2 diffusion is slow so that it is quickly reduced at the steel surface very near the holiday (less 5 gap sizes) before moving further into the crevice. Since the current can pass more easily than O_2 diffusion, the O_2 polarization very near the holiday dissipates into the crevice so that the corrosion rate inside the crevice is increased while near the holiday decreased. Even with this internal current, the rate at the holiday is still more significant than inside the crevice.

3.3 Steady State *Computational Results* with O_2 and CO_2 and Co-precipitation

In CO_2 dissolved solution, depending on CO_2 partial pressure, ferrous carbonate and ferrous hydroxide may precipitate simultaneously. Since the degree of freedom of this system is zero, under the condition that the crevice solution is in equilibrium this CO_2 pressure can be calculated to be 1.37×10^{-6} atm, a fixed value. This value can be computed from solving the

combination of Equations (2-32) and $c_3 = \frac{K_{sp} c_4^2}{k_w^2}$, with the latter representing saturation of ferrous hydroxide in the solution. In this solution, only c_1, c_2, c_4, and φ are independent variables. The transport equation for H^+, previously Equation (2-27), should be replaced by:

$$\frac{\partial(c_4+2c_3-c_{11}-2c_{12}-c_{13}+c_{15}+c_{16})}{\partial t} + \nabla(N_4 + 2N_3 - N_{11} - 2N_{12} - N_{13} + N_{15} + N_{16}) = \frac{2rFe-(r_H+r_{H2O}+4r_{O_2}+r_{H_2CO_3})}{a} \tag{3.4}$$

or

$$\frac{\partial(z_4c_4+z_3c_3+z_{11}c_{11}+z_{12}c_{12}+z_{13}c_{13}+z_{15}c_{15}+z_{16}c_{16})}{\partial t} + \nabla(z_4N_4 + z_3N_3 + z_{11}N_{11} + z_{12}N_{12} + z_{13}N_{13} + z_{15}N_{15} + z_{16}N_{16}) = \frac{2rFe-(r_H+r_{H2O}+4r_{O_2}+r_{H_2CO_3})}{a} \tag{3.5}$$

where the values of the stoichiometric parameters are just equal to the charges of the corresponding ions. Here, Equation (2-26) is not used because of the equilibrium relation between H^+ and Fe^{2+}.

The crevice corrosion potential and rate are obtained by solving simultaneously Equations (2-24 – 2-25), (2-30 – 2-31) and (3-4 or 3-5). The results obtained for the holiday solution containing dissolved O_2 pressure of 0.21 atm, pH=9.2. NaCl of about 0.003 mol/L is used to provide a resistivity of about 25 ohm·m for the soil solution. The results with CO_2 are compared with those without (Figure 3-25). The very small amount of dissolved CO_2 in the solution appears to have an insignificant effect on the crevice potential and corrosion current density. Without CP, although the crevice potentials are almost the same, the corrosion current density with CO_2 is smaller than without. With CO_2 the potential at the holiday is higher than without.

With co-precipitation, for the two holiday pHs, 8 and 9, the crevice potential and corrosion current density were computed and compared (Figure 3-26). The potential and current density in the low pH solution rather has a smaller corrosion rate because the equilibrium potential of the iron-ferrous ion redox reaction is higher. For the same electrode potential, the overpotential of this redox reaction is smaller.

3.4 Steady State *Computational Results* with use of Practical Geometry

3.4.1 Background

Crevice corrosion of steel pipelines under a disbonded coating depends on many parameters including soil chemistry, pipeline-operational and coating-performance conditions[4,12,14]. The crevice corrosion due to the presence of dissolved O_2 in soil with or without CP is a significant problem and has been modeled extensively in previous work,[7-10] where two Laplace's equations, governing respectively mass conservation for dissolved O_2 and charge conservation expressed by steel potential in the crevice solution, were solved. Two types

of common crevice geometries found in the field, rectangular shape (Figure 3-27(a)) approximating disbondment associated with high-density polyethylene (HDPE) coating and disc shape approximating that found under fusion-bonded epoxy (FBE) coating[10], were modeled. The effects on crevice corrosion rate and potential of the crevice length, CP potential, resistivity of the crevice solution, permeation of O_2 through the coating, the geometrical parameters of the crevice (gap, holiday size and coating thickness) and the environmental temperature were investigated.

To solve the complex system of coupled differential equations, several assumptions were made in the previous model[7-10]. First, the Laplace's equations in two dimensions (2D) were modified to semi-2D by assuming uniform potential and parabolic O_2 concentration across the crevice gap. The assumption of uniform potential was made on the basis of the relatively small dimension of the crevice gap compared to the length. On the other hand, O_2 concentration was rather neither assumed uniform nor linear because of its slow diffusion that considerable concentration gradient exists near the steel surface while such gradient near the disbonded coating is relatively insignificant due to the coating barrier. Second, like those used in laboratory tests[16-17], the model crevice does not consider any bare steel at the holiday (Figure 3-27(a)). Although excellent agreement between the model results and experimental data was demonstrated[7-8], questions remain on whether this simplification of the crevice geometry (no holiday steel) and the assumption of uniform potential and parabolic O_2 concentration would accurately represent the field crevice corrosion. Although a justification can be made that such geometry may be consistent with field geometry if the steel at the holiday is inactive due to its being covered by soil, deposit or coating, the accuracy of this justification is not fully certain. If the steel surface turns out to be active when there were no soil on the holiday steel or if the deposit were porous, this justification can be invalid. In this work, a full 2D crevice corrosion model is solved with the holiday steel being active. All parameters used in the computations are the same as those reported in the previous work[7-10,24-26].

Although the potential at the holiday mouth (left vertical boundary at z=0 of Figure 3-27(a)) can be measured in laboratory tests, this potential cannot be easily measured in the field for two reasons. First, a holiday location is usually unknown before a reference electrode (RE) is buried nearby the underground pipelines or even if the holiday can be located accurately, the RE usually cannot be moved from one location to another and hence the IR drop between the RE and the holiday steel is in practice unknown. What therefore can be measured in the field is the steel potential located some distance away from the holiday (B5 of Figure 3-27(b)). Second, even if the crevice holiday can be accurately located and the RE could be moved around during pipeline excavation or laboratory tests, the potential measured at the holiday mouth in Figure 3-27(b) may not be well represented by the holiday potential in Figure 3-27(a) because of the effect of exposed steel in Figure 3-27(b). Similar to potential, O_2 concentration at the holiday cannot be measured easily since an O_2 sensor cannot easily probe the crevice holiday.

In view of the above uncertainties due to the assumptions to the previous semi-2D model[7-10], it is necessary that a general crevice geometry consistent with field application be developed and a full 2D model solved. The previous semi-2D model would be still significant if

it were verified to be consistent with the full 2D model. Then, the semi-2D can be used to approximate the 2D model, avoiding complications of the 2D solution.

3.4.2 Validity of Laplace's Equation Simplification

Although this work improves over previous crevice corrosion modeling, the use of Laplace's equation to describe steel potential implies uniformity of solution conductivity or chemical composition along the entire crevice. In verifying this assumption, a set of Nernst-Plank (NP) transport equations is solved in semi-2D under the same conditions as in previous work[8-9] including: crevice gap (0.5 mm) and solution chemistry (bulk O_2 partial pressure of 0.21 atm, pH at the holiday determined by saturated $Fe(OH)_2$ of 9.2 and solution resistivity at the holiday of 25 Ω·m), the crevice corrosion potential and current density were computed at two holiday potentials (-0.8074 V and -0.9 V) and shown to be consistent with previous work (Figure 3-28). In this new computation using NP equations, the solution resistivity was adjusted by maintaining a concentration of NaCl at 3.13×10^{-3} mol/l at the holiday. Although the computed crevice solution pH varies in the range of 7.6 - 12 and the solution resistivity in the range of 2.5 - 25 Ω·m in the disbondment, the crevice corrosion rate and potential are not significantly affected by the simplified assumption of Laplace's equation. Details of the computational results using NP equations are to be discussed in a future publication. In this work, all potentials used are referenced to saturated $Cu/CuSO_4$.

The corrosion rate determination by use of the NP equations requires solving a set of non-linear differential-algebraic equations with non-linear boundary conditions. Hence, convergence is a problem and solution of such 2D crevice corrosion has not been reported. Solved in 1D, the result showed that that even for a system not containing O_2, the crevice potential and solution chemistry can vary in a number of ways.[27-28] For example, the crevice pH and potential can either increase or decrease into the crevice depending on the initial crevice solution chemistry and the holiday potential. In this work, this sophistication is not pursued. Instead, by assuming uniform ionic solution, the synergistic effect of O_2 and CP on the crevice corrosion can be discussed in detail and the full 2D solution obtained more readily.

3.4.3 Governing Equations and Boundary Conditions

3.4.3.1 The Model Geometry and Parameters

Figure 3-27(b) shows the model geometry where only half of the length of the crevice is shown due to symmetry considerations: the left boundary (B1) is the symmetry line. Two domains are connected via the holiday mouth. The upper domain (region above the holiday mouth) represents soil solution out of the crevice. Its top and right boundaries (B5) are assumed to be where an RE probe is possibly located to measure the local pipe potential and O_2 concentration can be assumed to be constant as dictated by the local soil conditions. These artificial boundaries can be expanded or shrunk without increasing complexity of the modeling. The holiday potential thus measured always contains ohmic potential (IR) drop with respect to the holiday steel potential whose value cannot be estimated accurately unless the mathematical equations describing the corrosion process are solved. The coordinates used for the modeling, z and y, represent the gap and length directions of the crevice respectively. The gap between the coating and the steel surface (a) and the coating thickness (δ_c) are also assumed to be inputs to

the model. Here, O_2 permeation through the coating is not considered because the previous work[7-10] has already investigated this effect and the result is applicable here.

Due to the small dimension of the crevice holiday compared to the upper domain, it is expected that the potential and O_2 concentration have approximately uniform distribution along the boundary B5. The IR drop in the bulk soil solution is insignificant because the soil volume area through which the external current can pass easily is large. This IR is even smaller when the external CP is not significant. Although O_2 diffusion always results in a decrease in O_2 concentration between B5 and the crevice holiday, this change of O_2 concentration becomes less away from the holiday because of the increasing volume area of O_2 diffusion. This leads to a relatively uniform O_2 concentration along B5.

Table 3-1 shows the geometrical parameters and conditions used for the crevice corrosion modeling. The holiday mouth length is 2 mm with half (1 mm) shown in Figure 3-27(b) due to symmetry of the crevice . The crevice gap is 0.5 mm, compromising the disbondment sizes from different types of coatings including fusion bonded epoxy (FBE) (several micro meters) and HDPE (several millimeters). The crevice length is chosen to simulate long disbondment (200 times of gap). B5 is assumed to be about 1 cm away from the holiday, where the potential and O_2 concentration are uniform. When there is no CP, zero flux of potential (or current) across B5 is used and the potential at B5 can be calculated. With CP, the potential at B5 is the measured value by an RE. The dissolved O_2 pressure along B5 is assumed to be 0.21 atm. The intermediate soil resistivity of 25 ohm.m is used for crevice solution. The total pressure is assumed to be 1 atm and temperature 25^{o}C.

Table 3-1. Geometrical Parameters and Modeling Conditions

Length of holiday mouth (m)	0.002	Solution resistivity (ohm.m)	25
Crevice gap (m)	0.0005	Temperature (^{o}C)	25
Crevice length (m)	0.1	Total pressure (atm)	1
Between steel and top (m)	0.01		
Width of upper domain (m)	0.01		

3.4.3.2 The Model Equations

Under steady-state conditions, mass conservation of dissolved O_2, expressed by O_2 concentration (c_{O2}), can be expressed by:

$$\frac{\partial^2 c_{O_2}}{\partial z^2} + \frac{\partial^2 c_{O_2}}{\partial y^2} = 0 \qquad (3\text{-}6)$$

Charge conservation, expressed by the Laplace's equation for steel potential measured by an RE in any location in the solution (ψ), is given by:

$$\frac{\partial^2 \psi}{\partial z^2} + \frac{\partial^2 \psi}{\partial y^2} = 0 \tag{3-7}$$

The boundary conditions for solving Equations (3-6 – 3-7) are described below. All boundaries except B2 (bottom) and B5 have zero flux. B1 (left) is a symmetrical boundary and the others zero flux boundaries due to insulation to current or O_2 diffusion. Uniform potential and uniform O_2 concentration are assumed at B5 when there is external CP. B2 is the pipe steel surface on which anodic and cathodic reactions occur. The anodic reaction is iron oxidation:

$$Fe \rightarrow Fe^{2+} + 2e^- \tag{3-8}$$

In the alkaline solution (pH=9.2) due to precipitation of ferrous hydroxide, the hydrogen ion reduction reaction can be neglected. Therefore, the cathodic reactions are: water reduction:

$$H_2O + e^- \rightarrow H + OH^- \tag{3-9}$$

and O_2 reduction:

$$O_2 + 2H_2O + 4e^- \rightarrow 4OH^- \tag{3-10}$$

With an RE located at B5 to measure the pipe potential (ψ_0), the potential anywhere in the solution can be expressed by: $\psi = \psi_0 - \chi$ where χ is the electrostatic potential in solution. With uniform ionic composition, the anodic and cathodic reactions at B2 can be written for iron vs. ferrous ion redox reaction, expressed by the Butler-Volmer equation, as:

$$i_{corr} = i^0_{Fe}\left(10^{\frac{\psi_s - E^{eq}_{Fe}}{b_{Fe}}} - 10^{\frac{-\psi_s + E^{eq}_{Fe}}{b_{Fec}}}\right) \tag{3-11}$$

where ψ_s is ψ at the steel surface, i^0_{Fe} is the exchange current density for the Fe/Fe^{2+} redox reaction, b_{Fe} and b_{Fec} are respectively the anodic and cathodic Tafel slope, E^{eq}_{Fe} is equilibrium potential.

The Tafel equations for water and O_2 reductions are:

$$i_{H_2O} = -i^0_{H_2O} 10^{\frac{-\psi_s + E^{eq}_{H_2O}}{b_{H_2O}}} \tag{3-12}$$

$$i_{O_2} = -i^0_{O_2\,Ref} \frac{c_{O_2 s}}{c_{O_2\,Ref}} 10^{\frac{-\psi_s + E^{eq\,Ref}_{O_2}}{b_{O_2}}} \tag{3-13}$$

where $i^0_{H_2O}$, b_{H_2O} and $E^{eq}_{H_2O}$ are respectively exchange current density, Tafel slope and equilibrium potential for water reduction. $i^0_{O_2\,Ref}$ is O_2 reduction exchange current density at a

reference concentration $c_{O_2\,Ref}$, which corresponds to an equilibrium potential of $E_{O_2}^{eq\,Ref}$. b_{O_2} is O_2 reduction Tafel slope and $c_{O_2 s}$ is O_2 concentration at the steel surface.

Note that the exchange current densities and equilibrium potentials are not dependent on locations at the steel surface because their values have been taken at a reference condition[29]. In the previous work[8,10], Equations (3-11 – 3-13) were expressed in a different but equivalent format where the constants and variables are separated explicitly.

At B2, the diffusion flux of O_2 equals the its reduction rate:

$$-D_{O_2}\left.\frac{dc_{O_2}}{dy}\right|_{y=0} = i_{O_2}/n_{O_2}F \tag{3-14}$$

Following ohm's law, the flux of potential equals the net current density multiplied by solution resistivity (ρ):

$$\left.\frac{d\psi}{dy}\right|_{y=0} = -\rho(i_{corr} + i_{O_2} + i_{H_2O}) \tag{3-15}$$

3.4.4 Computational Results and Discussion

3.4.4.1 Case 1: No CP

This is a case where the soil is relatively dry and CP current cannot reach the crevice holiday readily. Alternate scenarios may include shielding of the CP by rocks or other non-conductive solids. The flux of potential (or current) is zero across B5. With this and other boundary conditions, Equations (3-6) and (3-7) are solved for O_2 concentration (all converted to its partial pressure according to Henry's law) and steel potential in the entire geometry.

Figure 3-29 is a contour plot of dissolved O_2 partial pressure. The dashed line is drawn arbitrarily in the figure for later use. The pressure interval is 0.021 atm between adjacent contours. The axes are labeled as ratios of z and y dimensions over the gap size (a). O_2 cannot penetrate into the crevice more than a few gap sizes ($z/a<5$) due to its diffusion limitation. Since O_2 reduction occurs only at the steel surface (ferrous ion oxidation is neglected due to its insignificant role in O_2 diffusion[29]), the contour density is greatest in the holiday region and decreases toward the soil bulk solution. The O_2 pressure along the arbitrary line is shown in Figure 3-30 starting from the origin to the point at (10,20). The O_2 pressure varies significant near the holiday region because of the small area of O_2 diffusion. Not being produced or consumed in solution, the linear diffusion of O_2 shows a curvature between 5-10 of z/a because the holiday mouth is not symmetrically located with the outer boundary B5.

A clearer view of O_2 pressure contours near the steel surface is shown in Figure 3-31(a) where the pressure interval is reduced to 0.01 atm. Relatively horizontal contours are shown around the holiday mouth. The contours are relatively uniformly spaced in the y direction at the

holiday region. However, within the crevice, there is significant non-uniformity in the contour spacing along the y/a direction justifying earlier assumption of parabolic function of O_2 pressure in that direction [7-10]. In Figure 3-32, although O_2 pressure across the holiday mouth (z/a=0-2 and y/a=1) increases from left to right, this increase is less than 10% over the average (0.369 atm). If O_2 pressure across the holiday mouth is assumed uniform and if the O_2 pressure there can be known, a simpler geometry without the upper domain may approximate the whole geometry, reducing the complexity of the numerical solution. A comparison of the results obtained from different geometries including Figure 3-27(a) is made in the next section.

The reason why Figure 3-32 shows an increase of O_2 pressure from left to right is due to: (1) zero flux across the left boundary by which O_2 diffusion gradually diminishes as it approaches that boundary, and (2) the least distance that O_2 travels when diffusing into the crevice via the right point of the mouth.

Figure 3-31(b) shows the contour plot of potential in the holiday region. Although the potential seems to be non-uniform there, the potential variation is not significant considering the small potential interval used for the contours (0.2 mV). Slightly moving into the crevice, the contours are vertically positioned parallel with each other, indicating uniform potential in the y direction. This result indicates that the previous work[7-10] reasonably approximated the crevice potential by the assumption of uniform potential across the crevice gap.

Although, these potential variations are insignificant from a practical point of view, it may be noted that around the bottom-left corner the potential is greater than the potential at B5 calculated to be –0.836 V. The highest potential is located right at the corner about -0.835 V. There, intensive O_2 reduction at the steel surface anodically polarizes the steel surface and overbalances the internal cathodic polarization, which is to be described later.

A more macroscopic demonstration of the potential contours is shown in Figure 3-33. The potential drop within the holiday and upper domain is less than 3 mV, indicating approximately uniform potential in the holiday region and in the upper domain. The potential along B5 is calculated to be about uniform. The narrow and long crevice geometry restricts any current generated at the steel surface (due to electrochemical reactions) from flowing out to create any IR along B5. The open circuit potential (OCP) in the crevice is reached after about 122 gaps sizes.

The ionic current flow in the holiday region is shown in Figure 3-34(a) together with the same contours shown in Figure 3-33. The arrow represents the flow of positive current in the direction indicated. The local current density is proportional to the length of the arrowed line. Perpendicular to the contours, the current flows in the horizontal direction inside the crevice and changes direction near the holiday region, flowing to the steel surface. This current flow indicates anodic polarization inside the crevice, where the steel surface behaves as anode. In the holiday region, the steel surface is cathodically polarized and behaves as cathode. That the current flows to the steel surface in the holiday region is due to O_2 diffusion limitation.

The current is very small in the upper domain and it flows out from the right portion of the holiday mouth and then returns back from the left portion. The overall current flow across

the holiday mouth must be zero since there is no CP and the very small holiday confines the current within the crevice, not flowing out easily.

Although the cathodic current flowing to the holiday steel surface may decrease the corrosion rate there, the corrosion rate close to the holiday is still higher than in the crevice. This can be reflected from the flow of superficial net current: defined as summation of the ionic current and the current converted from O_2 diffusion. O_2 diffusion current is not a real current because O_2 carries zero charge. It is, however, equivalent to a current because at the steel surface it is electrochemically reduced and the steel is anodically polarized. This superficial net current flow (Figure 3-34(b)) flows from the steel surface into the upper domain indicating dominant net anodic polarization by O_2 reduction at the steel surface in the holiday region. There, O_2 diffusion current overbalances the ionic current with the net current anodic. Not clearly shown, the arrow lines have a large vertical component from the steel surface in the holiday region than inside the crevice indicating larger corrosion rate in the holiday region than inside the crevice. This net current is approximately equal to anodic current density due to small water reduction current. Inside the crevice this net current remains to flow from inside to the holiday region because of absence of O_2 and the more negative potential inside the crevice than in the holiday region.

In the upper domain the net current is approximately equal to O_2 diffusion current because ionic current is negligible as shown in Figure 4-34(a). This net current becomes smaller as approaching B5 due to increase of O_2 diffusion area.

The corrosion current density along with those of O_2 and water reductions and the net current density is shown Figure 3-35. The corrosion current density (i_{Fe}) monotonically decreases from the holiday into the crevice. O_2 reduction current density (i_{O2}) quickly diminishes less than 5 gap sizes indicating absence of O_2 further into the crevice. Water reduction current (i_{H2O}) is very small and showed a small decrease in the holiday region due to the superficial net current flowing out from the steel, indicating net anodic polarization there.

In the holiday region O_2 reduction current is much larger than the corrosion current (i_{Fe}) due to high O_2 pressure there and due to dissipation of current into the crevice by the ionic current flow as shown in Figure 3-34(a). i_{O2} looks flat near the holiday mouth because of zero flux across left boundary and the holiday mouth being horizontal. i_{net} is net polarization current flowing out from the steel surface defined by $i_{net} = i_{Fe} + i_{O_2} + i_{H_2O}$. i_{net} is zero at about 3.3 gap sizes. It is exactly this point that separates the anodic and cathodic polarization regions of the steel surface. The cathodic region is steel surface which receives current and has a potential which, although normally below OCP for uniform corrosion, here is above OCP because the crevice corrosion is localized. The steel potential in the holiday region, being cathode, can become more negative than OCP only when the external CP becomes significant. The anodic region is the steel surface which gives current and has a potential, here without CP, below OCP. In the holiday region, i_{net} is negative ($-i_{net}$ is labeled in the figure), indicating cathodic polarization. Since this current is positive inside the crevice, the steel surface there is anodically polarized (anode). Although the current flow in the holiday region is cathodic, water reduction current (i_{H2O}) has a little decrease because O_2 reduction current is equivalent to anodic polarization of the steel surface and more significant than corrosion current.

The cathodic and anodic regions can be shown approximately by the total ionic current in Figure 3-36. The total ionic current is obtained by integration of the ionic current across the crevice gap. For the calculation, a crevice width of 1 mm perpendicular to the geometry is used. Although the total current is exact inside the crevice due to no current flowing out from the coating, it is approximate in the holiday region because of the little current flowing into the upper domain across the holiday mouth which is not accounted in the total current. Although error resulting from this is minimal for the case of no CP, it can become significant when external CP is applied because then, the current flow in the upper domain becomes significant and cannot be ignored.

The current starts at about zero at the left boundary due to zero flux across that boundary. It increases to a maximum and then decreases slowly. A vertical broken line approximately separates the cathodic (in the holiday region) and anodic (inside the crevice) regions caused by the polarization of current to the steel surface.

The total current increases sharply in the holiday region because O_2 is quickly reduced electrochemically as soon as it reaches the steel surface in the holiday region, precluding it from diffusing further inside the crevice.

Figure 3-37 shows the average potential across the crevice gap starting from the steel surface. This average potential is found to equal approximately the potential at the steel surface and both potentials overlap when plotted in the same figure. The potential monotonically decreases from the holiday into the crevice covering a distance much greater than O_2 as indicated in Figure 3-35. Therefore, the crevice corrosion mechanism is that the corrosion is caused by an O_2 concentration cell and the cell spreads the crevice corrosion far inside the crevice due to current flow through the crevice solution.

3.4.4.2 Case 2: With CP, Its Effect on Potential and Current Flow

Since O_2 reduction is limited by its diffusion and CP varies only the kinetics of O_2 reduction, the CP does not have any significant effect on the O_2 pressure profile in the geometry. The contours at different CP levels were found to overlap each other and are the same as in Figure 3-29.

Appropriate CP: At B5 there exists a potential at which the CP current just consumes all O2 diffusing into the crevice. Figure 3-38 shows the total current vs. total O2 diffusion current, across the holiday mouth, at various CP or potentials at B5. The currents were calculated based on 1 mm width of the crevice. The potential at the cross point is -0.8705 V: external CP current just equals O2 diffusion current.

In Figure 3-38, O_2 diffusion current into the crevice appears almost constant regardless of CP levels, with, not clearly shown, a slight decrease as the potential becomes less negative or CP decreases. This verifies that CP has nearly no effect on O_2 diffusion.

The CP current seems to increase approximately linearly with decrease of potential at B5.

Figure 3-39 is a potential contour plot at -0.8705 V at B5. Strikingly, the potential contours appear to match exactly those of O_2 pressure as shown in Figure 3-29. It was found that by matching the potentials at the two end points of the arbitrary line in Figure 3-29 to p_{O2}, all potentials and p_{O2}'s match exactly in the interior of the entire line. This match may be explained as below. There is neither production nor consumption of O_2 and current in the solution. O_2 is reduced only at the steel surface and it is where CP current has to be consumed. When the same amount of current just consumes all O_2 at the steel surface, O_2 or current must travel at the same pace for the same distance between B5 and the steel surface.

In this alkaline solution (pH=9.2), since the corrosion rate at OCP due to water reduction alone is small which is not a concern for the pipeline service life, -0.8705 V at B5 is an appropriate potential in protection of the crevice steel. At this potential, the corrosion threat by O_2 in soil is just removed without sacrifice of any excess CP current. The role of excess CP is only in reducing water, while it does not decrease the corrosion rate significantly. Also, increasing CP could enlarge coating disbondment and result in hydrogen induced cracking.

Figure 3-40(a) shows the current flow in the holiday region. The positive current flows to and cathodically protects the steel surface in the holiday region. Since O_2 has only limited access into the crevice, the current diminishes quickly before moving any deeper into the crevice. At this potential, wherever O_2 exists at the steel surface is about where the external CP current reaches. The small current flowing into the crevice indicates slight excess current which increases water reduction.

Overprotection CP: When the potential at B5 is -0.9 V, excess current beyond consumption of O_2 exists. This excess CP functions to reduce water only. Although CP is mainly consumed by O_2 reduction in the holiday region, the remaining CP current can penetrate deep inside the crevice, as shown in Figure 3-41(a). Unlike O_2 whose kinetics is controlled by its diffusion, the slow kinetics of water reduction allows the CP to penetrate deep into the crevice. The solution resistance is another factor that can affect the penetration depth of excess CP. The greater the solution resistance the less can the CP penetrate into the crevice.[5,7-10]

Because of excess CP, the superficial net current flow (Figure 3-41(b)) flows in the same direction as the ionic current flow, although the magnitude of the current becomes smaller after balancing O_2 diffusion current.

For both ionic current and superficial net current, they are large on the right portion of the holiday mouth because the current flowing via there experiences the least resistance due to the least distance that the current needs to travel into the crevice.

Figure 3-42 is a potential contour plot for the potential of -0.9 V at B5. In this diagram, the contours are denser inside the crevice compared to the upper domain because the relatively large resistance in the crevice solution due to the small gap compared to relatively dimensions of the upper domain. The contour density decreases from the holiday into the crevice due to decreasing current flow inside the crevice.

Underprotection CP: For a potential of -0.850 V at B5, the CP current is insufficient to consume all O_2 diffusing to the steel. This current deficiency indicates that residual O_2 remains in the holiday region and higher corrosion rates there.

Figure 3-43(a) is a combined contour plot with current flow. The current flows from the upper domain to the holiday region because of existence of external CP. The current that flows from inside the crevice to the holiday region because of internal polarization induced by an O_2 concentration cell which dominates over the external CP. As Figure 3-43(a) shows, cathodic polarization occurs at the holiday and anodic polarization inside the crevice. As cathode, the steel in the holiday region is polarized cathodically by both external and internal cathodic polarization.

Since the external CP current is less than O_2 diffusion current, the superficial net current flows following the direction of O_2 diffusion current - in reverse direction to O_2 diffusion (Figure 3-43(b)), going out from inside the crevice into the upper domain. The net current still flows from inside the crevice to the holiday region, because the potential inside the crevice is less than that in the holiday region as shown by the contours.

3.4.4.3 Case 3: With CP, Its Overall Effect on Crevice Corrosion

Effect on Crevice Potential: Figure 3-44 shows that a more negative potential at B5 results in more negative potentials in the crevice. As the potential at B5 becomes more negative, the crevice steel is better protected.

With insufficient CP or with the potentials at B5 falling between -0.836 V (no CP) and -0.8705 V (appropriate CP), the potential decreases from the holiday into the crevice due to residual O_2 in the holiday region: O_2 diffusion current overbalances external CP current. As O_2 pressure decreases into the crevice, the crevice corrosion potential becomes more negative. For insufficient CP, internal current due to O_2 concentration cell still exists (Figure 3-43(a)).

At overprotection CP or at a potential below -0.8705 V at B5, all O_2 is fully reduced by external CP. The excess CP reduces water, similar to cathodic polarization in deaerated solution. The crevice potential becomes less negative from holiday into the crevice. Since this excess CP generates hydrogen, susceptibility of the steel to hydrogen induced cracking and coating disbondment could increase.

For appropriate CP or potential of -0.8705 V at B5, CP exactly reduces O_2 in the holiday region and hence, the potential quickly reaches the OCP after a very short distance from the holiday. The potential appears constant.

Effect on Crevice Corrosion Rate: Similar to potential, the crevice corrosion rate decreases as CP increases (Figure 3-45). With insufficient CP, the corrosion rate is greatest in the holiday region and decreases into the crevice. With overprotection CP, the corrosion rate increases from the holiday into the crevice. At appropriate CP, the corrosion rate is nearly uniform inside the crevice where the corrosion rate equals that at OCP.

For the same amount decrease of potential at B5, the corrosion rate is decreased more significant in the region of insufficient CP than in the region of overprotection CP. Due to nearly linear relation between CP current and potential (Figure 3-39), for the same amount of external CP current, the decrease of corrosion rate is more effective in the region of insufficient CP than in the region of overprotection CP. For overprotection CP, not only does the excess CP become less effective, the excess current increases cost and/or unwanted hydrogen generation.

3.4.5 Summary

◊ Although O_2 is present only in the holiday region, without CP its effect on the crevice corrosion extends deep inside the crevice.

◊ Under the model conditions used in this work, external CP just consumes all O_2 diffusing to the crevice steel at a potential of -0.870 V at B5. This potential would be an ideal CP in protection of pipelines.

◊ For insufficient CP between no CP (-0.836 V) and appropriate CP (-0.870 V), external CP cannot fully consume all dissolved O_2. The corrosion rate is greatest at the holiday and decreases into the crevice.

◊ For insufficient CP, residual O_2 still forms a concentration cell that drives a positive current flowing from inside the crevice to the holiday region. The steel in the holiday region is cathodically polarized and behaves as a cathode. Inside the crevice the steel is anodically polarized and behaves as an anode.

◊ For excess CP (potential at B5 below -0.870 V), all O_2 is consumed and the residual CP reduces water only. It does not decrease corrosion rate significantly while it increases CP cost and may generate unwanted hydrogen.

◊ For excess CP, current flows into the crevice only. The crevice steel behaves as cathode only.

3.5 Simplification of the Model for Practical Application

3.5.1 Background

Crevice corrosion of steel under a disbonded coating due to dissolved O_2 with and without CP has been modeled for a complex 2D geometry (Figure 3-27(a)) in 3.4. This follows the previous work[8-9] which resolved the problem by using a simpler crevice geometry (Figure 3-27(c)). Although this simpler geometry is consistent with laboratory crevices[16-17] designed to simulate field pipeline corrosion under disbonded coatings, it does not contain the upper portion of Figure 3-27(a) (above the crevice mouth) and the holiday steel exposing to soil which were included in Part 1 where the upper portion was claimed to be more practical in the field for the measurement of the steel potential at the holiday mouth. In the field, a reference electrode (RE) usually is never intentionally placed at a crevice holiday mouth to measure the potential there because the crevice may not exist or may be unknown when the pipeline is buried. If an RE happens to monitor the crevice holiday potential, it must be located

some distance away from the holiday, at boundary B5 of Figure 3-27(a) for instance. This was elaborated in more detail in Part 1.

In the earlier work[8-9], by assuming the steel at the holiday to be inactive due to being covered perhaps by dust, deposit, coating or other non-permeable substance, where the electrochemical reactions do not exist, the holiday steel in the normal field crevice geometry (Figures 3-27(a) - (b)) was ignored and simplified to Figure 3-27(c). By the assumption of uniform potential and parabolic O_2 concentration across the crevice gap along its entire length, the 2D crevice model was able to be simplified as semi-2D and solved using a MATLAB code.

For this same crevice geometry (Figure 3-27(c)), if uniform potential and parabolic O_2 concentration are imposed only at the left boundary, this crevice corrosion model is still 2D and solved in this work.

For the crevice geometry of Figure 3-27(b), the upper portion of Figure 3-27(a) is ignored. This assumes that the potential and O_2 concentration across the holiday mouth (boundary B5 of Figure 3-27(b)) can be either estimated, measured or known under certain circumstances, such as for a laboratory designed crevice. This model is also solved in this work.

In this work, the crevice corrosion rate and potential for the three crevice geometries (Figures 3-27(a) - (c)) associated with four models (three 2D and one semi-2D) have been solved and the results are compared. Approximation of the complex 2D model (Figure 3-27(a)) by the simpler ones, an 1D model and an explicit algebraic equation is made. All parameters used in the computations are the same as those in the earlier work[8-9,24-26].

3.5.2 The Model and Boundary Conditions

Regardless of the differences in the crevice geometry in Figure 3-27, the governing equations for solving all three 2D models and the one semi-2D model are the same. As described in Section 3.4 and earlier work[8-9], they are two Laplace's equations representing respectively mass conservation for O_2 and charge conservation for the steel potential. Since the boundary conditions for the two 2D models (Figures 3-27(b) - (c)) have not been defined, they are described below. Table 3-2 is a summary of the boundary conditions for all four models (Figure 3-27(a) --$2D^a$; Figure 3-27(b) --$2D^b$; Figure 3-27(c) in 2D --$2D^c$; Figure 3-27(c) in semi-2D --semi-$2D^c$), where the entire crevice steel surface (boundary B2 in Figure 3-27) is assumed active. When the section of steel at the holiday in Figures 3-27(a) - (b) is inactive, the boundary condition at B2 has to be modified, which is given in the next section.

For $2D^b$, the boundary conditions are: (1) uniform potential and uniform dissolved O_2 pressure across the crevice mouth which are equal to the averages across the crevice mouth computed from $2D^a$, (2) variable fluxes at the steel surface for O_2 pressure and potential, and (3) zero flux at each other boundary due to either geometry symmetry (at left boundary) or insulation to mass/charge transfer.

For 2D^c, uniform potential and parabolic O_2 pressure across the gap are assumed at the left boundary. The coefficients of the parabolic relation can be calculated from the given potential, zero flux and known O_2 pressure at the joint point between the crevice mouth and the coating in Figure 3-27(c). The calculation is the same as that given in the earlier work[8-9]. Variable fluxes of potential and O_2 pressure at the steel surface and zero flux at all other boundaries consist of the rest of the boundary conditions.

Table 3-2. The Crevice Boundary Conditions for Active Holiday Steel

Figure 3-27(a)	Figure 3-27(b)	Figure 3-27(c)	
Part 1 (2D^a)	(2D^b)	(2D^c)	Semi-2D^c)
B5: uniform p_{O2} and φ (or zero total potential flux if no CP)	same as 2D^a	B1: parabolic p_{O2} vs. y and uniform φ (or zero total potential flux if no CP)	B1, B3 and all z/a: parabolic p_{O2} vs. y and uniform φ (B1: zero total potential flux if no CP)
B2: variable fluxes	same as 2D^a	B2: same as 2D^a	B2: same as 2D^c
		B4: O_2 permeation	B4: same as 2D^c
Other boundaries: zero flux	same as 2D^a	same as 2D^a	same as 2D^a

Unlike in the earlier work[8-9] where the coating is permeable to O_2, although not restricted by this current model, the coating here is assumed impermeable to either O_2 or current.

With the governing equations solved together with their boundary conditions, the results obtained from the newer two 2D models (2D^b and 2D^c) are compared with those in Part 1 (2D^a) and with the semi-2D model in the earlier work (semi-2D^c)[8-9]. A 1D model for deaerated condition and an algebraic equation to approximate 2D^a are developed in the result section.

A finite element code, FEMLAB, is used in this work to calculate the crevice corrosion rate. Since this code is different from the code used in the earlier work[8-9], a comparison of the results obtained from the two different codes for the same model is made as a verification of the new code.

3.5.3 Independent Verification of Current Finite Element Code

Figure 3-46 shows the variation, along the crevice length, of average potential across the gap and the ratio of average O_2 pressure to that in the bulk, obtained from the semi-2D^c. The dashed thicker curves are reproduced from the earlier work[8-9] where an MATLAB code was used. The thin solid curves are obtained from this current FEMLAB code. There is no external CP assumed in the system. The results obtained from the two different codes are essentially overlapped with each other. The same overlap has been found with external CP.

3.5.4 Computational Results and Simplification of the Model

3.5.4.1 Results Obtained from Four Crevice Corrosion Models

Comparison is made for the computational results obtained from the four models, including crevice corrosion current density (1 A/m^2=1.17 mm/y), potential, average O_2 pressure across the crevice gap and the total current flow in the crevice. The comparison is made without CP when the holiday steel surface is active or inactive. The purpose of this comparison is to explore whether the simpler crevice geometries and their corresponding models can used to approximate the complex $2D^a$ and what the associated error is.

Inactive Holiday Steel Surface: For inactive holiday steel (parallel with the holiday mouth of Figures 3-27(a) - (b)) where no electrochemical reactions occur, the fluxes of p_{O2} and potential at this section are zero. These fluxes at the rest of the steel surface are still variable boundary condition. In Part 1, the entire steel surface is active.

No CP means zero external current or the total flux of potential across the holiday mouth is zero. Figure 3-47 shows the average steel potential across the crevice gap in the crevice when the average O_2 pressure across the holiday mouth of Figure 3-27(a) (0.0780 atm) is used for $2D^b$. For semi-$2D^c$, the result was computed in two methods: (1) this $2D^a$ average O_2 pressure across the holiday mouth and (2) the O_2 pressure at the right point of the holiday mouth in Figure 3-27(a) (0.0687 atm)) are respectively used as the O_2 pressure at the joint point between the holiday mouth (left boundary B1) and the coating in Figure 3-27(c). Method 1 refers to semi-$2D^c$ (average) and Method 2 to semi-$2D^c$ (right point). Only is Method 1 used for $2D^c$. The dotted line in Figure 3-46 passes through the right edge of the holiday mouth of Figure 3-27(a) or 3-27(b) or the left boundary of Figure 3-27(c).

All potentials are greater than OCP. The OCP corresponds to the steel potential deep inside the crevice where the potential does not depend on location and the solution is deaerated without O_2 penetration through the coating. The crevice potential continues to decrease even after 60 gap sizes deep into the crevice. This is contrary to O_2 which cannot diffuse more than 4 gap sizes into the crevice (to be shown later). The reason that the potential can go deep into the crevice without CP is because the O_2 concentration cell generates a positive ionic current that flows, through the crevice solution, from inside the crevice to the holiday region. This current has been discussed in detail in the previous work[7-10]. In Figure 3-47, all the simpler models seem to be close to but slightly overestimate the potential of $2D^a$ with the best approximation given by $2D^b$ followed by $2D^c$ and then by semi-$2D^c$ (average). The semi-$2D^c$ (right point) better approximates $2D^a$ than the semi-$2D^c$ (average) because O_2 pressure used for the former (0.0687 atm) is less than for the latter (0.0780 atm). That $2D^c$ and semi-$2D^c$ (right point) overestimate $2D^a$ because of the assumptions of uniform potential and parabolic O_2 pressure across the gap in Figure 3-27(c) which may have artificially forced more O_2 diffusing into the disbondment.

Similar to Figure 3-47, Figure 3-48 shows that the simpler models all approximate well the corrosion current density of $2D^a$ although they all give an overestimate. At the right point of the holiday mouth, the current density difference between the semi-$2D^c$ (right point) and $2D^a$, 1.8 mA/m^2, is about 16% overestimation of the corrosion current density

of $2D^a$, 11 mA/m^2. Note that, although the corrosion current density is zero for $2D^a$ and $2D^b$ at the holiday steel surface since this steel section is inactive, the potential is continuous as shown in Figure 3-47

A comparison of average O_2 pressure across the crevice gap is shown in Figure 3-49. O_2 is unable to penetrate beyond four gap sizes into the crevice. Because O_2 cannot be reduced at the inactive holiday steel surface, there the average O_2 pressure of $2D^a$ is relatively high in comparison to that computed when the holiday steel is active as illustrated in Part 1 and later in this work. Due to the high reduction kinetics of O_2 on active steel, the average O_2 pressure of $2D^a$ or $2D^b$ has a significant decrease as approaching into the disbondment where the steel is active. The average O_2 pressure across the holiday mouth in Figure 3-27(a) (0.0780 atm) is used as the O_2 pressure at the joint point between the holiday and the coating in Figure 3-27(c) (semi-$2D^c$ and $2D^c$). T he semi-$2D^c$ (right point) yields an average O_2 pressure (0.0477 atm) closer to that of $2D^a$ (0.0383 atm) than semi-$2D^c$ (average) does.

Active Holiday Steel Surface: Since here $2D^a$ has the potential and O_2 pressure different from those if the holiday steel is inactive, a new average O_2 pressure across the holiday mouth from $2D^a$ (same as that in Part 1) is used as a boundary condition for other simpler models. Without CP, zero potential flux is used across the holiday mouth, which allows for the calculation of the potential across the holiday mouth. The average potential across the holiday mouth was calculated to be -0.836 V, about 3 mV more positive than if the holiday steel surface is inactive.

In Figure 3-50, the corrosion current densities computed from $2D^a$ and $2D^b$ are greater than those in Figure 3-48 because active steel increases O_2 diffusion into the holiday and into the disbondment. The coupling current between the disbonded region and the active holiday steel increases the corrosion current density in the disbondment.

That the results from $2D^a$ and $2D^b$ are close to each other indicates consistency of the two models. The current densities of $2D^c$ and semi-$2D^c$ seem to be well below that of $2D^a$ with a difference as high as over 50% because $2D^c$ and semi-$2D^c$ neglect the transport process in the holiday and the electrochemical reactions at the holiday steel. Without CP, the potential at the holiday was computed based on zero flux of potential. Due to the electrochemical reactions at the holiday steel in Figures 3-27(a) - (b), clearly larger coupling currents of $2D^a$ and $2D^b$ are hown than those of $2D^c$ and semi-$2D^c$ (Figure 3-51). This larger anodic current in the disbondment represents increased corrosion current densities of $2D^a$ and $2D^b$ compared to those of $2D^c$ and semi-$2D^c$.

That the semi-$2D^c$ (average) seems to approximate $2D^a$ better than $2D^c$ is because the former assumed a parabolic O_2 pressure across the gap along the entire crevice length, which may have artificially forced more O_2 diffusion into the disbondment.

Although not clearly shown, in Figure 3-52 the average O_2 pressure and its gradient at the holiday mouth (left boundary of Figure 3-27(c)) calculated from the semi-$2D^c$ are greater than those calculated from $2D^c$. This larger gradient indicates more O_2 diffusion into the disbondment and thus more corrosion of the crevice steel. The total metal loss in the disbondment is

determined by the total amount of O_2 diffusing into the crevice when water reduction is, as being the case here, insignificant in this alkaline crevice solution (pH=9). This theory, although applicable to semi-$2D^c$ and $2D^c$, is not applicable for $2D^a$ and $2D^b$, where the coupling current between the holiday and the disbondment plays a significant role. Although the O_2 pressure and its gradient or the O_2 amount entering into the crevice of semi-$2D^c$ and $2D^c$ at z/a=0 are greater than those of $2D^a$ and $2D^b$, which should result in a greater corrosion current density inside the crevice, their corrosion current densities are however smaller because of the anodic current flow in $2D^a$ and $2D^b$ from the disbondment to the holiday. The average O_2 pressures of $2D^a$ and $2D^b$ are in similar magnitude and shown relatively flat along the holiday because O_2 diffusion to the steel surface is easier than into the disbondment.

Figure 3-53 is a comparison of average potential across the crevice gap. This average potential is overlapped with the potential at the steel surface due to the very small IR drop across the gap.

The above calculations, regardless of inactive or active holiday steel, are significant when the potential at the holiday is unknown. This unknown potential can be calculated from the no CP condition. Comparison of the computational results from all four models indicates that the simpler ones can be used to approximate the $2D^a$ although the approximation errors vary. The following deals with a situation when the potential at the holiday can be measured or known. Investigation is made on whether an 1D model or an algebraic equation can be used to approximate the complex $2D^a$ when CP is or is not present.

3.5.4.2 Polarization Approximation by $2D^b$ and 1D in Deaerated Condition

Approximation without CP: Since O_2 is present only near the holiday area due to its slow diffusion, since O_2 reduction is similar to anodic polarization, it is crucial to understand whether an anodic polarization imposed to the crevice holiday in deaerated condition would yield a crevice corrosion current density that quantitatively agrees with the rate when there is O_2 no CP.

In Figure 3-54, the corrosion current densities calculated from $2D^a$ for inactive and active holiday steel surfaces are reproduced respectively from Figures 3-48 and 3-50. For anodic polarization without O_2, only does the Laplace's equation for the steel potential as the governing equation need to be solved. The potentials across the holiday mouth of $2D^b$ (anodic) and 1D (anodic) are the same. They are -0.839 V and -0.836 V, respectively for inactive and active holiday steels and equal to the average potential across the holiday mouth of $2D^a$ with O_2 no CP. It is clear from the figure that regardless of active or inactive holiday steel, the corrosion current density computed from either $2D^b$ or 1D under anodic polarization in deaerated solution well approximates $2D^a$. Figure 3-50 shows a close approximation for the crevice potential. Figures 3-54 - 55 indicate that it is the potential at the holiday that determines the crevice corrosion current density; the IR drop across the crevice gap is negligible.

Approximation with CP: Since the simple 1D model with anodic polarization no O_2 approximates $2D^a$ well, it is expected that with CP, at a given potential at the holiday mouth, this 1D model will also approximate $2D^a$ well. Since approximation of the 1D model to $2D^a$ is similar regardless of active or inactive holiday steel, only are the results for active holiday steel presented.

Two CP conditions of $2D^a$ are approximated by the 1D model for active holiday steel: (1) appropriate CP for $2D^a$ by which O_2 in the crevice is just consumed by the CP current and (2) an overprotection CP. The average potential across the holiday mouth of $2D^a$ is calculated to be -0.866 V for condition (1) and -0.894 V for condition (2).

Figure 3-56 shows that the crevice corrosion current density and average potential computed from the 1D anodic polarization without O_2 for the above two conditions are in excellent agreement with that from $2D^a$ with O_2.

3.5.4.3 Simplification of the $2D^a$ into Algebraic Equations

The equations to describe the 1D anodic polarization was given previously as:[8]

$$\frac{d^2\varphi}{dz^2} = \frac{\rho}{a}(i_{corr} + i_{H_2O}) \tag{3-16}$$

where φ is average potential across the crevice gap measured by a reference electrode, ρ crevice solution resistivity and i_{H2O} water reduction current density. Hydrogen ion reduction is neglected because the crevice solution is alkaline due to ferrous hydroxide precipitation.

Given the potential at the holiday mouth and by using Tafel equation, the corrosion current density in the crevice is:

$$i_{corr} = i^0_{Fe} 10^{\frac{\varphi - E^{eq}_{Fe}}{b_{Fe}}} = i_{corr\_OCP} 10^{\frac{\varphi - E_{OCP}}{b_{Fe}}} \tag{3-17}$$

The Tafel equation for water reduction is:

$$i_{H_2O} = -i_{corr\_OCP} 10^{\frac{-\varphi + E_{OCP}}{b_{H_2O}}} \tag{3-18}$$

where E_{OCP} and i_{corr_OCP} are respectively OCP and the corrosion current density at OCP which both are measurable parameters.

By using dimensionless distance: $\xi = z/a$ and dimensionless potential: $\eta = \frac{F(\varphi - E_{OCP})}{RT}$, Equation (3-15) can be written as:

$$\frac{d^2\eta}{d\xi^2} = C(\exp(\alpha_{Fe}\eta) - \exp(-\alpha_{H_2O}\eta)) \tag{3-19}$$

where $C = \frac{F}{RT} a\rho i_{corr\_OCP}$, dimensionless.

By using first order Newton's expansion of the two terms in the bracket on the right side of Equation (3-19), the following equation is obtained:

$$\frac{d^2\eta}{d\xi^2} = C(\alpha_{Fe} + \alpha_{H_2O})\eta \tag{3-20}$$

Given potential at the holiday ($\eta_{\xi=0} = \eta_0$) and zero potential flux at the crevice end (z=L or $\xi_L = L/a$) or $\left.\frac{d\eta}{d\xi}\right|_{\xi_L} = 0$, integration of Equation (3-20) yields:

$$\eta = \eta_0 \frac{\mathrm{Cosh}[C_1(\xi_L - \xi)]}{\mathrm{Cosh}(C_1\xi_L)} \tag{3-21}$$

where $C_1 = \sqrt{C(\alpha_{Fe} + \alpha_{H_2O})} = \sqrt{\frac{a\rho}{R_p}}$, where the polarization resistance R_p replaces $i_{corr\text{-}OCP}$ in C. C_1 is a dimensionless number and determines the penetration distance of an anodic or cathodic polarization.

When the disbondment is sufficiently long as has been assumed so far in this work, Equation (3-21) becomes:

$$\eta = \eta_0 e^{-C_1\xi} \tag{3-22}$$

When the total current flowing in or out of the crevice through the holiday (I_0) can, for example in a lab setup, be measured over the crevice width (w) so that $I_{w0}=I_0/w$ and $\left.\frac{d\eta}{d\xi}\right|_{\xi=0} = \frac{F}{RT}\rho I_{w0}$, this current can be used either to estimate the corrosion current density in the holiday for Figures 3-27(a) - (b) or to verify the I_0 that can be computed from Equation (3-22) by: $\left.\frac{d\eta}{d\xi}\right|_{\xi=0} = -C_1\eta_0$.

If explicitly expressed by potential, Equation (3-22) can be written as:

$$\frac{\varphi - E_{OCP}}{\varphi_0 - E_{OCP}} = e^{-C_1\frac{z}{a}} \tag{3-23}$$

Equation (3-23) can determine the potential profile in a field crevice (pipeline steel under a disbonded coating) if the potential at the holiday, the OCP, R_p, and ρ are known. The latter three can be determined in lab by using simulated in-disbondment solution and a specimen of the same material as the pipe substrate. The corrosion density profile can be obtained from the Tafel equation (Equation (3-17)).

Figure 3-57 shows the average potential calculated from Equation (3-23) and the corresponding Tafel corrosion current density at a holiday potential that is equal to the

average potential across the holiday mouth of $2D^a$ under conditions of: (1) no CP with O_2 (-0.836 V), (2) CP that just consumes all O_2 diffusing into the crevice (-0.866 V) and (3) overprotection CP (-0.894 V). OCP is known, or $E_{OCP} = -0.866$ V. Since R_p can be calculated from i_{corr_OCP} (0.00234 A/m^2) to be 5.105 Ωm^2, C_1 is 0.0495. Excellent agreement between the results from Equation (3.23) and $2D^a$ is shown.

Agreement between experimental data and computational results from Equation (3-23) was published in the literature[8,30] where Equation (3-23) was derived from a different route and did not include O_2 and anodic polarization.

A theoretical plot of potential, computed from Equation (3-23), vs. z/a for a number of C_1 values is shown in Figure 3-58. The potential at the holiday is assumed to be -0.836 V. As C_1 increases, the curve shifts to the left and the polarization penetration distance is less.

Suppose the polarization is considered diminished if the ratio, as percentage, of the potential difference of φ-E_{OCP} to total polarization φ_0-E_{OCP} is less than θ, the maximum polarization penetration distance L_p can be calculated from Equation (3-23) to be:

$$L_p / a = -\frac{\ln \theta}{C_1} \tag{3-24}$$

In the case of C_1=0.0465 and θ=5% the penetration distances L_p is 64.4 gap sizes.

Figure 3-59 shows the variation of the crevice potential, computed from Equation (3-21), vs. z/a for four crevice lengths at C_1=0.0495. The potential at the holiday is assumed to be -0.836 V. The potential is shown not to reach OCP if the crevice is sufficiently short.

The potential at the end of the crevice ($\xi = \xi_L$) can be obtained from Equation (3-21) to be:

$$\frac{\varphi_L - E_{OCP}}{\varphi_0 - E_{OCP}} = \frac{1}{\mathrm{Cosh}(C_1 \xi_L)} = \frac{1}{\mathrm{Cosh}(C_2 \frac{L}{\sqrt{a}})} \approx \frac{1}{1 + \frac{L^2}{a}\frac{\rho}{2.3R_p}} \tag{3-25}$$

where the second order expansion of $\mathrm{Cosh}(C_1\xi_L) \approx 1 + \frac{(C_1\xi_L)^2}{2} = 1 + \frac{L^2}{a}\frac{\rho}{2.3R_p}$ is used and $C_2 = \sqrt{\frac{C_1}{a}} = \sqrt{\frac{\rho}{2.3R_p}}$.

The second equal sign of Equation (3-25) indicates that the potential at the end of the crevice is determined by the geometrical parameter: L^2/a and η_L can be proportional to a/L^2 when $\frac{L}{a} >> \sqrt{\frac{R_p}{a\rho}}$. Note that L^2/a has often been used as a scale-up parameter for crevice

corrosion. Here, if still C_2=0.0465 is used, the simplification by $\mathrm{Cosh}(C_2\frac{L}{\sqrt{a}}) = 1+\frac{L^2}{a}\frac{\rho}{2.3R_p}$ has an accuracy of <5%, if L/a<5.

3.5.4.4 Determination of Holiday Potential with Known only O_2 Pressure at the Holiday

In simulation of anodic polarization without CP, it has been clear that as long as the potential at the holiday is known, Equation (3-23) can be readily used to compute the potential inside the entire crevice for a long crevice where deep inside no O_2 exists, no external and internal polarization and OCP is valid and can be computed. However, there are cases where this holiday potential is unknown while the O_2 pressure there is known. Then, this potential at the holiday must be calculated in order to obtain potential inside the entire crevice.

When the holiday steel is inactive it has been shown that the $2D^a$ model can be approximated by the semi-$1D^c$. Hence, this semi-$1D^c$ model can become useful for crevices, whose length is just longer than 5 gap sizes by which O2 concentration is zero at the end of the crevice, that allow for computation of holiday potential with only known O_2 pressure at the holiday.

For this computation, the equation derived in the previous work can be used which is written below for the case of no O_2 permeation through the coating (with O2 permeation through the coating this approach is still valid):

$$\frac{d^2\varphi}{dz^2} = \frac{\rho}{a}(i_{corr} + i_{H_2O} + i_{O_2}) \tag{3-26}$$

where $i_{corr} = i_{corr0}10^{\frac{\varphi-\varphi_0}{b_{Fe}}}$, $i_{H_2O} = i_{H_2O0}10^{\frac{-\varphi+\varphi_0}{b_{H2O}}}$, $i_{O_2} = \frac{3\gamma\bar{p}_{O_2}}{3\lambda 10^{\frac{\varphi-\varphi_0}{b_{O_2}}} - a^2}$, $\lambda = \frac{an_{O2}FD_{O2}c_{5ref}}{i_{O_2ref\,0}}$,

$\gamma = an_{O_2}FD_{O_2}/H_{O_2}$ and $i_{O_2ref\,0} = i^0_{O_2ref}10^{\frac{-(\varphi_0-E^{Eqref}_{O_2})}{b_{O_2}}}$.

First integration of Equation (3-26) with use of the zero potential flux and zero O_2 at the end of the crevice yields:

$$\left(\frac{d\varphi}{dz}\right)^2 = \frac{\rho}{a\ln(10)}\left(b_{Fe}i_{corr} - b_{H_2O}i_{H_2O} + \frac{b_{O_2}3\gamma\bar{p}_{O_2}}{a^2}\ln(3\lambda - a^2 10^{\frac{-\varphi+\varphi_0}{b_{O_2}}}) - b_{Fe}i_{corre} + b_{H_2O}i_{H_2Oe}\right) \tag{3-27}$$

Without CP, the potential at the holiday can be calculated from:

$$0 = \frac{\rho}{a\ln(10)}\left(b_{Fe}i_{corr0} - b_{H_2O}i_{H_2O0} + \frac{b_{O_2}3\gamma\bar{p}_{O_20}}{a^2}\ln(3\lambda - a^2) - b_{Fe}i_{corre} + b_{H_2O}i_{H_2Oe}\right) \tag{3-28}$$

In the case of no CP in a short crevice where polarization deep inside the crevice is unknown and hence the potential there cannot be calculated, knowing only O_2 pressure at the holiday is not enough to calculate the potential at the holiday from explicit equations. To obtain the potential inside the whole crevice, the potential at the holiday must be known. Then, Equation (3-21) must be used to compute the potential in the entire crevice.

$$\frac{d\varphi}{dz} = \sqrt{\frac{\rho}{a\ln(10)}\left(b_{Fe}i_{corr} - b_{H_2O}i_{H_2O} + \frac{b_{O_2}3\gamma\bar{p}_{O_2}}{a^2}\ln\left(3\lambda - a^2 10^{\frac{-\varphi+\varphi_0}{b_{O_2}}}\right)\right)} \qquad (3\text{-}29)$$
$$\sqrt{-b_{Fe}i_{corre} - b_{H_2O}i_{H_2Oe} + \frac{b_{O_2}3\gamma\bar{p}_{O_2e}}{a^2}\ln\left(3\lambda - a^2 10^{\frac{-\varphi_e+\varphi_0}{b_{O_2}}}\right)\Bigg)}$$

3.5.5 Summary

◊ Four crevice corrosion models representing three crevice geometries have been solved and their results are compared. The calculation was made for the holiday steel surface either active or inactive.

◊ The above models can predict the crevice corrosion rate without knowledge of the potential at the holiday when there is no CP. $2D^b$ gives an excellent approximation to $2D^a$ for either active or inactive holiday steel. $2D^c$ and semi-$2D^c$ approximate $2D^a$ well (<20%) when the holiday steel surface is inactive, while this approximation is less accurate (>50%) when the holiday steel is active. This semi-1D allows for easy calculation of the crevice corrosion rate.

◊ O_2 reduction is equivalent to anodic polarization. Crevice corrosion due to an O_2 concentration cell can be reproduced by anodic polarization in deaerated solution.

◊ A simple algorithm has been developed that can reproduce the comprehensive crevice corrosion model derived in Part 1. Given no knowledge of O_2 content, the corrosion rate within a crevice formed on buried pipelines under a disbonded coating can be estimated from the algorithm with the need of only three measurable variables: potential at the crevice holiday, OCP and the linear polarization resistance (R_p) of the substrate material in the subject crevice solution which can be sampled and simulated in laboratory.

3.6 References

1. H. Leidheiser, W. Wang, L. Igetoft, Progress in Organic Coatings 11 (1983) 19-40.
2. C.G. Munger, Corrosion Prevention by Protective Coatings (NACE, 1984) 47-61.
3. J.M. Leeds, Pipe Line & Gas Industries, March (1995) 21-26.
4. M. Meyer, X. Campaignolle, F. Coeuille, M.E.R. Shanahan, "Impact of Aging Processes on Anticorrosion properties of Thick Polymer Coatings for Steel Pipelines", in Proceedings of the Corrosion/2004 Research topical Symposium: Corrosion Modeling for Assessing the Condition of Oil and Gas Pipelines, F. King and J. Beavers (eds.), Houston, TX: NACE/2004, 93-146.

5. F.M. Song, D.W. Kirk, D.E. Cormack and D. Wong, “Barrier Properties of Two Pipeline Coatings”. Materials Performance, 44 (4) (2005) 26-29.

6. F.M. Song, D.W. Kirk, D.E. Cormack and D. Wong, “Corrosion under Disbonded Coatings with Cathodic Protection”, Materials Performance, 42(9) (2003) 24-26.

7. Fengmei Song, “Corrosion of Coated Pipelines with Cathodic Protection”, Ph.D. thesis (2002), University of Toronto, Department of Chemical Engineering and Applied Chemistry.

8. F.M. Song, D.W. Kirk, J.W. Graydon and D.E. Cormack, “Steel Corrosion under a Disbonded Coating with a Holiday, Part 1: The Model and Validation”, Corrosion 58(12) (2002) 1015-1024.

9. F.M. Song, D.W. Kirk, J.W. Graydon and D.E. Cormack, “Steel Corrosion under a Disbonded Coating with a Holiday, Part 2: Corrosion Behavior”, Corrosion 59(1) (2003) 42-49.

10. F.M. Song, D.A. Jones and D.W. Kirk, “Corrosion and Current Flow within a Pipeline Disc Crevice”, Corrosion, 60(2) (2005) 145-154.

11. F.M. Song and N. Sridhar, “Predicting Pipeline SCC Conditions through Simulation of Under-Disbondment Chemistry and Potential”, International Pipeline Conference, Calgary, Alberta, Canada, Oct. 4-8, 2004.

12. N. Sridhar, “Modeling the Conditions under Disbonded Coating Crevices – A Review”, in Proceedings of the Corrosion/2004 Research topical Symposium: Corrosion Modeling for Assessing the Condition of Oil and Gas Pipelines, F. King and J. Beavers (eds.), Houston, TX: NACE/2004, 53-92.

13. N. Sridhar, D.S. Dunn, and M. Seth, 2001, Application of a General Reactive Transport Model to Predict Environment under Disbonded Coatings, Corrosion, 57 (7), 598-613.

14. Orazem, M.E., D.P. Reimer, C. Qiu and K. Allahar, “Computer Simulations for Cathodic Protection of Pipelines”, in Proceedings of the Corrosion/2004 Research topical Symposium: Corrosion Modeling for Assessing the Condition of Oil and Gas Pipelines, F. King and J. Beavers (eds.), Houston, TX: NACE/2004, 25-52.

15. R.R. Fessler, A.J. Markworth, R.N. Parkins, Corrosion 39 (1) (1983) 20-25.

16. T.R. Jack, G.V. Boven, M. Wilmott, R.L. Sutherby, R.G. Worthingham, MP (8) (1994) 17-21.

17. A. Turnbull and A.T. May, Materials Performance, 22 (1983) 34.

18. J.J. Perdomo and I. Song, Corrosion Science 42 (2000) 1389.

19. M.H. Peterson and T.J. Lennox, Jr., Corrosion 29 (1973) 406.

20. A.C. Toncre and N. Ahmad, Materials Performance 19(6) (1980) 39.

21. M.D. Orton, Materials Performance 24(6) (1985) 17.

22. F. Gan, Z.-W. Sun, G. Sabde, and D.-T. Chin, Corrosion 50(10) (1994) 804.

23. R. Brousseau and S.Qian, Corrosion 50 (12) (1994) 907-911.

24. F.M. Song, D.W. Kirk and D.E. Cormack, "Modeling CO_2 Corrosion in Oil and Gas Transmission Systems". Held April 3-7, 2005 (Houston, TX: NACE, 2005) Paper: 05180.

25. F.M. Song, D.W. Kirk, J.W. Graydon and D.E. Cormack, "CO_2 Corrosion of Bare Steel under an Aqueous Boundary Layer", Corrosion 60(8) (2004) 736-748.

26. F.M. Song, D.W. Kirk, J.W. Graydon and D.E. Cormack, "CO_2 Corrosion of Bare Steel under an Aqueous Boundary Layer with Oxygen", Journal of The Electrochemical Society, 149(11) (2002) B479-B486.

27. G.R. Engelhardt, D.D. Macdonald, M. Urquidi-Macdonald, Corros. Sci. 41, 12 (1999): p. 2,267.

28. A. Turnbull, "Modeling of the Chemistry and Electrochemistry in Cracks—A Review", Corrosion 57(2) (2000) 175-189.

29. F.M. Song, D.W. Kirk, J.W. Graydon and D.E. Cormack, "Effect of Ferrous Ion Oxidation on Corrosion of Active Iron under an Aerated Solution Layer", Corrosion 58(2) (2002) 145-155.

30. Z. Li, F. Gan and X. Mao, "A Study on Cathodic Protection against Crevice Corrosion in Dilute NaCl Solutions", Corrosion Science 44 (2002) 689-701.

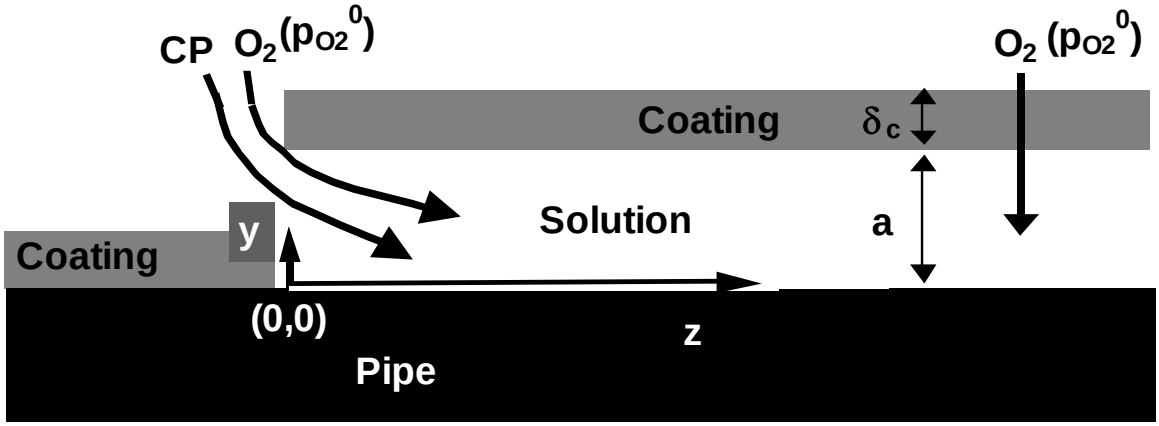

Figure 3-1. Schematic diagram of the model geometry.

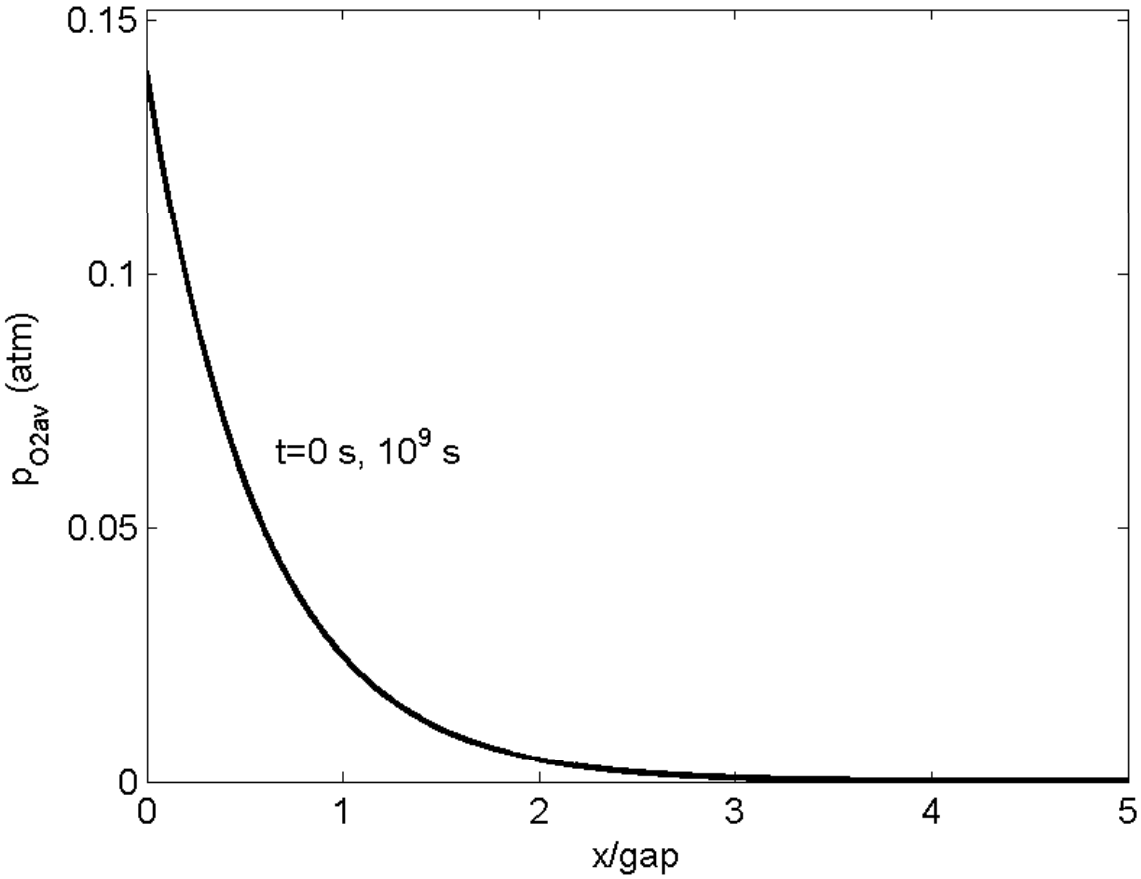

Figure 3-2. With or without CP, the transient O_2 pressure in the crevice at time zero and 10^9 s. It shows that once O_2 diffusion reaches steady state in the crevice, this profile does not change with time regardless of potential and ionic transport.

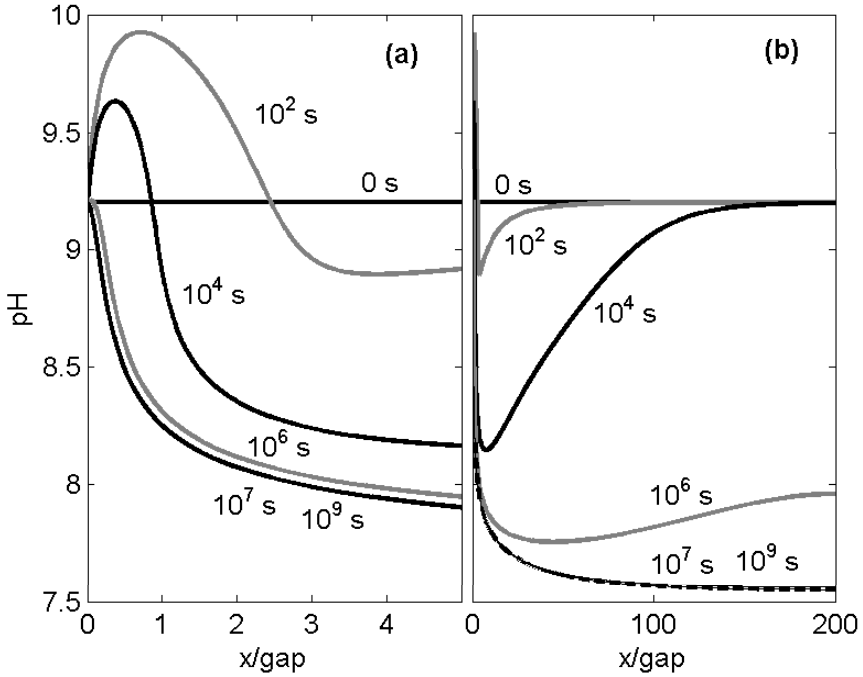

Figure 3-3. Without CP, the transient variation of crevice pH. The two curves at times of 10^7 and 10^9 s are overlapped. In (a), the near-holiday region of the overall distribution in (b) is expanded to see the local spatial pH change.

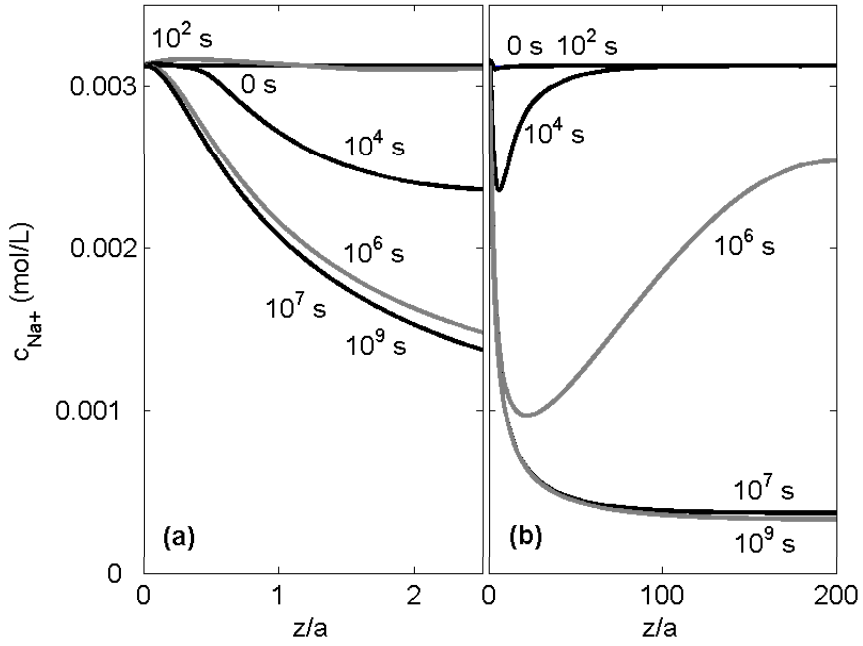

Figure 3-4. Without CP, the variation of Na^+ concentration. In (a), the near-holiday region of the overall concentration profile in (b) is expanded to see the local spatial change of concentration.

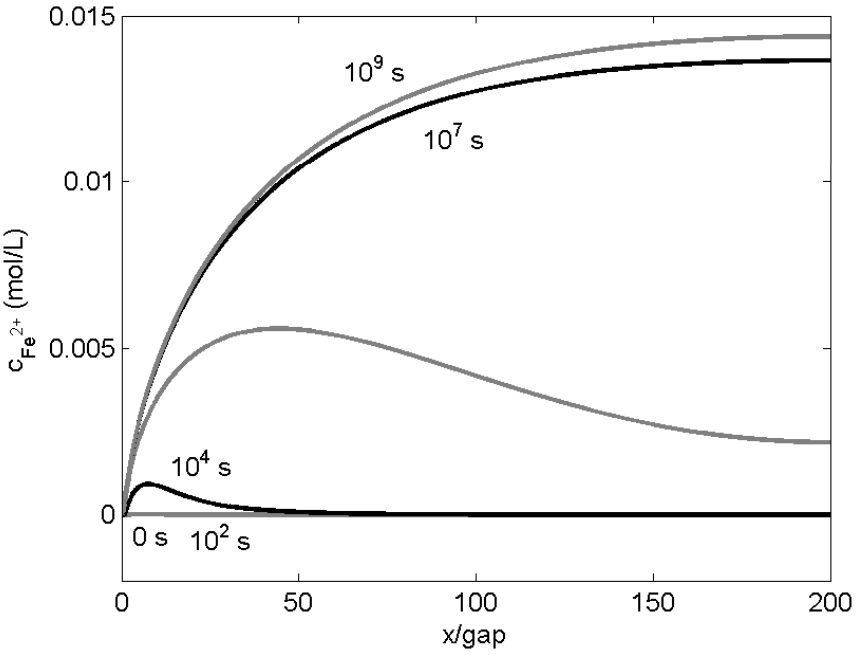

Figure 3-5. Without CP, the transient variation of Fe^{2+} concentration. The two curves at times of 0 and 10^2 s are overlapped.

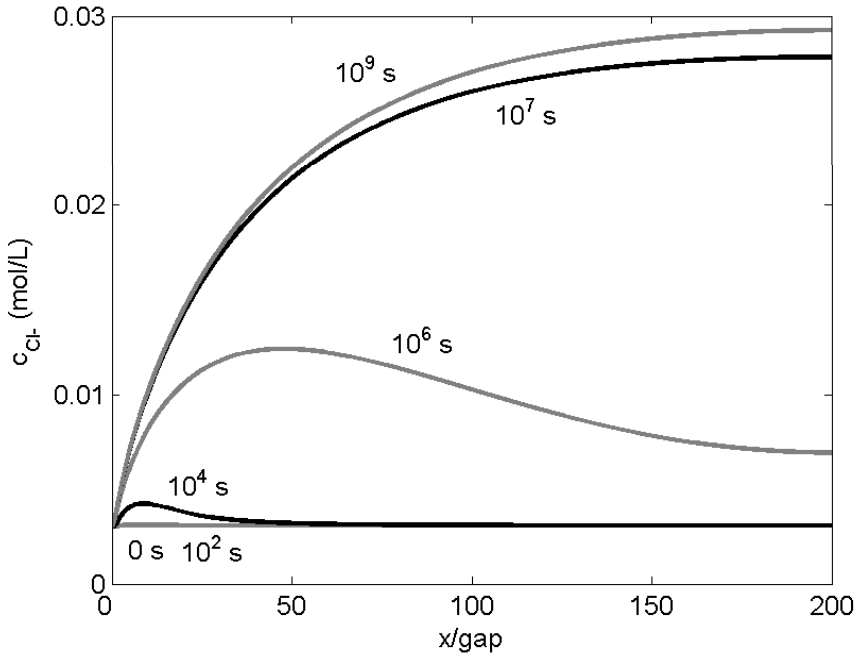

Figure 3-6. Without CP, the transient variation of Cl^- concentration. The two curves at times of 0 and 10^2 s are overlapped.

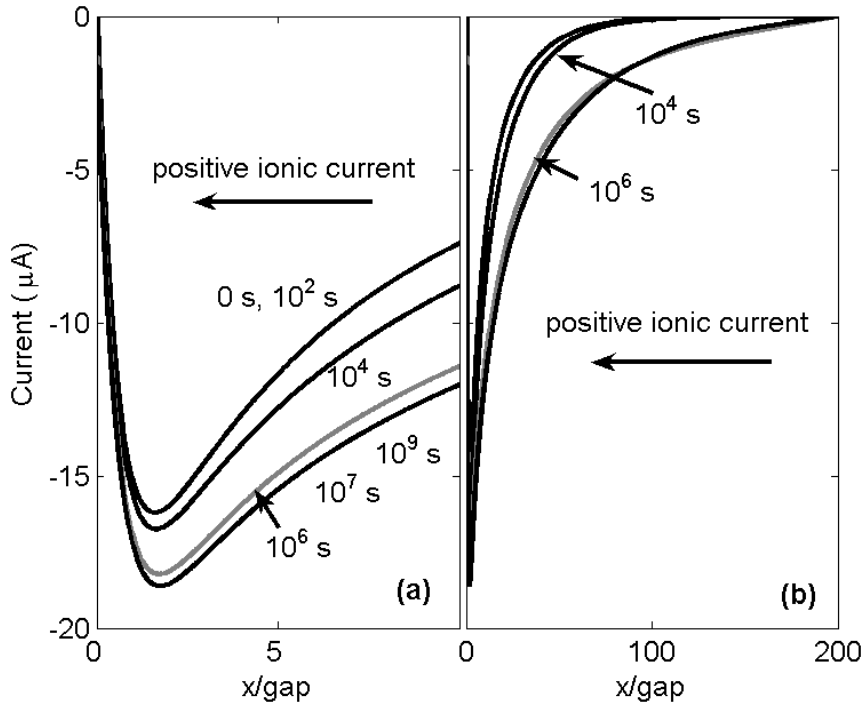

Figure 3-7. Without CP, the transient internal current in the crevice that flows from inside to the holiday region. The two curves at times of 0 and 10^2 s are overlapped. In (a), the near-holiday region of the overall current profile in (b) is expanded to see the local spatial change of the current.

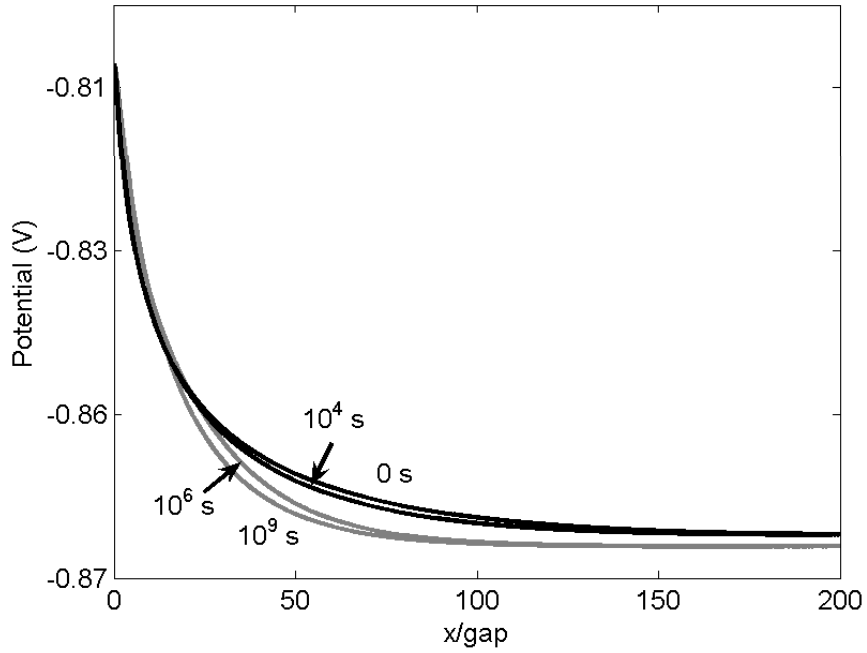

Figure 3-8. Without CP, the transient crevice potential profile.

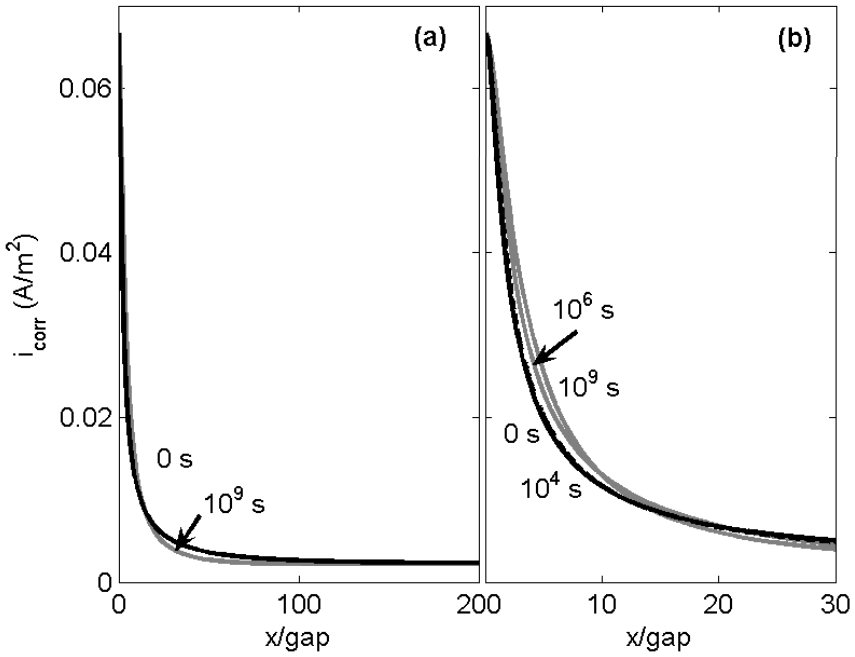

Figure 3-9. Without CP, the transient crevice corrosion current density profile. In (b), the near-holiday region of the overall current profile in (a) is expanded to see the local spatial change of the current.

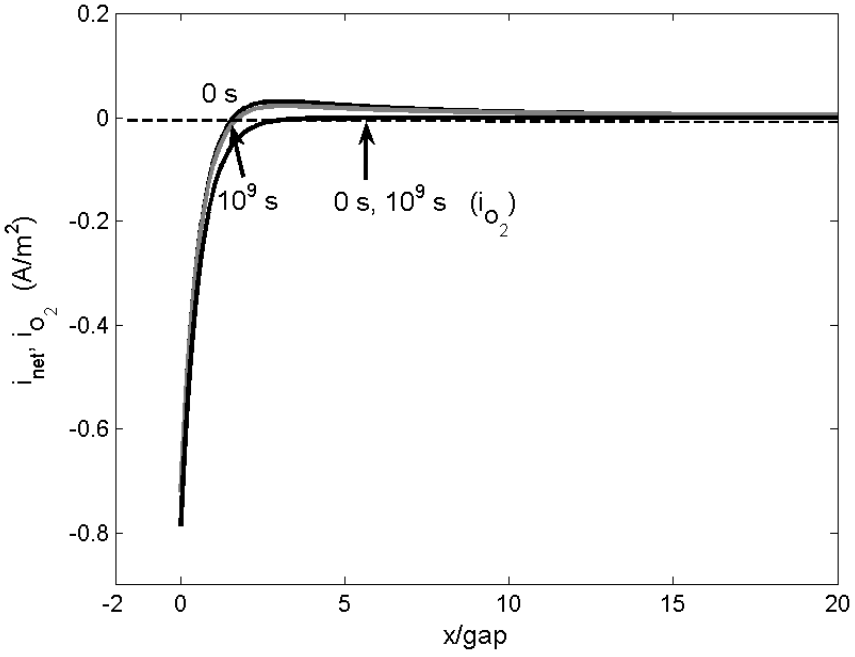

Figure 3-10. Without CP, the net current density profile which flows into the crevice solution from the steel surface and the transient O_2 reduction current density profile.

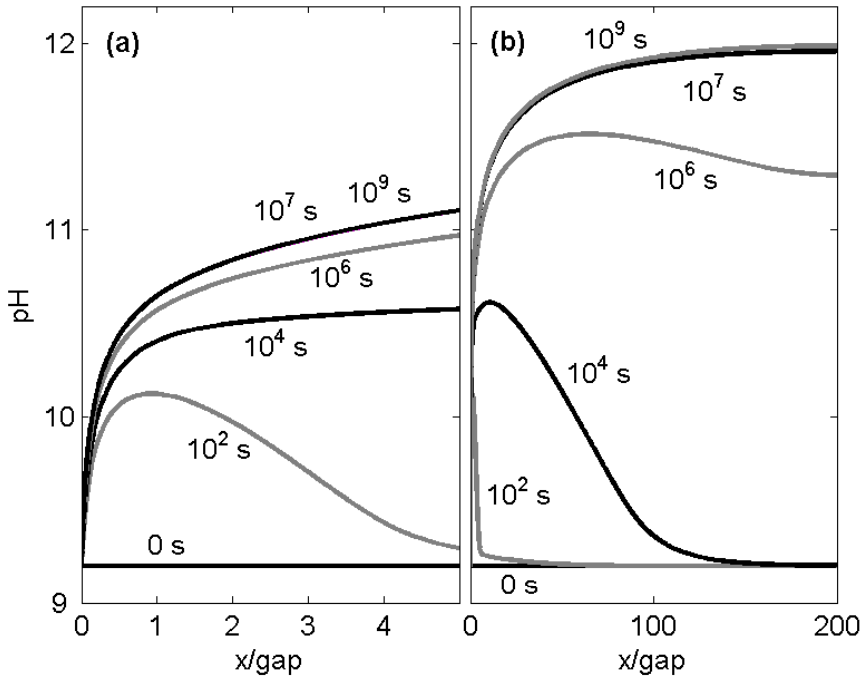

Figure 3-11. With CP, the transient variation of pH. In (a), the near-holiday region of the overall current profile in (b) is expanded to see the local spatial change of the current.

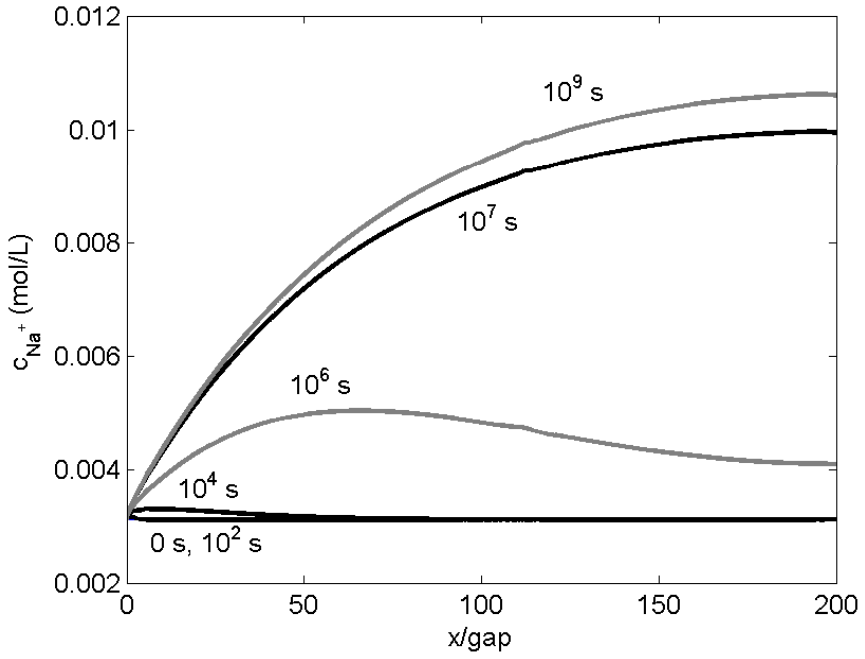

Figure 3-12. With CP, the transient variation of Na^+ concentration. The two curves at times of 0 and 10^2 s are overlapped.

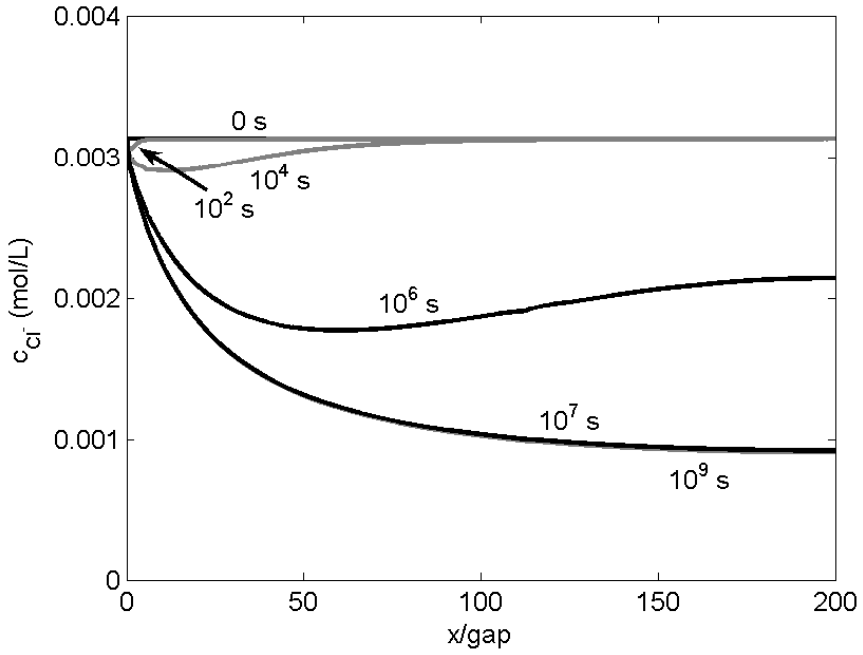

Figure 3-13. With CP, the transient variation of Cl^- concentration. The two curves at times of 10^7 and 10^9 s are overlapped.

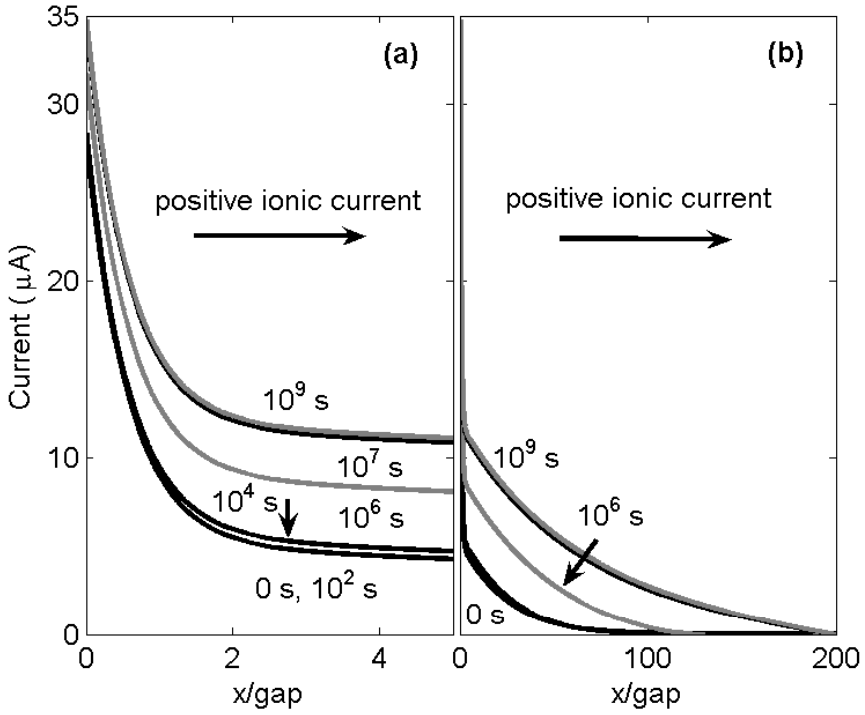

Figure 3-14. With CP, the transient variation of current in the crevice. In (b), the near-holiday region of the overall current profile in (a) is expanded to see the local spatial change of the current.

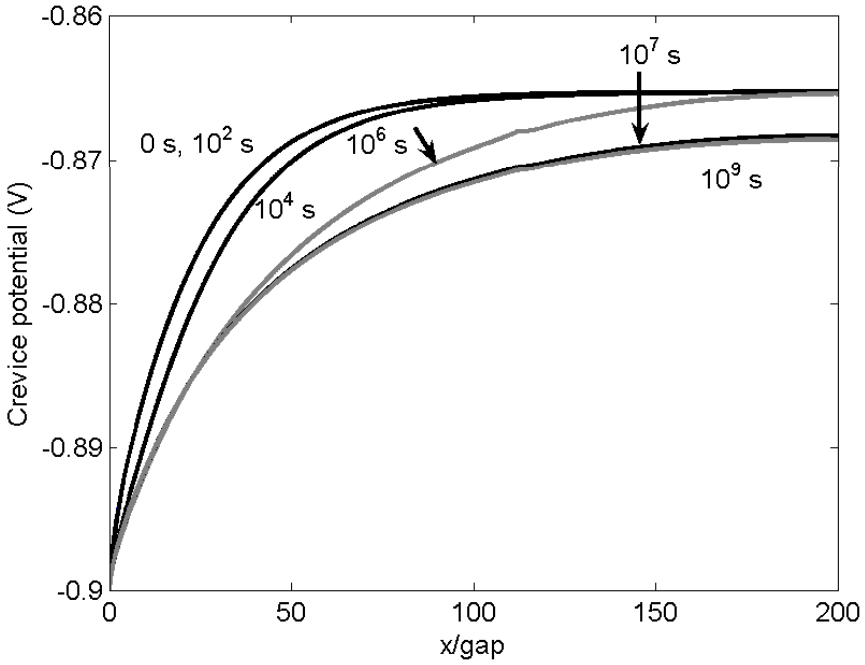

Figure 3-15. With CP, the transient variation of crevice potential. The two curves at times of 0 and 10^2 s are overlapped.

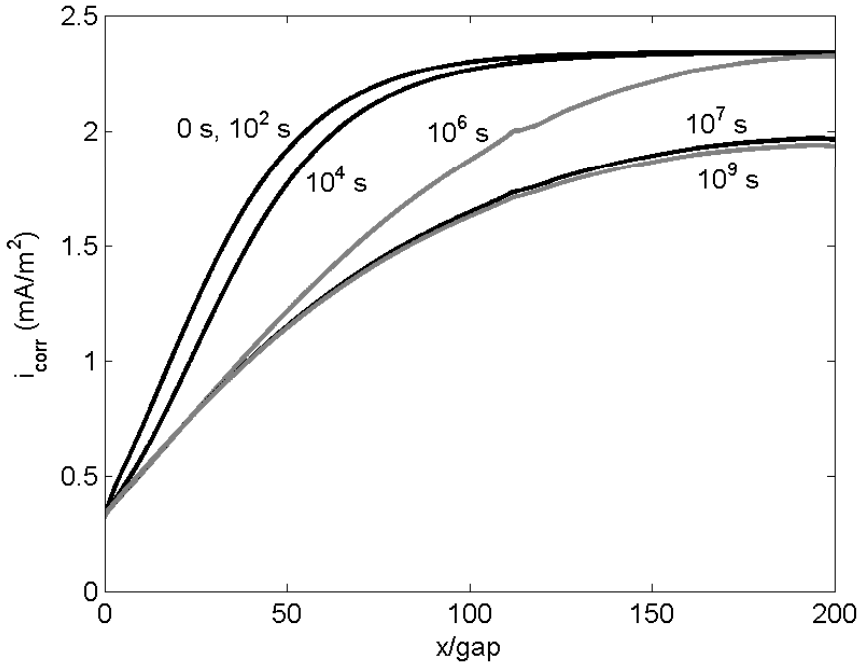

Figure 3-16. With CP, the transient variation of crevice corrosion current density. The two curves at times of 0 and 10^2 s are overlapped.

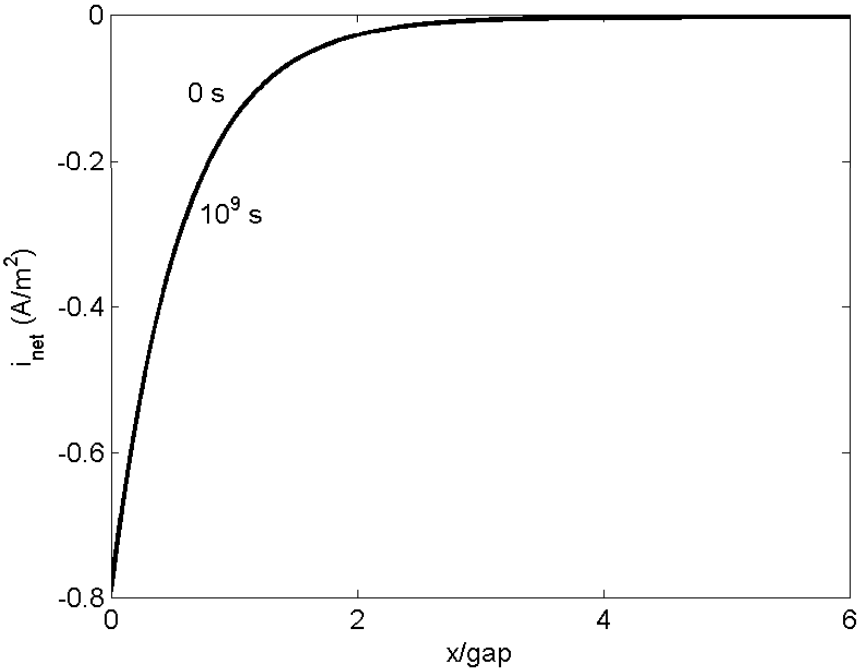

Figure 3-17. With CP, the transient variation of net current density in the crevice.

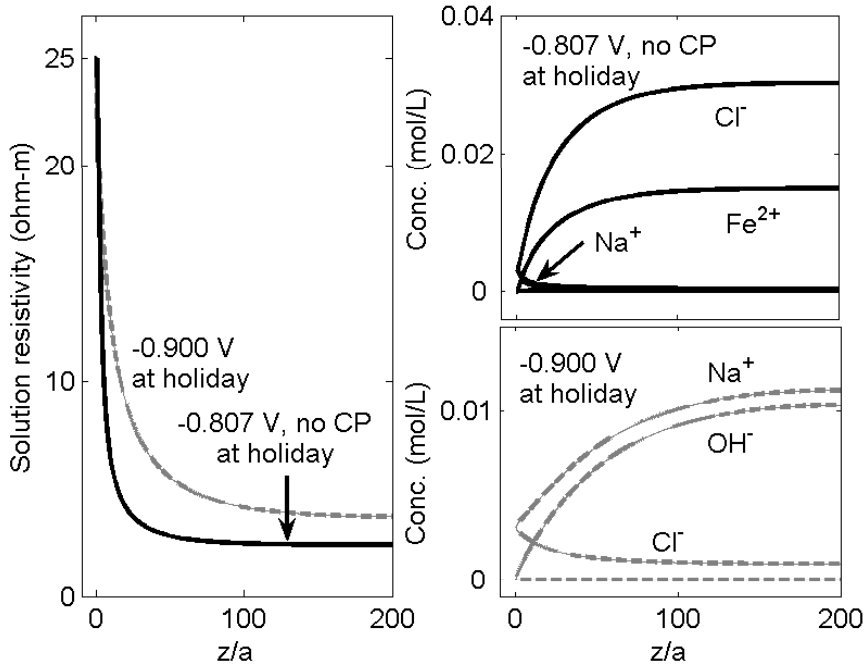

Figure 3-18. With and without CP, the crevice solution resistivity and chemistry at steady state obtained by using Tafel for Fe vs. Fe^{2+} redox reaction.

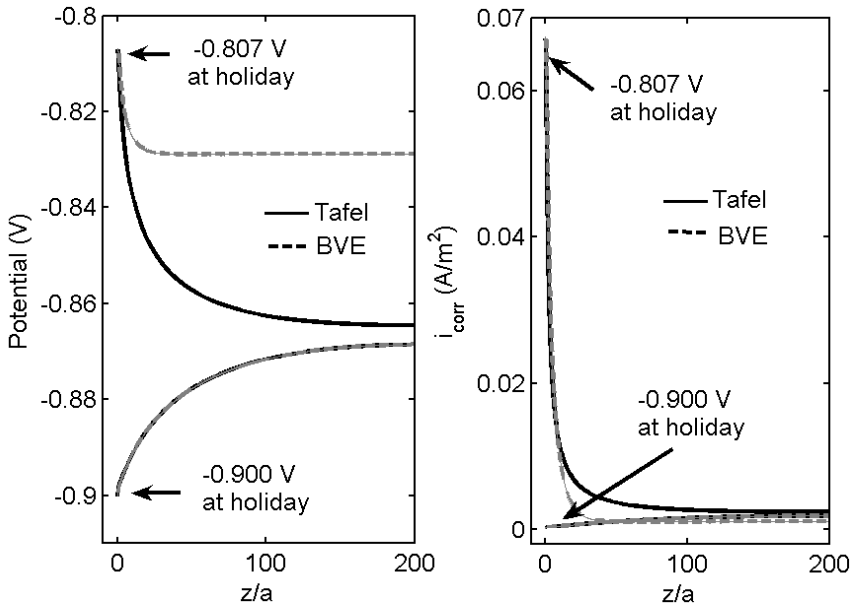

Figure 3-19. Without CP, comparison of crevice potential and corrosion current density calculated from using Tafel and BVE for Fe vs. Fe^{2+} redox reaction.

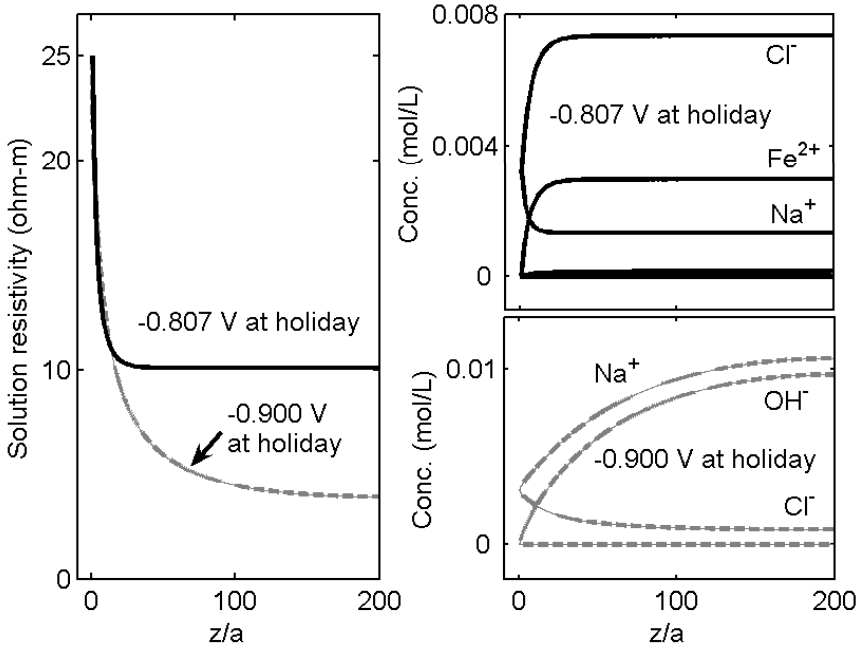

Figure 3-20. With and without CP, the crevice solution resistivity and chemistry at steady state obtained by using Tafel and BVE for Fe vs. Fe^{2+} redox reaction.

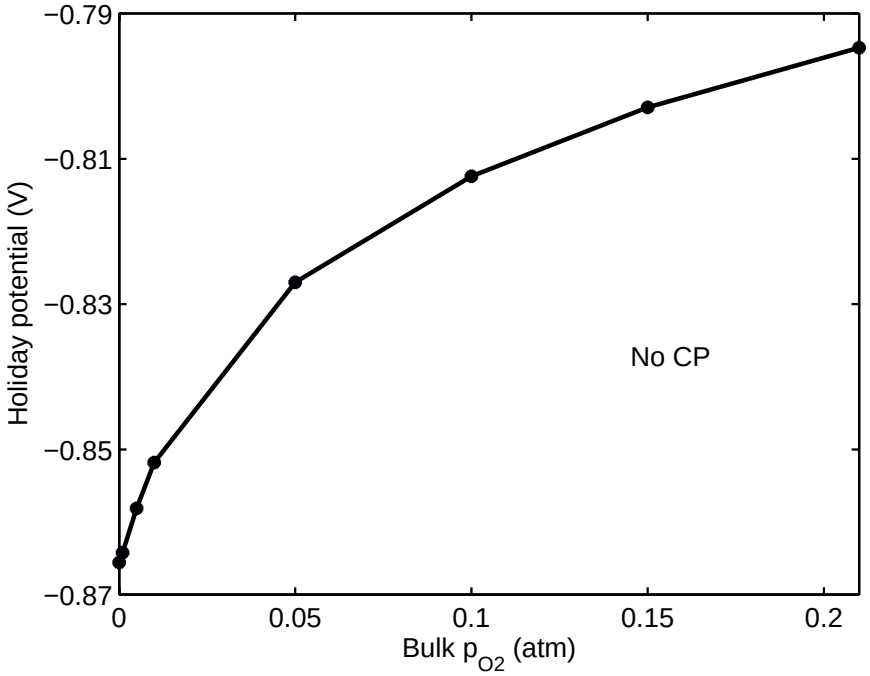

Figure 3-21. The holiday potential vs. bulk O_2 pressure calculated from using BVE for Fe vs. Fe^{2+} redox reaction.

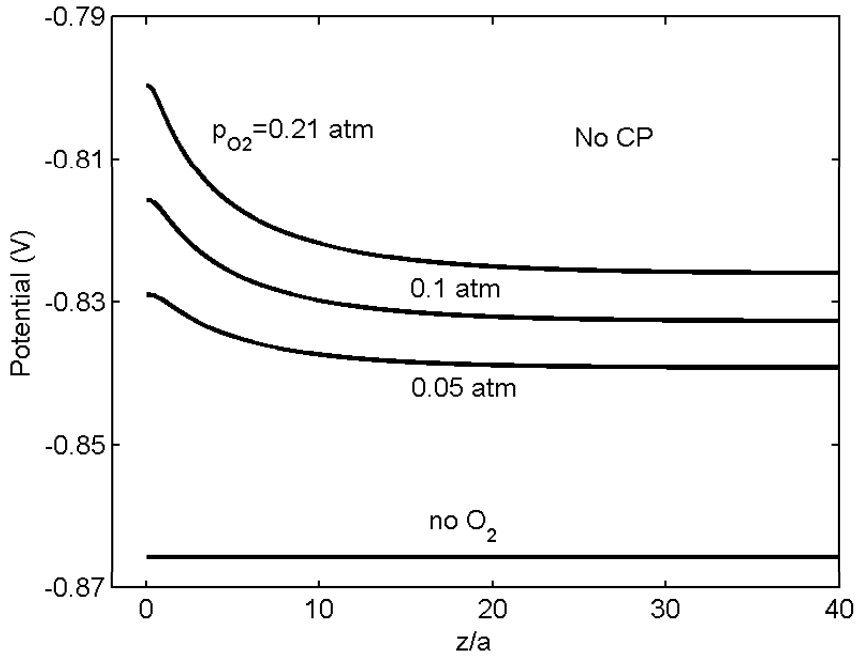

Figure 3-22. The potential profile vs. bulk O_2 pressure calculated from using BVE for Fe vs. Fe^{2+} redox reaction.

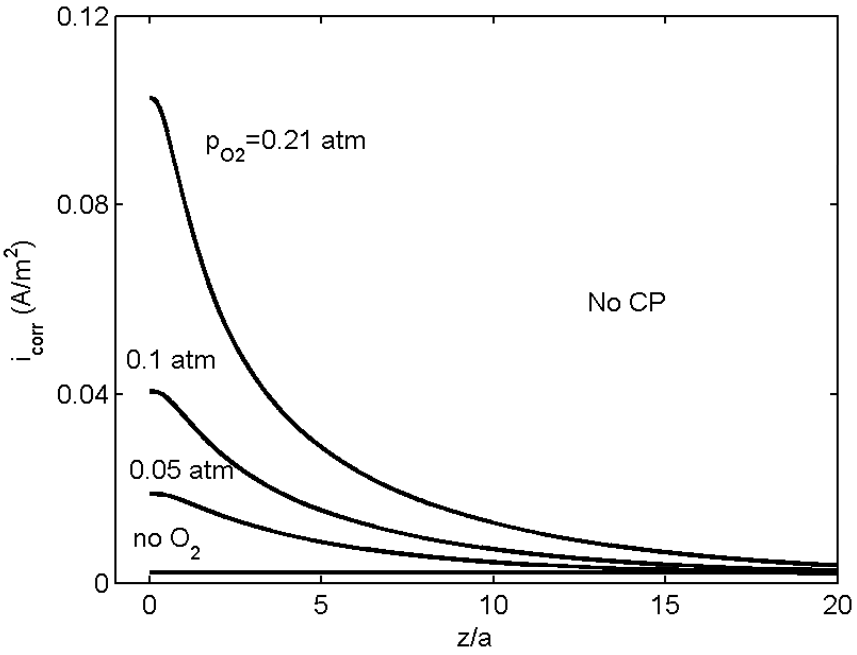

Figure 3-23. The crevice corrosion current density profile vs. bulk O_2 pressure calculated from using BVE for Fe vs. Fe^{2+} redox reaction.

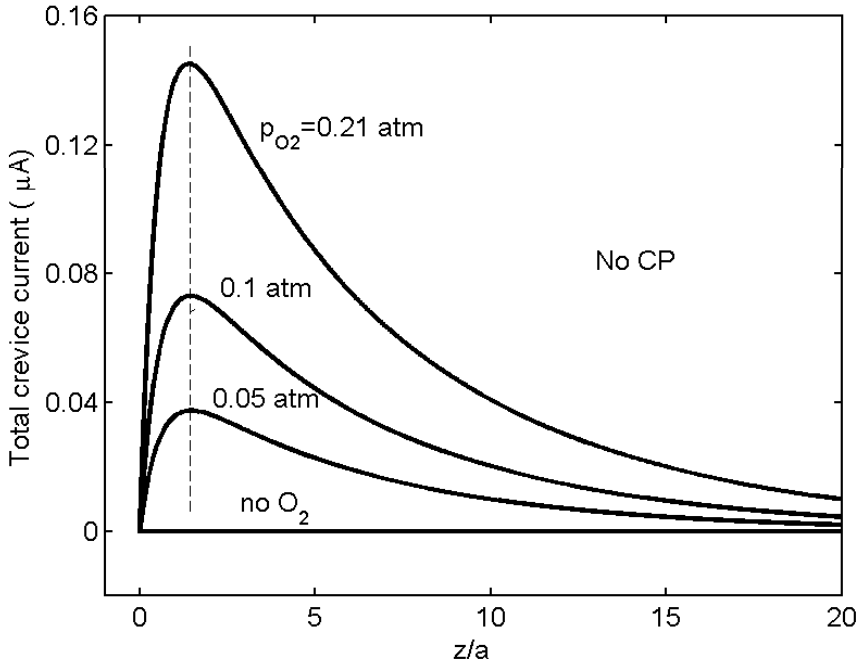

Figure 3-24. The total internal current profile vs. bulk O_2 pressure calculated from using BVE for Fe vs. Fe^{2+} redox reaction.

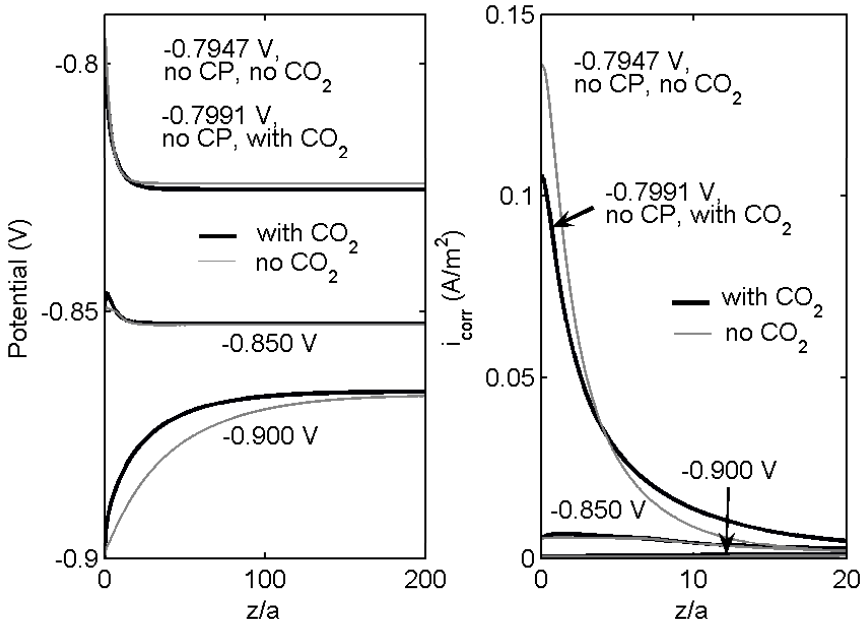

Figure 3-25. Crevice corrosion potential and current density without CO_2 and those with CO_2 under co-precipitation of $FeCO_3$ and $Fe(OH)_2$, under conditions with and without CP.

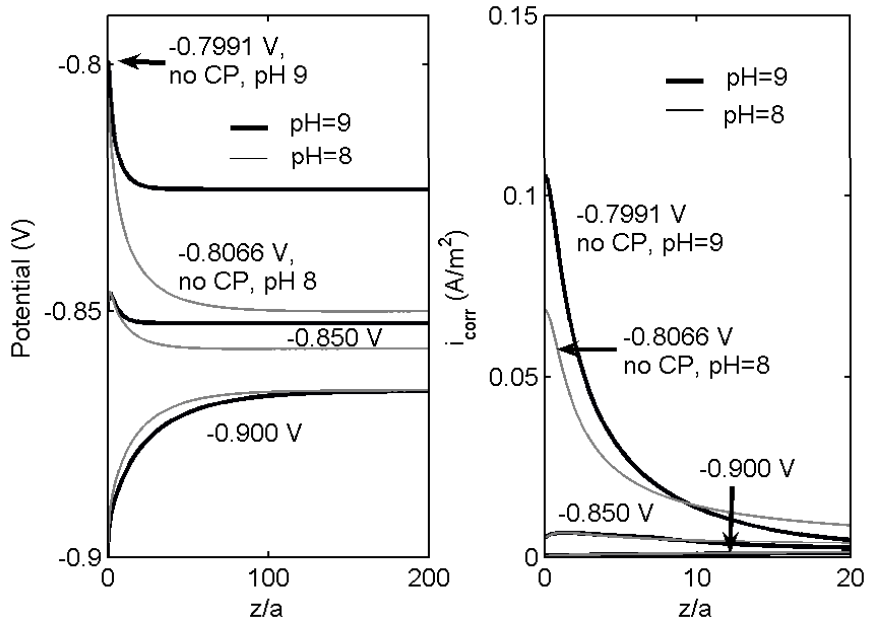

Figure 3-26. Crevice corrosion current densities and potentials under co-precipitation of $FeCO_3$ and $Fe(OH)_2$, when there are CP and no CP. The pH at the holiday is 9 and 8, charge balanced by Cl^-.

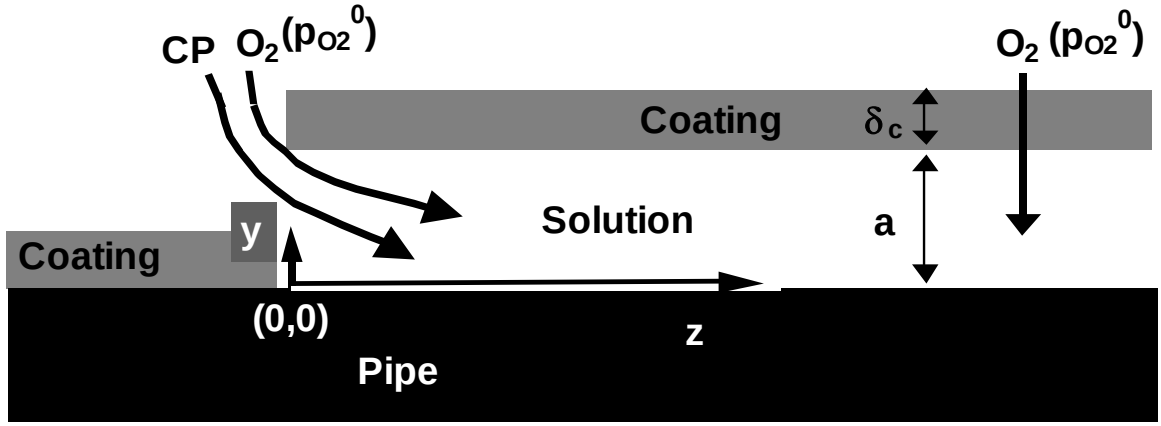

(a)

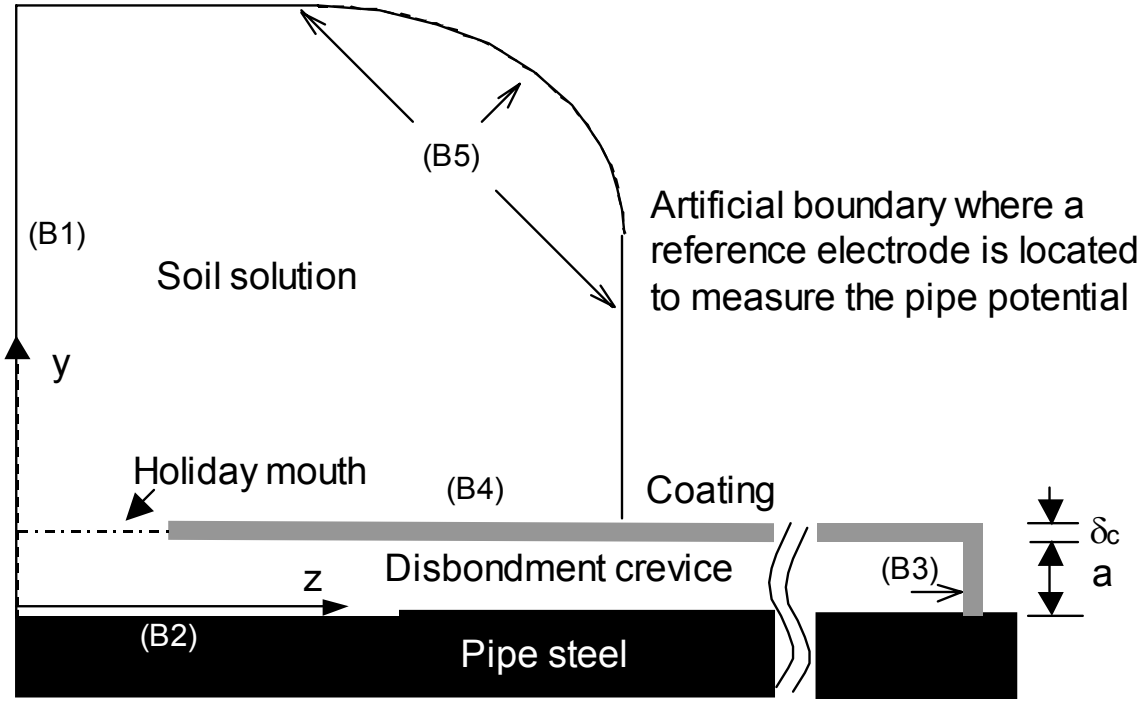

(b)

Figure 3-27. Schematic diagram of the model geometry. (a) previous work and (b) this work. Boundaries in Figure 3-27b are labeled. B1—symmetry boundary; B2—steel surface, flux boundary; B3 and B4—impermeable coating, no flux boundary; B5—measure boundary, constant O_2 concentration and either zero flux of potential for no CP or constant potential with external polarization.

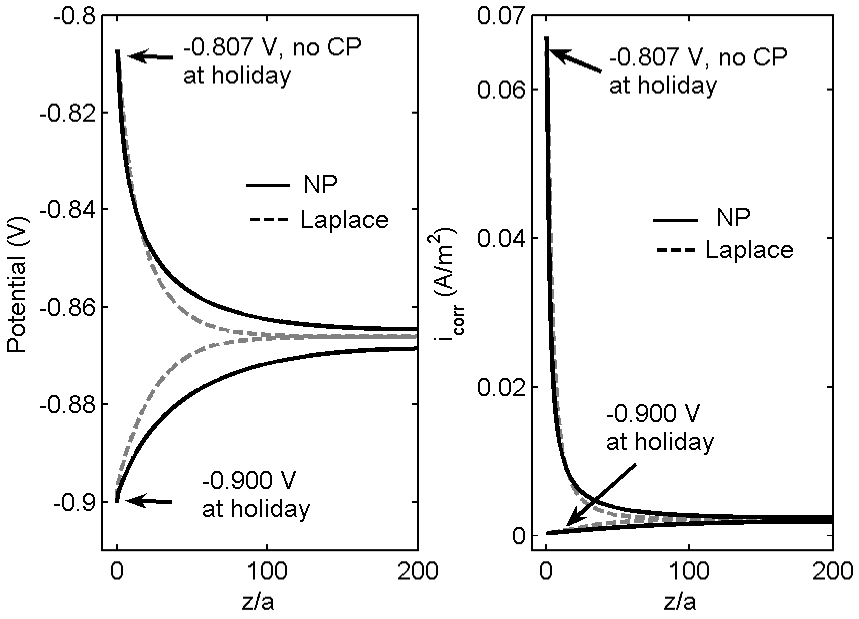

Figure 3-28. Crevice corrosion potential and current density computed from a semi-2D model by using Nernst-Plank transport equations in comparison with results in previous work computed from solving Laplace's equations.

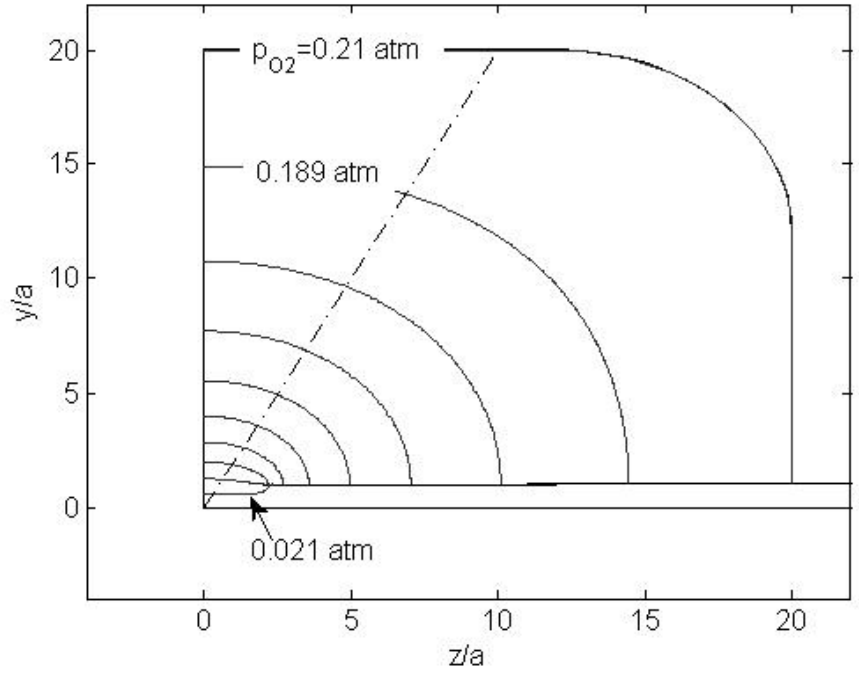

Figure 3-29. A contour plot of dissolved O_2 pressure in and outside of the disbondment crevice.

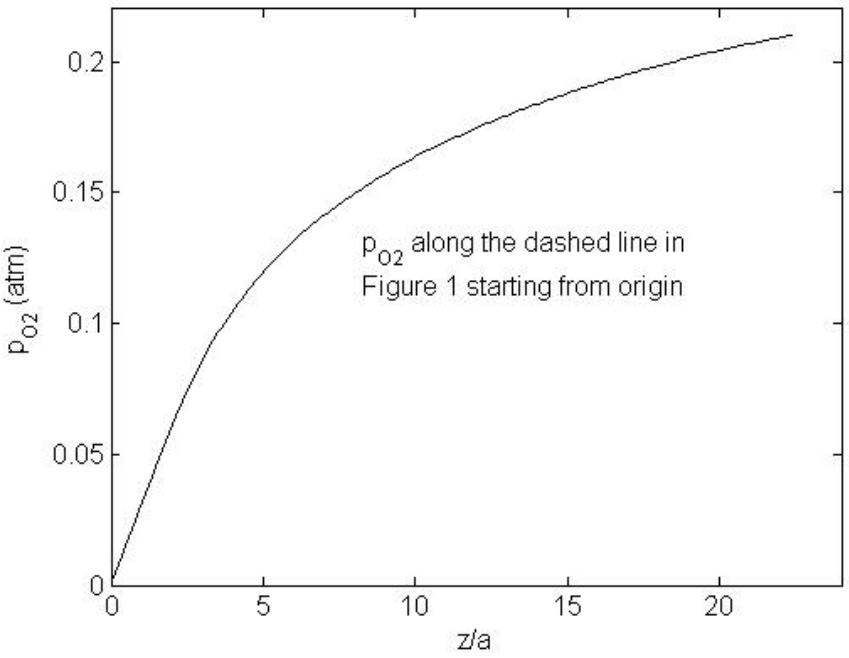

Figure 3-30. Dissolved O_2 partial pressure along the arbitrary dashed line drawn in Figure 3-27(b) starting from the origin.

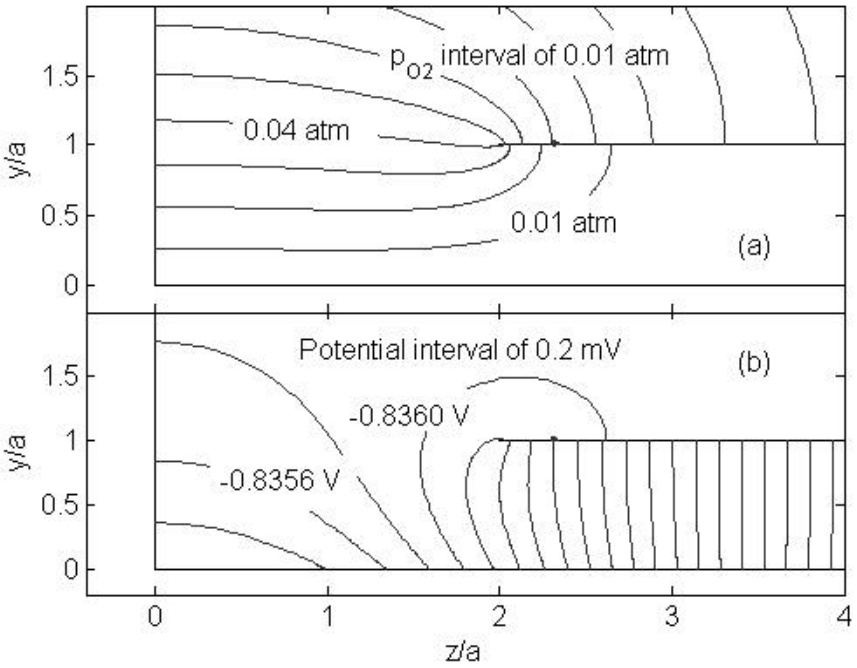

Figure 3-31. A contour plot of. (a) dissolved O_2 pressure and (b) steel potential, expanded in the holiday region.

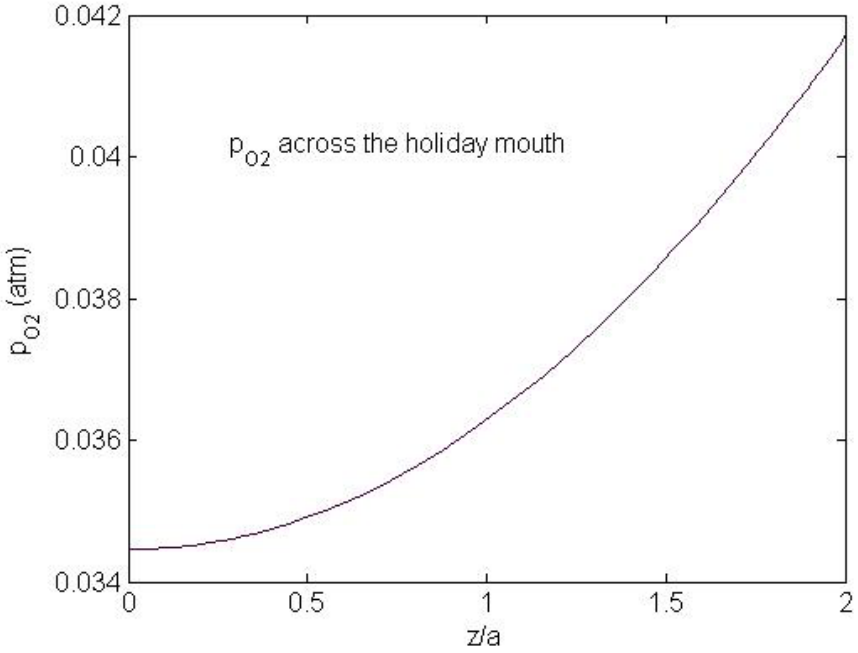

Figure 3-32. Dissolved O_2 partial pressure across the holiday mouth.

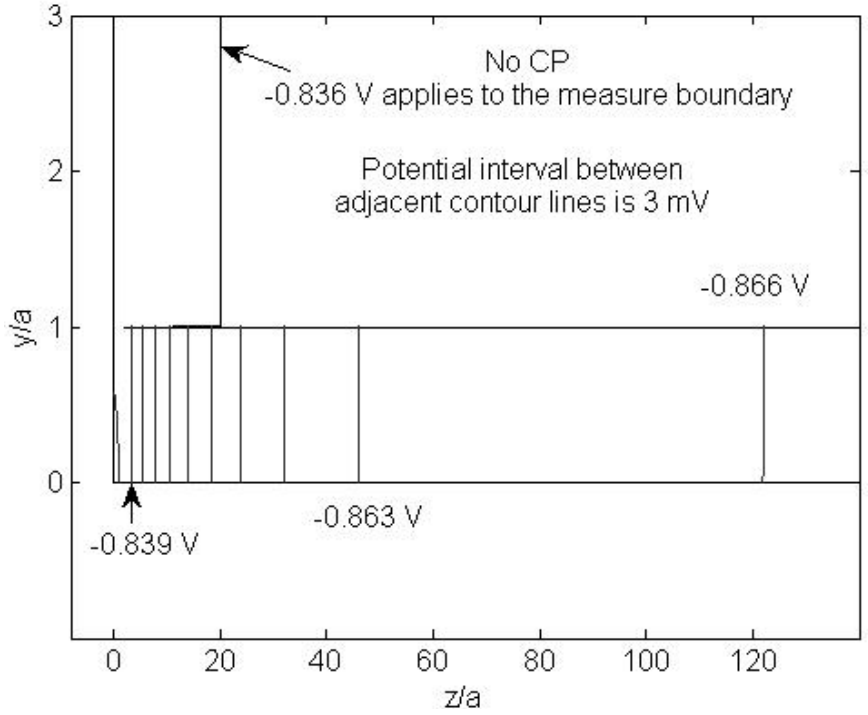

Figure 3-33. A contour plot of steel potential in and outside of the disbondment crevice. OCP reaches at about 122 gap sizes.

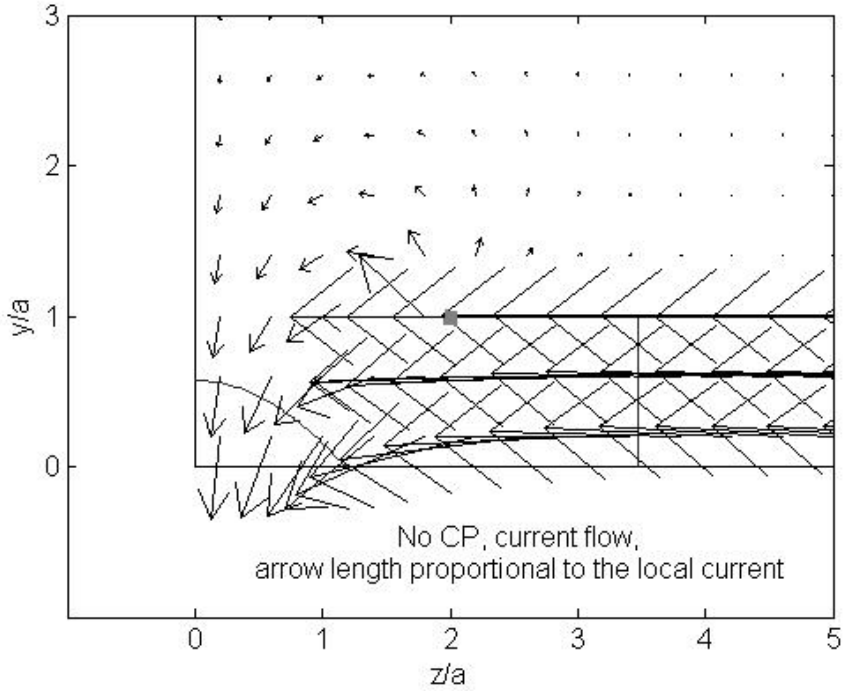

(a)

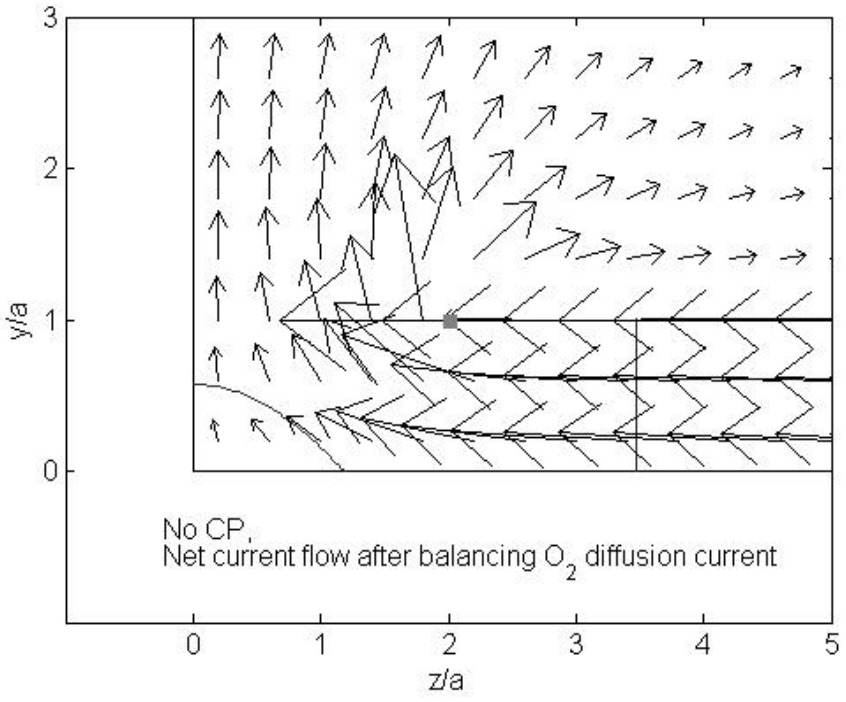

(b)

Figure 3-34. Without external CP, (a) ionic current and (b) superficial net current flow in and outside of the crevice described by the arrows whose length is equivalent to the magnitude of the local current. The gray point is the right end of the crevice holiday mouth.

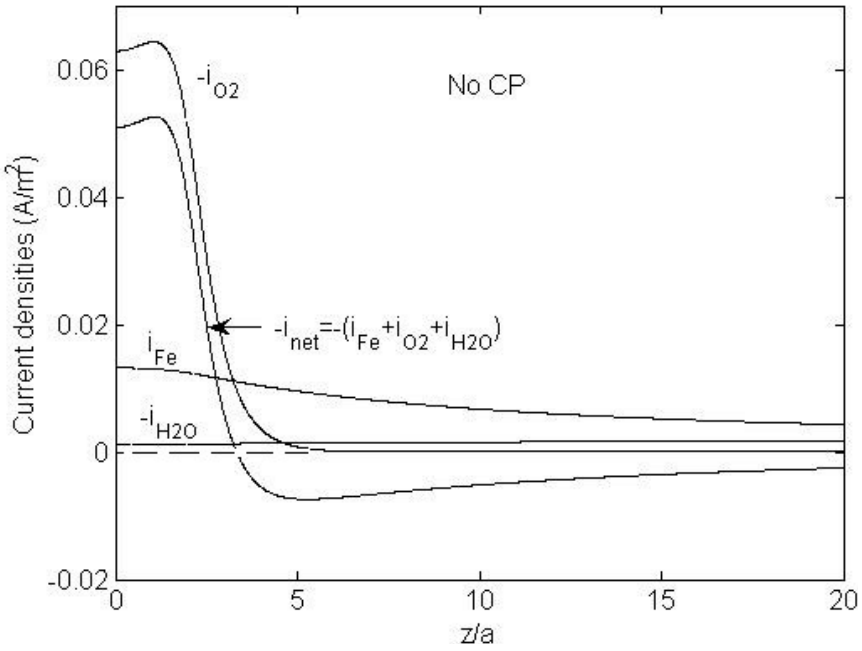

Figure 3-35. Without CP, current densities at the steel surface, where i_{Fe} is corrosion current density.

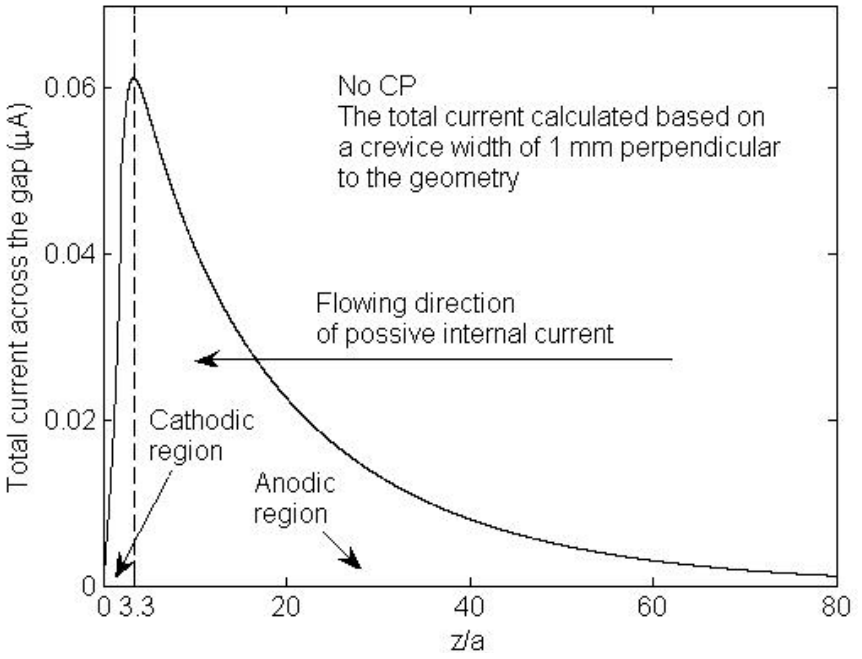

Figure 3-36. Without external CP, the total current across a gap size from the steel surface (the width of the crevice perpendicular to the geometry is assumed to be 1 mm in the calculation). The direction of current flow and the cathodic and anodic region of the crevice steel are labeled.

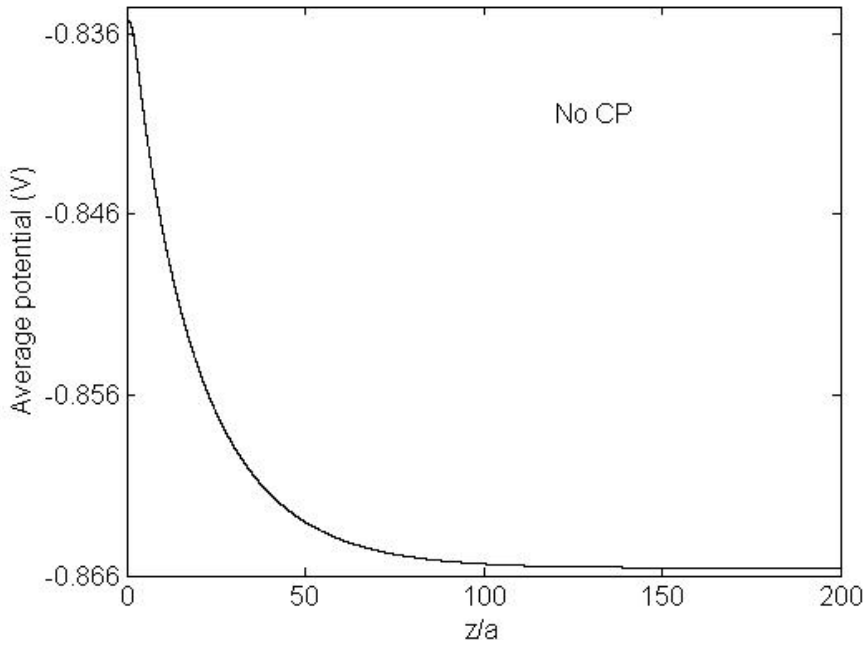

Figure 3-37. Average crevice potential obtained by averaging the steel potential across a gap size from the steel surface.

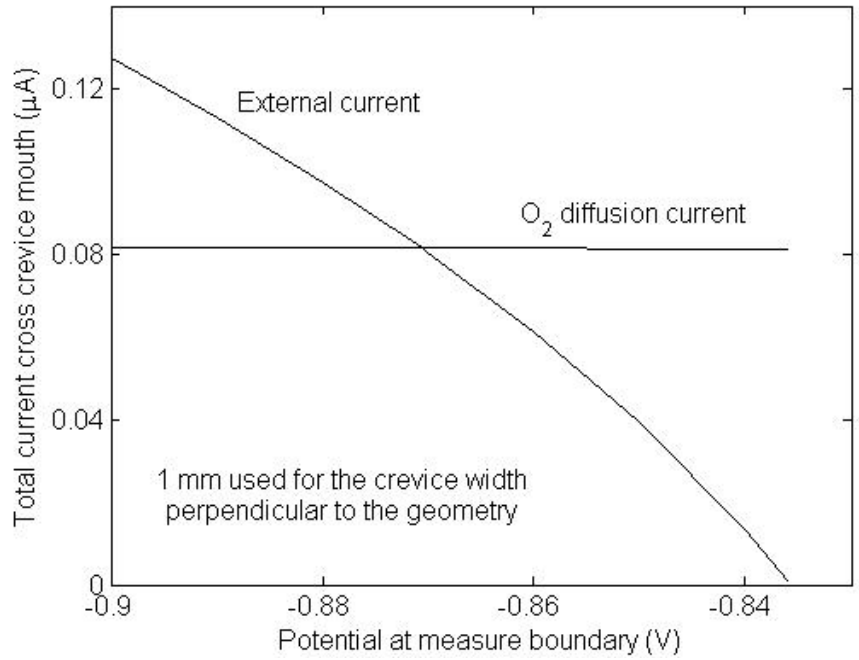

Figure 3-38. At different potentials at B5 (indication of different levels of CP), the total external current and the total O_2 diffusion current across the holiday mouth. 1 mm is assumed for width of the crevice perpendicular to the crevice geometry.

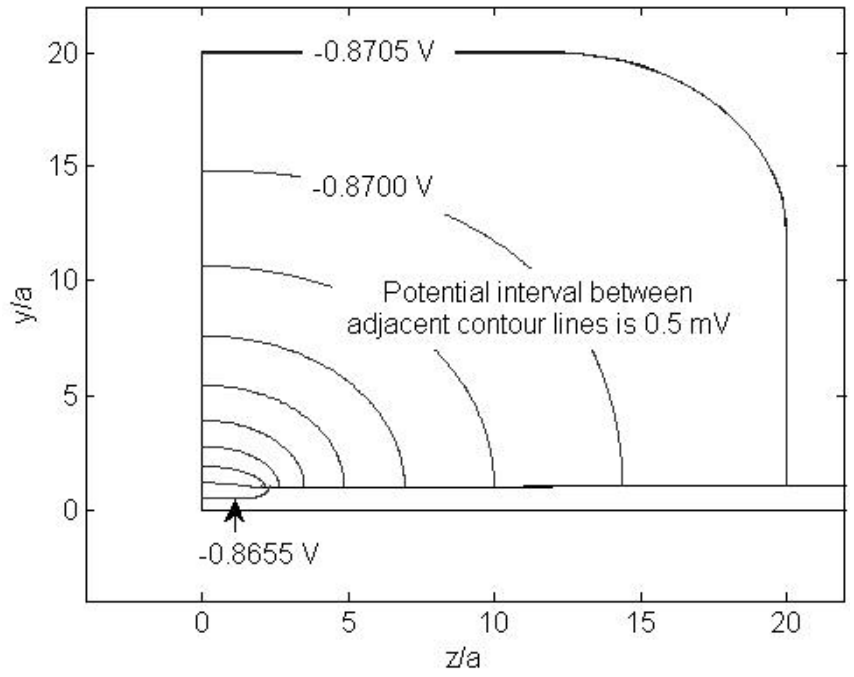

Figure 3-39. A contour plot of steel potential in and outside of the disbondment crevice for the potential at B5 of -0.8705 V.

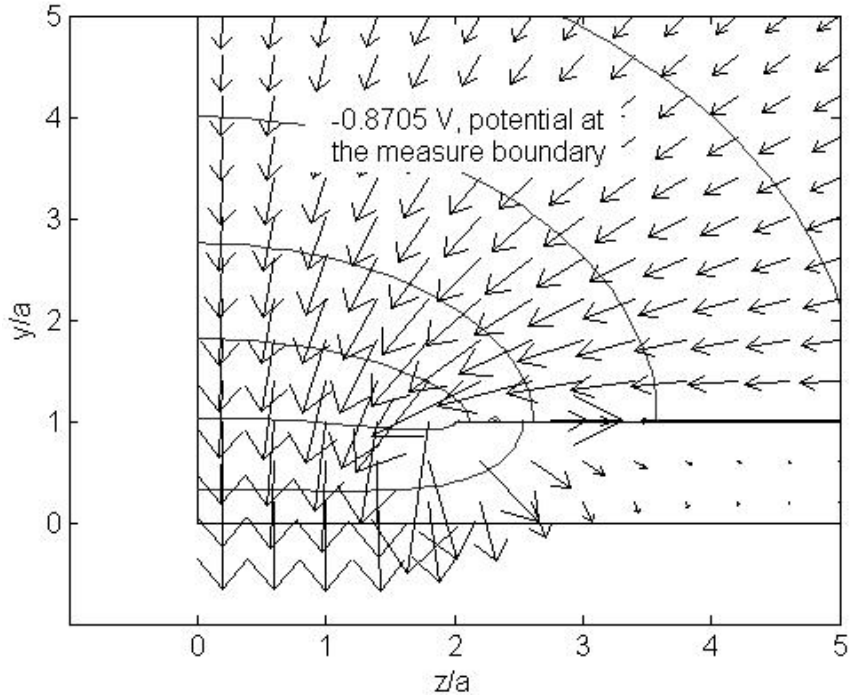

Figure 3-40. Ionic current flow in and outside of the crevice at a potential of -0.8705 V at B5. The length of an arrowed line measures the magnitudes of local current.

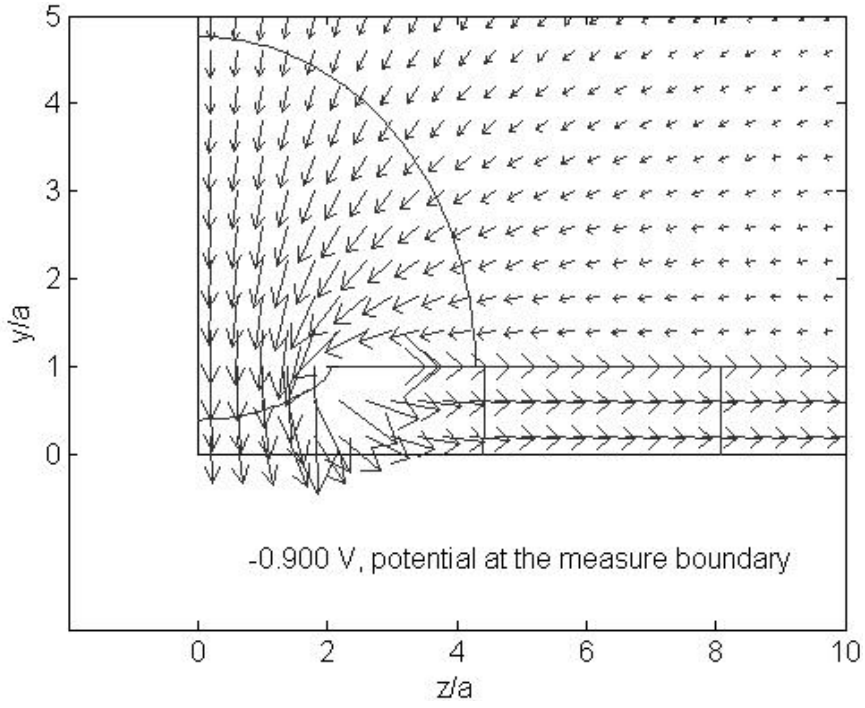

(a)

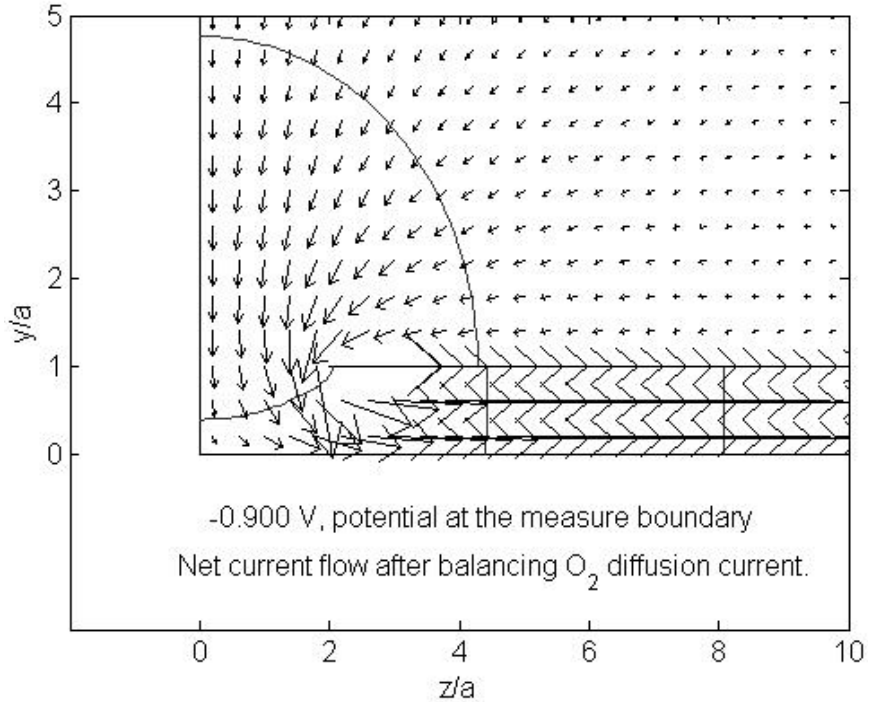

(b)

Figure 3-41. (a) Ionic current and superficial net current flow in and outside of the crevice for a potential of -0.9 V at B5. The arrow lengths measure the magnitude of the local current.

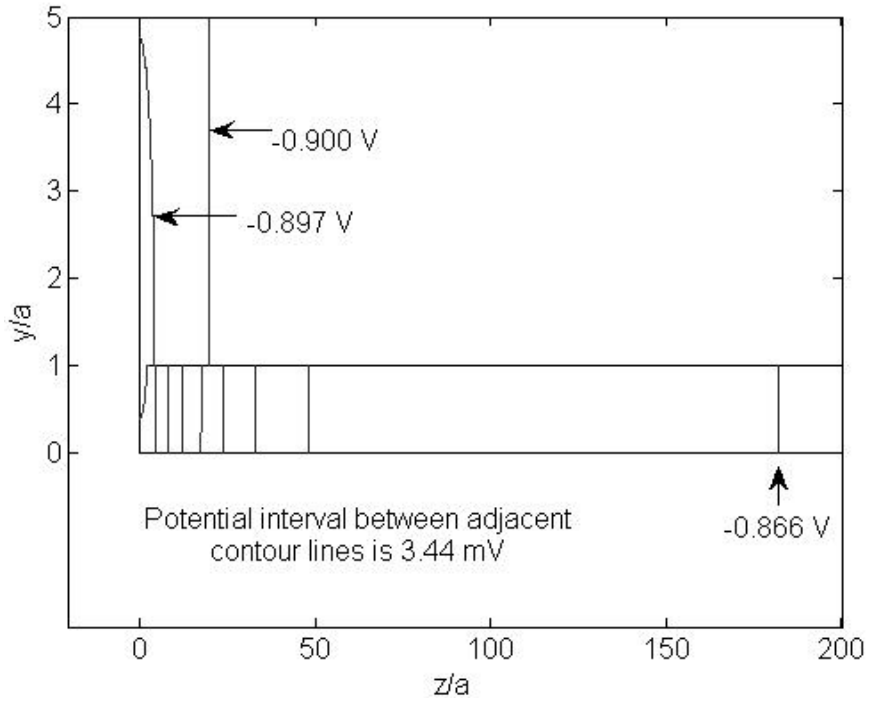

Figure 3-42. A contour plot of steel potential in and outside of the disbondment crevice for a potential of -0.900 V at B5.

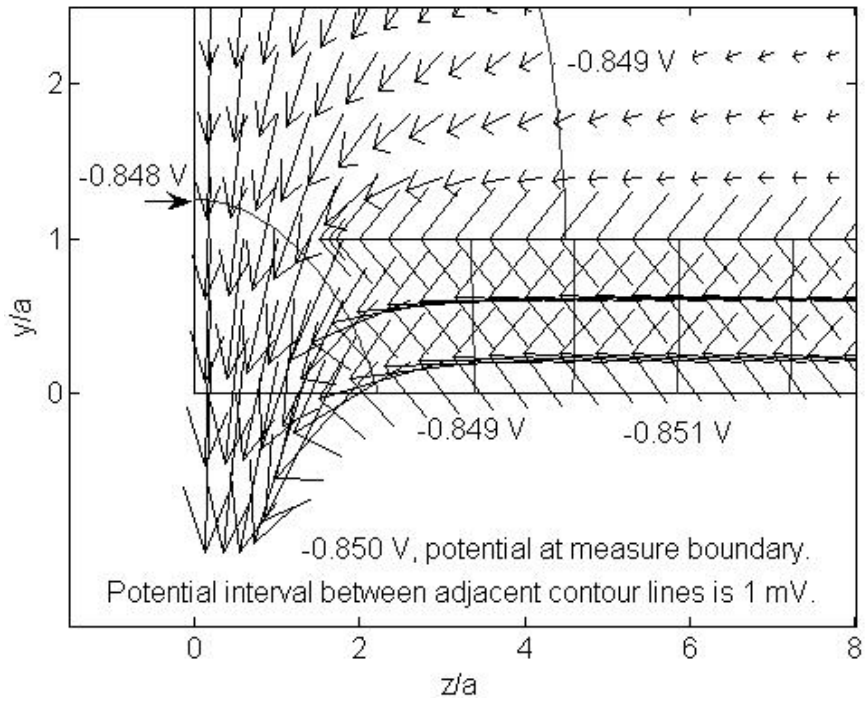

(a)

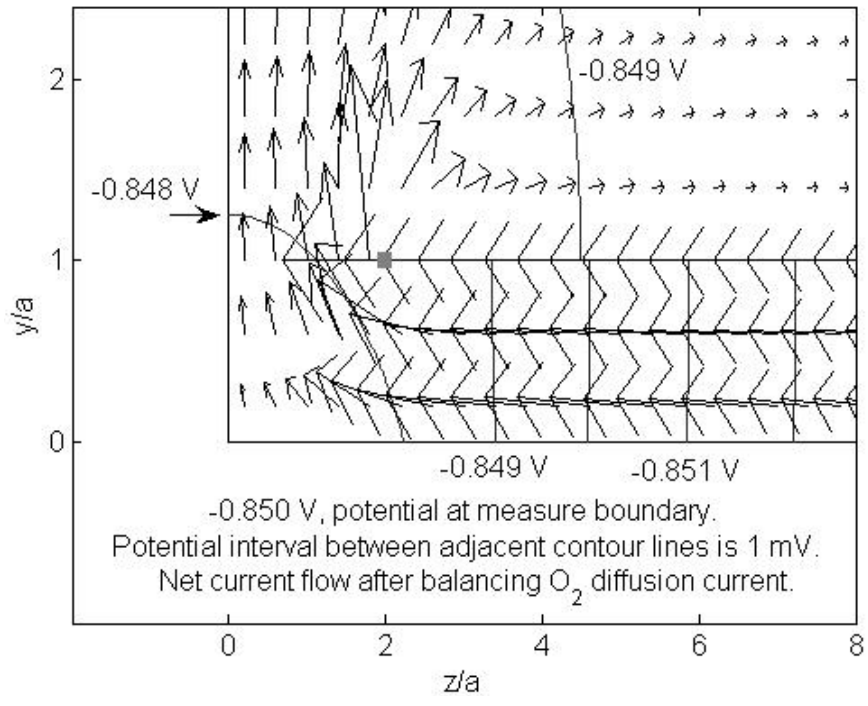

(b)

Figure 3-43. A contour plot and (a) ionic current and (b) superficial net current flow in the holiday region for a potential of -0.850 mV at B5.

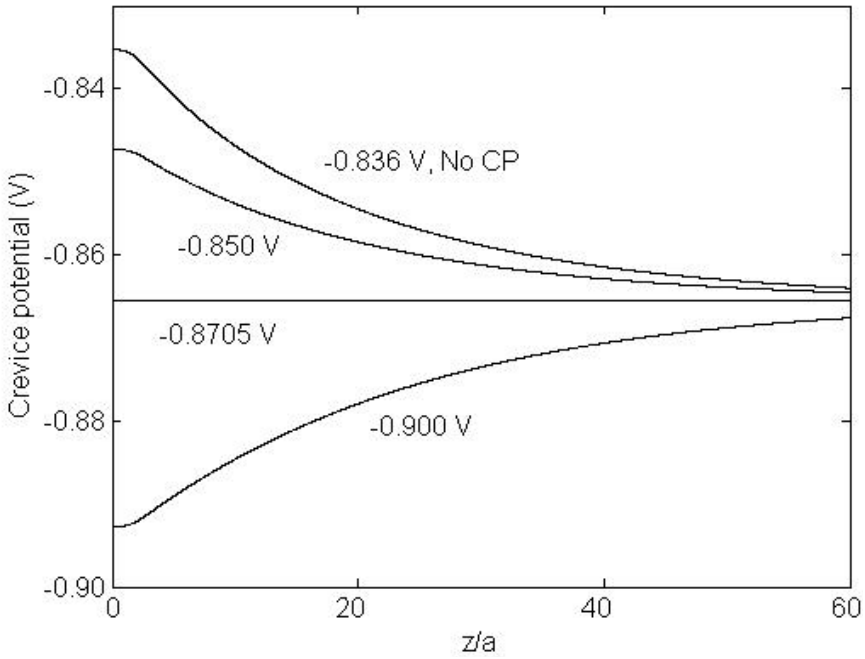

Figure 3-44. Effect of external CP on crevice potential at the steel surface. Potentials as labeled are steel potentials at B5.

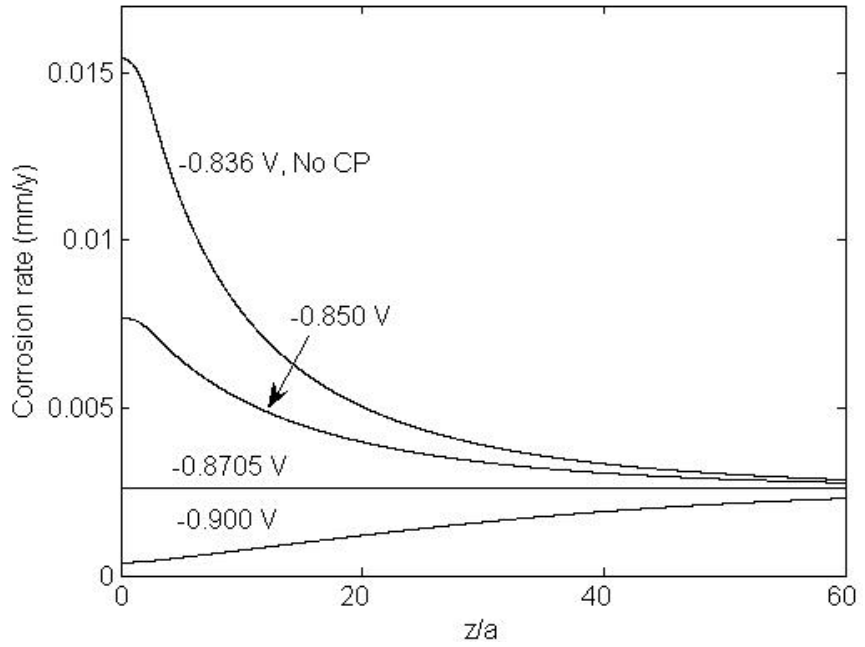

Figure 3-45. Effect of external CP on crevice steel corrosion rate. Potentials labeled are those measured at B5.

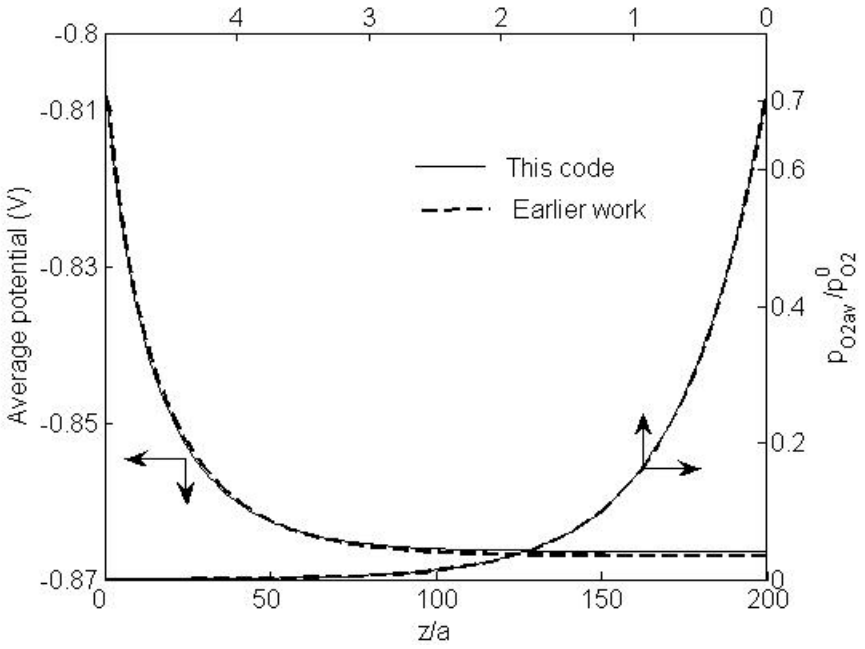

Figure 3-46. Verification of the current code by comparison of the average crevice potential and average O_2 pressure computed in this work and in an earlier work. “a” is the crevice gap size.

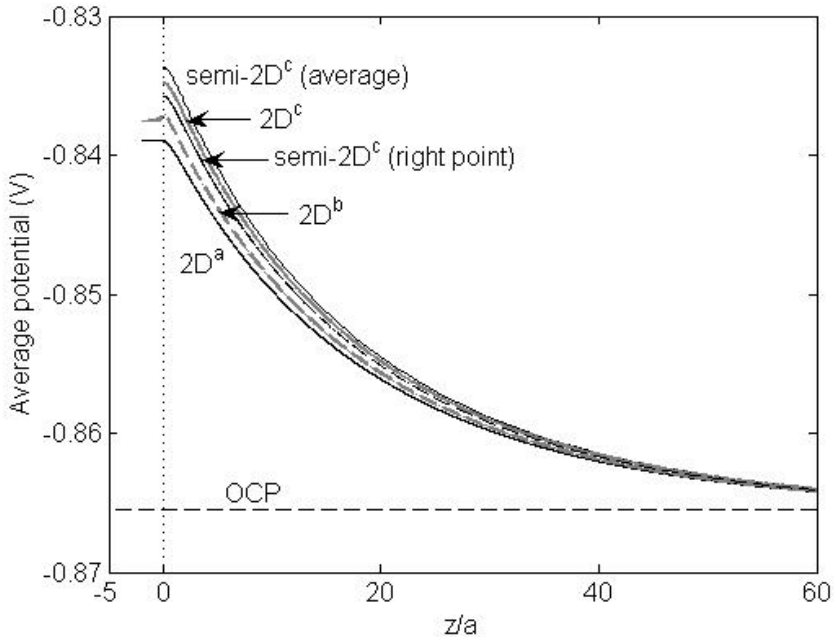

Figure 3-47. For inactive holiday steel with O_2 no CP, a comparison of the average crevice potential across the crevice gap. O_2 pressure is assumed uniform across the mouth of $2D^b$ and is equal to the average O_2 pressure of $2D^a$ across its holiday mouth. This average O_2 pressure of $2D^a$ is assumed for $2D^c$ and semi-$2D^c$ (average) at the joint point between the holiday mouth and the coating in Figure 3-27(c). At this joint point, the O_2 pressure at the right point of the $2D^a$ holiday mouth is used for semi-$2D^c$ (right point). The four models correspond to the geometries shown in Figures 3-27a ($2D^a$), 3-27b ($2D^b$) and 3-27c ($2D^c$ and semi-$2D^c$).

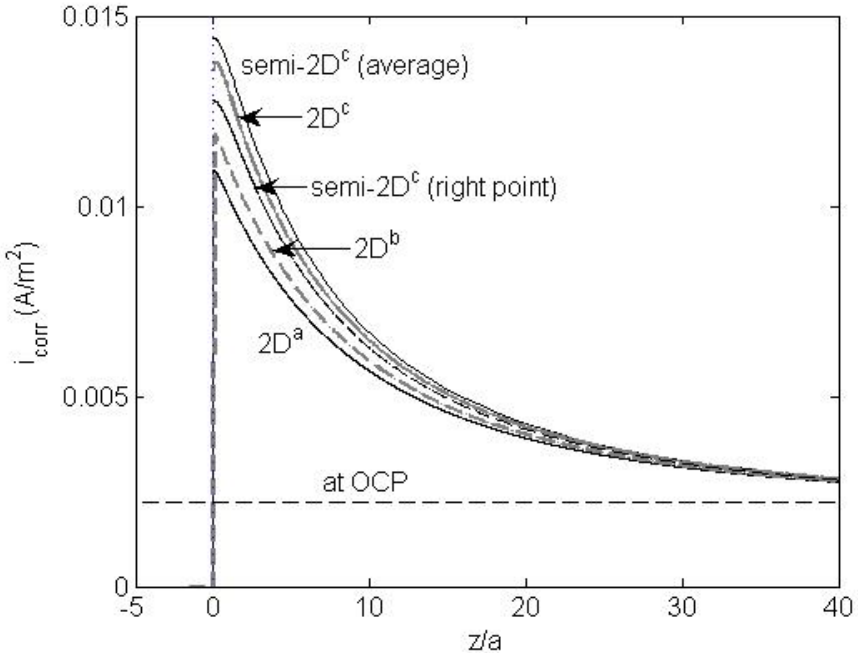

Figure 3-48. For inactive holiday steel with O_2 no CP, a comparison of the crevice corrosion current density.

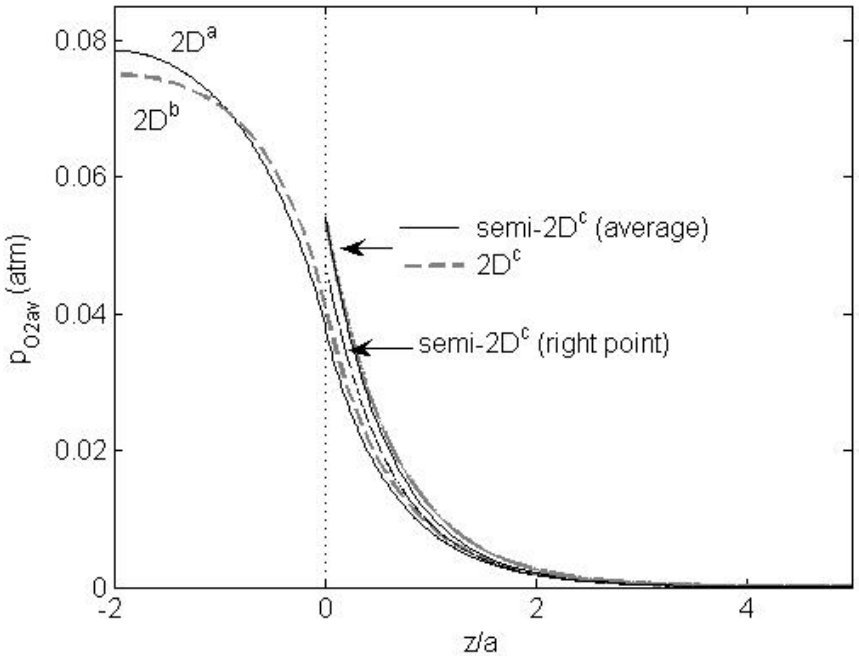

Figure 3-49. For inactive holiday steel with O_2 no CP, a comparison of the average O_2 pressure across the crevice gap.

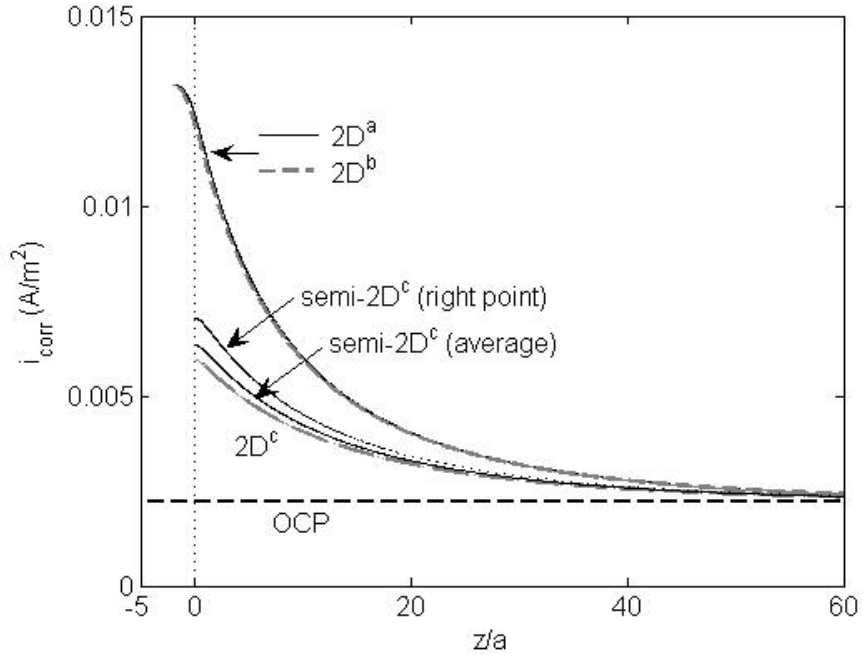

Figure 3-50. For active holiday steel with O_2 no CP, a comparison of the crevice corrosion current density calculated from all four models.

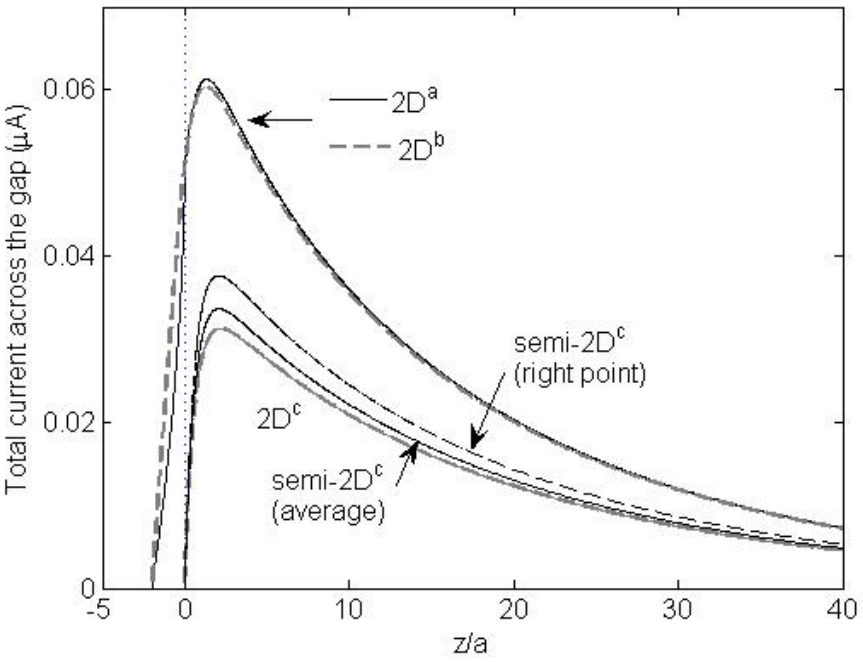

Figure 3-51. For active holiday steel with O_2 no CP, a comparison of the positive current which flow through the crevice solution from inside the crevice to the holiday region.

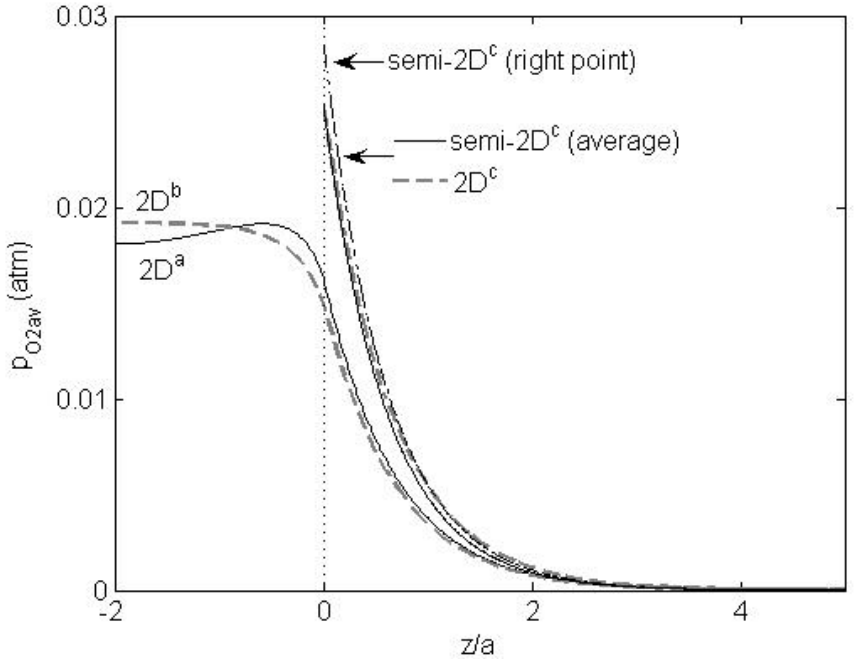

Figure 3-52. For active holiday steel with O_2 no CP, a comparison of the average O_2 pressure across the crevice gap.

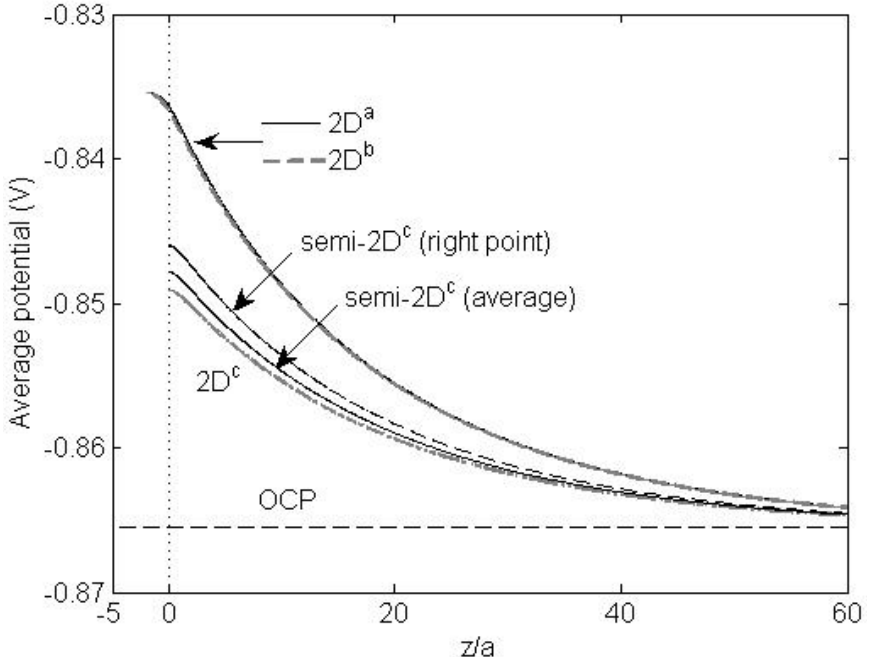

Figure 3-53. For active holiday steel with O_2 no CP, a comparison of the average crevice potential across the crevice gap.

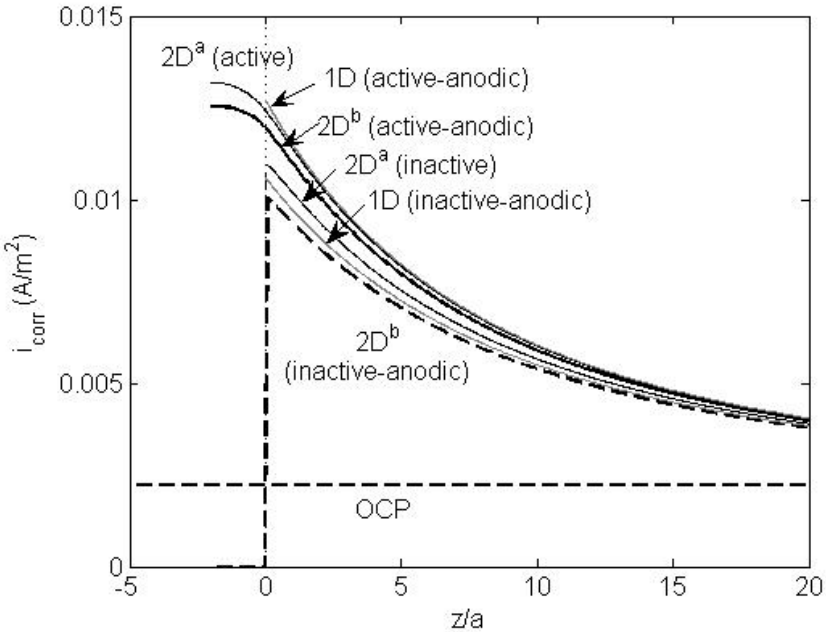

Figure 3-54. Approximation of the 2D^a crevice corrosion current density (with O_2 no CP) by simple anodic polarization without O_2 when the holiday steel surface is active and inactive. The average potential across the holiday mouth of 2D^a is used for the holiday potential of 2D^b and the 1D model.

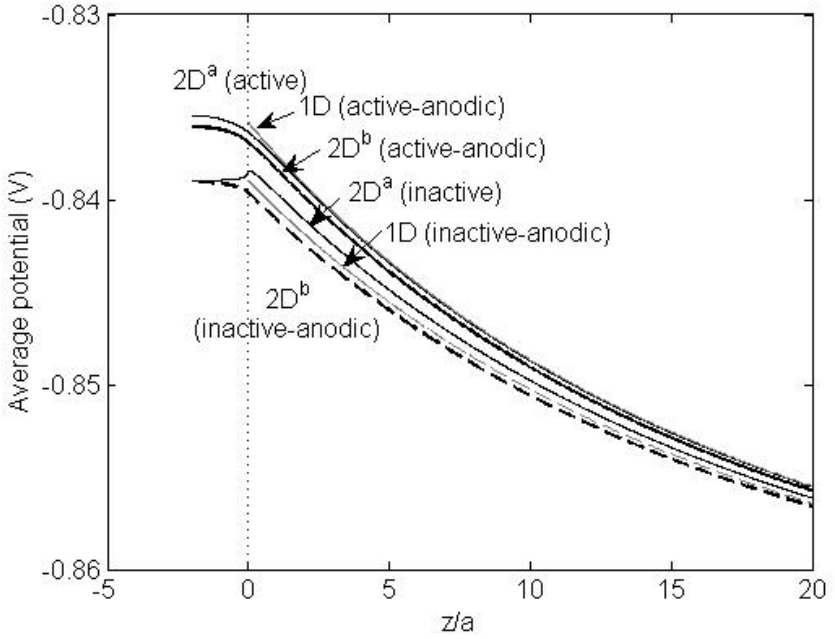

Figure 3-55. Approximation of the average potential across the crevice gap of 2D^a with O_2 no CP by anodic polarization without O_2 (2D^b and 1D), same as described in Figure 3-54.

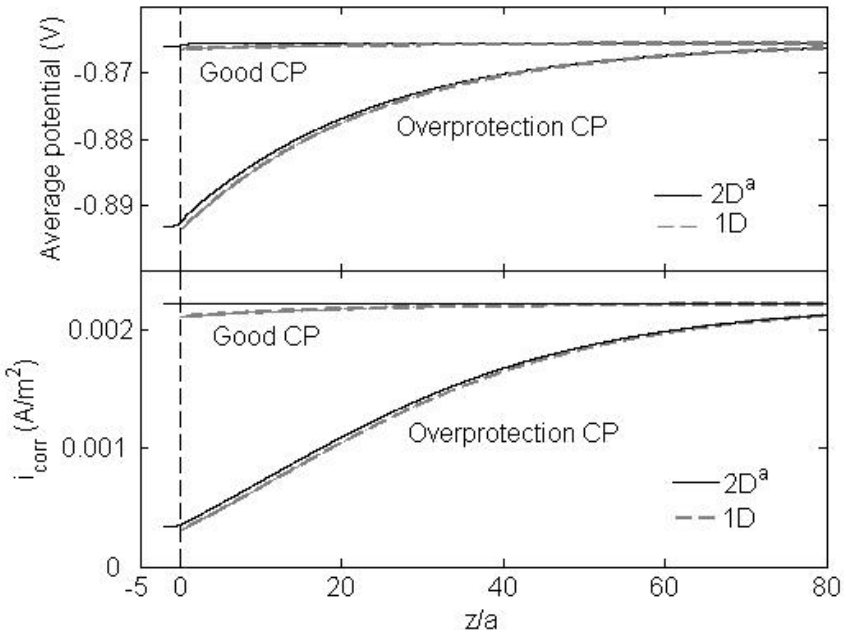

Figure 3-56. Approximation of the average potential across the crevice gap and the corrosion current density of $2D^a$ with good CP and overprotection CP by 1D model anodic polarization no O_2. The holiday steel surface of $2D^a$ is active.

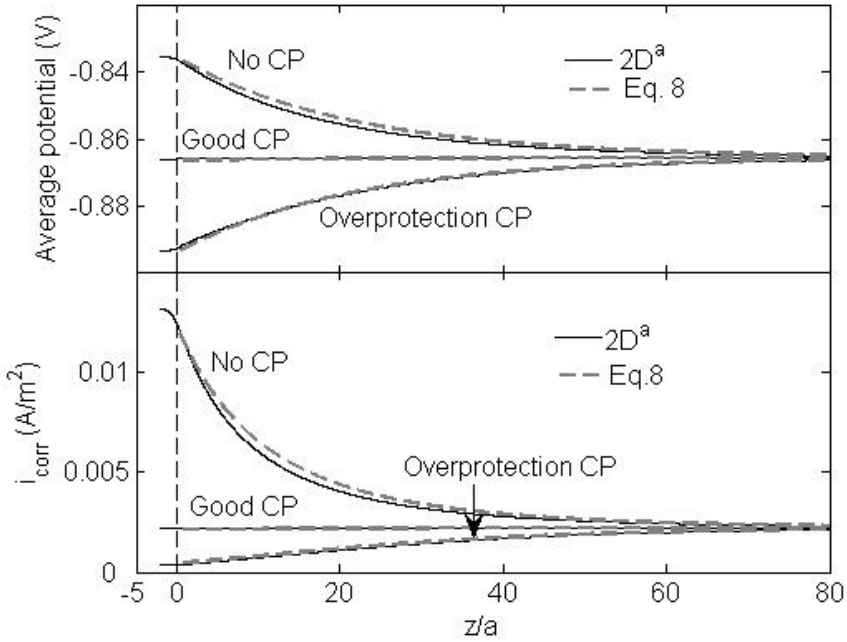

Figure 3-57. Approximation of the average potential across the crevice gap and the corrosion current density of $2D^a$ with no CP, good CP and overprotection CP by a simple algorithm developed in this work (Equation 8)). The holiday steel surface of $2D^a$ is active.

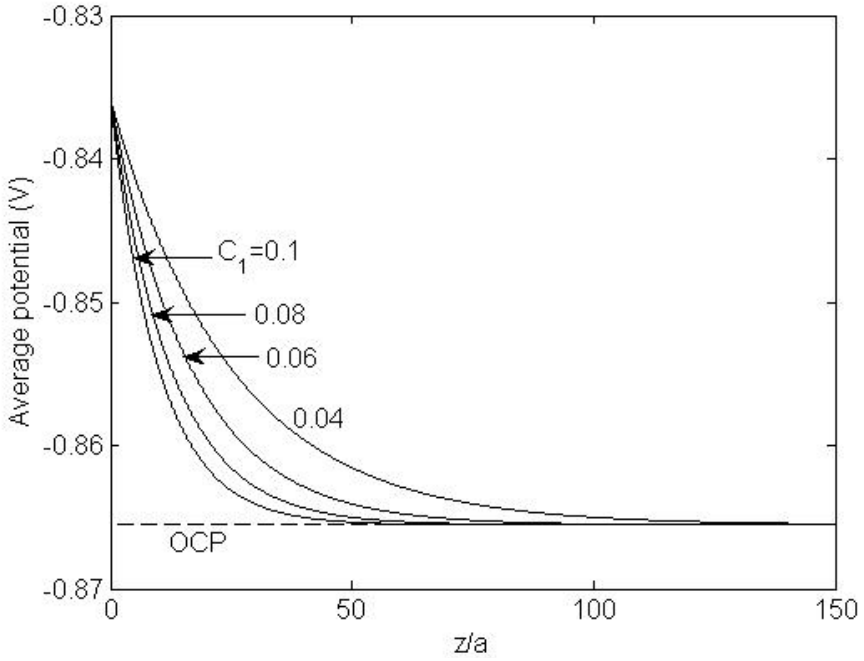

Figure 3-58. Crevice potential profile at different penetration numbers (C_1).

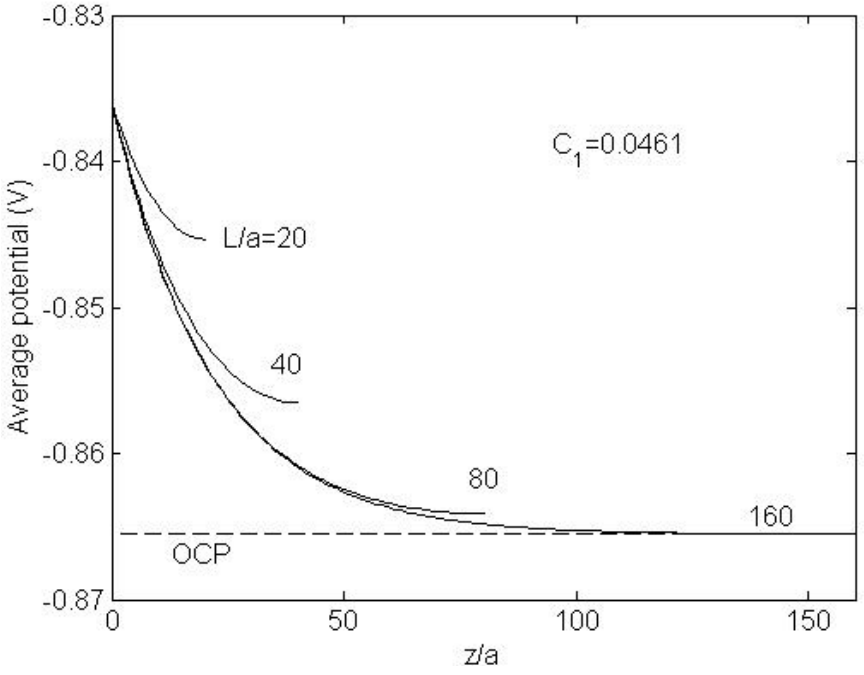

Figure 3-59. At Penetration Number C_1=0.0461, the crevice potential profile for various crevice lengths.

4.0 INTERNAL CORROSION RATE CALCULATION (TASK 2)

4.1 Background

Internal corrosion of gas pipelines was modeled previously to compute the CO_2 corrosion rate under two conditions[1-5]: (1) no CP, solution containing dissolved CO_2 alone[1] and (2) no CP, solution containing dissolved CO_2 and O_2[2]. CP was discussed for external pipeline corrosion[3]. The effects of CO_2 lone and CO_2 and O_2 together on the steel corrosion rate were investigated and discussed. It was assumed that no species other than CO_2, water, steel and their reaction products were present in the solution. The corrosion rate was computed by considering only the most significant reactions and transport processes. Good agreement was shown between numerous independent experimental data and corresponding computational results[2-3]. There, the Nernst-Plank transport equation was not used considering that the solution has supporting ions and the potential drop within the solution boundary layer at the steel surface is insignificant.

In this program, Nernst-Plank equation will be used for ionic transport and comparison is made of the computational results between those in the previous work[1-2] and those obtained in this project with the use of Nernst-Plank transport equations for different levels of supporting electrolyte of NaCl. This is to verify whether the assumption of neglecting the supporting ions in this CO_2 corrosion system is valid.

Here, the model equations are the same as derived in Section 3. Since CO_2 corrosion that is to be dealt with here is uniform and hence, this is a 1D problem with the boundaries located at the boundary layer surface or the bulk (uniform concentrations) and at the steel surface (flux boundary).

If it is verified that the model in the previous work is valid to predict CO_2 corrosion, then, the simpler format of the model can be used by further simplification to derive analytical or algebraic equations. The goal is for the model to be applied into practice conveniently. The pipeline operators donot have to understand the fundamental details of the modeling work but can use the model to estimate the pipeline internal corrosion rate effectively. In this project, the system is focused to have a constant temperature of 25^{o}C.

A critical assumption was made in the previous work[1-2] that the presence of the supporting ions, Fe^{2+} and HCO_3^-, allows for neglect of the migration portion of ionic transport. To verify this assumption, additional supporting electrolyte, NaCl, is added, its concentration in the solution is varied and its effect on the CO_2 corrosion rate is investigated.

4.2 Effect of NaCl Concentration in Solution on the Corrosion Rate

The calculation was made for a typical solution boundary layer of 0.55 mm in thickness and when present, for an O_2 pressure of 0.2 atm in bulk solution. The model system is shown in Figure 4-1. By using Nernst-Plank equation, for various levels of NaCl concentration as additional supporting electrolyte, the CO_2 corrosion rate was calculated. In Figure 4-2, the CO_2 pressure (p_{CO2}) refers to its value in the bulk, not at the steel surface. The corrosion rate computed from N-P equation is slightly greater than that from the previous work (the additional

supporting ion concentration is zero)[1]. Since the model in the previous work already slightly overestimates the measured steel corrosion rate in lab tests, the N-P result further overestimates the steel corrosion rate. In both types of calculations, the models assume active steel or the barrier properties of the precipitates to the ionic transport were neglected. The above computation was done using the same conditions. There are no species other than Fe^{2+} and HCO_3^-, of CO_2, water, steel and the reaction products in the solution. The effect on the corrosion rate of supporting ions due to dissolution of other salts, NaCl for example, is investigated next.

NaCl is assumed to be present in the bulk solution. The effect of its concentration on the steel corrosion rate is investigated. It has been argued in the previous work[1-2] that with NaCl the supporting ions in the solution Fe^{2+} or HCO_3^- are sufficient to reduce any potential drop within the boundary layer and the potential-driven migration of hydrogen ion in solution can be neglected. Figure 4-3 shows that the variation of the NaCl concentration indeed has a negligible effect on the steel corrosion rate. Increasing NaCl concentation from $1e^{-7}$ mol/L to 0.5 mol/L slightly decreases the corrosion current density from 0.04211 to 0.04207 A/m^2, less than 0.1%. This proves that the solution of CO_2 corrosion contains sufficient supporting ions relative to the small concentration of hydrogen ion.

Since the CO_2 model in the previous work is simpler to use without involving the complex N-P transport differential equations, it will be used to estimate the internal corrosion rate of pipeline steel due to CO_2 and, if present, O_2.

4.3 Simplified Models to Estimate the CO_2 Corrosion Rate (No NaCl)

The previous work[2-3] derived the CO_2 corrosion rate expression by first expressing the carbonic acid diffusion current density by:

$$i_{dH_2CO_3} = i_{LH_2CO_3}(1 - u_{H_2CO_3 s}) \tag{4-1}$$

where $i_{LH_2CO_3} = c_{H_2CO_3}^{eq0}(1+K_h)FD_{H_2CO_3}\sqrt{A}/(\delta_s k_h\sqrt{A} + \frac{e^{\sqrt{A}\delta_s} - e^{-\sqrt{A}\delta_s}}{e^{\sqrt{A}\delta_s} + e^{-\sqrt{A}\delta_s}})$, $u_{H_2CO_3} = \frac{c_{H_2CO_3 s}}{c_{H_2CO_3}^{eq0}}$, $A = \frac{k_b}{D_{H_2CO_3}}$ and $u_{H_2CO_3 s} = \frac{c_{H_2CO_3 s}}{c_{H_2CO_3}^{eq0}} = \frac{H_{CO_2} c_{H_2CO_3 s}}{K_h p_{CO_2}^0}$.

Since $K_h << 1$ and in the denominator of i_{LH2CO3} the second term is greater than the first as long as the boundary layer thickness is not greater than 1 mm and the second term can be approximated by unity as long as the layer thickness is not smaller than 20 μm, for a boundary layer thickness in the range of 20 μm ~ 1 mm, the limiting current density may be approximated by:

$$i_{LH_2CO_3} = F\frac{p_{CO_2}^0}{H_{CO_2}}\sqrt{K_f K_h D_{H_2CO_3}} \tag{4-2}$$

The total cathodic diffusion current of hydrogen ion and carbonic acid i_t is:

$$i_t = FD_{H_2CO_3}\left(\frac{dc_{H_2CO_3}}{dy} + \frac{dc_{H^+}}{dy}\right)_{y=0} = i_{dH_2CO_3}\left(1 + \frac{1}{\frac{dc_{H_2CO_3}}{dc_{H^+}}}\right) \quad (4\text{-}3)$$

where $\frac{dc_{H_2CO_3}}{dc_{H^+}}$ is a function of hydrogen ion concentration at the steel surface.

It was found from computations that Equation (4-3) is equivalent to:

$$i_t = F\left(D_{H_2CO_3}\left.\frac{dc_{H_2CO_3}}{dy}\right|_s + D_{H_2CO_3}\frac{c^0_{H^+} - c_{H^+s}}{\delta_R}\right) \quad (4\text{-}3a)$$

This is because c_{H2CO3} reduction controls the cathodic reaction rate for a higher p_{CO2}. It is generally accepted that at low p_{CO2}, CO_2 hydration controls the corrosion rate.

At the steel surface, charge conservation requires:

$$i_{corr} + i_{H^+} + i_{H_2CO_3} = 0 \quad (4\text{-}4)$$

Tafel equations may be used to express the current densities. Transformation of these Tafel equations was made in previous[1-4] and summarized below.

The corrosion current density is:

$$i_{corr} = i_{Fes}{}^0 e^{\frac{2.303(\varphi - E_{Fe}{}^{eqs})}{b_{Fe}}} \quad (4\text{-}5)$$

The hydrogen ion reduction current density is:

$$i_{H^+} = \lambda_{H^+} i_{corr}{}^{-\omega_{H^+}} \quad (4\text{-}6)$$

where $\lambda_{H^+} = \mu_{H^+} c_{H^+s} c_{Fe^{2+}s}^{-\frac{\alpha_{H^+}}{n_{Fe}}}$, $\omega_{H^+} = \frac{b_{Fe}}{b_{H^+}}$, $\mu_{H^+} = -i^0_{H^+\,Ref} c_{H^+\,Ref}^{\frac{\alpha_{H^+}}{n_{H^+}}-1} i^0_{Fe\,Ref}{}^{\omega_{H^+}} 10^{\frac{E_{H^+}{}^0 - E_{Fe}{}^0}{b_{H^+}}} \sqrt{1000}$.

Here, $\sqrt{1000}$ is a coefficient resulting from unit conversion when the concentration in Nernst equation (in mol/L) is converted to SI (mol/m^3).

The H_2CO_3 reduction current density is:

$$i_{H_2CO_3} = \lambda_{H_2CO_3} i_{corr}{}^{-\omega_{H_2CO_3}} \quad (4\text{-}7)$$

where $\lambda_{H_2CO_3} = \mu_{H_2CO_3} c_{H_2CO_3 s} c_{Fe^{2+}s}^{-\frac{\alpha_{H_2CO_3}}{n_{Fe}}}$, $\omega_{H_2CO_3} = \frac{b_{Fe}}{b_{CA}}$, and

$\mu_{H_2CO_3} = -i_{H_2CO_3\,Ref}{}^{0}\left(\frac{c_{H^+Ref}}{k_{11H_2CO_3}/K_h}\right)^{\frac{\alpha_{H_2CO_3}}{n_{H_2CO_3}}} \frac{i^0_{FeRef}{}^{\omega_{H_2CO_3}}}{c_{H_2CO_3\,Ref}} 10^{\frac{E_{H_2CO_3}{}^0 - E_{Fe}{}^0}{b_{H_2CO_3}}} \sqrt{1000}$. Hence, the first dissociation constant of H_2CO_3 ($H_2CO_3 \leftrightarrow H^+ + HCO_2^-$) is $K_{11H_2CO_3}/K_h$ where $K_{11H2CO3}$ is the equilibrium constant of the reaction: $CO_2(aq) + H_2O \leftrightarrow H^+ + HCO_2^-$.

Equations (4-4 – 4-7) allow for the computation of i_{corr} for a given c_{H+s} because the concentrations at the steel surface and their derivatives to c_{H+s} of all other species can be calculated based on the thermodynamic relations. The thermodynamic relations are given in the subsections.

$p_{CO2}{}^0$ is linked to c_{H+s} through Equation (4-3) and the following equation:

$$i_t = i_{corr} \tag{4-8}$$

where Equations (4-3 – 4-4) are combined.

$p_{CO2}{}^0$ at the boundary layer surface or bulk solution allows for the computation of concentrations of all other species there.

4.3.1 Corrosion due to Dissolved CO_2 Alone

Equilibrium in the solution allows the concentration of ferrous ion to be expressed by that of hydrogen ion. For example, at the steel surface the exact solution is:

$$c_{Fe^{2+}s} = \frac{-c_{H^+s} + \frac{K_w}{c_{H^+s}} + \sqrt{(c_{H^+s} - \frac{K_w}{c_{H^+s}})^2 + 8(2K_{2H_2CO_3} + c_{H^+s})\frac{K_{csp}}{K_{2H_2CO_3}}}}{4} \tag{4-9}$$

where c_{H+} and c_{Fe2+s} are concentrations at the steel surface.

The derivative of c_{Fe2+s} over c_{H+}, which will be used to express diffusion rate of Fe^{2+} by that of H^+, is:

$$\frac{dc_{Fe^{2+}s}}{dc_{H^+}} = -\frac{1}{4}\left(1 + \frac{K_w}{c^2_{H^+s}}\right) + \frac{\frac{1}{4}(c_{H^+s} - \frac{Kw}{c_{H^+s}})(1 + \frac{K_w}{c^2_{H^+s}}) + \frac{K_{csp}}{K_{2H_2CO_3}}}{\sqrt{(c_{H^+s} - \frac{Kw}{c_{H^+s}})^2 + 8(2K_{2H_2CO_3} + c_{H^+s})\frac{K_{csp}}{K_{2H_2CO_3}}}} \tag{4-10}$$

Since the solution in the corrosion system is acidic, OH^- concentration is small relative to H^+ concentration. Since K_{2H2CO3} is small compared to H^+ concentration, Equations (4-9 - 4-10) can be simplified to:

$$c_{Fe^{2+}s} = \frac{-c_{H^+s} + \sqrt{c^2_{H^+s} + 8c_{H^+s}\frac{K_{csp}}{K_{2H_2CO_3}}}}{4} \tag{4-11}$$

$$\frac{dc_{Fe^{2+}s}}{dc_{H^+}} = -\frac{1}{4} + \frac{\frac{c_{H^+s}}{4} + \frac{K_{csp}}{K_{2H_2CO_3}}}{\sqrt{c^2_{H^+s} + 8c_{H^+s}\frac{K_{csp}}{K_{2H_2CO_3}}}} \tag{4-12}$$

By calculation for a pH range of 2 - 7, it was found that Equations (4-11 - 4-12) can be further simplified to:

$$c_{Fe^{2+}s} = \sqrt{\frac{c_{H^+s}K_{csp}}{2K_{2H_2CO_3}}}, \tag{4-13}$$

$$c'_{Fe^{2+}s} = \frac{c_{Fe^{2+}s}}{2c_{H^+s}} \tag{4-14}$$

By use of Equations (4-13 - 4-14), the concentrations of other species can be expressed by:

$$c_{H_2CO_3s} = \frac{c^2_{H^+s}K_{spFeCO_3}}{c_{Fe^{2+}s}(K_{11H_2CO_3}/K_h)K_{2H_2CO_3}} \tag{4-15}$$

$$\frac{dc_{H_2CO_3s}}{dc_{H^+}} = c_{H_2CO_3s}\left(\frac{2}{c_{H^+s}} - \frac{c'_{Fe^{2+}s}}{c_{Fe^{2+}s}}\right) = \frac{3c_{H_2CO_3s}}{2c_{H^+s}} \tag{4-16}$$

Transformation of Equation (4-4 - 4-7), i_{corr} can be expressed by c_{H+s} as:

$$i_{corr} = (-\lambda_{H_2CO_3} - \lambda_{H^+})^{\frac{3}{4}} = c^{-\frac{3\alpha_{H^+}}{4n_{Fe}}}_{Fe^{2+}s}(-\mu_{H_2CO_3}c_{H_2CO_3s} - \mu_{H^+}c_{H^+s})^{\frac{3}{4}} \tag{4-17}$$

Equations (4-8) and (4-17) allow for calculation of p^0_{CO2}.

$$\begin{aligned} p^0_{CO_2} &= \frac{i_{corr}H_{CO_2}}{F\sqrt{K_fK_hD_{H_2CO_3}}\left(1+\frac{1}{\left.\frac{dc_{H_2CO_3}}{dc_{H^+}}\right|_s}\right)} + \frac{c_{H2CO3s}H_{CO_2}}{K_h} \\ &= \frac{i_{corr}H_{CO_2}}{F\sqrt{K_fK_hD_{H_2CO_3}}\left(1+\frac{2c_{H^+s}}{3c_{H_2CO_3s}}\right)} + \frac{c_{H2CO3s}H_{CO_2}}{K_h} \end{aligned} \tag{4-18}$$

Using Equation (4-13) and since $c^0_{CO_3^{2-}} = \frac{p^0_{CO_2}K_{11H_2CO_3}K_{2H_2CO_3}}{H_{CO_2}(c^0_{H^+})^2}$ and $c^0_{Fe^{2+}} = \frac{K_{csp}}{c^0_{CO_3^{2-}}}$, by combination with Equations (4-13 - 4-14), the bulk H^+ concentration can be calculated:

$$c^0_{H^+} = (p^0_{CO_2}\frac{K_{11H_2CO_3}}{H_{CO_2}}\sqrt{\frac{K_{2H_2CO_3}}{2K_{csp}}})^{\frac{2}{3}} \tag{4-19}$$

If Equations (4-11 - 4-12) are used, the bulk H^+ concentration is:

$$c_{H^+}^0 = \frac{1}{3\gamma_1}(-2 + 4\sqrt[3]{\frac{2}{\gamma_3}} + \sqrt[3]{\frac{\gamma_3}{2}}) \quad (4\text{-}20)$$

where $\gamma_1 = \frac{4H_{CO_2}K_{csp}}{p_{CO_2}^0 K_{11H_2CO_3} K_{2H_2CO_3}}$, $\gamma_2 = \frac{8K_{csp}}{K_{2H_2CO_3}}$ and $\gamma_3 = -16 + 27\gamma_1\gamma_2 + 3\sqrt{3\gamma_1\gamma_2(27\gamma_1\gamma_2 - 32)}$.

Note that the results from Equations (4-19 - 4-20) are approximately the same.

4.3.2 Corrosion due to Dissolved CO_2 and O_2

If there is O_2 present in the system, the diffusion limiting current density of O_2, $i_{O_2L} = \alpha p_{O_2}{}^0 (>0)$, and $\alpha = n_{O_2} F D_{O_2} / H_{O_2} \delta_s$, where $p_{O_2}{}^0$ is O_2 pressure in bulk solution, D_{O_2} and H_{O_2} are, respectively, the diffusion coefficient and Henry's law constant. can used to approximate its reduction current density since O_2 diffusion is generally controls its reduction rate at the steel surface.

To compute corrosion current density, with O_2 Equation (4-17) must be replaced by:

$$p^4 - i_{O2L} p + (\lambda_{H_2CO_3} + \lambda_{H^+}) = 0 \quad (4\text{-}21)$$

where $p = i_{corr}^{\frac{1}{3}}$.

The solution of Equation (4-21) is:

$$p = 0.5(\sqrt{-\alpha_2 + \alpha_3} + \sqrt{\alpha_2 - \alpha_3 + \alpha_4}) \quad (4\text{-}22)$$

where $\alpha_1 = 9i_{O_2L}^2 + \sqrt{3(27i_{O_2L}^4 + 256B^3)}$, $B = -(\lambda_{H_2CO_3} + \lambda_{H^+})$, $\alpha_2 = \frac{4B\sqrt[3]{2}}{\sqrt[3]{3\alpha_1}}$, $\alpha_3 = \sqrt[3]{\frac{\alpha_1}{18}}$, and $\alpha_4 = \frac{2i_{O_2L}}{\sqrt{-\alpha_2 + \alpha_3}}$. The other three solutions of Equation (4-21) are all negative, not a solution. For reference only, they are written done as: $p_1 = 0.5(-\sqrt{-\alpha_2 + \alpha_3} - \sqrt{\alpha_2 - \alpha_3 - \alpha_4})$, $p_2 = 0.5(-\sqrt{-\alpha_2 + \alpha_3} + \sqrt{\alpha_2 - \alpha_3 - \alpha_4})$, and $p_3 = 0.5(\sqrt{-\alpha_2 + \alpha_3} - \sqrt{\alpha_2 - \alpha_3 + \alpha_4})$.

The corrosion current density can be calculated by combining its relation with p and Equation (4-22):

$$i_{corr} = [(\sqrt{-\alpha_2 + \alpha_3} + \sqrt{\alpha_2 - \alpha_3 + \alpha_4})/2]^3 \quad (4\text{-}23)$$

Substitution of Equation (4-23) into Equations (4-18 - 4-19) allows for the calculation of $p_{CO2}{}^0$ and $c_{H+}{}^0$.

It has been verified that if i_{O2L} is directly added to i_{H2CO3} for corrosion rate with CO_2 and O_2, the result is close to that obtained from using the Nernst-Plank equation.

4.3.3 Corrosion due to Dissolved CO_2 and H_2S

With H_2S in the system, the complete solution of Fe^{2+} concentration expressed by H^+ concentration is:

$$c_{Fe^{2+}s} = \frac{-(c_{H^+s} - \frac{K_w}{c_{H^+s}}) + \sqrt{(c_{H^+s} - \frac{K_w}{c_{H^+s}})^2 + 8[(2K_{2H_2CO_3} + c_{H^+s})\frac{K_{csp}}{K_{2H_2CO_3}} + (2K_{2H_2S} + c_{H^+s})\frac{K_{ssp}}{K_{2H_2S}}]}}{4} \quad (4\text{-}24)$$

$$\frac{dc_{Fe^{2+}s}}{dc_{H^+}} = -\frac{1}{4}(1 + \frac{K_w}{c^2_{H^+s}}) + \frac{\frac{1}{4}(c_{H^+s} - \frac{Kw}{c_{H^+s}})(1 + \frac{K_w}{c^2_{H^+s}}) + \frac{K_{csp}}{K_{2H_2CO_3}} + \frac{K_{ssp}}{K_{2H_2S}}}{\sqrt{(c_{H^+s} - \frac{K_w}{c_{H^+s}})^2 + 8[(2K_{2H_2CO_3} + c_{H^+s})\frac{K_{csp}}{K_{2H_2CO_3}} + (2K_{2H_2S} + c_{H^+s})\frac{K_{ssp}}{K_{2H_2S}}]}} \quad (4\text{-}25)$$

When the solution contains both $FeCO_3$ and FeS precipitates, the solution chemistry is dominated by dissolved CO_2. FeS has very low solubility and the effect of H_2S on pH is negligible. The dependence of Fe^{2+} concentration on pH is the same as when H_2S is absent, following Equations (4-13 - 4-14).

Taking advantage of Equations (4-13 - 4-14), the H_2CO_3 concentration is:

$$c_{H_2CO_3s} = \frac{c^2_{H^+s} K_{spFeCO_3}}{c_{Fe^{2+}s}(K_{11H_2CO_3}/K_h)K_{2H_2CO_3}} \quad (4\text{-}26)$$

$$\left.\frac{dc_{H_2CO_3}}{dc_{H^+}}\right|_s = c_{H_2CO_3s}\left(\frac{2}{c_{H^+s}} - \frac{c'_{Fe^{2+}s}}{c_{Fe^{2+}s}}\right) \quad (4\text{-}27)$$

The H_2S partial pressure at the steel surface can be expressed by:

$$p_{H_2Ss} = \beta_1 c^{\frac{3}{2}}_{H^+s} \quad (4\text{-}28)$$

where $\beta_1 = \frac{H_{H_2S}K_{spFeS}}{K_{1H_2S}K_{2H_2S}}\sqrt{\frac{2K_{2H_2CO_3}}{K_{csp}}}$

$$c_{HS^-s} = \frac{p_{H_2Ss}K_{1H_2S}}{c_{H^+s}H_{H_2S}} = \frac{\sqrt{c_{H^+s}}\beta_1 K_{1H_2S}}{H_{H_2S}} = \beta_2 p^{\frac{1}{3}}_{H_2Ss} \quad (4\text{-}29)$$

where $\beta_2 = \frac{\beta_1^{\frac{2}{3}}K_{1H_2S}}{H_{H_2S}}$.

With FeS and $FeCO_3$ co-precipitation, the ratio of c_{H2S} to c_{H2CO3} can be calculated to be roughly:

$$\frac{p_{H_2S}}{p_{CO_2}} = \frac{H_{H_2S}K_{spFeS}K_{11H_2CO_3}K_{2H_2CO_3}}{H_{CO_2}K_{1H_2S}K_{2H_2S}K_{spFeCO_3}} = 7.25\times10^{-4} \quad (4\text{-}30)$$

The above ratio in Equation (4-30) indicates that if p_{H2S} is more than 7.25×10^{-4} times greater than p_{CO2} in the bulk, there is likely preferred precipitation of FeS and less likely precipitation of $FeCO_3$. Conversely, if this ratio is less than that value, precipitation of FeS becomes unlikely and the precipitate of $FeCO_3$ is dominant. For a 4% of CO_2 in natural gas, the required pressure of H_2S for precipitation of FeS is 29 ppm or more.

To relate corrosion rate to passive scale formation of FeS, the coverage of this scale may be assumed to follow the Langmir adsorption theory for the reaction $Fe + 2HS^- \rightarrow FeS + H_2$ and the coverage depends on the concentration of HS^- and is derived to be[6]:

$$\theta_{FeSs} = \frac{j_i}{l_i(1+\frac{j_i}{l_i})} = \frac{q_i\sigma_{HS^-}}{1+q_i\sigma_{HS^-}} = \frac{q_i\frac{K_{HS^-}c_{HS^-}}{1+K_{HS^-}c_{HS^-}}}{1+q_i\frac{K_{HS^-}c_{HS^-}}{1+K_{HS^-}c_{HS^-}}} = \frac{\frac{K_2c_{HS^-}}{1+K_1c_{HS^-}}}{1+\frac{K_2c_{HS^-}}{1+K_1c_{HS^-}}} = \frac{K_2c_{HS^-}}{1+(K_1+K_2)c_{HS^-}} \tag{4-31}$$

The average corrosion current density with consideration of surface coverage is given by:

$$i_{corr} = i_{corr\_noscale}(1-\theta_{FeSs}) \tag{4-32}$$

Since co-precipitation of $FeCO_3$ and FeS requires much less H_2S than CO_2 as shown by Equation (4-30), the effect of H_2S on the solution chemistry is negligible and its contribution to the steel corrosion rate can be done only through the surface coverage.

To replace Equation (4-5) by Equation (4-32), Equation (4-4) can be rearranged to:

$$i_{corr\_noscale} = c_{Fe^{2+}s}^{-\frac{3\alpha_{H^+}}{4n_{Fe}}}\left(\frac{-\mu_{H_2CO_3}c_{H_2CO_3s}-\mu_{H^+}c_{H^+s}}{1-\theta_{FeSs}}\right)^{\frac{3}{4}} \tag{4-33}$$

or

$$i_{corr} = i_{corr\_CA}(1-\theta_{FeSs})^{1/4} \tag{4-34}$$

If corrosion rate data are available, the coefficients in Equation (4-31) can be obtained through optimization.

4.3.4 Corrosion due to Dissolved CO_2 and H_2S but Precipitate being either $FeCO_3$ or FeS, Not Both

Section 4.3.3 shows that regardless of the corrosion system containing CO_2 alone or both CO_2 and H_2S, if the solution is saturated by $FeCO_3$, the solution pH or other chemistry is essentially the same. Addition of H_2S could only have an effect on the steel corrosion rate when there is presence of FeS precipitate and when FeS can provide passivity to the steel surface. In this section, the effect H_2S on the crevice corrosion when the precipitate is FeS will be discussed.

When CO_2 does not heavily dominate the solution chemistry, FeS can be the only precipitate. Then, if there is not foreign electrolyte such as NaCl, if FeS is passive, the corrosion rate is relatively small.

4.3.4.1 No CO_2

Suppose there is no CO_2 in solution. The complete expression of c_{Fe2+s} by c_{H+} is:

$$c_{Fe^{2+}s} = \frac{-c_{H^+s} + \frac{K_w}{c_{H^+s}} + \sqrt{(c_{H^+s} - \frac{K_w}{c_{H^+s}})^2 + 8(2K_{2H_2S} + c_{H^+s})\frac{K_{ssp}}{K_{2H_2S}}}}{4} \tag{4-35}$$

Since the solution is acidic, the Fe^{2+} concentration can be simplified to:

$$c_{Fe^{2+}s} = \frac{-c_{H^+s} + \sqrt{c^2_{H^+s} + 8c_{H^+s}\frac{K_{ssp}}{K_{2H_2S}}}}{4} \tag{4-36}$$

The concentrations of other species are:

$$c_{HS^-s} = \frac{c_{H^+s}K_{ssp}}{c_{Fe^{2+}s}K_{2H_2S}} \tag{4-37}$$

$$c_{H_2Ss} = \frac{c^2_{H^+s}K_{ssp}}{c_{Fe^{2+}s}K_{1H_2S}K_{2H_2S}} \tag{4-38}$$

$$p_{H_2Ss} = \frac{c^2_{H^+s}K_{ssp}H_{H_2S}}{c_{Fe^{2+}s}K_{1H_2S}K_{2H_2S}} \tag{4-39}$$

Transformation of Equation (4-4 – 4-7), through the use of Equation (4-31) and (4-32), i_{corr} can be expressed as a function of H^+ concentration at the steel surface c_{H+s} as:

$$i_{corr} = (\frac{-\lambda_{H^+}}{1-\theta_{FeSs}})^{\frac{3}{4}}(1-\theta_{FeSs}) = c^{-\frac{3\alpha_{H^+}}{4n_{Fe}}}_{Fe^{2+}s}(-\mu_{H^+}c_{H^+s})^{\frac{3}{4}}(1-\theta_{FeSs})^{\frac{1}{4}} \tag{4-40}$$

To link the chemistry in bulk with that at the steel surface, transport equations must be used. Unlike CO_2 corrosion whose solution chemistry can be simply determined by CO_2 hydration, here all equilibrium processes must be considered.

Since the corrosion is uniform, the transport equation is:

$$\sum_j z_j F N_j = 0 \tag{4-41}$$

$$\frac{dc_{H^+}}{dx}\sum_j z_j D_j \frac{dc_j}{dc_{H^+}} + \frac{d\varphi}{dx}\sum_j \frac{z_j^2 F}{RT} D_j c_j = 0 \tag{4-42}$$

Since the concentrations of all other species can be expressed as c_{H+}, the relation between φ and c_{H+} can be established. If φ in bulk is taken as zero, then the relation between φ_s and c_{H+s} at the steel surface can be established provided pH_0 in the bulk is known.

Integration of Equation (4-42) yields:

$$\varphi_s = \int_{c_{H^+s}}^{c^0_{H^+}} \frac{\sum_j z_j D_j \frac{dc_j}{dc_{H^+}}}{\sum_j \frac{z_j^2 F}{RT} D_j c_j} dc_{H^+} \tag{4-43}$$

By use of Equation (4-43), the corrosion current density $i_{corr\_noscale}$ is now a function of c_{H+s} only. Since the total current density at the steel surface is zero, c_{H+s} and the corrosion current density can be calculated from:

$$i_{corr} = i_{corr\_noscale}(1-\theta_{FeSs}) \tag{4-44}$$

and

$$i_{corr} + i_{H^+} = 0, \tag{4-45}$$

First, by combining Equations (4-44 – 4-45) to yield:

$$k_1 x^4 - k_2 x - 1 = 0 \tag{4-46}$$

where $k_1 = \frac{-\mu_{H^+} c_{Fe^{2+}s}^{-\frac{\alpha_{H^+}}{n_{Fe}}} c_{H^+s}}{(1-\theta_{FeSs})}$; $k_2 = \frac{\mu_{H^+} c_{Fe^{2+}s}^{-\frac{\alpha_{H^+}}{n_{Fe}}} c_{H^+s}}{i_{H^+L}}$; $x = i_{corr\_noscale}$; and the solution is:

$$x = 0.5(\sqrt{A_2 - A_1} + \sqrt{A_1 - A_2 + A_3}) \tag{4-47}$$

where $A = (9k_2^2 + \sqrt{3(256k_1 + 27k_2^2)})^{\frac{1}{3}}$; $A_1 = \frac{4}{A}(\frac{2}{3k_1})^{\frac{1}{3}}$, $A_2 = \frac{A}{(18k_1^2)^{\frac{1}{3}}}$, $A_3 = \frac{2k_2}{k_1\sqrt{A_2 - A_1}}$. The other three roots which are negative are: $x_1 = 0.5(-\sqrt{A_2 - A_1} - \sqrt{A_1 - A_2 - A_3})$; $x_2 = 0.5(-\sqrt{A_2 - A_1} + \sqrt{A_1 - A_2 - A_3})$ and $x_3 = 0.5(\sqrt{A_2 - A_1} - \sqrt{A_1 - A_2 + A_3})$.

Since the corrosion current density is:

$$i_{corr} = x(1-\theta_{FeSs}) \tag{4-48}$$

by substituting Equation (4-43) into the Tafel equation and then by combining with Equation (4-48), c_{H+s} can be obtained.

The relation between bulk pH and $p_{H2S}{}^0$ is:

$$p_{H_2S0} = \frac{c^2_{H^+0} K_{sp} H_{H_2S}}{c_{Fe^{2+}0} K_{1H_2S} K_{2H_2S}} \tag{4-49}$$

In the case of equilibrium the concentration gradient in the solution would be small and the bulk solution concentration may be used to calculate the corrosion rate.

4.3.4.2 With CO_2 but Precipitate is FeS Only

When there is sufficient H_2S in the system, the precipitation of FeS does not require high H_2S content compared to CO_2. Unlike the case that $FeCO_3$ is the only precipitate and in Equation (4-11) the second term under the square-root is significantly larger than the first one, here the second term can be smaller than the first when the pH is less than 6. Hence, the complete expression of c_{Fe2+s} must be used for the calculation of Fe^{2+} concentration. This calculation is described as below:

Suppose the solution boundary layer is saturated by FeS. Given p_{CO2}^0 and p_{H2S}^0 in gas phase the concentrations of all carbon and sulfur species in the boundary layer can be expressed by c_{H+}^0 through equilibrium relations. Since c_{Fe2+}^0 is related to c_{S2-}^0 through FeS saturation, c_{Fe2+}^0 can also be expressed by c_{H+}^0. If there is no other independent species such as Na^+ or Cl^-, electroneutrality allows c_{H+}^0 to be calculated and so are the concentrations of other species. The relation between the concentrations of other solution species vs. that of H^+, dissolved CO_2 and H_2S can be expressed as shown below.

$$c_{H_2CO_3} = \frac{p_{CO_2} K_h}{H_{CO_2}} \tag{4-50}$$

$$c_{HCO_3^-} = \frac{K_{1H_2CO_3} c_{H_2CO_3}}{c_{H^+}} \tag{4-51}$$

$$c_{CO_3^{2-}} = \frac{K_{2H_2CO_3} c_{HCO_3^-}}{c_{H^+}} \tag{4-52}$$

$$c_{H_2S} = \frac{p_{H_2S}}{H_{H_2S}} \tag{4-53}$$

$$c_{HS^-} = \frac{K_{1H_2S} c_{H_2S}}{c_{H^+}} \tag{4-54}$$

$$c_{S^{2-}} = \frac{K_{2H_2S} c_{HS^-}}{c_{H^+}} = \frac{p_{H_2S}}{H_{H_2S}} \frac{K_{1H_2S} K_{2H_2S}}{c_{H^+}^2} \tag{4-55}$$

$$c_{Fe^{2+}} = \frac{K_{ssp}}{c_{S^{2-}}} \tag{4-56}$$

$$c_{Fe^{2+}} = \frac{-p + \sqrt{p^2 - 8q}}{4} \tag{4-57}$$

where $$p = c_{H^+} - \frac{K_w}{c_{H^+}} - c_{HCO_3^-} - 2c_{CO_3^{2-}} = c_{H^+} - \frac{K_w}{c_{H^+}} - \frac{p_{CO_2} K_h}{H_{CO_2}} \frac{K_{1H_2CO_3}}{c_{H^+}} (1 + \frac{2K_{2H_2CO_3}}{c_{H^+}})$$ and

$$\approx c_{H^+} - \frac{K_w}{c_{H^+}} - \frac{2p_{CO_2} K_h}{H_{CO_2}} \frac{K_{1H_2CO_3}}{c_{H^+}}$$

$$q = -(2K_{2H_2S} + c_{H^+}) \frac{K_{ssp}}{K_{2H_2S}} \approx -c_{H^+} \frac{K_{ssp}}{K_{2H_2S}}.$$

If H_2S diffusion is not rate limiting and the sulfur species has a uniform concentration across the boundary layer, by use of Equations (4-1 – 4-2) H_2CO_3 concentration at the steel surface is linked to that in the bulk through $i_{H2CO3d}=i_{H2CO3}$, i.e., the diffusion current density equals the activation current density. Since in the aqueous solution under study, the H^+ concentration in solution may not be dominated by H_2CO_3 dissociation when CO_2 pressure is not high, since H_2S hydration is not rate-limiting, the previous concept that the combined diffusion current of H_2CO_3 and H^+ (i_t) equals the corrosion current in the case of corrosion with dissolved CO_2 alone, does not fully apply here. Given the sulfur species uniform in the boundary, whose concentrations are known at the steel surface (equal to bulk), electroneutrality allows all concentrations of carbon species including c_{H2CO3s} to be expressed by c_{H+s}. If the relation of $i_{H2CO3d}=i_{H2CO3}$ is used, i_{corr} can be expressed by c_{H+s}.

By use of charge conservation at the steel surface:

$$i_{corr} = i_{H^+} + i_{H_2CO_3} \tag{4-58}$$

c_{H+s} can be computed and so can all other variables.

The detailed calculation procedure is given below:

From the following equation:

$$\frac{Kssp}{c_{S^{2-}}} = c_{Fe^{2+}s} = \frac{-p_s + \sqrt{p_s^2 - 8q_s}}{4} \tag{4-59}$$

c_{H2CO3s} can be expressed by c_{H+s} as:

$$c_{H_2CO_3 s} = \frac{c_{H^+s}^2 (\frac{2Kssp}{c_{S^{2-}}} + c_{H^+s} - \frac{K_w}{c_{H^+s}} + \frac{q_s c_{S^{2-}}}{Kssp})}{K_{1H_2CO_3} (c_{H^+s} + 2K_{2H_2CO_3})} \tag{4-60}$$

where $p_s = c_{H^+s} - \frac{K_w}{c_{H^+s}} - \frac{c_{H_2CO_3 s} K_{1H_2CO_3}}{c_{H^+s}} (1 + \frac{2K_{2H_2CO_3}}{c_{H^+s}})$ and $q_s \approx -c_{H^+} \frac{K_{ssp}}{K_{2H_2S}}$, since $c_{S^{2-}} = c_{S^{2-}}^0$ is assumed without transport limitation.

By use of the following equations:

$$i_{LH_2CO_3} = F \frac{p_{CO_2}^0}{H_{CO_2}} \sqrt{K_f K_h D_{H_2CO_3}} \tag{4-61}$$

$$i_{dH_2CO_3} = i_{LH_2CO_3}(1 - u_{H_2CO_3 s}) \tag{4-62}$$

$$i_{H_2CO_3} = \lambda_{H_2CO_3} i_{corr}^{-\omega_{H_2CO_3}} \tag{4-63}$$

$$i_{H_2CO_3} = i_{H_2CO_3 d} \tag{4-64}$$

i_{corr} can be expressed by c_{H+s}.

From this following equation:

$$i_{corr} = i_{H^+} + i_{H_2CO_3} \tag{4-65}$$

or

$$i_{corr} = (-\lambda_{H_2CO_3} - \lambda_{H^+})^{\frac{3}{4}} = c_{Fe^{2+}s}^{-\frac{3\alpha_{H^+}}{4n_{Fe}}} (-\mu_{H_2CO_3} c_{H_2CO_3 s} - \mu_{H^+} c_{H^+ s})^{\frac{3}{4}} \tag{4-66}$$

$$i_{H_2CO_3} = \lambda_{H_2CO_3} \sqrt[4]{\frac{c_{Fe^{2+}s}^{\frac{\alpha_{H^+}}{n_{Fe}}}}{-\mu_{H_2CO_3} c_{H_2CO_3 s} - \mu_{H^+} c_{H^+ s}}} \tag{4-67}$$

c_{H+s} can be computed and so are other variables.

The overall equation is:

$$i_{dH_2CO_3} = F \frac{p_{CO_2}^0}{H_{CO_2}} \sqrt{K_f K_h D_{H_2CO_3}} \left(1 - \frac{c_{H_2CO_3 s}}{c_{H_2CO_3}^0}\right) \tag{4-68}$$

$$\lambda_{H_2CO_3} = \mu_{H_2CO_3} c_{H_2CO_3 s} c_{Fe^{2+}s}^{-\frac{\alpha_{H_2CO_3}}{n_{Fe}}} \tag{4-69}$$

4.4 References

1. F.M. Song, D.W. Kirk and D.E. Cormack, "Modeling CO_2 Corrosion in Oil and Gas Transmission Systems". Held April 3-7, 2005 (Houston, TX: NACE, 2005) Paper: 05180.
2. F.M. Song, D.W. Kirk, J.W. Graydon and D.E. Cormack, "CO_2 Corrosion of Bare Steel under an Aqueous Boundary Layer", Corrosion 60(8) (2004) 736-748.
3. F. M. Song, Kirk, D.W., Graydon, J.W. and Cormack, D.E., 2002, J. of Electrochem. Soc., 149(11) (2002) B479-B486.

4. F.M. Song, D.W. Kirk and D.E. Cormack, "Determination of Precipitates for CO_2 Corrosion of Steel under an Aqueous Boundary Layer", Journal of Corrosion Science and Engineering, Volume 3, Paper 24 (2004).

5. Fengmei Song, "Corrosion of Coated Pipelines with Cathodic Protection", Ph.D. thesis (2002), University of Toronto, Department of Chemical Engineering and Applied Chemistry.

6. A. Anderko and Young, R.D., "Simulation of CO2/H2S Corrosion Using Thermodynamic and Electrochemical Models, Corrosion/99, Paper 31, Houston, TX: NACE International.

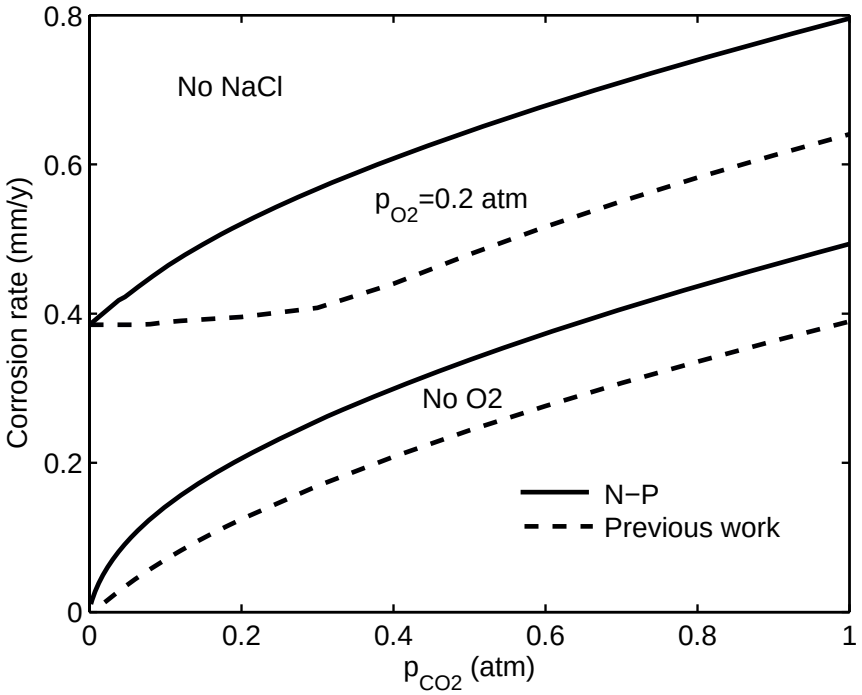

Figure 4-1. Comparison of the complete results from N-P with those from the previous work.

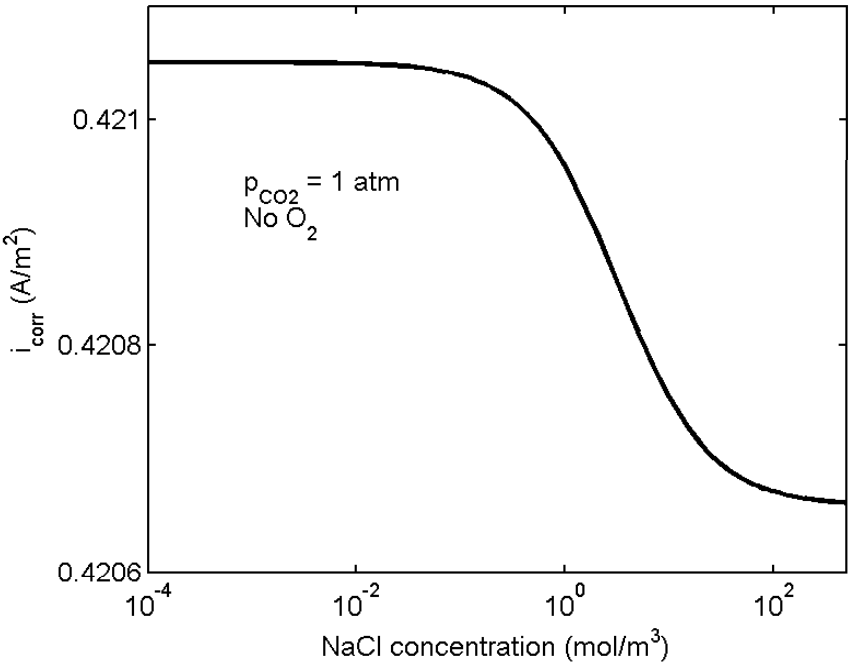

Figure 4-2. Effect of NaCl as supporting electrolyte salt on the CO_2 corrosion rate.

5.0 VALIDATION OF THE EXTERNAL CORROSION RATE CALCULATION (TASK 3)

Significant laboratory tests were conducted to simulate pipeline corrosion under disbonded coatings. However, most of the publications did not provide sufficient information that allows for the model validation. Attempts have been made in this project to validate the model using as many data as possible. Figure 5-1 shows the model geometry without flow in the disbondment. If there is flow in the disbondment, this figure may be considered that the right end of the disbondment is open. Regardless of presence of flow, O_2 can transport into the disbonded region only through the holiday and through the coating. The CP protects the steel surface by providing positive ionic current flowing to the steel surface through the holiday(s). The coating is typically ionically non-conductive . The model will be validated starting from a simple case: no O_2 and no flow.

5.1 Without O_2 and without Flow

Validation of the model is done using laboratory data from two independent sources. For the first source[1], three sets of experimental data obtained at 25°C and 1 atm were used. The test conditions are shown in Table 5-1 including external potential (potential applied at the holiday), initial solution resistivity, gap between the disbonded coating and the steel surface, and the potential far inside the crevice, where CP can not reach and the potential is the open circuit potential (OCP).

Table 5-1. Experimental Data

Set No.	Ext. Potential (V)	Resistivity (Ω m)	Gap (mm)	OCP (V)
1	-1.015	18.5	2	-0.764
2	-1.042	2.5	2	-0.77
3	-0.95	12.2	5	-0.68

As shown in Figure 5-2 the experimental data of Set 1 in Table 1 (solid dots) is consistent with the model result (solid curve). The pH near the steel surface is calculated to be 7.8 based on mixed potential theory: $i_{Fe} + i_{H_2O} = 0$. This pH value is only slightly higher than the experimentally measured average pH (7.2~7.5) of the crevice solution.

Figures 5-3 and 5-4 respectively show the validation of the model using the experimental data of Sets 2 and 3 respectively. There is good agreement between the model results and the experimental data. The pHs at the steel surface calculated are respectively 7.8 for Set 2 and 6.7 for Set 3. The latter pH (6.7) is less than experimental pH (7.2-7.5) probably because of the solution at the steel surface which may not be saturated by ferrous hydroxide in the presence of chloride. The model calculation was done based on the solution being saturated by ferrous hydroxide.

Although not considered as a strict validation of the model, Figure 5-5 is a duplication of a figure in the literature[2] where the same model was validated with experimental data.

5.2 Model Validation with Experimental Data Generated by Gaz de France with and without Flow[3,4]

5.2.1 Background

Field investigations during pig runs found large disbondments (several meters long and a few mm high) on pipelines with old bituminous coatings. Upon excavation significant corrosion attacks were found under disbonded coatings and the observation seemed to indicate that the corrosion was caused by a draining flow passing through the disbondments. The presence of two or more holidays in the disbondment provided the entrance and exits for the solution flow. Since there is limited CP penetration into the disbondment, any O_2 carryover into the disbonded area could increase the steel corrosion rate there where CP is ineffective. Based on the above observation, Gaz de France studied the steel corrosion under disbonded coating with and without circulation of aerated solution. The experimental study aimed to evaluate the effect of O_2 content, flow velocity and CP application on the corrosion rate of the underlying metal surface. In the following three subsections 5.2.2-5.2.4, the Gaz de France tests[3-4] are summarized.

5.2.2 Experimental Setup

The experimental setup used by Gaz de France is schematically shown in Figure 5-6(a), where the steel plate, the electrochemical cell and the counter, reference and pH electrodes are shown. A thick PMMA plate is used to substitute for an impermeable coating. Since PMMA is transparent, the disbondment is not seen clearly. The plate was designed to be 4 mm thick and 500 mm long. A 2 cm diameter hole was drilled on the right portion of the plate to simulate a holiday in the coating. Counter and reference electrodes were used to control CP imposed to the steel plate through a Potentiostat. The solution was aerated by zero air (80%N_2/20%O_2) and it was continuously flowing into the cell to renew the solution. The solution in the cell was further mixed by a stirring and aerated by bubbling zero air. Due to the large volume of solution used, natural underground tap water was used for the solution after treatment. The final pH was 7.4, a resistivity 15.7 Ωm and a total oxidant content (mainly ClO_2) 0.15 mg/L. The disbondment can be artificially divided into six lots, as shown in Figure 5-6(b), with each, except Lot 1, consisting of a micro reference electrode, a pH electrode and an O_2 probe inserted through the PMMA plate and of three identical 1 cm^2 coupons in triangular arrangement (one directly under the reference electrode which can not be seen) embedded in and insulated from the steel plate. The lots are approximately evenly spaced, about every 9 cm from the holiday. In Lot 1, facing to bulk solution right below the holiday the coupon cannot be seen clearly. The experimental setup is schematically shown in Figure 5-7(a) and the coupons are more clearly seen in Figure 5-7(b). Coupon 1 is the directly under the holiday.

Figure 5-8 shows instruments used to measure the currents flowing between any arbitrary coupon and the steel plate (i_n). The coupons are connected to the steel plate through a current converter that transforms current signal into potential signal by a resistor and an amplifier. The real-time potential, equivalent to a current due to Ohm's law, can be measured. In this setup, the

current flowing between the counter electrode and the steel plate (i_p) and between the counter electrode and steel plate as wellas the coupons (i_{tot}) can also be measured. For corrosion rate measurement, the coupons were removed at the end of a test and weight loss method was used following the ASTP G1-90. Since the weight loss method include aggravating errors due to the large sizes of the couples, it is estimated that the most likely error could be in the order of 40 μm/y in terms of corrosion rate. In data processing, any corrosion rate below 40 μm/y was assumed to be zero. Each test was conducted for about three weeks.

Since the geometry of the test and that of the model are not consistent, a quantitative validation of the model will not be conducted. Instead, a qualitative comparison is to be made.

5.2.3 Qualitative Model Validation with Data without Flow

In the case of no flow, Figure 5-9 shows that without CP the corrosion rate is greatest at the holiday and decreases into the crevice. This is consistent with the model results as shown in Figure 3-45 without CP.

With CP for a potential of -950 mV CSE at the holiday, Figure 5-9 shows that CP is effective only near the holiday. The corrosion rate increases as moving slightly deeper into the crevice. Further deeper inside the crevice, however, there is no O_2 and the corrosion rate becomes smaller. This result is approximately consistent with the model results in Figure 3-45 but holiday potential of -850 mV where the corrosion rate decreases into the crevice. That the model prediction for the same holiday potential (-950 mV) would however be inconsistent with the experimental results can be explained by the following reasons: (1) the model geometry (rectangle holiday) is different from the test geometry (circular holiday), (2) the stirring of the bulk solution that disturbs the solution in the crevice near the holiday region was not accounted for by the model and in the test O_2 may be carried into the crevice by convective flow, and (3) the deposit near the holiday, as seen in Figure 5-9(b), was not considered in the model and it may have a preference for CP penetration to O_2 diffusion.,

5.2.4 Experimental Data with Flow for Model Validation

The qualitative model validation will be done in 5.3.3. Here, only the experimental results are discussed.

Figure 5-10 shows that with flow in the disbondment, CP is not effective inside and the corrosion rate there is significant. The corrosion rate is relatively uniform inside indicating that the O_2 content there are relatively uniform. The convective flow forces much O_2 into the disbondment where CP is absent. This is consistent with model result to be shown in 5.3.3.

Figure 5-11 is a summary of the experimental results with and without flow and in the case of no flow, with and without CP. Clearly, the corrosion rate with flow has a much larger corrosion rate than if the flow is absent.

5.3 Model Validation with Data Obtained for Disbondment Corrosion with Flow

5.3.1 Mathematical Model for Disbondment Corrosion with Flow

For any 2D geometry with convective flow, the solution chemistry under disbonded coatings is expected to be uniform. Hence, Laplace's equation can be used to describe charge conservation in the crevice solution:

$$\frac{\partial^2 \psi}{\partial z^2} + \frac{\partial^2 \psi}{\partial y^2} = 0 \tag{5-1}$$

Under steady-state condition, mass conservation of dissolved O_2 can be expressed by:

$$-D_{O_2}\left(\frac{\partial^2 c_{O_2}}{\partial z^2} + \frac{\partial^2 c_{O_2}}{\partial y^2}\right) + u\frac{\partial c_{O_2}}{\partial z} + v\frac{\partial c_{O_2}}{\partial y} = 0 \tag{5-2}$$

The Navier-Stocks equations for momentum balance are:

$$\rho\left(u\frac{\partial u}{\partial z} + v\frac{\partial v}{\partial y}\right) - \mu\left(\frac{\partial^2 u}{\partial z^2} + \frac{\partial^2 v}{\partial y^2}\right) + \frac{\partial p}{\partial z} = 0 \tag{5-3a}$$

$$\rho\left(u\frac{\partial u}{\partial z} + v\frac{\partial v}{\partial y}\right) - \mu\left(\frac{\partial^2 u}{\partial z^2} + \frac{\partial^2 v}{\partial y^2}\right) + \rho g = 0 \tag{5-3b}$$

The equation of continuity is:

$$\rho\left(\frac{\partial u}{\partial z} + \frac{\partial v}{\partial y}\right) = 0 \tag{5-4}$$

The boundary conditions for solving the above equations depend on the model geometry, which will be described in 5.3.3. The experiment test conduced in the current project is described next.

5.3.2 Experimental Approach

Although the Gaz de France experimental study provides very useful information on disbondment corrosion with flow, the experimental cell in such design cannot ensure the flow laminar and quiescent near the mouth due to a circular holiday being fully open to the bulk solution which is constantly being stirred. Also, the test cannot ensure the velocity in parallel with the longitude direction of the crevice. Due to the large spatial separation between the coupon lots, the sensitive local current and O_2 concentration close to the holiday cannot be measured. The above design using a thick PMMA plate as the crevice cover also eliminated the possibilities of measuring the effect of O_2 permeation through the coating.

In this project, a new experimental setup was therefore designed to compensate the shortcomings of the Gaz de France design. Although the time and budget constraint of the current project didnot permit enough tests to be conducted, the tests performed provided useful information and facilities for future research in this area. New features in the current design are described below.

Figure 5-12 is the front view of the new setup. It has the following pieces: (1) the cell containing bulk solution, Pt counter electrode, reference electrode, an O_2 probe, a Pt wire, a stir, the entrances and exits for solution circulation, (2) the steel plate, (3) a sandwich disbondment with a HPDE coating located between two compartments bounded by a PMMA plate at the top and the steel plate at the bottom. The lower compartment simulates the disbondment on the pipeline and the upper one in the test was filled with renewing aerated solution through circulation and allows for measurement of the effect of O_2 penetration through the coating.

Not shown is a narrow long rectangular solid PMMA ribbon. It was inserted in the middle of the upper compartment parallel in the longitude to provide support of the coating. Holes were drilled through the ribbon allowing micro reference and micro pH electrodes to be inserted passing through the upper compartment and the coating to measure the steel potential and disbondment solution pH in the lower compartment. Each of the reference electrodes was placed in a location approximately facing a coupon so that the potential of the coupon can be measured. In Figure 5-14, the coupons are arranged to be closer near the crevice mouth because with low flow rate the current is larger and its change is more significant there. The dimensions are shown in the figure about the space between coupons and the dimensions of the steel plate. The thickness of the steel plate is 5 mm and that of the coating 1 mm.

In the steel plate the coupons were insulated from the steel plate by epoxy while each was connected to the steel plate through a thin cable wire passing through a switch. The switch allowed the current between the coupon and the steel plate to be measured through a zero resistance ammeter (ZRA) or a pico-ampere KEITHLEY meter. The results measured using both methods were found to be consistent. The OCP of the coupons facing or near a reference electrode was measured relative to the reference electrode by switching off. Pt wires were also embedded in the steel plate and insulated from the steel plate by epoxy. Their Pt potentials relative to the Pt wire in the bulk solution reflects the relative O_2 contents in the lower compartment solution since the relative effect of ionic solution chemistry such as pH may be insignificant to affect the Pt potential.

Figure 5-15 is a 3D view of the test cell and the two compartments abovementioned. Small holes were drilled in the PMMA plate to serve as the holiday mouth and the bulk solution was allowed to pass through into the lower compartment. The design is supposed to reduce the flow turbulence and maintain a uniform O_2 concentration near the mouth and to ensure the flow to be uni-directional along the longitude of the lower compartment. A triangular gap near the solution exit on the left in the lower compartment was used to ensure the flow to remain uniform as passing through the last coupon. Circulation of the aerated solution through the upper compartment to the bulk cell ensures a uniform O_2 concentration near the coating surface.

In the test, two 20-liter aerated bulk solution reservoirs connected to each other were used to provide constant aerated solution through pumping into the electrochemical cell at a steady rate. The O_2 concentration in the electrochemical cell was measured by a micro O_2 probe. The exit solution from the lower compartment was pumped into drain at a steady, calibrated rate through an O_2 probe to measure the O_2 concentration. This rate determined the flow velocity in the disbondment. The bulk solution and the exit solution were collected periodically into two separate beakers and their pHs and conductivities were measured. The potentials of the steel plate and the pHs of the solution in the lower compartment were measured at different locations along the length by micro reference and pH electrodes.

This set-up allows for the measurement of local coupon current, steel potential, solution pH and relative O_2 content in the disbondment solution. The effects of flow rate, CP potential and O_2 content on the above parameters can be tested.

5.3.3 Experimental Results and Model Validation

The experimental tests were conducted and the disbondment corrosion potential, local current flowing between the coupons and the steel plate and the O_2 content at the entrance and exit of the disbondment were measured and used to validate the model.

A total of three tests were conducted. In the first test, unlike described in 5.3.2 the reference and pH electrodes were rather inserted into the lower compartment through the steel plate and problems were found that there was loss of the conductivity of the electrodes. In the second test, the reference and pH electrodes were inserted into the lower compartment through the PMMA ribbon (as described in 5.3.2). During the test, leaking of the solution was discovered and the test was stopped without completion. To prevent the leakage, care was taken in the third test and the experimental data appears reasonable.

Many parameters were measured in Test 3, including steel potential, pH, relative O_2 content in the disbonded region and current flow from the coupons to the steel plate. Since the reference electrodes and pH electrodes closest to the holiday were still some distance from the holiday, the change of the potential near the holiday could not be measured. Hence, the measured potentials are relatively uniform (Figure 5-16). The stability of measured pH was not satisfactory.

Since it was found after the test that the platinum tips were covered by corrosion product (Figure 5-17, upper holes in brown color), it is unclear how accurate the measured data are. Figure 5-18 seems to indicate that the O_2 content is smaller near the holiday than in the disbondment due to the change of Pt potential.

The few parameters measured that are relatively robust include the O_2 concentration in entrance (0.21 atm) and at the exit (0.02 atm) of the lower compartment and the local currents flowing between coupons and the steel plate (Figure 5-19). The solution pHs at the inlet and at the outlet are measured which are roughly stable being approximately 4.7 at inlet and 5.4 outlet. The conductivity of the solution at the entrance (300 micro siemens/cm) is slightly larger than at

the entrance (250 micro siemens/cm). Note that in the third test, the solution used was saturated by 5% CO_2 and zero air.

The experimental results were simulated through modeling using consistent entrance and exit pHs (average taken 4), entrance (0.21 atm) and exit O_2 concentration (0.02 atm), and conductivity of 30 ohm.m. The simulated currents between coupons and the steel plate (Figure 5-20) are comparable to experimentally measured data. Although there are discrepancies, the shapes of the curves are roughly similar. The different magnitude of current may result from the IR drop through the meshed holiday. It is unclear why there are two peak currents in the measured current data.

Model simulation for the solution flow in the disbondment is shown in Figure 5-21 where only the left portion of the geometry is shown as for the right portion the flow pattern has no variation. The average velocity on the very right boundary is about 0.3 cm/min. The velocity very near the holiday is much higher than inside the disbondment because the holiday size is much smaller than the cross-sectional area in the flow direction of the disbondment. Due to the convective flow, dissolved O_2 is forced to enter into the disbondment. Since the velocity is not greater, it is clear that the concentration of O_2 is higher near the holiday and decreases along the flow direction (Figure 5-22). Although mainly consumed by CP near the holiday, dissolved O_2 in the disbondment is rather consumed mainly by iron oxidation as where CP is not available.

The effect of flow velocity on the crevice corrosion rate is shown in Figure 5-23. This result is consistent with the experimental result conducted by Gaz de France in Figures 5-10 - 11. The corrosion rate is small near the holiday due to CP and increases to a maximum where O_2 is, by flow, forced to move down closer to the steel surface. O_2 decreases slowly into the disbondment. The flow continuously carries O_2 into the disbondment. The corresponding corrosion potential is shown in Figure 5-24. Wherever the corrosion rate is greater the corrosion potential is more positive.

Figure 5-25 shows that the O_2 concentration near the coating is approximately the same as in the bulk because there is no electrochemical reaction at the coating surface. Near the steel surface, O_2 is reduced by steel and its concentration is smaller.

5.4 References

1. T.R. Jack, G.V. Boven, M. Wilmott, R.L. Sutherby, R.G. Worthingham, MP (8) (1994) 17-21.
2. Z. Li, F. Gan and X. Mao, “A Study on Cathodic Protection against Crevice Corrosion in Dilute NaCl Solutions”, Corrosion Science 44 (2002) 689-701.
3. Xavier Campaignolle, Stéphane Gastaud, Sébastien Karcher, Michel Meyer, “Corrosion of Pipelines under CP in the Presence of Coating Disbonding”, EUROCORR/2004, Paper 074.
4. Stéphane Gastaud, Thèse en Génie des Matériaux, “Influence de l'état du revêtement hydrocarboné sur le risque de corrosion des canalisations enterrées de transport de gaz” (2002) Institut national des sciences appliquées de Lyon.

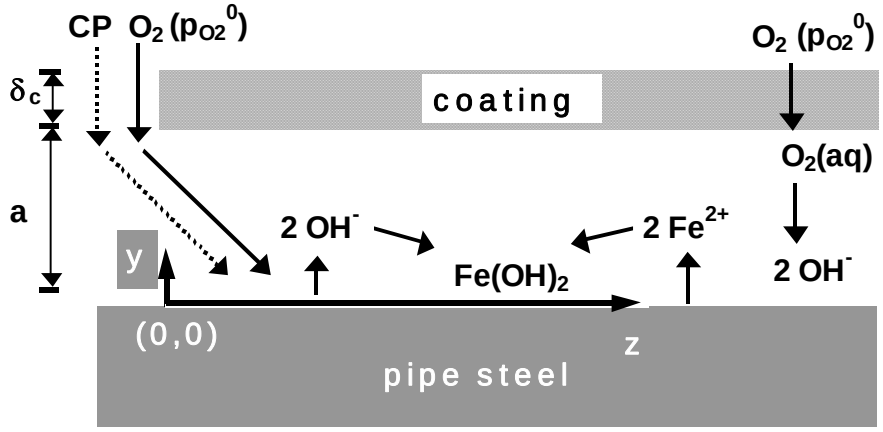

Figure 5-1. The geometry describing pipe corrosion under disbonded coating with a holiday on the left when there is CP and O2. O2 permeation through the coating is not considered in the current program. “a” is gap between coating and the steel surface.

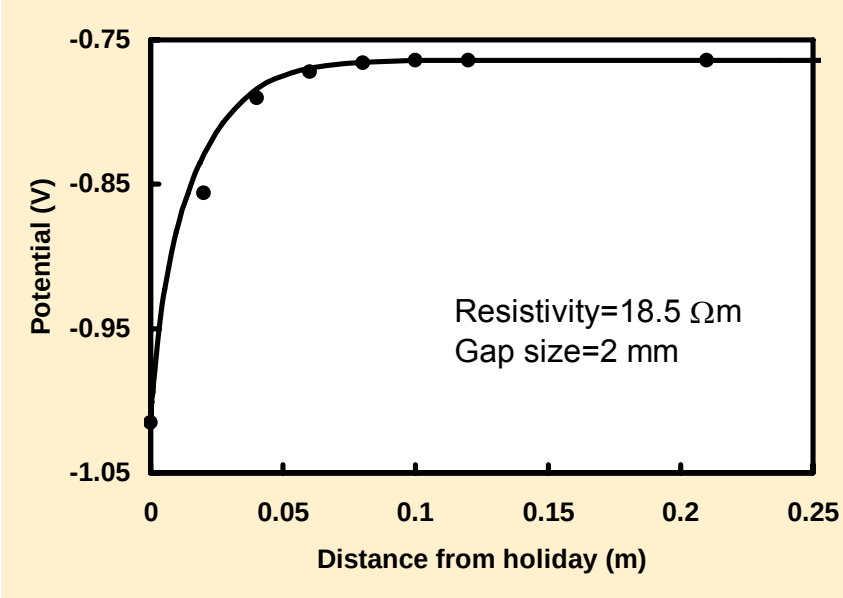

Figure 5-2. Model validation using test data published in the literature. The test setup has the same geometry as Figure 5-1. The potential at the holiday is -1.015 V CSE. There is no O_2 in the system.

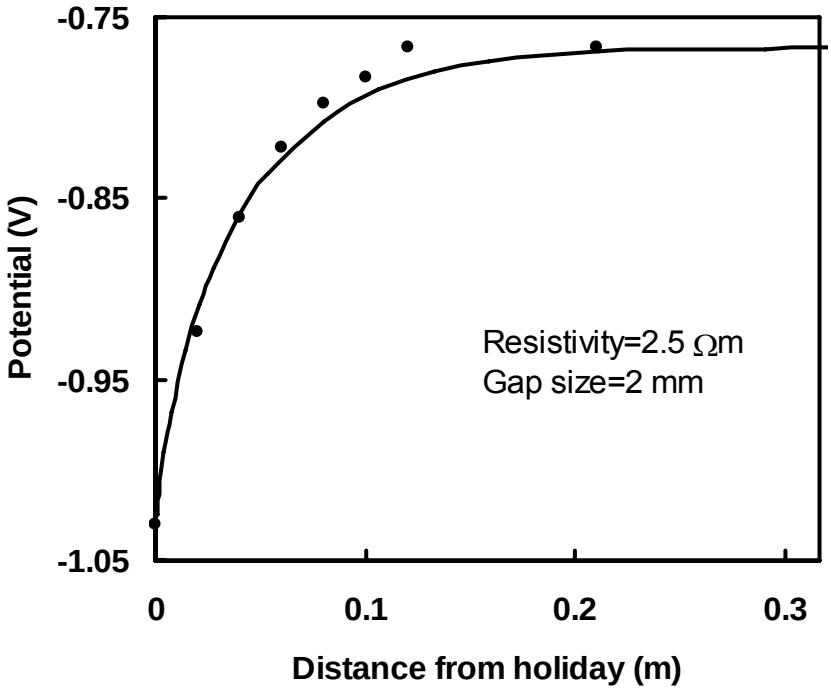

Figure 5-3. Model validation using test data published in the literature. The test setup has the same geometry as Figure 5-1. The potential at the holiday is -1.042 V CSE. There is no O_2 in the system.

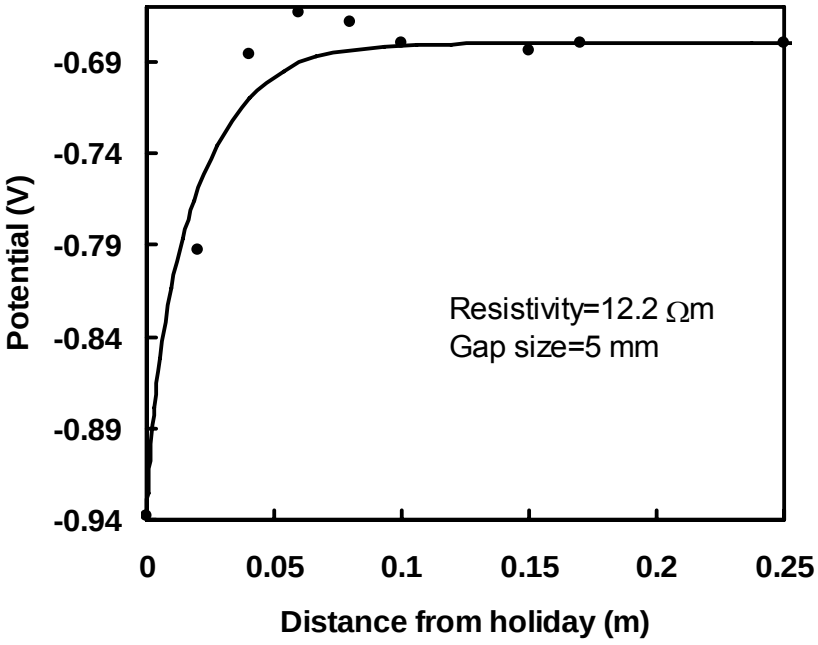

Figure 5-4. Model validation using test data published in the literature. The test setup has the same geometry as Figure 5-1. The potential at the holiday is -0.95 V CSE. There is no O_2 in the system.

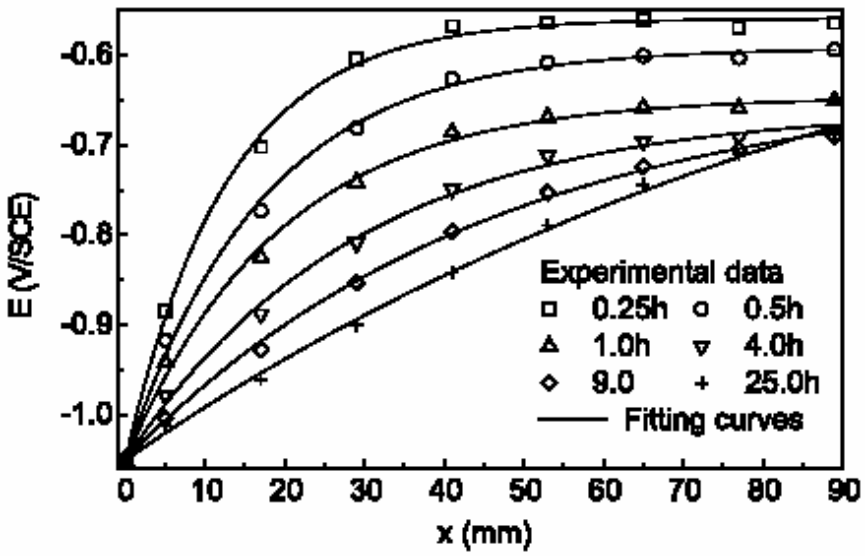

Figure 5-5. Potential profile under disbondment. Test conducted in 0.006 mol/L NaCl solution for various times. Gap is 1 mm and the holiday potential is -1.05 SCE. Picture taken from Li et al., Corrosion Science.

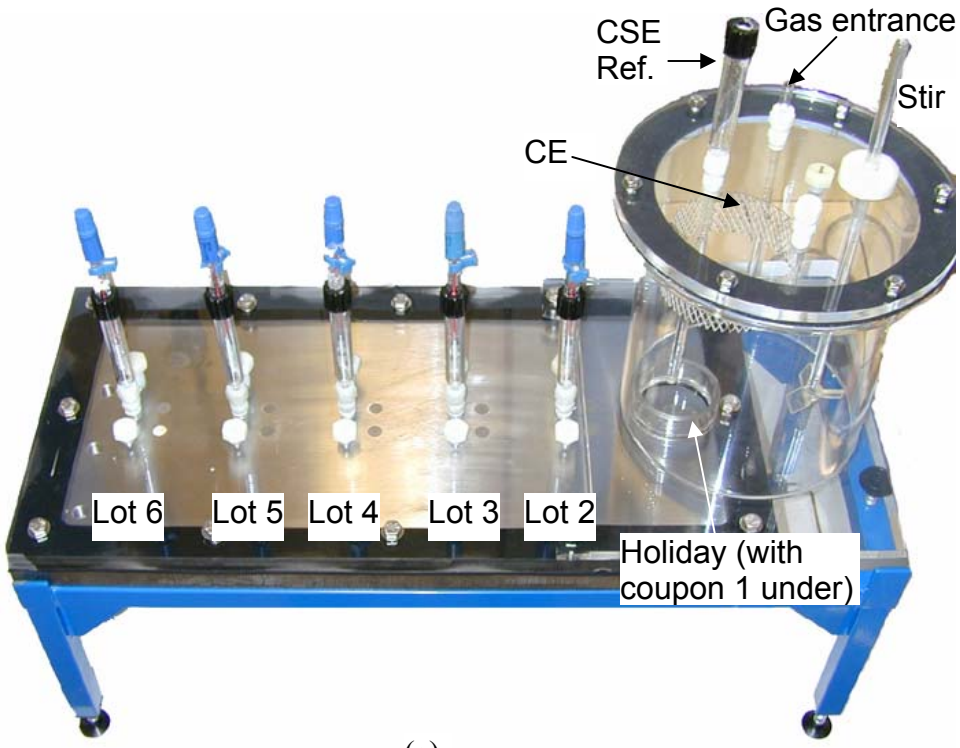

(a)

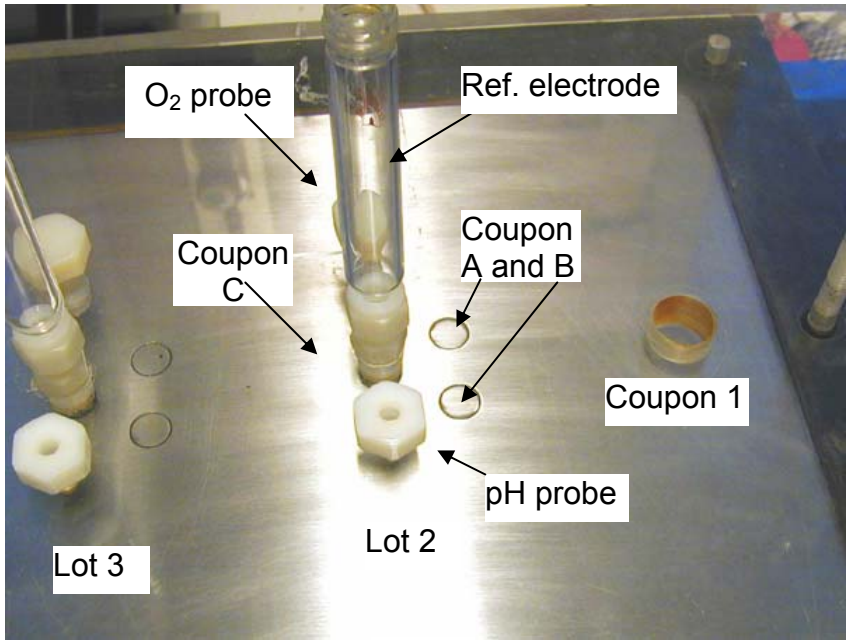

(b)

Figure 5-6. Gaz de France experimental setup to measure disbondment corrosion with and without flow. In (b), the ring on the right is the holiday and beneath is Coupon 1.

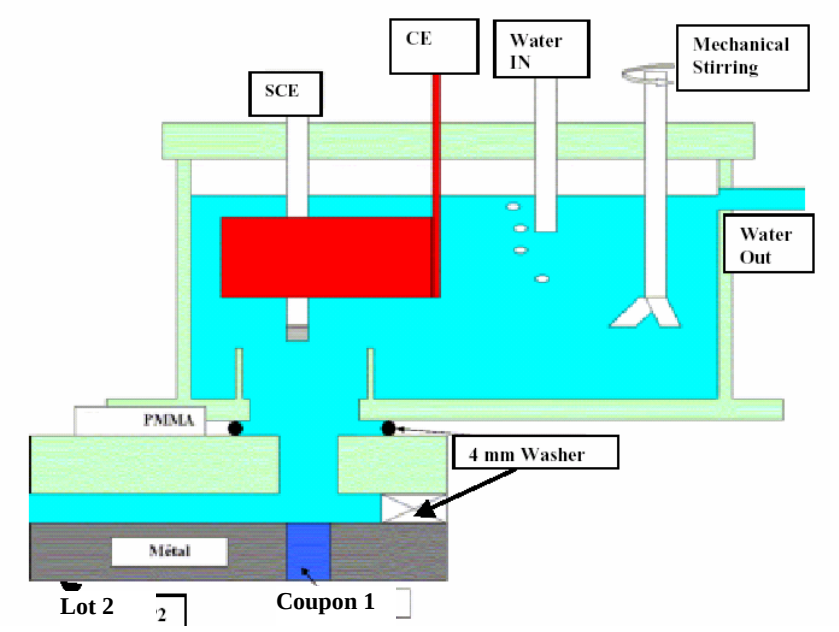

(a)

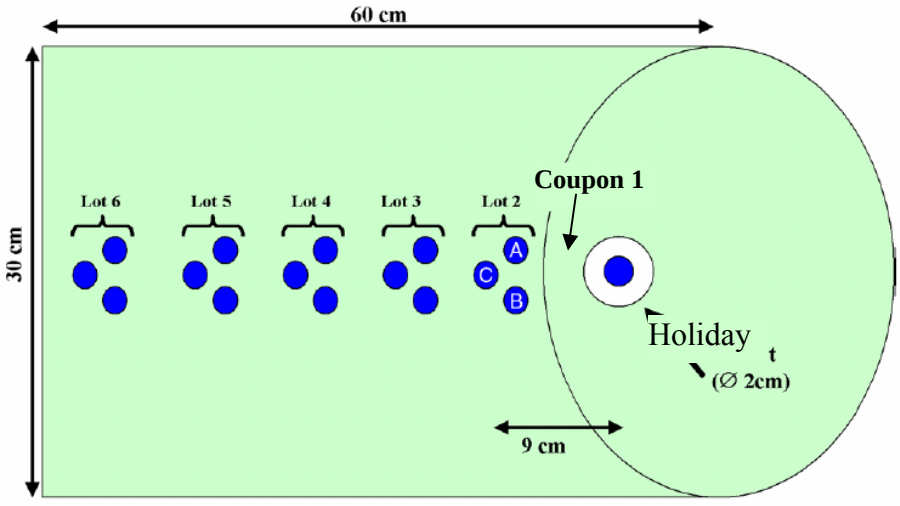

(b)

Figure 5-7. Schematical showing of the Gaz de France experimental setup: (a) side view and (b) coupon distribution in the steel plate.

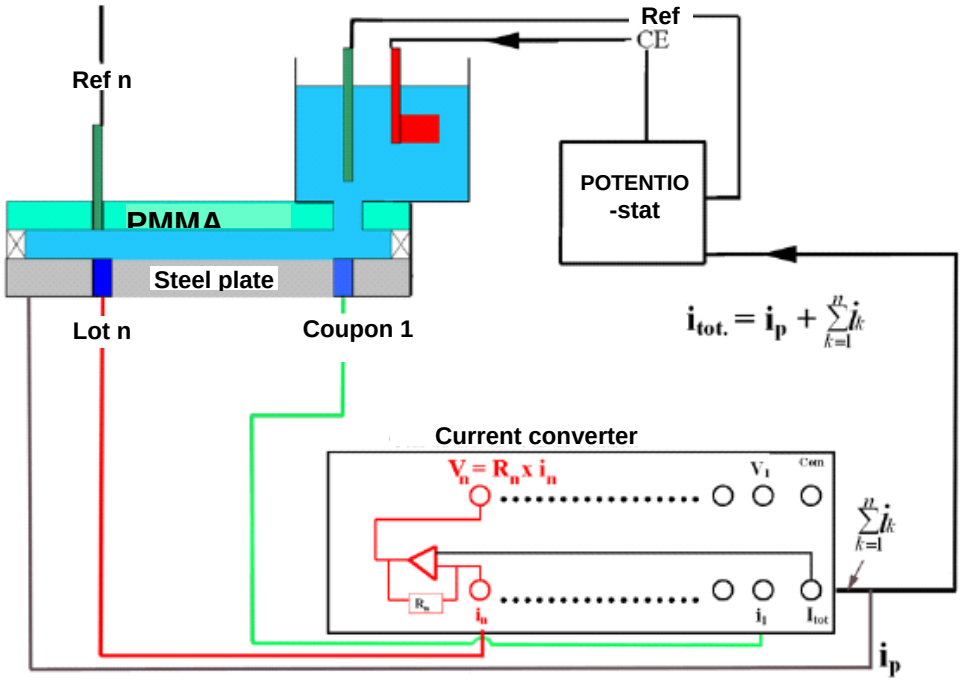

(a)

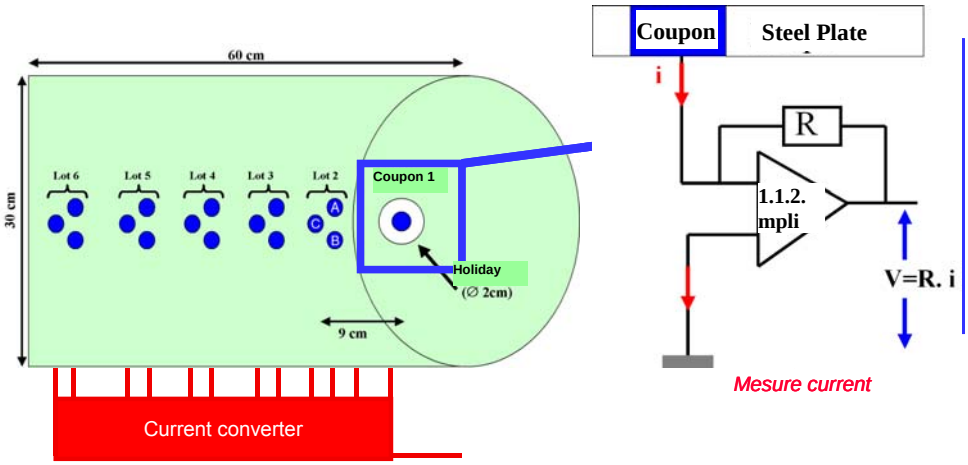

(b)

Figure 5-8. Schematical showing of the Gaz de France experimental setup with electronic system to measure the current flow from the coupons to the steel plate.

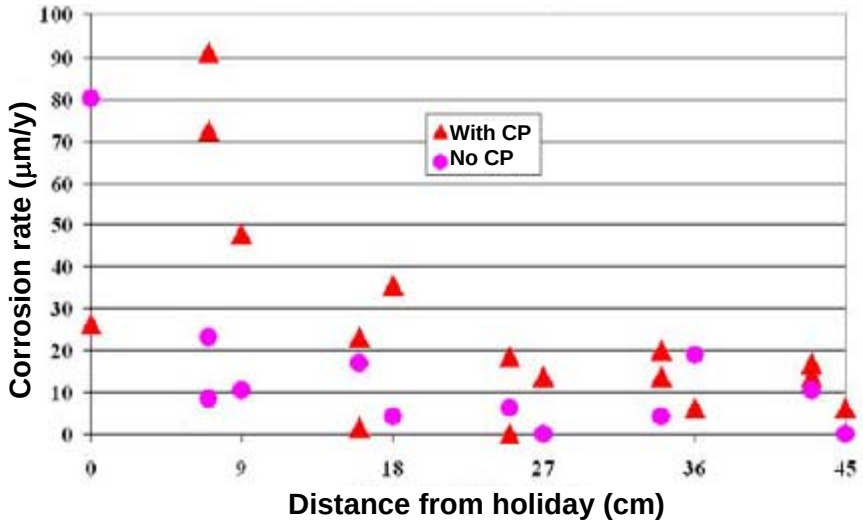

(a)

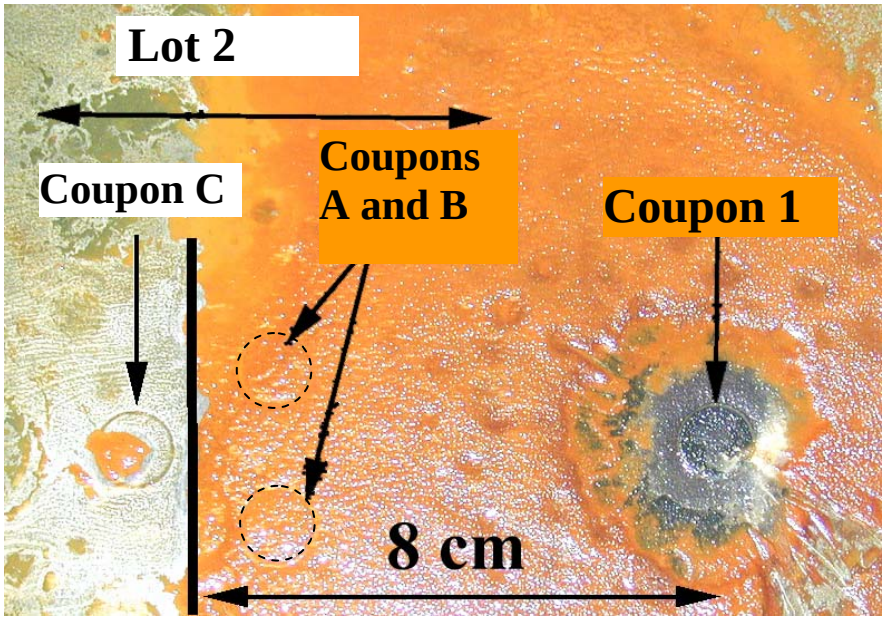

(b)

Figure 5-9. Without flow, (a) the corrosion rate of the steel plate in the disbondment with and without CP and (b) with CP, the corrosion view of the steel plate surrounding the holiday or around Coupon 1 which is underneath of the holiday.

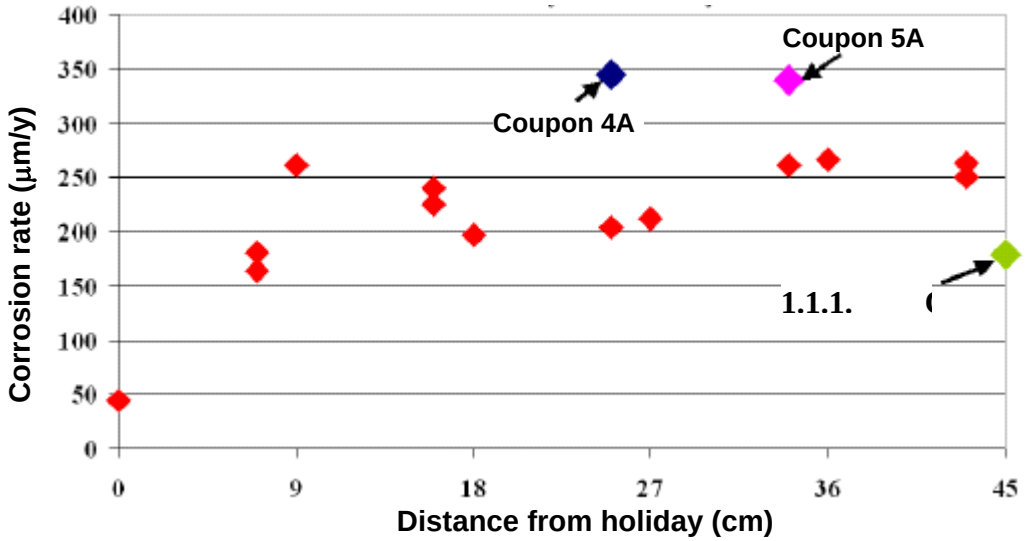

(a)

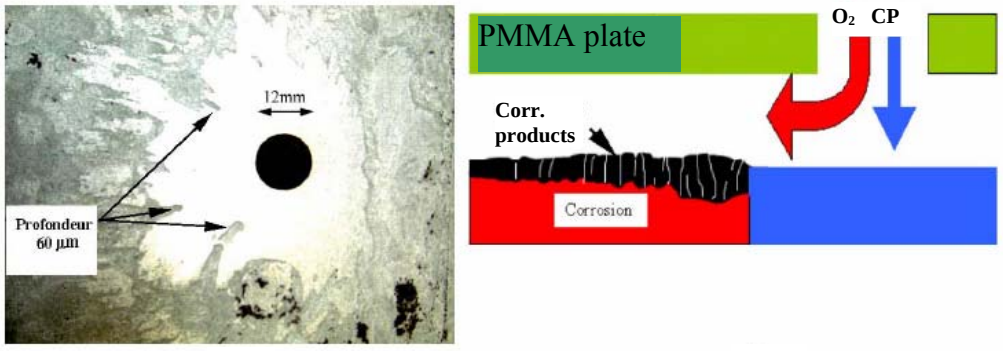

(b.1) (b.2)

(b)

Figure 5-10. With CP and flow, (a) the corrosion rate of the steel plate in the disbondment and (b) the corrosion view.

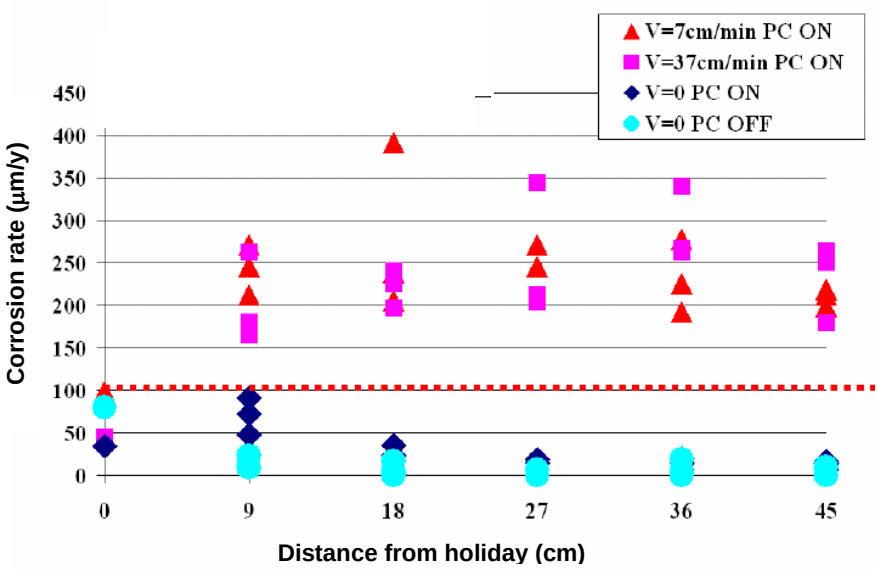

Figure 5-11. A comparison of the corrosion rates measured with and without CP and with and without flow.

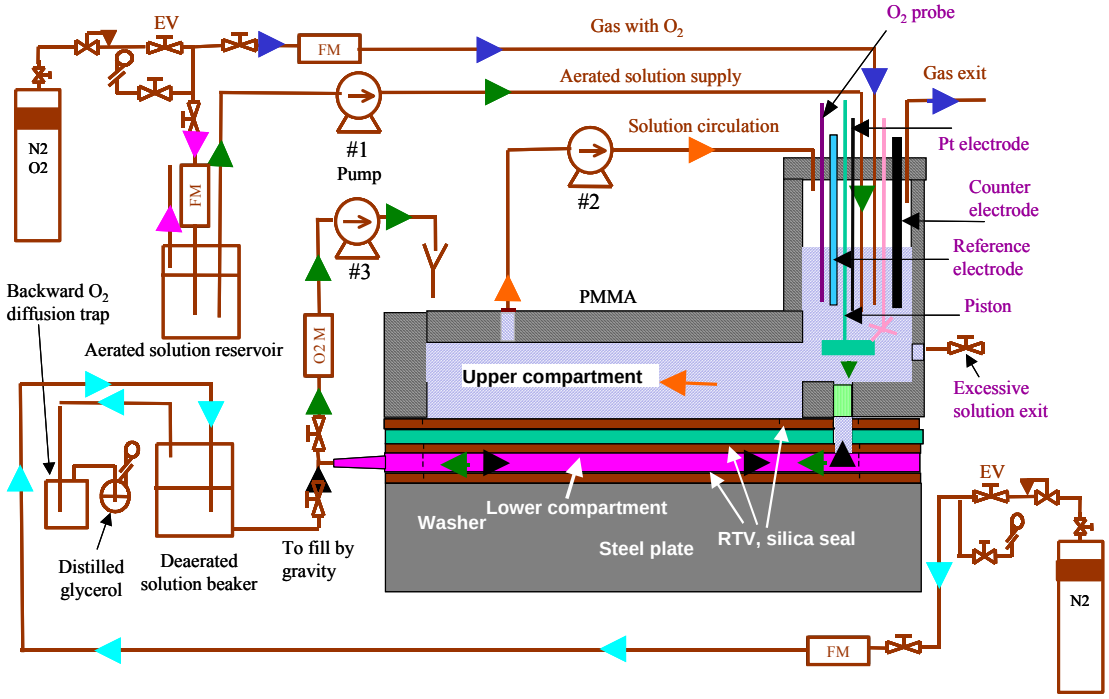

Figure 5-12. Overall experimental setup for disbondment corrosion with flow without the electronic control (two Potentiostats. One for CP supply and one for ZRA) and data collection and recording portions (Keithley multichannel and computer recording).

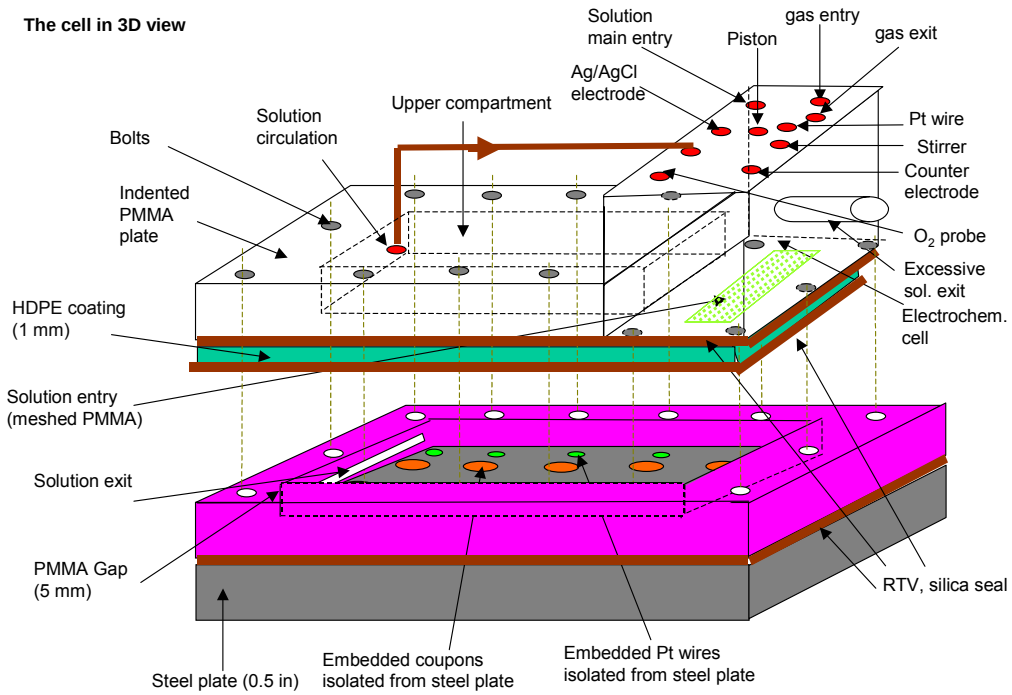

Figure 5-13. The test cell in 3D view.

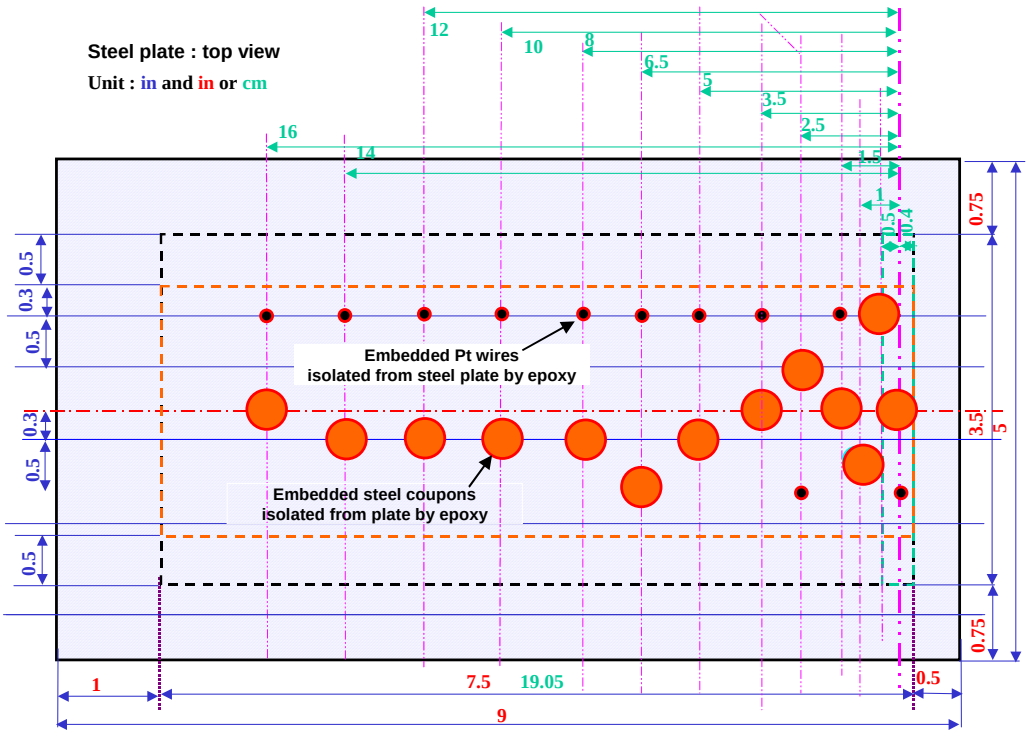

Figure 5-14. The steel plate with embedded coupons and Pt wires and their locations on the steel plate. Note the right side is holiday area.

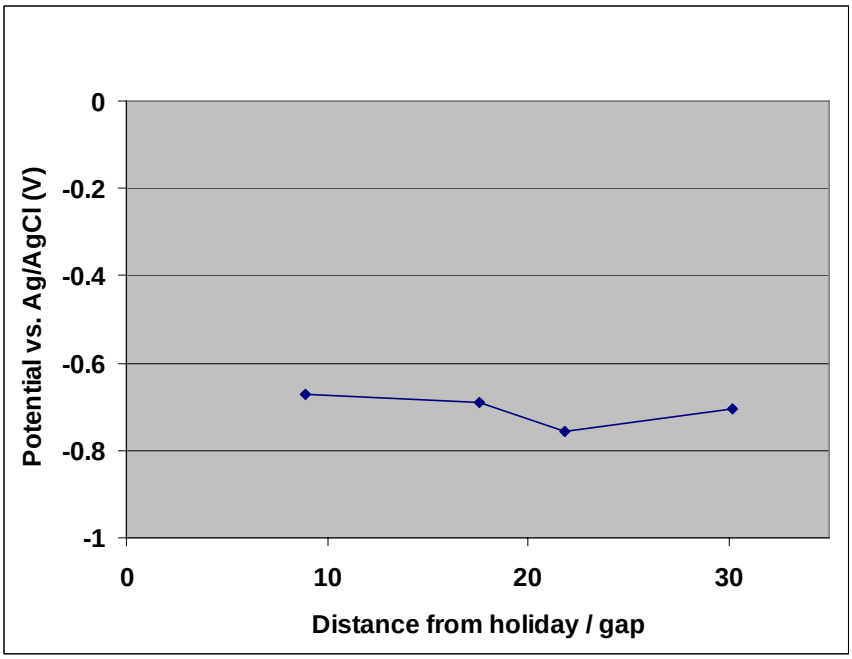

Figure 5-15. Steel potential distribution in the lower compartment (entrance on the left).

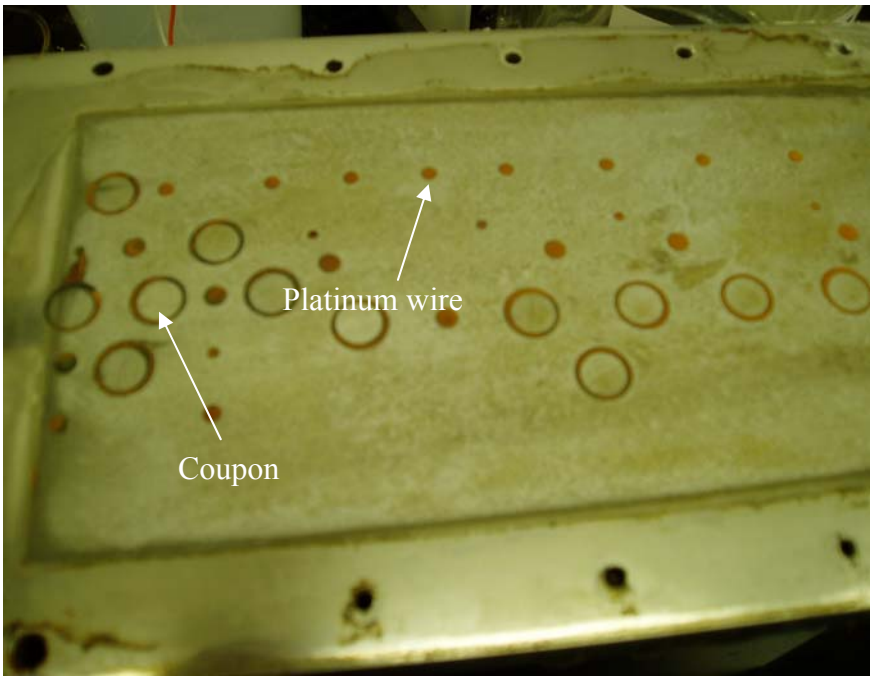

Figure 5-16. Appearance after slight polish of the coupons and the steel plate after they experienced 3-week corrosion in the aerated solution (entrance on the left).

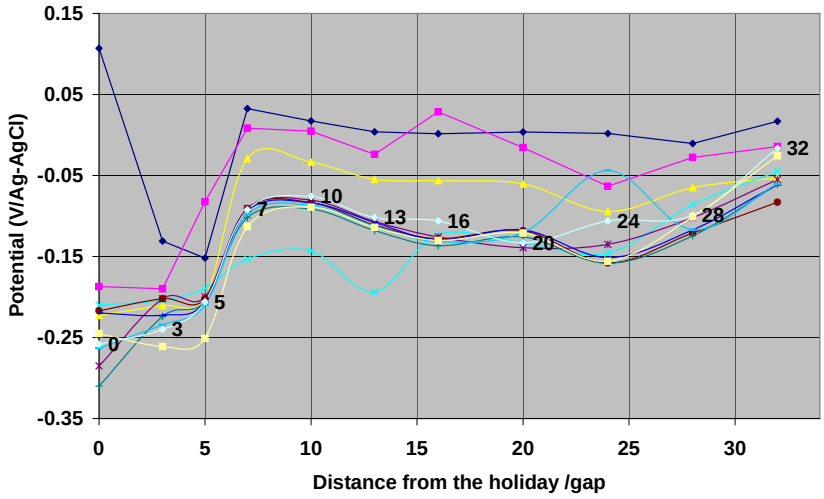

Figure 5-17. Potential distribution of platinum wires at different times in the lower compartment (from left to right).

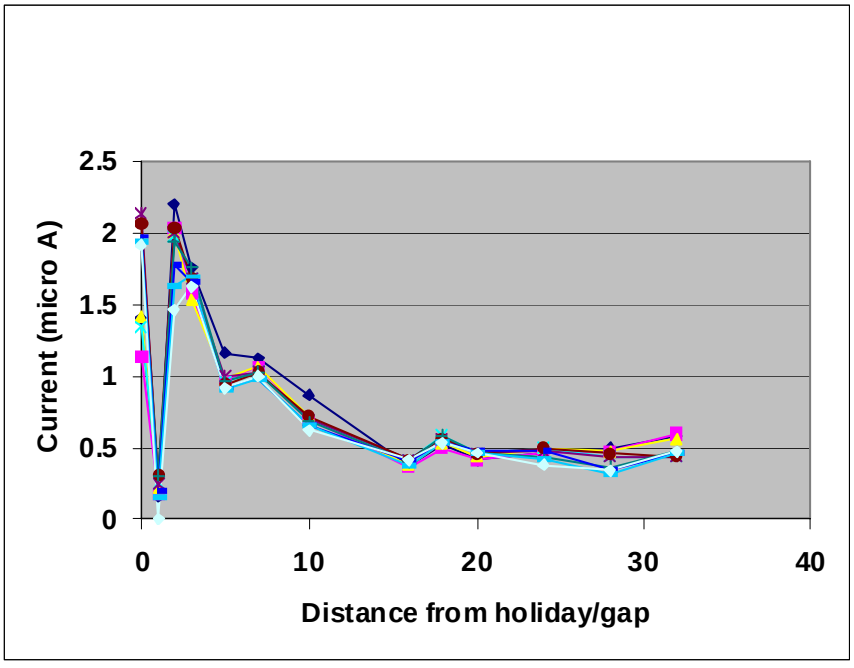

Figure 5-18. The currents flowing from the coupons to the steel plate measured at different times (from left to right).

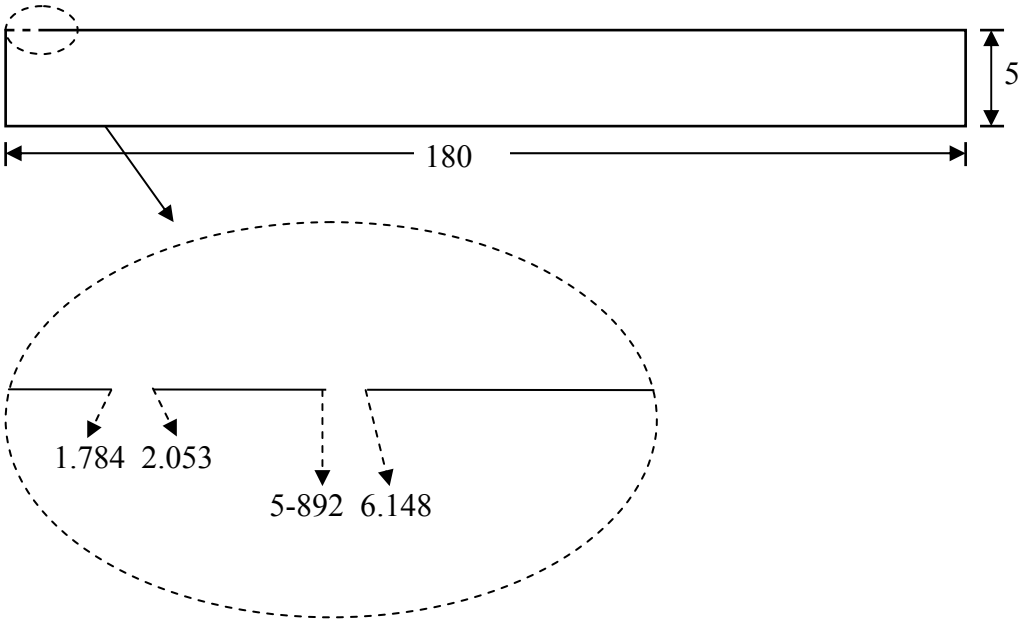

Figure 5-19. Schematic diagram as a simulation of the test geometry (to be shown soon) with the dimensions labeled, unit in mm. The top boundary is coating, bottom boundary is steel surface and very left boundary is PMMA plate with zero flux or flow. The very left part of the coating, which is expanded with the distances from the very left labeled, contain two small holes from which the aerated solution enters. The solution exits from the very right boundary after reaction with the steel surface.

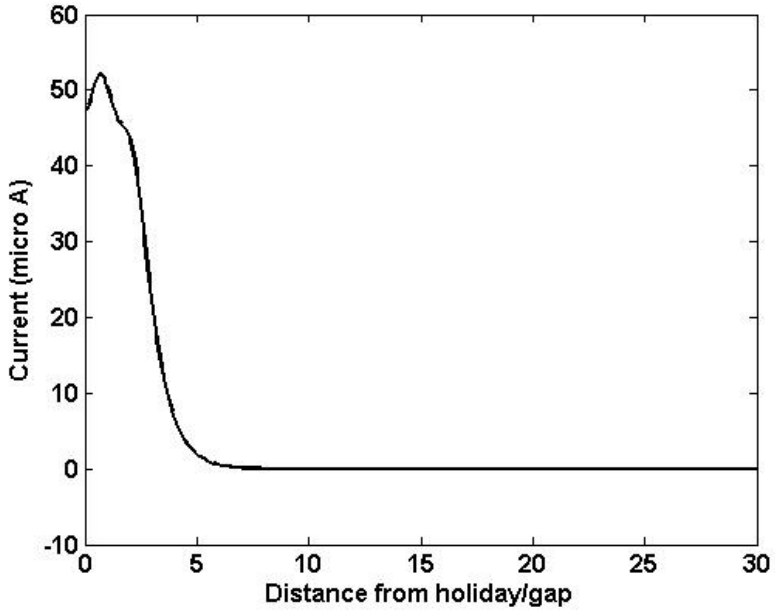

Figure 5-20. The simulated currents that flow from the coupons to the steel plate measured at different times (from left to right).

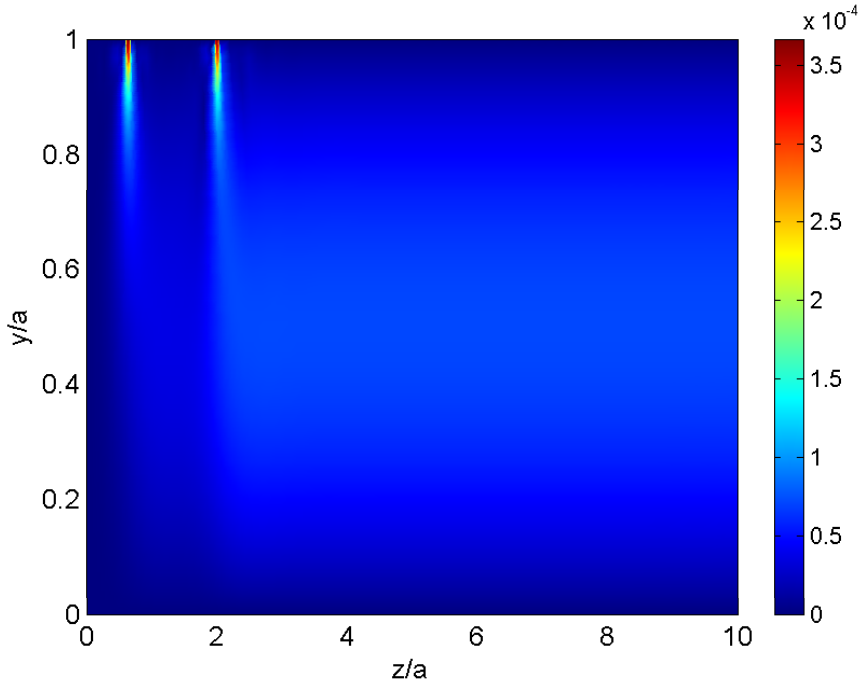

Figure 5-21. Velocity profile in the left portion of the 2D geometry (average velocity along the right boundary is 4.8×10^{-5} m/s or 0.29 cm/min).

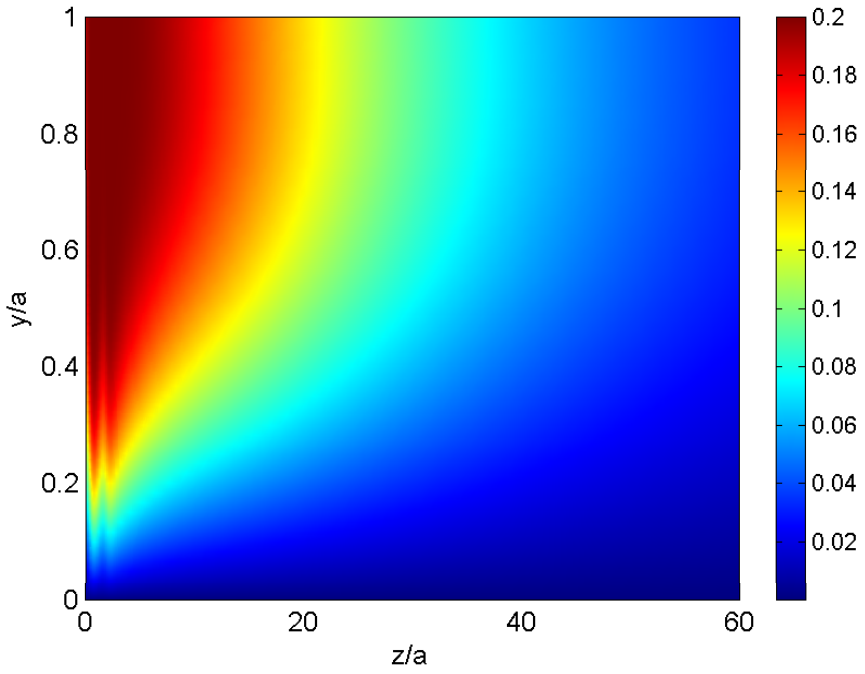

Figure 5-22. Dissolved O_2 partial pressure profile in the 2D geometry (average flow velocity along the right boundary is 7.14×10^{-5} m/s or 0.29 cm/min).

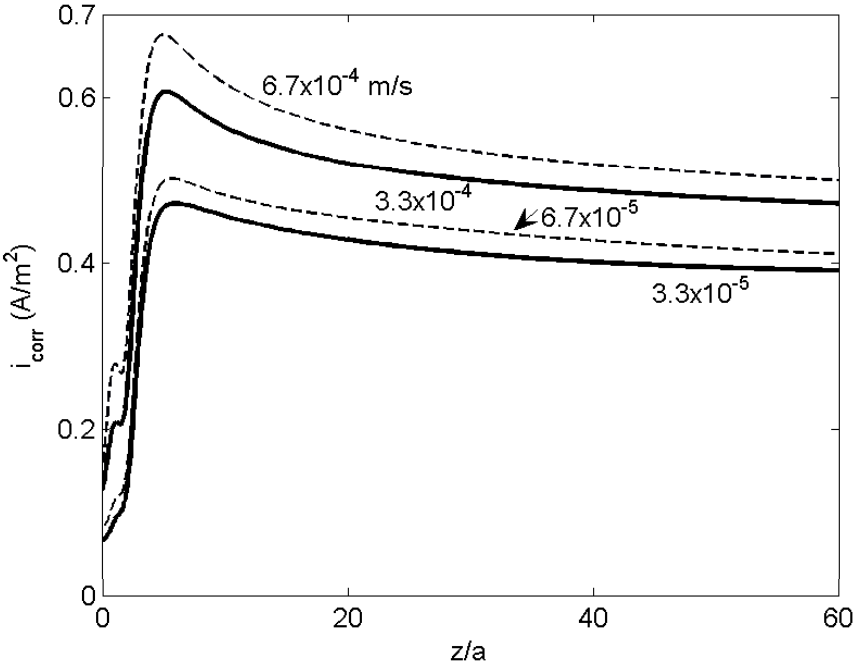

Figure 5-23. Steel corrosion current density profiles, in the left portion of the 2D geometry, for four average flow velocities in m/s.

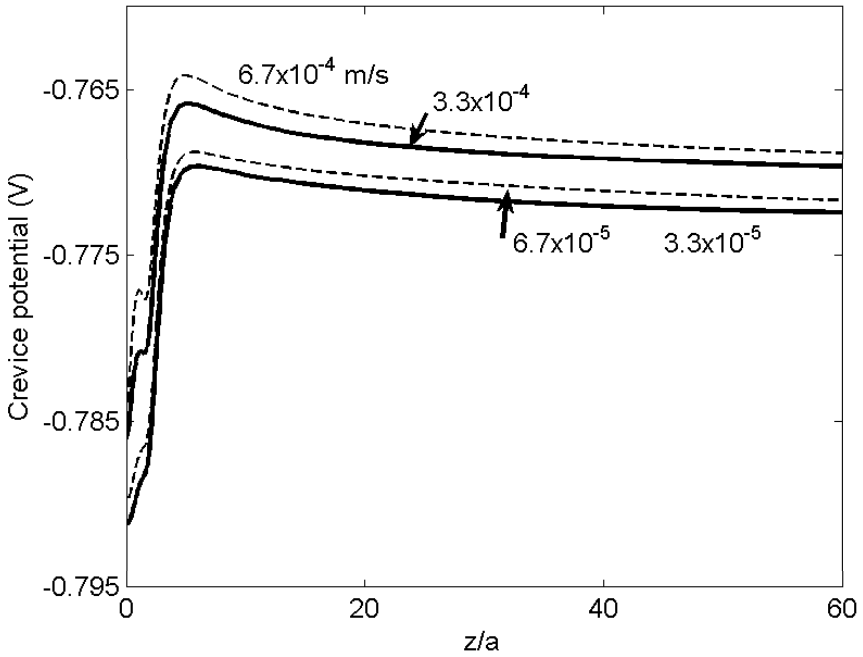

Figure 5-24. Steel corrosion potential profiles, in the left portion of the 2D geometry, for four average flow velocities in m/s.

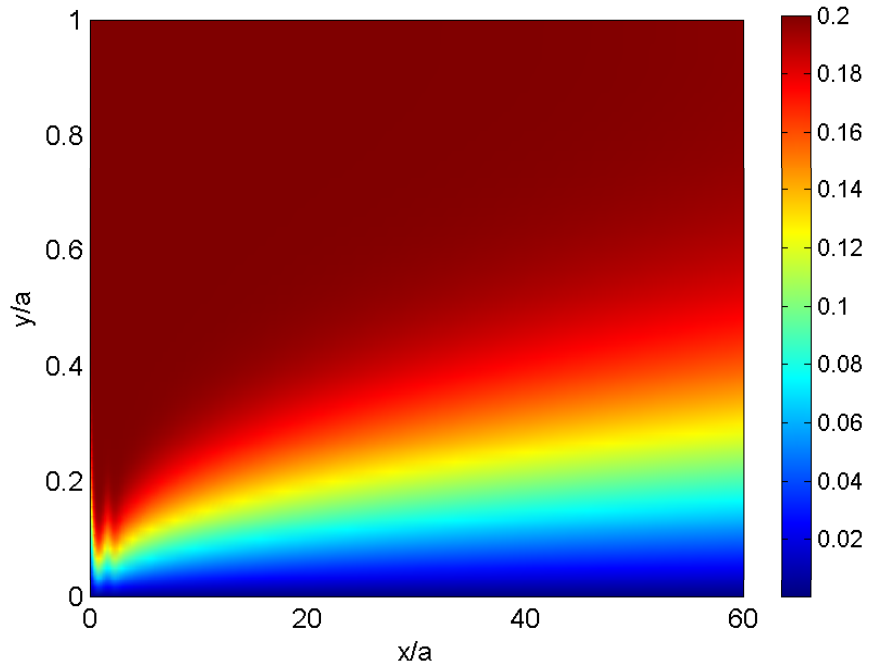

Figure 5-25. Dissolved O_2 partial pressure profile in the 2D geometry (the average flow velocity along the right boundary is 6.7×10^{-4} m/s or 4 cm/min).

6.0 FIELD VALIDATION OF THE INTERNAL CORROSION RATE CALCULATION (TASK 4)

Validation of the model using field data is not straightforward because the exact evolution of the environment at a corroding location is normally unknown. The chemistry sampling during excavation can only provide information at that particular time. This one-time sampling data can be misleading if the environmental conditions had experienced significant changes due to flow, gas composition and operational variations. Thus, without historical information the model validation can be mistaken. An effective validation would be to use data generated under controlled environment. Laboratory data can provide such use. Since the aim of developing this model is rather to predict field corrosion, the consistency check between the model results and field corrosion data is performed.

6.1 Validation of the Model with Literature Laboratory Data

The corrosion of the steel occurs often under a solution boundary layer. For corrosion due to dissolved CO_2, this boundary layer may be saturated by ferrous carbonate. Unsaturation can also be possible. In the absence of H_2S or in the presence of H_2S in the gas but in lower content, the model was verified against published experimental data under two broad conditions: (1) boundary layer saturated with ferrous carbonate, and (2) boundary layer unsaturated with ferrous carbonate.

6.1.1 Saturated Boundary Layer

For saturated condition, the model yields a unique corrosion rate for a given temperature, CO_2 pressure and boundary layer thickness. No adjustable variable is needed for the corrosion rate calculation. The experimental data of Videm and Dugstad[1] and Rhodes and Clark[2] were used for the model validation. For the validation, the diffusion boundary layer thickness needs to be calculated first. The calculation was performed based on the experimental work from independent sources based on the justification that despite differences of the solution chemistry between this work and that in the literature, the physical diffusion layer thickness should not vary significantly with the chemistry. The experimental data in the literature[3-4] allowed for the boundary layer thickness to be calculated for the three temperatures: 25, 60 and 90°C. It is 0.55 mm for 25°C, 0.35 mm for 60°C and 0.21 mm for 90°C respectively. Details of the calculation have been described elsewhere[5-7]. The boundary layer thickness for 15°C, 0.60 mm, was extrapolated from those at the above three temperatures. The above layer thicknesses were used for the model validation.

Figure 6-1 shows the experimental data of Rhodes and Clark[2] at 25°C. The CO_2 pressure is up to 10.5 atm. The model prediction is greater but within a factor of 1.6 of the experimental corrosion rates. For the experimental data of Videm and Dugstad[1] at 90°C (Figure 6-1), the model slightly overpredicts the experimental corrosion rates. Both Figures 6-1 and 6-2 show a reasonable agreement between the model results and the experimental data, with the prediction slightly conservative.

6.1.2 Unsaturated Boundary Layer

For an unsaturated boundary layer, a saturation factor is used to compensate the unknown extent of saturation of the boundary layer. The factor is defined as the ratio of the concentration product of ferrous ion and carbonate ion to the solubility product of ferrous carbonate. The greater the saturation factor, the closer is the boundary layer to saturation by ferrous carbonate. Here, this saturation factor is used as the only adjustable variable to fit the model corrosion rates to the experimental data. The consistency between the model results and the experimental data can be tested.

The sensitivity of the saturation factor on the corrosion rate at 25°C is shown in Figure 6-3. The greater the saturation factor, the smaller is the corrosion rate. Nearly all of the experimental data fall in the range of saturation factors between 0.01 and 0.1, while at a saturation factor of 0.03, the model results are shown to best fit the experimental data.

For 90°C with CO_2 pressures up to 6 atm at a saturation factor of 0.1, the model corrosion rate is shown in Figure 6-4 to be in good agreement with the experimental data.[1]. Good agreement between model prediction and experimental data[4,8] is also shown in Figure 6-5 for CO_2 pressures up to 1 atm and temperature of 60°C at a saturation factor of 0.1.

In Figure 6-6, the corrosion rate was calculated for 15°C at a saturation factor of 0.004 and compared with experimental data[8]. Again, good agreement is shown. The saturation factor which fits data the best decreases with increasing temperature, probably due to lower corrosion rates at the lower temperatures.

6.2 Validation of the Model with Field Data

Field internal corrosion data were obtained from SoCal Gas. The FSM-IT monitoring matrices were installed to monitor the internal corrosion on drip leg and pipe bend segments as shown in the drawing (Figure 6-7) and as photos (Figure 6-7).

6.2.1 Field Data

The FSM-IT data on most locations indicates wall loss very near or below the detection threshold of 0.5% of the wall thickness. These locations are therefore considered to be very slight or no corrosion.

The FSM-IT matrix on the L-1005, 20" bend and drip leg shows minor wall loss (Figure 6-9). The most recent readings were taken on August 4, 2005. The wall loss is typically general in nature but some localized attacks have also been detected. The FSM-IT matrices record a maximum wall loss of 15 mils (2.7% reduction in wall thickness) and 17 mils (4.6% reduction in wall thickness) respectively for slightly over two years. For the bend at the location of deepest wall loss the average corrosion rate is approximately 11 mpy and the greatest instant corrosion rate is approximately 24 mpy. For the drip leg the above two corrosion rates are respectively 7 mpy and 28 mpy. Since there was noise in the readings due to overhead high voltage power line, error arising from this noise may exist in the corrosion

rate. Accumulated wall loss measured using FSM-IT for L-1005, 22.5" bend and drip leg is shown in Figure 6-10 and for L-1170, 20" drip leg; L-160-070, 20" bend; L-1004, 16" bend in Figures 6-11.

A summary of the accumulated wall loss and the corresponding corrosion rate in average and maximum instant rate is given Table 6-1. The corrosion rate is between 0 and 28 mpy or equivalent to 0~0.71 mm/y.

Table 6-1. Summary of the FSM-IT Monitoring Results for the Four L-1005 Pipeline Installation Locations (Measurement Conducted Between June 2004-Aug. 2005)

FSM-IT Corrosion Monitoring Parameter	L-2005 22" Bend	L-1005 Drip Leg	L-1005 20" Bend	L-1005 20" Drip Leg	L-1170 20" Drip Leg	L-160.070 20" Bend	L-1004 16" Bend Carpinteria	L-1004 20" Drip Leg Carpinteria
Nominal Wall Thickness (mils)	562	375	562	375	375	562	375	500
Maximum Initial Wall Loss (mils)	0	0	0	0	0	0	0	0
Original Wall Loss (5)	0.0%	0.0%	0.0%	0.0%	0.0%	0.0%	0.0%	0.0%
Maximum NEW Wall Loss Detected within Matrix Area (mils)	7	2	15	17	1	3	1	1
NEW Wall Loss Detected with the Matrix Area %)	1.2%	0.4%	2.7%	4.6%	0.2%	0.7%	0.3%	0.2%
Minimum Remaining Wall Thickness (mils)	555	373	547	358	374	558	374	499
Long Term Average Corrosion Rate of Deepest Wall Loss	5	1	11	7	0	3	1	2
Maximum Corrosion Rate of Deepest Wall Loss Area	17	2	24	28	1	5	1	2
Current Corrosion Rate of Deepest Wall Loss Area	0	0.3	10	28	1	2	1	0
Current Corrosion Rate of Most Active PinPair	5	1	19	35	1	5	1	2
Predicted time to Failure (Number of Years based on average rate of deepest wall loss)	119.4	296.6	28.4	50.6	772.9	163.6	272.1	325.7

6.2.2 Model Prediction to Compare with Field Data

The pipelines normally carry dry gas with a total gas pressure of normally 1000 psi for L 1005 20" bend and drip leg, L-1005 22" bend and drip leg and 465 psi for L-1170 20" drip leg. The total pressures of the other bends and drip legs are unknown. Since the gas has a 3% of CO_2 and 4 ppm of H_2S, the partial pressures of the two gases for a total pressure 1000 psi are equivalent to 2 atm for CO_2 and $2.7x10^{-4}$ atm for H_2S. Neglecting H_2S, the uniform corrosion rate computed from the model based on solution constantly present at the pipe surface is at 25^{o}C roughly 0.61 mm/y (Figure 6-2). Considering the complex field conditions that the corrosion is localized increasing the rate while the pipeline experience long dry conditions decreasing rate,

the model prediction provides a reasonable conservative prediction of the field corrosion rate, which is in the range of 0~0.71 mm/y.

6.3 Summary

- The model results are in good agreement with laboratory data from independent sources.
- The model prediction provides a reasonable conservative prediction of the field corrosion rate.

6.4 References

1. K. Videm and A. Dugstad, Materials Performance, March (1989) 63.
2. F.H. Rhodes and M. Clark, Industrial and Engineering Chemistry 28, 9 (1936) 1078.
3. H. Uhlig, D. Triadis, and M. Stern, J. Electrochem. Soc. 102 (1955) 59.
4. G.T. Skaperdas and H.H. Uhlig, Industrial and Engineering Chemistry 34, 6 (1942) 748.
5. F.M. Song, D.W. Kirk, J.W. Graydon and D.E. Cormack, "Effect of Ferrous Ion Oxidation on Corrosion of Active Iron under an Aerated Solution Layer", Corrosion 58(2) (2002) 145-155.
6. F.M. Song, D.W. Kirk, J.W. Graydon and D.E. Cormack, "CO_2 Corrosion of Bare Steel under an Aqueous Boundary Layer", Corrosion 60(8) (2004) 736-748.
7. F.M. Song, D.W. Kirk, J.W. Graydon and D.E. Cormack, "CO_2 Corrosion of Bare Steel under an Aqueous Boundary Layer with Oxygen and Cathodic Protection", Corrosion 60(9) (2004) 845-851.
8. C. de Waard and D.E. Milliams, Corrosion 31, 5 (1975) 177.

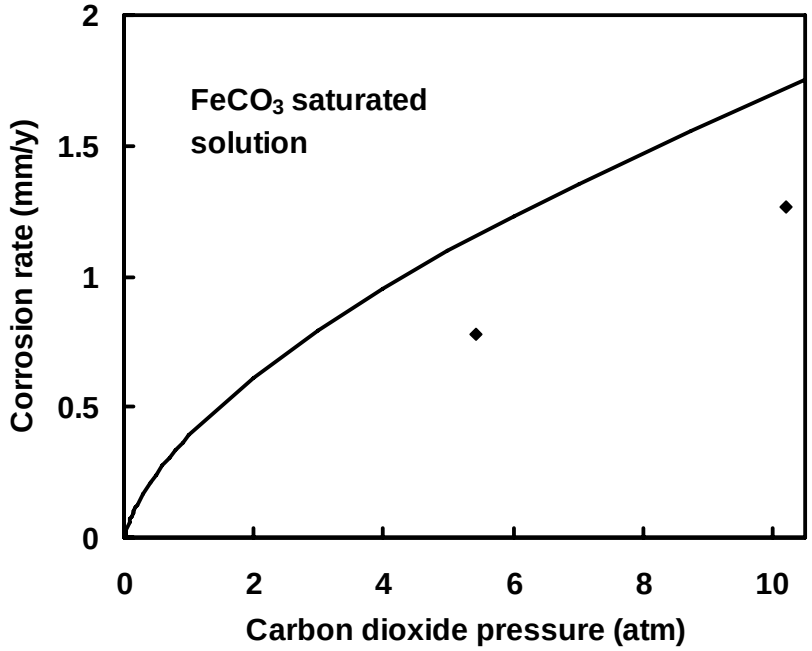

Figure 6-1. Model validation with experimental data under saturated condition (♦, Rhodes and Clark[2]) for 25°C a boundary layer thickness of 0.55 mm.

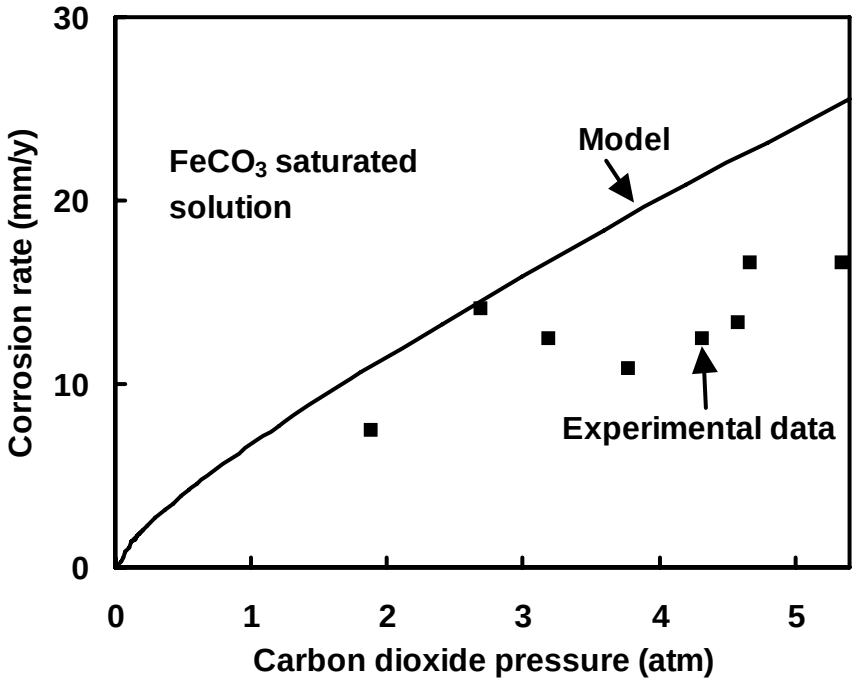

Figure 6-2. Model validation with experimental data under saturated condition (■, Videm and Dugstad[1]) for 90°C and a boundary layer thickness of 0.21 mm.

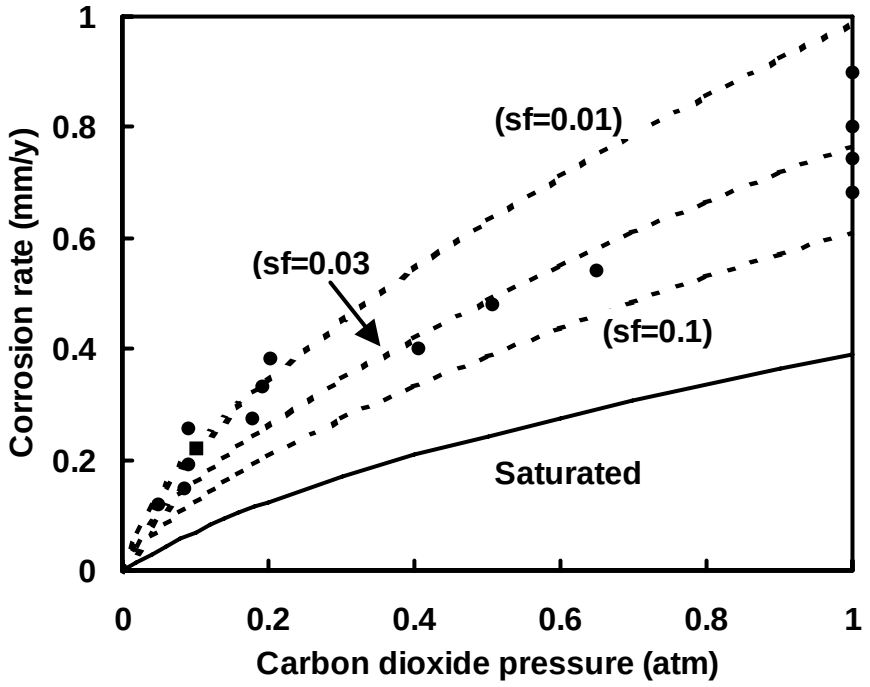

Figure 6-3. Results at 25°C under unsaturated conditions (•, de Waard and Milliams[8]; ■, Videm and Dugstad[1]), showing effect of saturation factor on corrosion rates, boundary layer thickness of 0.55 mm.

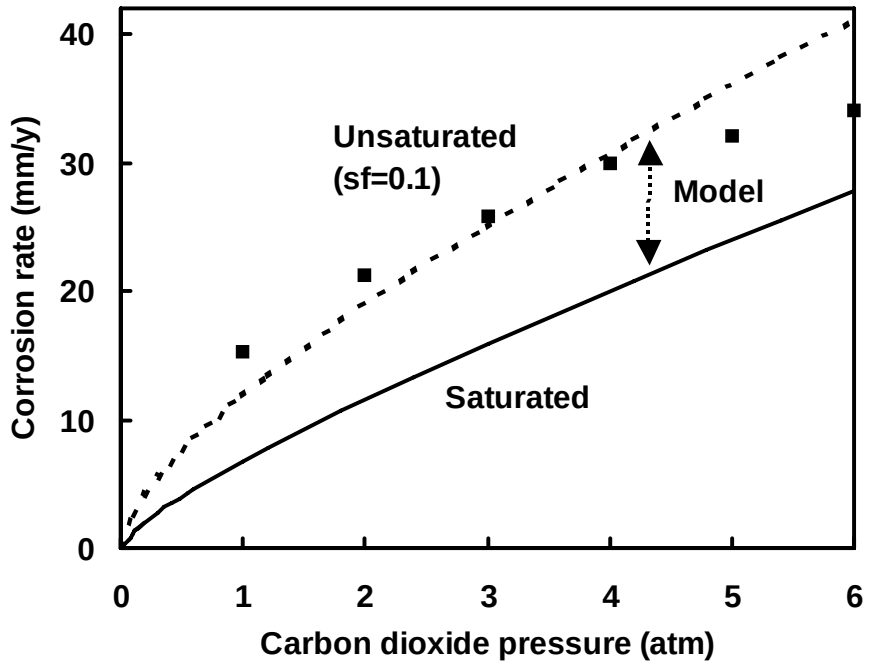

Figure 6-4. Comparison for results at 90°C (■, Videm and Dugstad[1]), for a boundary layer thickness of 0.21 mm.

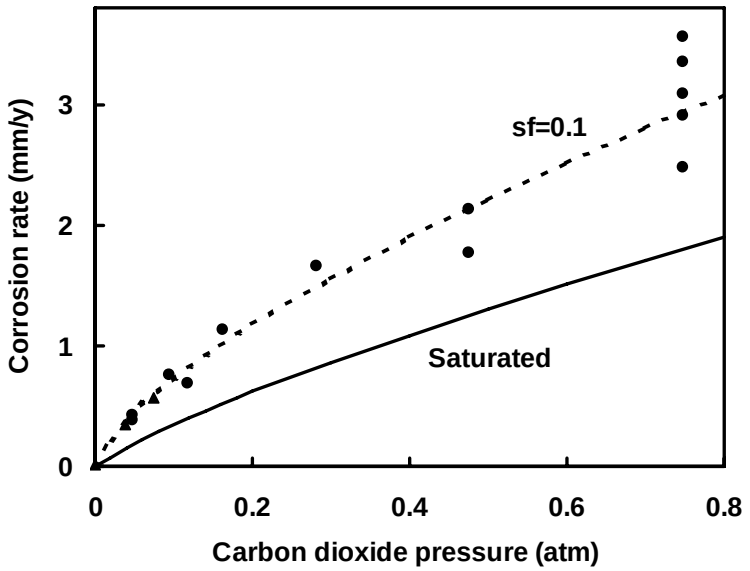

Figure 6-5. Comparison for results at 60°C (•, de Waard and Milliams[8]; ▲, Skaperdas and Uhlig[4]), for a boundary layer thickness of 0.35 mm.

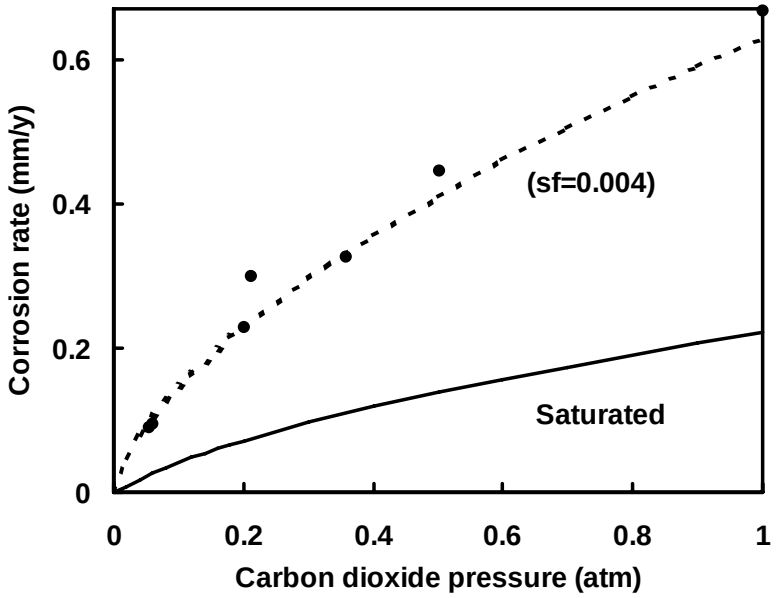

Figure 6-6. Comparison for results at 15°C (•, de Waard and Milliams[8]), for a boundary layer thickness of 0.6 mm.

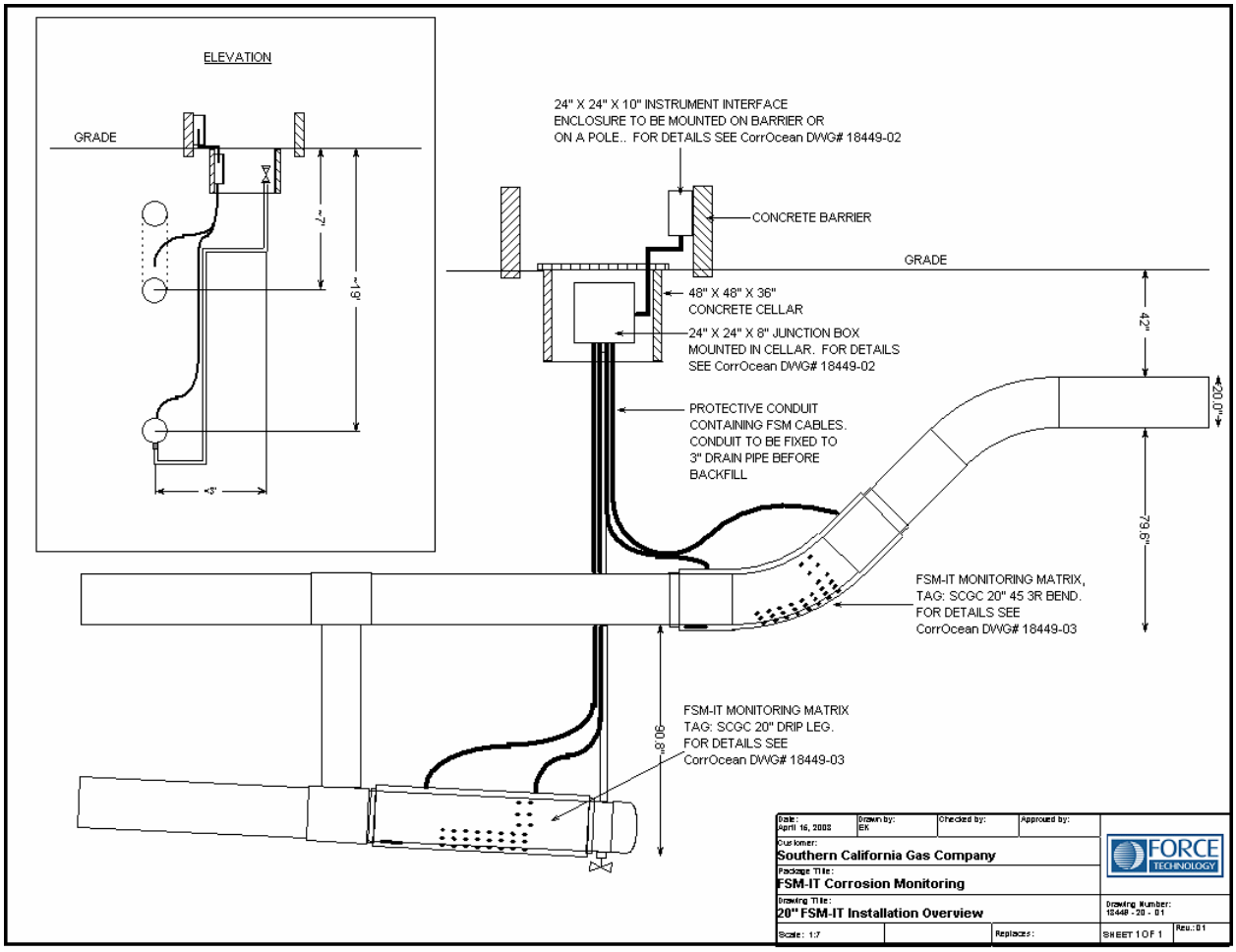

Figure 6-7. Schematic drawing of FSM installations to monitor internal corrosion of a drip leg and a bend.

Figure 6-8. Photos of FSM installation for monitoring internal corrosion.

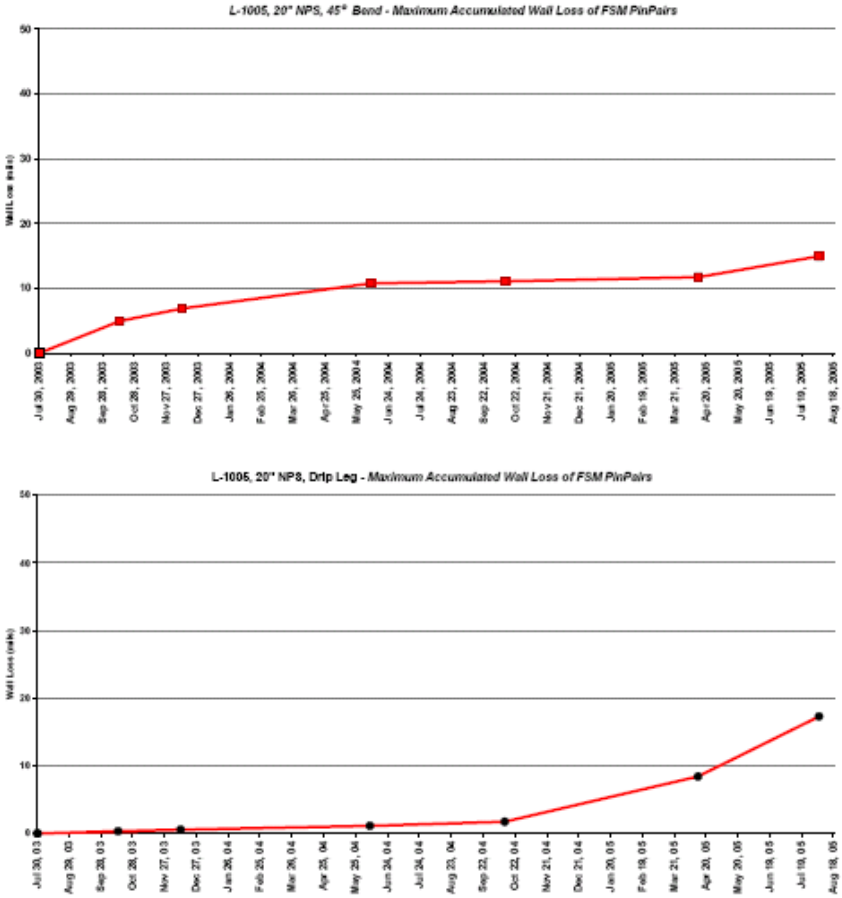

Figure 6-9. Accumulated wall loss in mil based on the FSM-IT matrix measured for L-1005, 20” bend and drip leg.

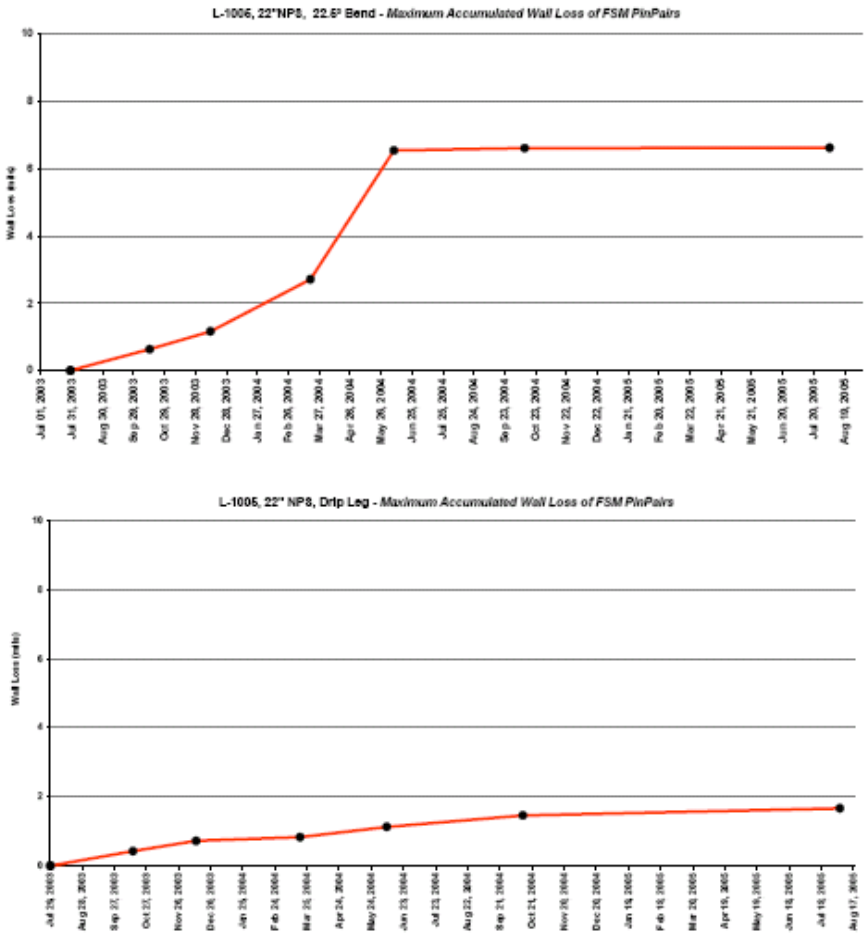

Figure 6-10. Accumulated wall loss based on the FSM-IT matrix measured for L-1005, 22.5” bend and drip leg.

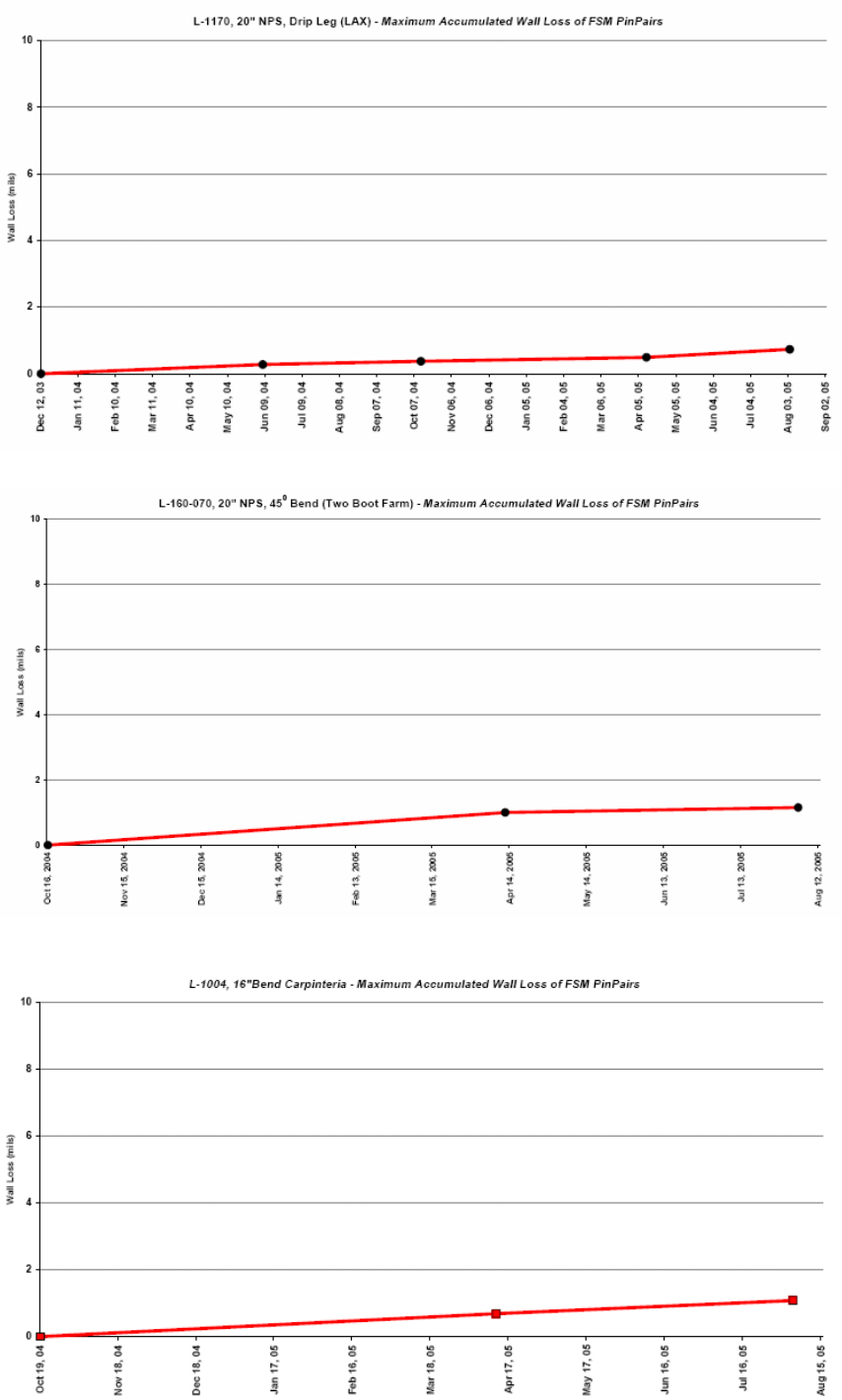

Figure 6-11. Accumulated wall losses based on the FSM-IT matrix measured for L-1170, 20” drip leg; L-160-070, 20” bend; L-1004, 16” bend.

7.0 TASK 5: CONCLUSIONS AND RECOMMENDATIONS

7.1 Conclusions

Detailed corrosion models were developed based on sound fundamental principles to predict the rate of external crevice corrosion and the rate of internal uniform corrosion of natural gas pipelines. Although the field conditions can be quite complex and detailed modeling of these complex conditions poses significant challenge, the modeling approaches can be used to provide sound technical bases for simplified models and help identify gaps in our understanding of the corrosion mechanisms and corrosion rate data.

Based on controlling mechanisms the models were simplified to algebraic equations that are still fundamentally sound and easy for use by pipeline operators. The models were validated with extensive independent laboratory data and by field data available from industrial sponsors. Using the models, significant findings were found and summarized below.

7.1.1 External Corrosion

7.1.1.1 No Flow in the Disbondment

◊ For pipeline steel corrosion under disbonded coating with a holiday, CP is effective only near the holiday region. For corrosion in aerated solution with neutral or alkaline pH, the rate near the holiday and in the disbondment is minimal provided there is adequate CP.

◊ Without CP or with inadequate CP, O_2 can be present at the holiday and diffuse into the disbondment. Since O_2 enters into the disbondment more easily from the holiday than through the disbonded coating, a differential O_2 concentration cell exists. The corrosion rate is greater near the holiday and decreases into the disbondment.

◊ Without CP or with inadequate CP, because of the differential O_2 concentration cell, there exists a positive ionic internal current that flows from inside the disbondment to the holiday region. This internal current polarizes the steel surface cathodically near the holiday and anodically inside the disbondment. Because of this current, the corrosion rate near the holiday is decreased, while inside the disbondment it is increased.

◊ With inadequate CP, the steel at the holiday is polarized cathodically by both the external and the internal currents. Like in the case of no CP, the corrosion rate is still greatest near the holiday and decreases into the disbondment.

◊ Excessive CP is not beneficial to protecte the pipeline because it is ineffective in further reducing the corrosion rate. Meanwhile it increases CP current cost and the susceptibility of further coating disbonding and hydrogen inducing cracking.

◊ The model can used to predict pipeline steel corrosion rate under a disbonded coating without the knowledge of the potential at the holiday, when it is known that CP is not present in the case of shutdown of the CP system.

◊ The pipeline corrosion under a disbonded coating with a holiday in aerated soil solution can be treated as such crevice corrosion in deaerated solution with the same holiday potential. This is valid regardless of presence of CP.

◊ A simple algorithm has been developed following sound fundamental principles, validated quantitatively with extensive independent laboratory data and can be used to estimate the corrosion rate in the disbondment.

◊ Based on the simple algorithm, a procedure is developed for pipeline operators who need only to measure the critical variables to be able to estimate the corrosion rate in the entire disbondment. The variables include the potential at the holiday, disbondment gap, OCP and the linear polarization resistance (R_p) of the substrate material in the soil solution. The holiday potential can be measured by direct current voltage gradient (DCVG) technique, gap can be estimated based on historical experience, and the OCP and R_p can be measured in lab using simulated solution. The above estimation does not depend on the presence of O_2.

◊ For the same degree of aeration in the bulk soil solution, without CP being a worse case scenario, the crevice corrosion rate is smaller than the uniform corrosion rate.

◊ In the case of neutral and alkaline disbondment solution, the corrosion rate in disbondment can generally never exceed 0.4 mm/y regardless of presence of CP. In such a case, the current estimate for reassessment interval based on the uniform corrosion rate of 0.4 mm/y is conservative.

◊ The current seven-year reassessment interval for external corrosion of pipelines in the absence of CO_2 in the soil environment may be conservative.

7.1.1.2 With Flow in the Disbondment

◊ A crevice corrosion model with consideration of convective flow was developed to describe pipeline corrosion under disbonded coating with two holidays allowing aerated soil solution to pass through the disbondment.

◊ The model was validated qualitatively with laboratory data generated by Gaz de France and by the current program.

◊ With or without CP, the corrosion rate inside the disbondment is higher because the convective flow carries dissolved region into the disbonded region where CP is effective.

◊ Depending on rate, convective flow can carry dissolved O_2 into the disbondment much faster than its diffusion. Since the O_2 inside the disbondment cannot be consumed by corrosion, relatively uniform but high corrosion rate is present in the disbondment.

◊ The easy and fast ingress of dissolved O_2 into the disbonded region due to convective flow results in a corrosion rate of the steel in the disbondment greater than 0.4 mm/y. In such a case, the current estimate for reassessment interval based on the uniform corrosion rate of 0.4 mm/y is conservative.

◊ The current seven-year reassessment interval for external corrosion of pipelines in aerated soil in the presence of flow may be non-conservative. Considering the above conclusion is based on continuous flow in the disbondment and fully aerated soil solution while those conditions are not often present in the field, the long-term disbondment corrosion rate can be smaller.

7.1.2. Internal Corrosion

◊ A comprehensive corrosion model with sound fundamental bases was developed to describe internal pipeline corrosion.

◊ The model was simplified to simple equations that are fundamentally sound.

◊ These simple equations can be used conveniently to estimate the corrosion rate of the internal pipeline corrosion, appropriate for field application.

◊ The model was validated quantitatively with extensive independent laboratory data and field data.

◊ For a normal total pressure of 1000 psi and CO_2 content of 3%, the partial pressure of CO_2 can be approximated to be 2 atm. The corrosion rate was calculated to be roung 0.61 mm/y, consistent with field measured values less than 0.71 mm/y measured by Solcal.

◊ Depending on temperature, pressure, gas quality and water content, the internal corrosion rate varies. Assuming constant presence of water on the pipe wall, the pipeline internal corrosion rate was calculated for various CO_2 partial pressures.

◊ Depending on the effectiveness of the inhibitor used and the gas quality in terms of CO_2 content, the seven-year reassessment interval may or may not be conservative. The conservativeness can be more case specific.

7.2 Recommendations

Practical application of the computational results is recommended. In addition, due to time and resource constraint, the effect of many factors on the external and internal corrosion rate of pipelines needs to be examined while neglected in the present project.

7.2.1 External Corrosion

◊ Given no knowledge of O_2 content, the corrosion rate within a crevice formed on buried pipelines under a disbonded coating can be estimated from the algorithm with the need of only three measurable variables: the potential at the holiday, OCP and the linear polarization resistance (R_p) of the substrate material in the soil solution. The disbondment gap may be estimated from historical experience. The holiday potential can be measured

by direct current voltage gradient (DCVG) technique, and the OCP and R_p can be measured in lab using simulated solution. The above estimation does not depend on the presence of O_2.

◊ The effect of CO_2 on the crevice corrosion has been addressed limiting to co-precipitation of ferrous carbonate and ferrous hydroxide. In the presence of ferrous carbonate precipitate alone, this CO_2 effect needs to be addressed further.

7.2.2 Internal Corrosion

◊ The simple equations developed in the program are recommended to use by pipeline operators for evaluation of the internal pipeline corrosion rates, with knowledge of gas temperature, pressure, composition and the presence of water.

◊ The effect of H_2S being not passive has been addressed in the work. Its effect with passivity needs to be addressed.

◊ The combined effect of CO_2 and H_2S needs to be investigated further.

8.0 EXTENSION OF THE PROJECT: EFFECT OF FLOW IN THE DISBONDED REGION ON CORROSION RATE

8.1 Background

Field investigation of external corrosion of underground pipelines indicated possible flow patterns under disbonded coatings[1]. It is speculated that the flow could possibly be driven by gravity moving between holidays connected through disbondments. Although temporary flow may occur in a one-holiday disbondment, this type of flow would quickly diminish as the disbondment is saturated with soil ground water. For a disbondment with two holidays, each at an end, the under-flow could last for quite a long time depending on water table flow velocity, disbondment length, geometry, orientation and surface condition, among other factors. Since this two-holiday flow has more practical significance as the corrosion would be more severe, it is the focus of this work. Depending on the magnitude of flow velocity, the underneath flow could render the otherwise effective CP to become ineffective. The flow velocity varies with factors including disbondment length, orientation, and soil permeability near the holiday. Previous work[2-6] showed that without flow, dissolved oxygen in soil cannot penetrate deep into the disbonded region and a reasonably applied CP at the holiday could sufficiently reduce all oxygen and, thus, fully remove the oxygen corrosion threat. The complication by flow is that it brings corrosive species, such as oxygen, deeper into the disbonded region where CP is shielded and corrosion can be significant. For that reason, a superficially appropriate potential imposed at the holiday cannot stop corrosion caused by the oxygen flowing into the disbondment. The significance of the crevice corrosion could depend on solution resistivity, pH, level of oxygen in soil, coating type, and other factors. The effects of these factors on disbondment corrosion have mostly been studied in earlier work[2-6] under the no-flow condition. This work focuses on the effect of flow velocity and that of the crevice geometry (holiday and gap sizes).

A major difficulty confronted with this study is the exact flow velocities in field conditions. The flow velocity in the disbonded region can be affected by many factors including the relative height between holidays, the configuration, orientation and dimensions of the disbondment channel, the channel's porosity and tortuosity due to the presence of dusts or deposits, the type of soil and the water permeability in it near the holiday mouths, etc. Too slow a water permeability of soil near the entrance and exit (holiday mouths) could significantly delay the underneath flow. The complex flow conditions, which are mostly unknown, determine that the flow velocity in real field conditions is by no means known clearly, although the velocity range could be estimated roughly, which will be discussed later in this work. Since an accurate prediction of the flow effect on the underneath corrosion rate appears to be an impossible task, it is the goal of this work to gain an understanding of the effect of flow velocity in the disbonded region on pipe corrosion rate so that pipeline operators can assess the limiting rates of corrosion. The following approach is taken. Since there is a lack of significant amount of experimental data in the area of flow effect for external pipeline corrosion, the possibility to derive a simple methodology or algorithm through correlation of such data is precluded. Numerical simulation is, therefore, alternatively chosen whose validity will be confirmed through comparison with known experimental results. In the first step of this endeavor, the effect of flow velocity on corrosion rate in the disbonded region will be investigated through comprehensive numerical modeling built on sound fundamental principles. Following that, the numerical solution will be

analyzed and simple equations or algorithms, that can conservatively duplicate the comprehensive numerical corrosion rate, will be derived. A simple methodology, useful for estimating bounding or the possible greatest corrosion rate under a disbonded region, will be developed.

Since the bounding corrosion rates can be used for a "conservative" (higher than real) estimation of corrosion rate, such rates would help pipeline operators to execute proactive mitigation or preventive measures. An additional benefit of the result of this work is that unlike software packages, the approach developed in this work can be easily implemented and requires no training and maintenance cost as otherwise associated. Also, such an approach is more compatible with and can be more readily translated into terms of regulations and standards due to the obvious relation between corrosion rate and flow velocity.

8.2 Fundamental Equations

The general equations for the investigation of flow effect are described in this section. For a 2D rectangular disbondment geometry, as shown in Figure 8-1, the solution ionic chemistry under disbonded coatings is expected to be uniform under the influence of convective or forced flow. Therefore, Laplace's equation can be used to describe charge conservation in this crevice solution:

$$\frac{\partial^2 \psi}{\partial z^2} + \frac{\partial^2 \psi}{\partial y^2} = 0 \tag{8-1}$$

where ψ is steel potential measured by an arbitrary reference electrode inserted in the crevice solution. z and y are respectively geometry coordinators in the horizontal and vertical direction as shown in Figure 8-1.

Under steady-state condition, mass conservation of dissolved O_2, in the presence of flow is expressed by:

$$-D_{O_2}\left(\frac{\partial^2 c_{O_2}}{\partial z^2} + \frac{\partial^2 c_{O_2}}{\partial y^2}\right) + u\frac{\partial c_{O_2}}{\partial z} + v\frac{\partial c_{O_2}}{\partial y} = 0 \tag{8-2}$$

where D_{O_2} and c_{O_2} are, respectively, diffusion coefficient and concentration of dissolved oxygen in crevice solution. u and v are velocities, respectively, in z and y direction.

The Navier-Stocks equations for momentum balance are:

$$\rho\left(u\frac{\partial u}{\partial z} + v\frac{\partial v}{\partial y}\right) - \mu\left(\frac{\partial^2 u}{\partial z^2} + \frac{\partial^2 v}{\partial y^2}\right) + \frac{\partial p}{\partial z} = 0 \tag{8-3}$$

$$\rho\left(u\frac{\partial u}{\partial z} + v\frac{\partial v}{\partial y}\right) - \mu\left(\frac{\partial^2 u}{\partial z^2} + \frac{\partial^2 v}{\partial y^2}\right) + \rho g = 0 \tag{8-4}$$

where ρ and μ are, respectively, density and viscosity of crevice solution. g is standard acceleration of gravity and p is solution pressure.

The equation of continuity is:

$$\rho(\frac{\partial u}{\partial z}+\frac{\partial v}{\partial y})=0 \tag{8-5}$$

Although it is anticipated, and shown later in the results, that simple parabolic flow applies inside the disbonded region, Equations (8-4 - 8-5) are still used because flow near the holiday involves change of direction and therefore, the velocity in "y" direction (Figure 8-1) cannot be neglected. In fact, this velocity rather dominates near the holiday mouth.

The boundary conditions for solving the above equations are listed in Table 8-1, corresponding to boundary numbers of Figure 8-1. In Table 8-1, "L" is the total length of the crevice or the distance between Boundaries 1 and 3 in Figure 8-1. "a" is crevice gap between the inner surface of coating and the steel surface. ψ_0 and $c^0_{O_2}$ are, respectively, potential and O_2 concentration at the holiday mouth. n_{O2} is number of electrons transferred in the elemental O_2 reduction reaction, and F is Faraday's constant.

Since Boundary B1 is a symmetry boundary, the flux of ψ (or equivalent to current by dividing the flux by the solution conductivity λ) and those of c_{O_2} and "u", horizontal velocity, are zero. As a slip boundary, v = 0. At Boundary B3 or exit of the crevice, there is no current flow and the diffusive flux of oxygen is negligible due to either low concentration at low velocity and relatively large convective flux to diffusion. There, the pressure is assumed to be zero. Note that it is the elevation difference between the boundaries of the holiday mouth and exit that determines the crevice flow condition. Since the orientation of the disbondment varies, the pressure at the holiday mouth relative to the crevice exit, which varies with factors including crevice length and orientation, is assumed at Boundary B5. At B5, constant potential ψ_0 and oxygen concentration $c^0_{O_2}$ are assumed. Since there is no mass and current penetration through the coating at Boundary B4, the fluxes of ψ and c_{O_2} are zero. This no-slip boundary determines zero velocity in both y and z directions. Such no-slip boundary also applies to Boundary B2. At this boundary, electrochemical anodic and cathodic reactions occur.

The anodic reaction is iron oxidation:

$$Fe \rightarrow Fe^{2+} + 2e^- \tag{8-6}$$

In the alkaline solution (pH=9.2), by neglecting hydrogen ion reduction the cathodic reactions are water reduction:

$$H_2O + e^- \rightarrow \frac{1}{2}H_2 + OH^- \tag{8-7}$$

and O_2 reduction:

$$O_2 + 2H_2O + 4e^- \rightarrow 4OH^- \tag{8-8}$$

With a reference electrode placed at B5 to measure the pipe potential (ψ_0), the potential anywhere in the solution can be expressed by: $\psi = \psi_0 - \chi$ where χ is electrostatic potential of solution. By assumption, the anodic and cathodic reactions at B2 can be written, for iron vs. ferrous ion redox reaction, in the form of the Butler-Volmer equation as:

$$i_{corr} = i^0_{Fe}(10^{\frac{\psi_s - E^{eq}_{Fe}}{b_{Fe}}} - 10^{\frac{-\psi_s + E^{eq}_{Fe}}{b_{Fec}}}) \tag{8-9}$$

where ψ_s is ψ at the steel surface, i^0_{Fe} is the exchange current density for the Fe/Fe^{2+} redox reaction, b_{Fe} and b_{Fec} are, respectively, the anodic and cathodic Tafel slopes, and E^{eq}_{Fe} is the equilibrium potential.

The Tafel equations for water and O_2 reductions are, respectively:

$$i_{H_2O} = -i^0_{H_2O} 10^{\frac{-\psi_s + E^{eq}_{H_2O}}{b_{H_2O}}} \tag{8-10}$$

and

$$i_{O_2} = -i^0_{O_2\,Ref} \frac{c_{O_2 s}}{c_{O_2\,Ref}} 10^{\frac{-\psi_s + E^{eq\,Ref}_{O_2}}{b_{O_2}}} \tag{8-11}$$

where $i^0_{H_2O}$, b_{H_2O} and $E^{eq}_{H_2O}$ are, respectively, exchange current density, Tafel slope and the equilibrium potential for water reduction. $i^0_{O_2\,Ref}$ is O_2 reduction exchange current density at a reference concentration $c_{O_2\,Ref}$, which corresponds to an equilibrium potential of $E^{eq\,Ref}_{O_2}$, b_{O_2} is O_2 reduction Tafel slope, and $c_{O_2 s}$ is O_2 concentration at the steel surface.

Note that the above exchange current densities and equilibrium potentials are taken at their reference conditions independent of locations at the steel surface. For iron oxidation and water reduction, the exchange current densities and equilibrium potentials are constant regardless of spatial differences. For O_2, the reference condition is 1 atm partial pressure and pH 9[7]. In the previous work[4], Equations (8-9 – 8-11) were expressed in a different but equivalent format where the constants and variables are separated explicitly.

At B2, the diffusion flux of O_2 equals its reduction rate:

$$-D_{O_2}\left.\frac{dc_{O_2}}{dy}\right|_{y=0} = i_{O_2}/n_{O_2}F \tag{8-12}$$

Following Ohm's law, the flux of potential equals the net current density multiplied by solution conductivity λ:

$$\left.\frac{d\psi}{dy}\right|_{y=0} = -(i_{corr} + i_{O_2} + i_{H_2O})/\lambda \tag{8-13}$$

In Table 8-1, I_{net} is net current density flowing to or out of the steel surface, equal to:

$$i_{net} = i_{corr} + i_{O_2} + i_{H_2O} \tag{8-14}$$

8.3 Deaerated Soil Chemistry: Effect of Flow and CP

In the absence of oxygen, Equation (8-2) does not apply. The presence of flow helps to even the ion chemical composition in the disbonded region, while the flow itself does not contribute to corrosion as exhibited in Equation (8-1) which along with the associated boundary conditions fully determines the corrosion process. Here, the porous precipitate, $Fe(OH)_2$, in the disbonded region is assumed to be unaffected by flow since it provides no passivity and there is no erosion corrosion.

In the presence of CP, the corrosion rate in the disbonded region is greater than near the holiday mouth and, therefore, the corrosion rate under open-circuit condition gives a conservative estimate of the overall disbondment corrosion rate. This corrosion rate can be measured in the laboratory using simulated solution. This in-disbondment solution would not have much difference from the soil solution near the holiday.

The effect of holiday size and gap on crevice corrosion rate is negligible and the conservative corrosion rate in the disbonded region is still that measured at OCP.

8.4 Aerated Soil Chemistry: Effect of CP

Depending on flow velocity, CP may or may not have an effect on the steel corrosion rate in the disbonded region.

8.5 Low Velocity

When flow velocity is low, CP can play a significant role as demonstrated in previous work[2-6]. Such applied CP could completely remove the O_2 concentration cell and decrease, significantly, the corrosion rate in the entire disbonded region.

In this case of low flow velocity, hydrogen reduction at low pH condition could have an impact on the corrosion rate. Such low pH solution could arise inside the disbonded region only when CP is ineffective and residual oxygen is present near the holiday (oxygen concentration cell is still effective). The hydrogen reduction effect, however, decreases when the flow velocity increases. At higher velocity, O_2 reduction is predominant, which produces hydroxyls and increases pH.

8.6 Higher Flow Velocity

At a higher but still low flow velocity, the effect of CP is limited near the holiday only. This is because CP itself is not affected by flow while the transport of O_2 is. In this velocity range, corrosion in the disbonded region is mainly affected by the flow-enhanced O_2 transport. Due to the limited effect of CP, such an effect will not be considered in the rest of this work. The potential at the holiday is assumed to maintain at –0.850 V vs. $Cu/CuSO_4$. In this work, all potentials used are relative to $Cu/CuSO_4$, which is 0.316 V more positive than standard hydrogen electrode.

8.7 Computational Results

The focus of calculations below is based on a rectangular disbondment as shown in Figure 8-1 where a symmetrical half of the holiday is shown. In the investigation of flow effect, the holiday with half its length being 5 mm (the total length of the holiday mouth is 10 mm) and the disbondment gap of 3 mm between the inner surface of the coating and steel surface are mainly used. The total length of the disbondment is assumed to be 30 cm regardless of other dimensions of holiday and gap used. The range of half holiday size is 10-30 mm, and that of the gap is 0.1-4 mm. The potential at the holiday mouth is always assumed to be -0.85 V. It is assumed that the steel surface in the disbonded region is covered by saturated ferrous hydroxide having a pH of 9 based on its own solubility. The oxygen concentration at the holiday mouth is 8.3 ppm, corresponding to a partial pressure of 0.21 atm based on Henry's law. The effect of ferrous ion oxidation is neglected as was done earlier with justification[2,4,7]. The temperature and total pressure concerned in the disbonded region are, respectively, 25°C and 1 atm. This work explores the effect of velocity on corrosion rate first, followed by the effect of holiday size and then that of gap size.

8.7.1 *Effect of Velocity*

In this section, the disbondment gap is assumed to be 3 mm, half of the holiday length of 5 mm and the potential at the holiday mouth maintained at –0.85 V. Since the boundary condition at the holiday mouth is set up by a constant pressure, the velocity there is not uniform, which is, as shown in Figure 8-2a, higher near the right edge and lower on the left edge. The obvious reason is that flow tends to enter into the disbonded region through the shortest route, which is the left end. The flow fluctuates near the holiday due to change of flow direction. Not far from the holiday into the disbondment, parabolic laminar flow quickly develops. The velocity field shown in Figure 8-2a is only a portion near the holiday. The rest follows the same parabolic flow pattern. The average velocity in the parabolic region is 0.15 mm/s.

Figures 8-2b-d are the contour plots of O_2 concentration at velocities of 0.15, 0.015 and 0 mm/s, respectively. Along the mouth, the O_2 concentration is higher on the right end because of a greater flow velocity there. Any O_2 diffusion to the steel surface, which tends to reduce O_2 concentration, can easily be replenished by flow. Due to flow, O_2 penetrates deeper into the disbondment as shown. The greater the flow velocity, the deeper O_2 is carried inside.

Figure 8-3 shows variation of corrosion rate vs. distance from left to right at average flow velocities of 0.25, 0.15, 0.05, 0.015, 0.005, and 0 mm/s. Clearly, increasing velocity greatly increases corrosion rate in the disbonded region. With no flow, the corrosion rate decreases monotonously from holiday into the disbondment. With flow, but at a velocity above a certain value (this value was not accurately determined although it is shown below 0.005 mm/s), the corrosion rate first increases with distance into disbondment, then reaches a maximum still near the holiday and finally, decreases with further increase of distance. The existence of this maximum results from the balance among the effect of external CP, the O_2 concentration cell in the crevice and the influence of flow. With O_2 brought inside and limited CP penetration in the disbonded region, the O_2 concentration in the disbondment determines the corrosion rate underneath. Since O_2 concentration is greatest near the intersection between holiday and disbondment, the corrosion rate nearby is greatest. Water reduction in this crevice corrosion contributes little to the rate because of alkaline pH assumed in the disbonded region.

The O_2 concentration cell in the disbonded region results in an ionic current that flows from inside the disbondment and to the holiday region. This current has been discussed extensively in previous work[2-6]. The highest potential is located in where the corrosion rate is greatest due to their Tafel relation. The potential distribution at the above flow velocities is shown in Figure 8-4.

A plot of highest (maximum) corrosion rate at a given flow velocity in Figure 8-3 vs. average flow velocity is presented in Figure 8-5. The two seem to follow an exponential relation. This relation will be elaborated in more detail when the effect of disbondment gap on the corrosion rate is later discussed. The plateau of the maximum corrosion rate (about 0.2 mm/y) is significant because this would represent the highest possible corrosion rate in this disbondment at given dissolved oxygen concentration. Note that the corrosion rate by pitting and cracking is not included.

8.7.2 Effect of Velocity at Different Holiday Sizes

In the section below, the corrosion rate is calculated for a fixed gap size of 3 mm at three holiday lengths of 5 mm, 10 mm and 15 mm.

As shown in Figure 8-6, the holiday size does not seem to have a great effect on flow velocity both near the holiday and inside the disbondment, as long as the average flow velocity is the same. This insignificant effect determines that the corrosion rate is not greatly affected by the holiday size, particularly in the disbonded region. Although the change of holiday size resulted in a slight change of corrosion rate near the holiday area as is shown in Figure 8-7, the maximum corrosion rate is virtually the same. Note that much of the disbonded region is not shown in the figure in order to accent the holiday region where corrosion rate changes the most.

As a conservative estimation of corrosion rate using the maximum corrosion rate, it may be concluded that the effect of holiday size on this maximum corrosion rate does not seem to be significant in the presence of flow.

It has been shown in earlier work[2-6] that in the absence of flow, holiday size could have a significant effect on the disbondment corrosion rate. In the presence of flow, O_2 is brought into the disbonded region and the corrosion rate becomes significant. Without flow, the larger the holiday size the more significant is access of dissolved O_2 to steel surface and the greater is the corrosion rate.

8.7.3 Effect of Velocity at Different Gap Sizes

In this section, the numerical solution was obtained for a disbondment solution of pH 9, holiday length of 10 mm, at five gaps: 4 mm, 3 mm, 2 mm, 1 mm, 0.5 mm and 0.1 mm.

Figure 8-8 shows an increase of velocity with increasing gap size, although the same pressure, as a boundary condition is imposed at the holiday mouth relative to the solution exit. This increased velocity results from solution gravity because the height of solution level at the holiday mouth relative to center of the exit is increased. It is expected that field disbondments contain porosity and tortuosity and, therefore, this effect of relative pressure on velocity would be small. To retain the same velocity, a greater static pressure needs to be imposed at the holiday mouth. In laboratory tests to simulate field corrosion conditions[1], the laboratory apparatus to study the flow effect has so far not been introduced of porosity and tortuosity. It is uncertain how deviated this artifact would lead to, from the actual field flow effect. The porosity and tortuosity could vary widely in the field and no data is readily available. Therefore, in this present model simulation, the effect of porosity and tortuosity is not neglected.

Due to the increase of velocity by increase of gap, the corrosion rate in the disbonded region increases with increasing gap as shown in Figures 8-9 – 8-10. In Figure 8-9, at relative pressure of 0.002 Pa (corresponding to an average velocity of 0.005 mm/s for the gap of 3 mm), the increase of corrosion rate due to increase of velocity occurs in the entire disbondment. Here, the gravity flow is dominant. The total flow enhances the transport of O_2 to the steel surface. For the relative pressure of 0.006 Pa (corresponding to an average velocity of 0.015 mm/s for the gap of 3 mm), the corrosion rate at greater gaps is rather smaller at and around the holiday (Figure 8-10). This is because the velocity there is relatively small and diffusion of O_2 to steel surface is less efficient due to the increased gap. However, regardless of flow velocity, Figures 8-9 – 8-10 clearly show that as gap increases, the maximum corrosion rate for a given gap increases with increasing gap.

When there is no flow, previous work[2-6] showed that the corrosion rate near the holiday is smaller for a larger gap size, while inside the disbonded region this rate is greater. Near the holiday, O_2 has to go a greater distance to reach the steel surface, while with a larger gap, more O_2 diffuses into the disbonded region and a greater corrosion rate results.

Recall Figures 8-3 and 8-5, which showed, respectively, corrosion rate vs. distance into disbondment and plateau corrosion rate vs. velocity especially for the disbondment gap

of 3 mm. Similar diagrams were also found with other gaps of 4 mm, 2 mm, 1 mm, 0.5 mm and 0.1 mm. Since the maximum corrosion rate for a given flow velocity represents a conservative estimation of corrosion rate in disbondment at that velocity, the maximum corrosion rate vs. average velocity is plotted for all of the gaps, by the use of Pelect number $Pe = \frac{au_{av}}{D_{O_2}}$ to combine average velocity (u_{av}) and gap (a). The following simple empirical equation is derived to give a good approximation to the comprehensive model results as shown in Figure 8-11.

$$\frac{r_{max} - r_{max\,m}}{r_{max\,0} - r_{max\,m}} = e^{-0.03Pe} \tag{8-15}$$

Note that such a fit was also found for gap sizes of 0.5 mm and 0.1 mm, although the fitting curves are not shown. In Equation (8-15), r_{max0} and r_{maxm} are, respectively, maximum corrosion rate at no flow and that at a flow rate that is large enough to attain the plateau corrosion rate r_{maxm}. r_{max0} and r_{maxm}, calculated from Equations (8-1 – 8-5) for various gaps, are presented in Table 8-2.

Equation (8-15) is useful because if variation, with gap, of the large flow plateau corrosion rate r_{maxm} is determined, any maximum corrosion rate at any given velocity can be determined. Note that in no flow condition, the maximum corrosion rate, r_{max0}, at different gaps is not so different and can be approximated roughly by 0.008 mm/y. By neglecting r_{max0}, as it is much smaller than r_{maxm}, Equation (8-15) is reduced to:

$$r_{max} = r_{max\,m}(1 - e^{-0.03Pe}) \tag{8-16}$$

This plateau corrosion rate r_{maxm} varies with gap as shown in Figure 8-12 and can be expressed by:

$$r_{max\,m} = \frac{7}{40} a^{-\frac{3}{4}} \tag{8-17}$$

An excellent agreement between Equation (8-17) and the model computational results is demonstrated. In Equation (8-17), the unit of "a" is in mm.

The combination of Equations (8-16 – 8-17) yields:

$$r_{max} = \frac{7}{40} a^{-\frac{3}{4}}(1 - e^{-0.03Pe}) \tag{8-18}$$

which correlates the maximum corrosion rate at a flow velocity vs. gap.

8.7.4 Effect of Velocity at Different Gap Sizes, with a Different Exchange Current Density of Iron vs. Ferrous Ion

Since corrosion kinetics can vary with the change of conditions of steel surface and environments, and this change varies corrosion rate, it is useful to examine whether this change

would affect format of the above empirical relations. Below is an investigation into the effect of increasing exchange current density of iron vs. ferrous redox reaction from the current 2×10^{-4} A/m^2 to 10^{-3} A/m^2 to reflect change of steel surface condition.

Repeating computations just done in 8.7.3, it was found that the exact format of Equation (8-16) is still valid. For gaps of 0.5 mm and 0.1 mm, a slight discrepancy is observed. The values of r_{max0} and r_{maxm}, calculated from Equations (8-1 – 8-5) for various gaps, are presented in Table 8-3.

By comparison of Tables 8-2 – 8-3, it was found that r_{maxm} is roughly the same except at gaps of 0.5 mm and 0.1 mm. A plot of r_{maxm} vs. gap in mm for this new exchange current density is shown in Figure 8-13 and the curve-fit equation is:

$$r_{max\,m} = 0.2a^{-\frac{4}{5}} \tag{8-19}$$

The correlation of the maximum corrosion rate at a flow velocity vs. gap is found to be:

$$r_{max} = 0.2a^{-\frac{4}{5}}(1 - e^{-0.03Pe}) \tag{8-20}$$

for the new exchange current density.

8.8 Discussion

Equations (8-18) and (8-20) show variation of the highest corrosion rate at a given flow velocity in the disbonded region vs. gap. These two algorithms provide a simple way of conservatively estimating the corrosion rate in the disbonded region when flow exists in the disbonded region. Difficulties exist for field application of these two equations because the flow velocity is hardly known. However, it is known that the velocity should be small. If controlled by flow in soil before entering the disbonded region through the holiday, a rough estimate of the flow velocity may be undertaken below.

When a disbondment is vertically oriented between two holidays, the gradient of the hydraulic head of 1. Therefore, given the typical hydraulic conductivity in the range of $0.1\sim10^{-4}$ cm/s corresponding to the three types of soils: well-sorted sand, sand and gravel, and very fine sand and silt, by taking a typical soil porosity of 0.5 based on that of sandy soil in the range 0.36~0.43 and clay soil in 0.51-0.58, the ground water flow velocity is calculated, based on Darcy's law, to be in the range of $2\times10^{-3}\sim2$ mm/s. The algorithms developed in this work are well suited to estimating corrosion rates within this velocity range.

The significance of Equations (8-18) and (8-20) is that they provide a simple, conservative but quantitative understanding of the possible effect of flow on corrosion in the disbonded region, although a complete understanding of the effect in the entire disbonded region as shown in Figures 8-2 – 8-3 still requires detailed modeling.

Although the two equations appear slightly different in format due to different kinetic parameters of iron vs. ferrous ion used in simulation, which represent different steel surface conditions, the plateau corrosion rates r_{maxm} are roughly the same as shown in Tables 8-2 – 8-3. This result indicates that for the same gap, if the iron oxidation kinetics is altered, the flow velocity for reaching the highest corrosion rate (r_{max}) is correspondingly changed.

The model results in Figure 8-3 are consistent with the experimental results[1]. The corrosion rate in the disbonded region increases with increasing underneath flow velocity and at high velocities, the maximum corrosion rate in the disbonded region is nearly the same or approaches a constant.

In determination of corrosion rates, the steel surface is, in this work, assumed to be active everywhere, both at the holiday and in the disbonded region. In cases where the steel surface at the holiday could become inert due to the presence of calcareous deposits, or the steel near the holiday is passive due to presence of oxygen and alkalinity, the corrosion rate in the disbonded region may be different from the active steel surface. However, the current conservative estimate of corrosion rate is still valid . A more reliable estimate of the rate under passive conditions require knowledge of the passive behavior of the steel in the subject environment.

8.9 Conclusions

- The effect of flow velocity in the disbonded region on the underneath pipe steel corrosion rate was quantitatively studied using model simulation and the results are shown to be qualitatively consistent with available experimental data.

- By analyzing and studying results obtained from detailed modeling considering mass transport, fluid flow and electrochemical reactions, simple algorithms are developed that reproduce results from detailed modeling and reveal the relation between underneath corrosion rate vs. flow velocity and the gap of coating disbondment.

- Although these algorithms can be conveniently used to provide understanding on the effect of flow for a given disbondment gap on the underneath corrosion rate, direct implementation of the algorithms into field application still present difficulties in that the disbondment gap and flow velocity cannot be easily known in field conditions.

8.10 References

1. Xavier Campaignolle, Stéphane Gastaud, Sébastien Karcher, Michel Meyer, “Corrosion of Pipelines under CP in the Presence of Coating Disbonding”, EUROCORR/2004, Paper 074.

2. F.M. Song and N. Sridhar, Corrosion, 62(8) (2006) 676-686.

3. F.M. Song and N. Sridhar, Corrosion, 62(10) (2006) 873-882.

4. F.M. Song, D.W. Kirk, J.W. Graydon and D.E. Cormack, Corrosion 58(12) (2002) 1015-1024.

5. F.M. Song, D.W. Kirk, J.W. Graydon and D.E. Cormack, Corrosion 59(1) (2003) 42-49.

6. F.M. Song, D.A. Jones and D.W. Kirk, Corrosion, 60(2) (2005) 145-154.

7. F.M. Song, D.W. Kirk, J.W. Graydon and D.E. Cormack, Corrosion 58(2) (2002) 145-155.

Table 8-1. Boundary Conditions Used to Solve for Corrosion in Disbonded Region with Under-flow

Boundary→ /Quantity	B1	B2	B3	B4	B5
ψ	$\left.\frac{\partial \psi}{\partial z}\right\|_{z=0} = 0$	$\left.\frac{\partial \psi}{\partial y}\right\|_{y=0} = \frac{i_{net}}{\lambda}$	$\left.\frac{\partial \psi}{\partial z}\right\|_{z=L} = 0$	$\left.\frac{\partial \psi}{\partial y}\right\|_{z=a} = 0$	$\left.\psi\right\|_{y=a} = \psi_0$
c_{O2}	$\left.\frac{\partial c_{O_2}}{\partial z}\right\|_{z=0} = 0$	$\left.\frac{\partial c_{O_2}}{\partial y}\right\|_{y=0} = \frac{i_{O2}}{n_{O2} F D_{O2}}$	$\left.\frac{\partial c_{O_2}}{\partial z}\right\|_{z=L} = 0$	$\left.\frac{\partial c_{O_2}}{\partial y}\right\|_{y=a} = 0$	$\left.c_{O_2}\right\|_{y=a} = c^0_{O_2}$
u	$\left.\frac{\partial u}{\partial z}\right\|_{z=0} = 0$	u=0	/	u=0	/
v	$v\|_{z=0}$=0	v=0	/	v=0	/
p	/	/	$\left.p\right\|_{z=L} = 0$	/	$\left.p\right\|_{y=a} = p_0$

Table 8-2. No Flow and Large Flow Corrosion Rates at Various Gaps ($i^0_{Fe} = 2\times10^{-4}$ A/m^2)

r (mm/y)/ gap (mm)	4	3	2	1	0.5	0.1
r_{max0}	0.00814	0.0083	0.0077	0.00852	0.00852	0.00828
r_{maxm}	0.0551	0.0723	0.1063	0.200	0.352	0.9
r_{maxm}/r_{max0}	6.77	8.71	13.8	23.5	41.3	109

Table 8-3. No Flow and Large Flow Corrosion Rates at Various Gaps (New) ($i^0_{Fe} = 10^{-3}$ A/m^2)

r (mm/y)/ gap (mm)	4	3	2	1	0.5	0.1
r_{max0}	0.03415	0.0368	0.0391	0.0409	0.00852	0.0412
r_{maxm}	0.0563	0.0739	0.1095	0.200	0.215	1.28
r_{maxm}/r_{max0}	1.65	2.01	2.8	23.5	5.26	31.2
β	*0.0294*	*0.0294*	*0.0294*	*0.0294*	*0.01764*	*0.0049*

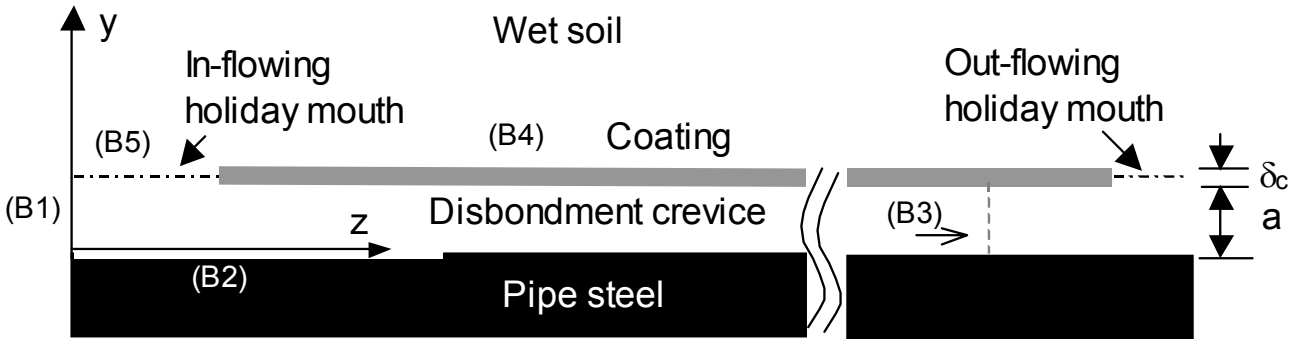

Figure 8-1. Model geometry with under-flow passing through the coating disbonded region.

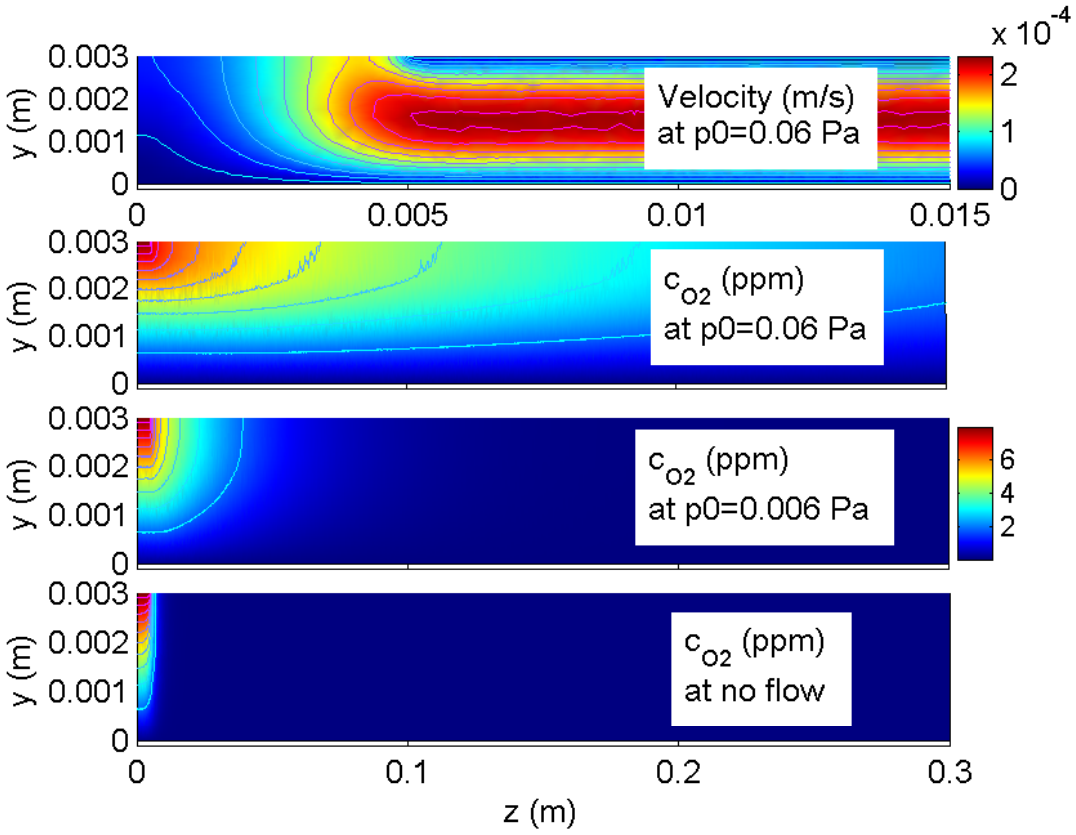

Figure 8-2. Flow and O_2 concentration field at different holiday mouth pressures (Boundary 5) relative to Boundary 3.

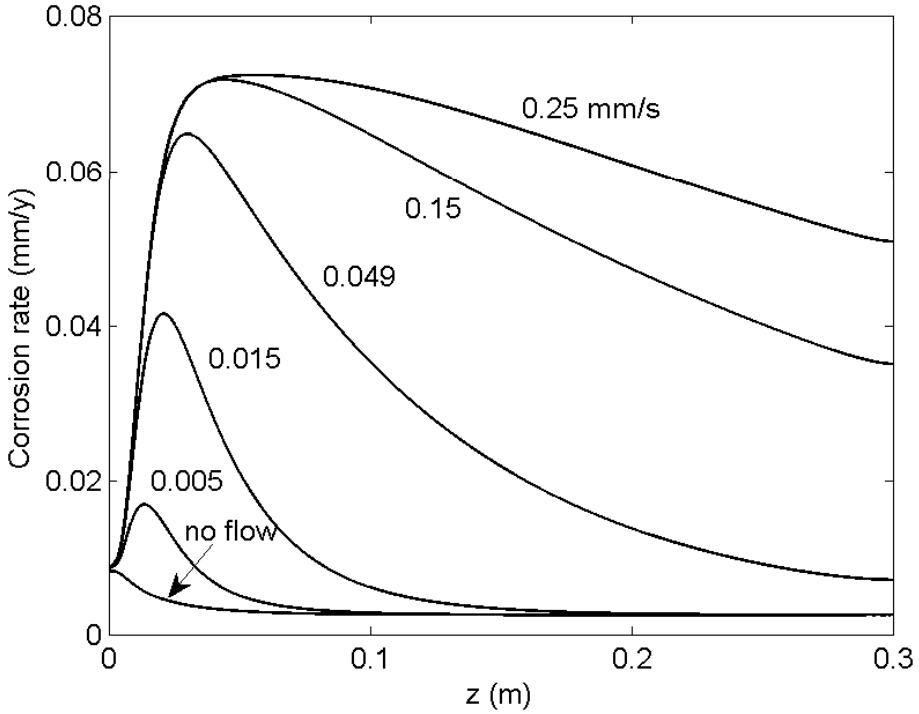

Figure 8-3. Corrosion rate distribution along the longitude of disbondment at five different flow velocities labeled by the relative pressure of holiday mouth to Boundary 3.

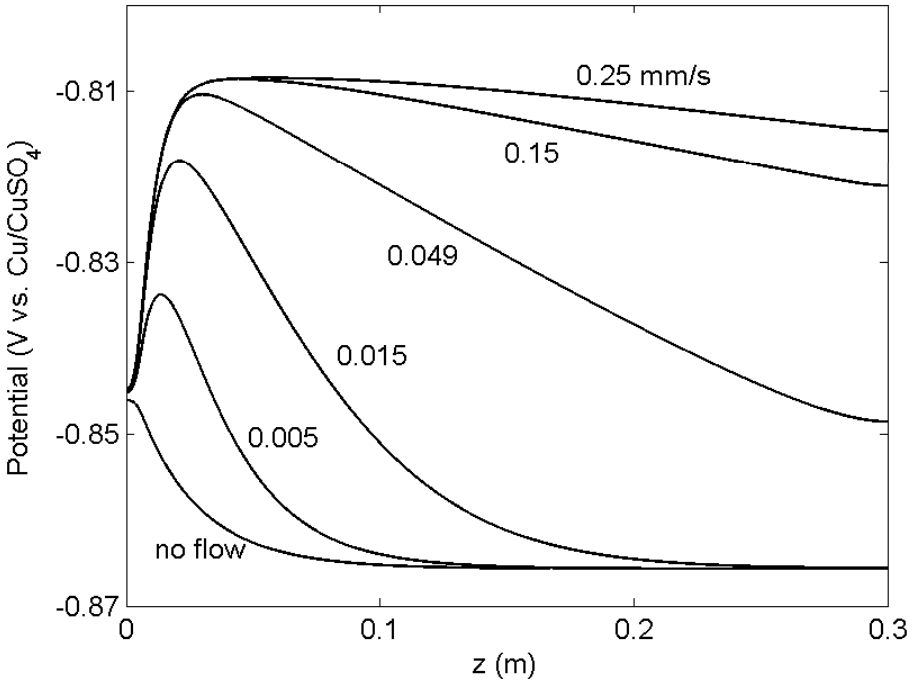

Figure 8-4. Corrosion rate distribution along the longitude of disbondment at five different flow velocities.

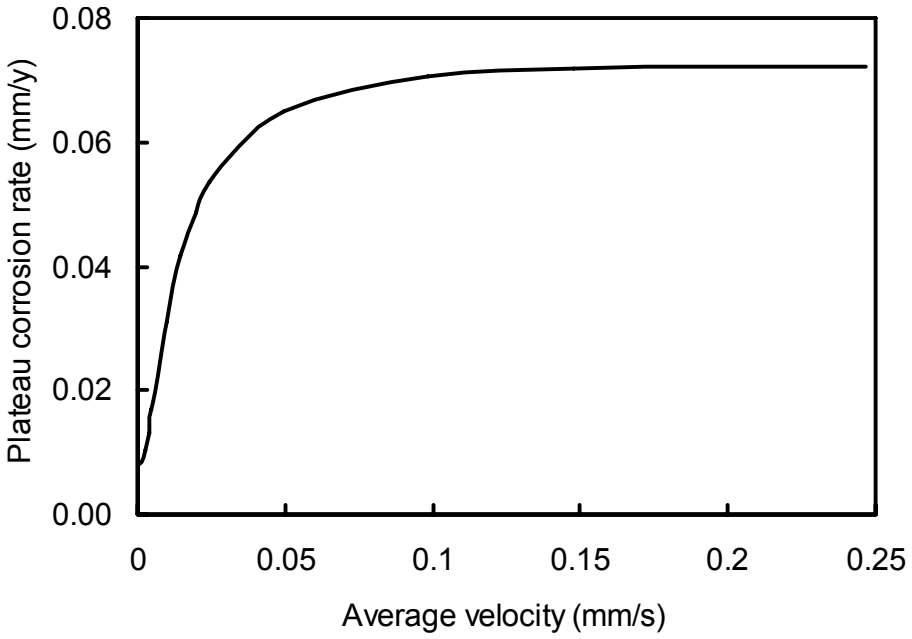

Figure 8-5. Plateau corrosion rate vs. average velocity in disbonded region.

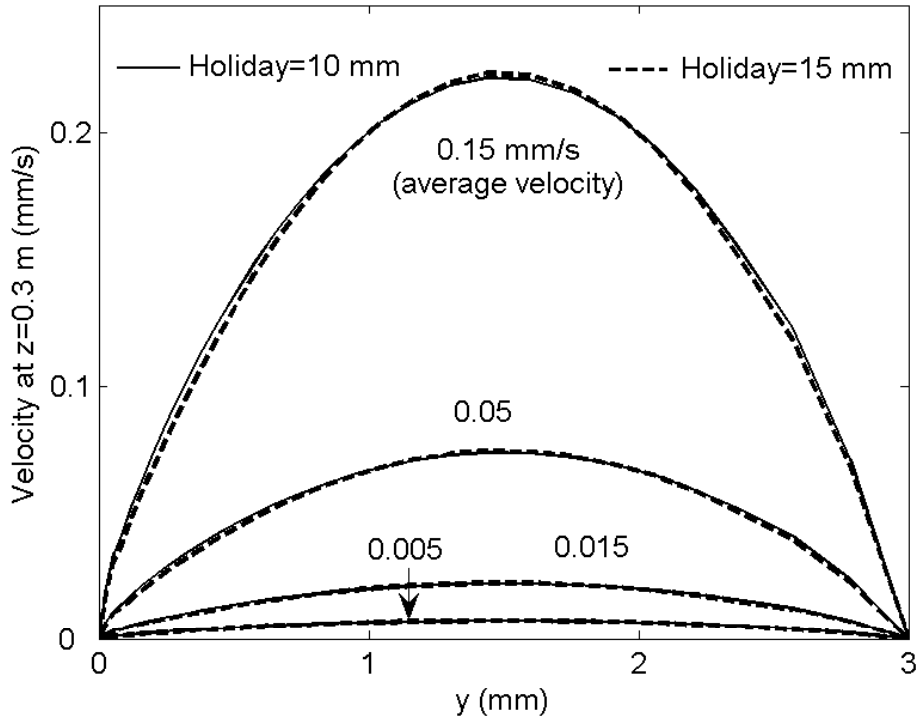

Figure 8-6. Comparison of velocity distribution along gap dimension at two different holiday lengths but at the same relative pressure of holiday mouth to Boundary 3.

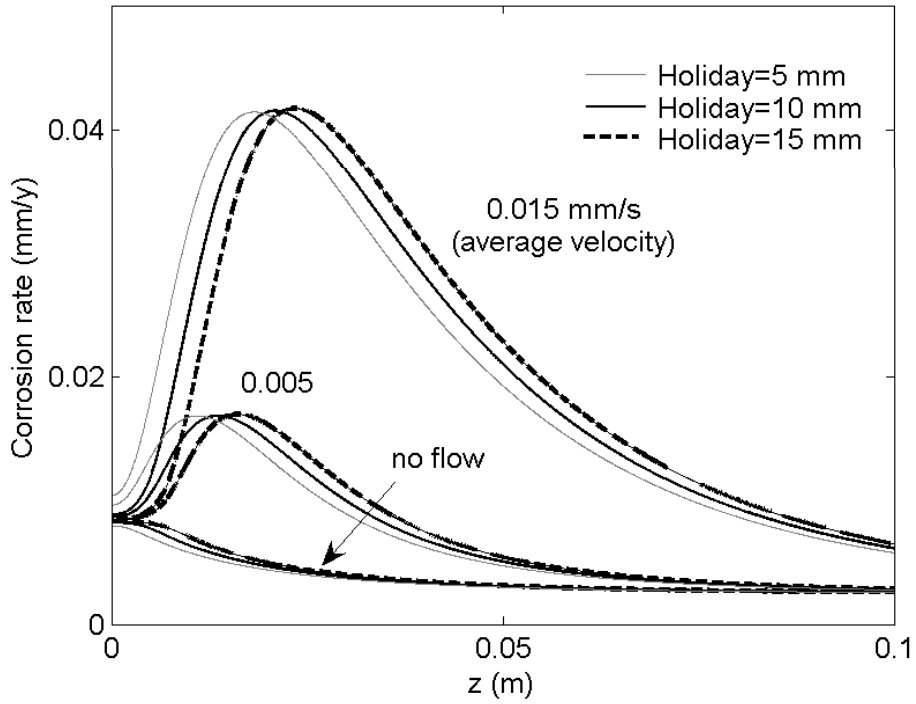

Figure 8-7. Corrosion rate profile along the disbondment longitude at different flow velocity and different holiday lengths.

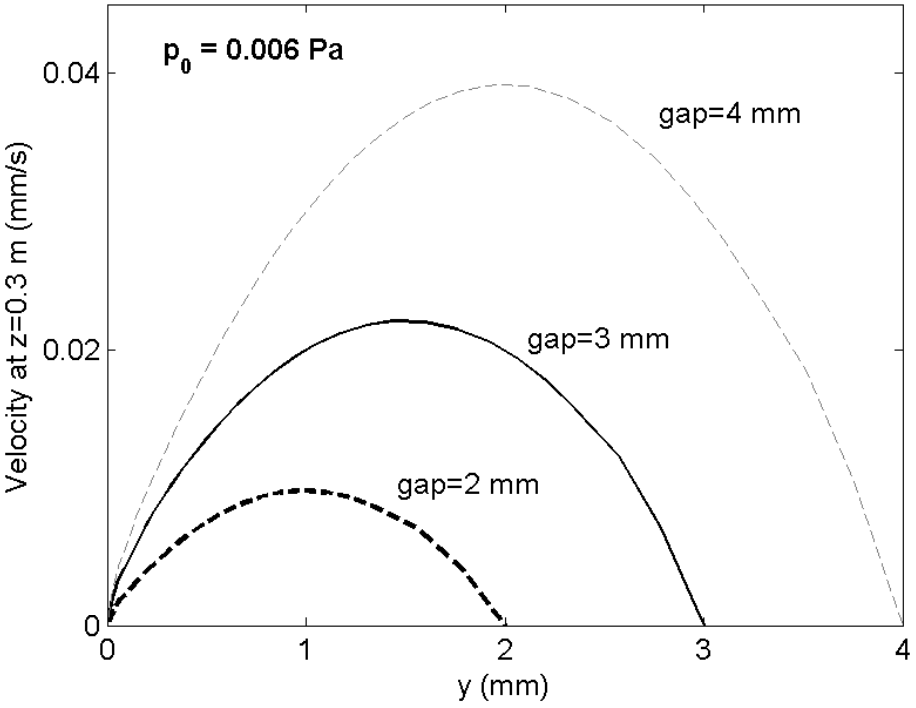

Figure 8-8. Flow velocity profiles in y direction at z=0.3 m for different gaps. The relative pressure imposed at holiday mouth relative to that at the exit is 0.006 Pa.

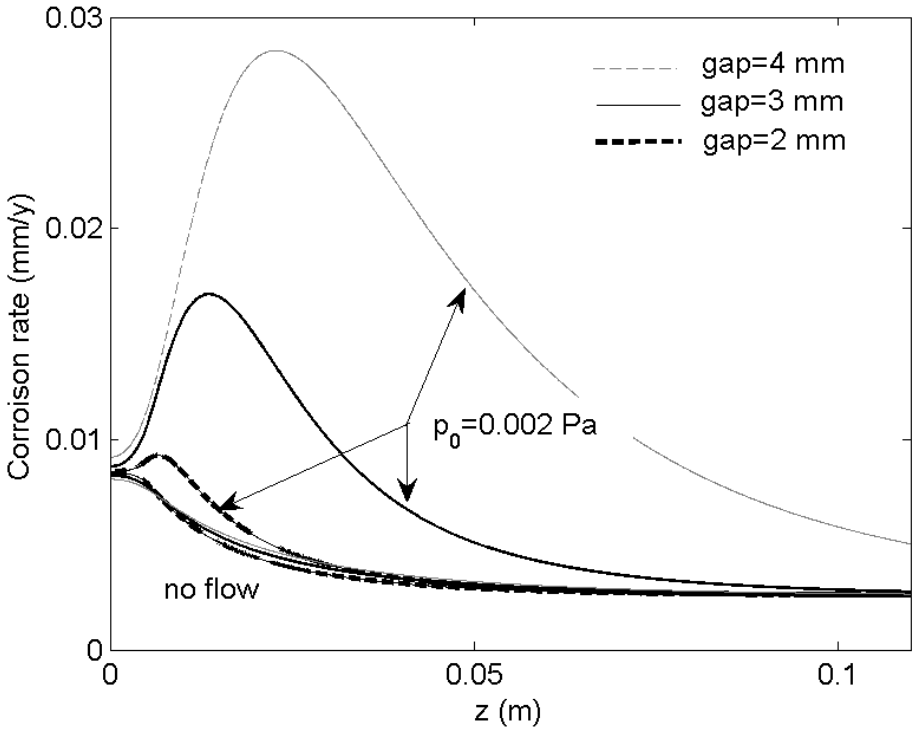

Figure 8-9. Potentials at different gaps for a relative pressure of 0.002 Pa.

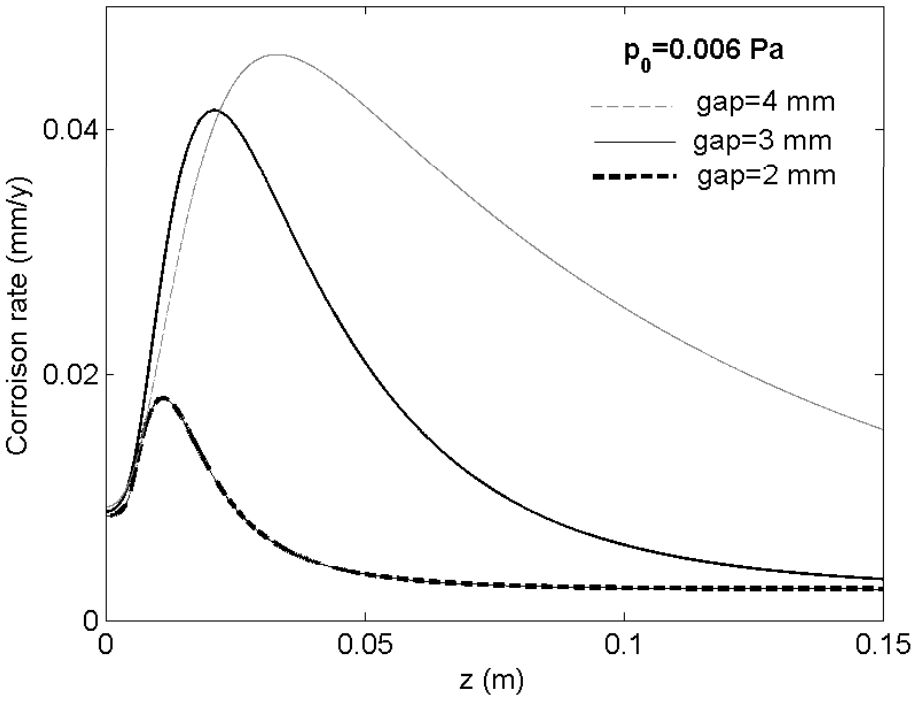

Figure 8-10. Corrosion rates profiles at different gaps for a relative pressure of 0.006 Pa.

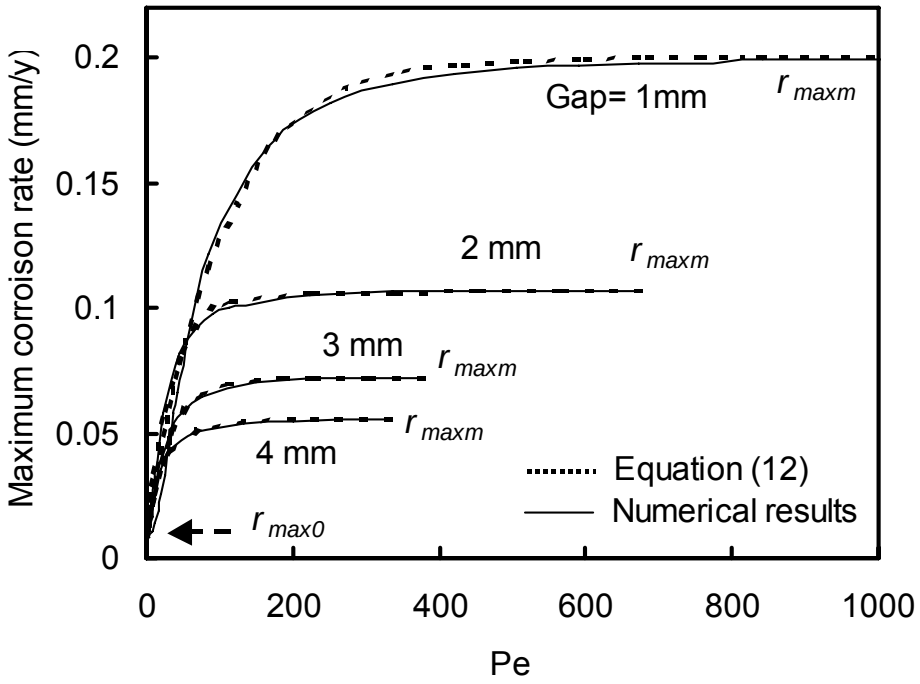

Figure 8-11. Maximum corrosion rate at each velocity vs. average velocity in coating disbonded region. Broken curves are fitting curves computed from Equation (8-15) at β=0.03.

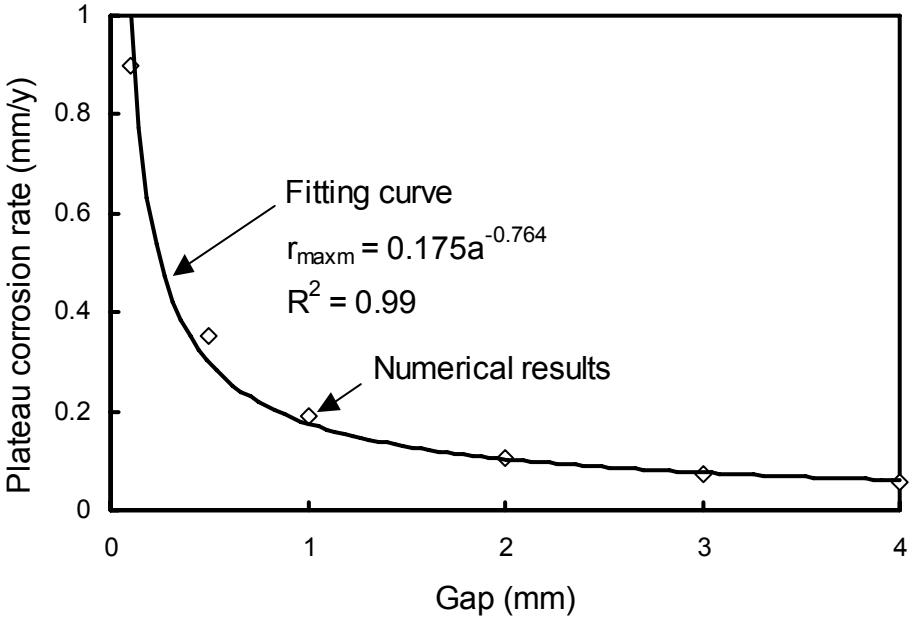

Figure 8-12. Plateau corrosion rate, a rate at which maximum corrosion rate hardly varies with increasing velocity, vs. gap, at exchange current density of iron vs. ferrous ion of 2×10^{-4} A/m^2.

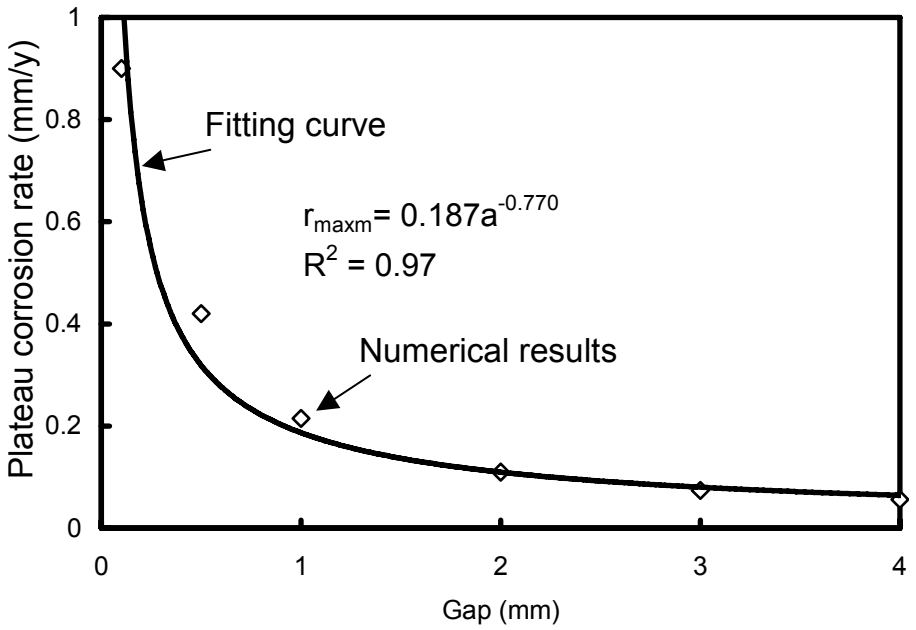

Figure 8-13. Plateau corrosion rate, a rate at which maximum corrosion rate hardly varies with increasing velocity, vs. gap, at exchange current density of iron vs. ferrous ion of 10^{-3} A/m^2.